University of Southampton
FACULTY OF ENGINEERING AND THE ENVIRONEMENT
Aerodynamics and Flight Mechanics

Modelling for turbulent autoignition with split fuel injection

by Nabil Haque MEAH

Thesis for the degree of Doctor of Philosophy

29th October 2016

I, Nabil H. Meah, declare that the thesis entitled *Modelling for turbulent autignition with split fuel injection* and the work presented in the thesis are both my own, and have been generated by me as the result of my own original research. I confirm that :

- this work was done wholly or mainly while in candidature for a research degree at this University;
- where any part of this thesis has previously been submitted for a degree or any other qualification at this University or any other institution, this has been clearly stated;
- where I have consulted the published work of others, this is always clearly attributed;
- where I have quoted from the work of others, the source is always given. With the exception of such quotations, this thesis is entirely my own work;
- I have acknowledged all main sources of help;
- where the thesis is based on work done by myself jointly with others, I have made clear exactly what was done by others and what I have contributed myself;
- none of this work has been published before submission

Signed:.....
Date:.....

Acknowledgements

A lot happened between learning about combustion and investigating a model applied in the field of turbulent combustion. The initial enthusiasm for the project rapidly faded away as I found myself overwhelmed due to the complexity of the project. The journey was punctuated with sparks of excitements along the way that provided me with hope. As it takes time to develop an advanced mathematical modelling, it was unfortunately towards the end of the journey that I was able to indulge in my work. This work could not have been realised without the help of many people who at times motivated me when needed, supported me when needed, helped me with the work when needed and to whom I am very grateful.

The work presented in my thesis could not have been realized without my supervisor, Dr. Edward Richardson. I would like to express my gratitude to him for acting as a mentor, his support during difficult times, and providing me with a stimulating environment to grow.

I am very grateful to the people in the team for the useful discussions and their help. I would like to thank in particular Tom with whom we saw our team growing, for his tremendous help and clever ideas. Bruno and Mark for their help and for having patiently listened to my problems and Stefan for reminding me at times that it is possible to complete a PhD while being a young dad. I would like to thank the seniors in the team, particularly Dr. DongHyuk Shin who shared a part of the journey studying split-fuel injection, for the useful discussions and Dr. Ranga Dinesh for his support. I would like to thank the people for their company at the University, Dr. Jianyue Zhu, Helmizar, Shekar, Hisham, Abdul-Aleem, Ibrahim, Tak, Jawad, Edrees, Sarah, I could not have made it without your support.

The completion of this project could not have happened without the women in my life. I thank my mother who encouraged me at difficult times. I thank my wife, Anisa, for her unwearing patience, particularly for bearing with me during the times I worked during the evenings and weekends. Finally, I thank my little daughter, Maryam, simply for her presence.

I would like finally to express my gratitude to EPSRC for the funding provided.

Abstract

Split-injection is applied in automotive diesel engines in order to control heat release and pollution production. Injecting fuel prior to the main fuel injection, known as pilot injection, increases premixing and tends to reduce NO_x emission. Injecting a portion of the fuel after the main injection has potential for reducing particulate emissions. In order to meet increasingly stringent emission and fuel consumption regulations, modern automotive diesel injectors have been developed with the capacity to deliver of the order of ten separate injection pulses during a single engine stroke. Simulation methods for split-injection engines are required in order to develop more advanced injection strategies with two or more separate fuel-injections. A range of additional combustion applications involve mixing and combustion between multiple streams such as Exhaust Gas Recirculation (EGR) and dual fuel injections. Modelling for the turbulent combustion interactions in multi-stream problems is developed in this thesis in the context of Conditional Moment Closure (CMC) methods.

The CMC approach provides modelling of chemical processes in turbulent flows by linking composition fluctuations to the variation of a small number of conditioning variables such as mixture fraction. In order to achieve good accuracy, the conditioning variables must be chosen to minimise compositional fluctuations around the conditional mean. Split-injection diesel engine operation results in complex combustion behaviour in which a single conditioning variable may be insufficient. However multiple-conditioned moment closures, or even double conditional moment closures (DCMC) have not been exploited previously. The objective of this study is to identify the most appropriate conditioning variables for modelling of split-injection diesel engines and to formulate, validate and demonstrate a practical implementation of the DCMC approach for engine-relevant simulations.

The thesis begins by developing a new formulation of the DCMC approach that is applicable to a general set of non-conserved conditioning variables, and a set of numerical solution approaches is demonstrated and verified. The choice of conditioning variables is then investigated through direct numerical simulations of autoignition in a turbulent flow with up to three separate fuel injections. In the case with a single injection, fluctuations around the mixture fraction-conditioned mean arise due to variation in mixture fraction dissipation rate affecting the progress of ignition differently at different points in space. In cases with multiple injections, the repeated addition of unreacted fuel also adds to fluctuations around the conditional mean. The high level

of conditional fluctuations leads to large errors when employing singly-conditioned first-order conditional moment closure. Alternative doubly conditional moment closure approaches are tested using a priori and a posteriori analyses. Single conditioned first order closure gives extremely poor agreement with the DNS, and the study indicates that double conditioning on mixture fraction and progress variables, such as the sensible enthalpy, outperforms double conditioning on multiple mixture fractions.

The feasibility of the zero-dimensional DCMC approach for practical predictive design calculations is then assessed further through simulations of n-heptane spray ignition in constant volume research vessels with single or multiple injections. The experimental flows are simulated by coupling the zero-dimensional first order double conditional moment closure (0D-DCMC) with a commercial CFD code and an efficient Operator Splitting solution method is demonstrated. The predictions show the same trends as the experimental observations, however ignition delays and lift off lengths agree with the measurements only approximately. Reasons for the discrepancies include the uncertainty in the chemical modelling as well as in the ambient temperature surrounding the spray in the experiments. The modelling of conditional cross-scalar dissipation rate is also found to have a significant influence on the flame evolution, with the limiting cases of modelling corresponding to zero correlation or unity correlation between mixture fraction and progress variable giving unrealistic predictions. Conditional cross-dissipation rate modelling corresponding to negative unity correlation gives reasonable predictions, and an argument for why negative mixture fraction–progress variable correlation is expected to be dominant in autoignitive lifted jet flames involving multiple fuel injections is presented. Other aspects of modelling uncertainty with regard to conditional dissipation rates, presumed joint mixture fraction-progress variable probability density functions and first order source term closures will also contribute to the model error, and further development of models suitable for spray autoignition cases would be beneficial.

In comparison with the established three-dimensional singly-conditioned moment closure (3D-CMC), the 0D-DCMC model is a promising approach which is expected to be substantially faster than the 3D-CMC approach in most problems of engineering interest. Not withstanding the imperfect predictions, the ability of the zero-dimensional DCMC to describe the whole split-injection process and to provide new insight into the mechanisms involved is encouraging: this implies that only a few DCMC control volumes may be needed in order to model a wide range of flows involving very complex physics, of which split-injection is just one example, and the DCMC approach is therefore recommended for further development.

Contents

Nomenclature

α_v	The fractional volume occupied by the fluid
$\Delta h^0_{f,k}$	Enthalpy of formation
δ_l	Flame thickness
δ_{ij}	Kronecker delta
$\dot{\omega_k}$	Molecular production rate
$\dot{\omega_{Y_c}}$	Reaction source term of the progress variable
$\dot{m_{td}}$	The mass transfer rate per unit of surface area
$\dot{S_d}$	Spray source term
$\dot{S_{d,v}}$	Spray source of the progress variable
ϵ	Dissipation rate of the turbulent kinetic energy
η	Sample space variable of the mixture fraction
η_1	Sample space variable of the mixture fraction 1
η_2	Sample space variable of the mixture fraction 2
η_k	Kolmogorov length scale
λ	Thermal conductivity
λ_m	Average thermal conductivity
μ	Molecular viscosity
ϕ	Equivalence ratio
ρ	Density

ρ_L	Density of the liquid phase
τ_{ign}	Ignition delay time
τ_{ij}	The stress tensor
φ_f	Averaged equivalence ratio
ξ	Kinematic viscosity fraction
ξ	The mixture fraction
ξ_1	Mixture fraction of the first injection
ξ_2	Mixture fraction of the second injection
ξ_{mr}	The most reactive mixture fraction
ξ_{st}	Stoichiometric mixture fraction
ζ	Sample space variable of the normalised progress variable
a	The speed of sound
A_d	The surface area of a droplet
c	Normalised progress variable
c_t	Temporal normalised progress variable
$c_{p,d}$	Droplet specific heat
$c_{p,k}$	Heat capacity at constant pressure
D	Diffusion coefficient
D_a	Damköhler number
d_d	Droplet diameter
D_m	Diffusion coefficient of the mixture
e_0	Specific total energy
f	volumetric forces
h_k	Enthalpy of the species k

h_t Heat transfer coefficient

k Turbulent kinetic energy

L_T Turbulent length scale

L_{11} Auto-correlation length scale

le Most energetic length scale

Le_k Lewis number

m_d Mass of the droplet

N_ξ The scalar dissipation rate

N_c Scalar dissipation term of the progress variable

N_u Nusselt number

$N_{\xi,c}$ Cross scalar dissipation term of the mixture fraction and normalised progress variable

N_{ξ_1,ξ_2} Cross scalar dissipation rate of ξ_1 and ξ_2

N_{ξ_1} Scalar dissipation rate of ξ_1

N_{ξ_2} Scalar dissipation rate of ξ_2

p Pressure

$P(\eta)$ Probability density function of the mixture fraction

$P(\eta,\zeta)$ Joint-probability density function of the mixture fraction and the normalised progress variable

$P(\zeta)$ Probability density function of the normalised progress variable

Pr Prandtl number

q The heat flux

Q_k Conditional mean of the mass fraction species

R_u Universal gas constant

Re_d Reynolds number of the droplet

Re_g Reynolds number of the gas phase

Re_T Turbulence Reynolds number

S_h Sherwood number

s_L Laminar flame speed

Sc_k Schmidt number

T Temperature

T_a Ambient temperature

T_b Bulk temperature

T_d Temperature of the droplet

u Velocity of the gas phase

u_d Velocity of the droplet

V_d Volume of the droplet

V_{ij} Species mass diffusion velocity

W Mean molecular weight

W_k Molecular weight

W_{e_g} Weber number

X Proportion of the total fuel injection

X_k Molar fraction species

Y_c Progress variable

Y_k Mass fraction species

y_k'' Conditional fluctuation

$Y_{c,eq}$ Progress variable at equilibrium conditions

List of Figures

Chapter 1

Introduction

The increasing consumption of gas, electricity, and bio-energy over the last few decades has barely offset the dominant use of petroleum fuels in the UK. According to the Environment Audit Committee (2010), liquid fossil fuel use accounted for 50 % of the total overall energy consumption in 1970, only falling to 45 % in 2013 as depicted in Fig.1.1. Most experts from the industrial and transport sectors (Petroleum, 2015) – which are the principal consumers of petroleum – seem to agree that it will continue to play a large role in the near-to-medium future. However, the finite resources of petroleum in combination with the steady increase of the world population, which is estimated to be 20 % higher by 2050, suggests that more efficient and less polluting combustion devices will play a significant role in future energy strategies.

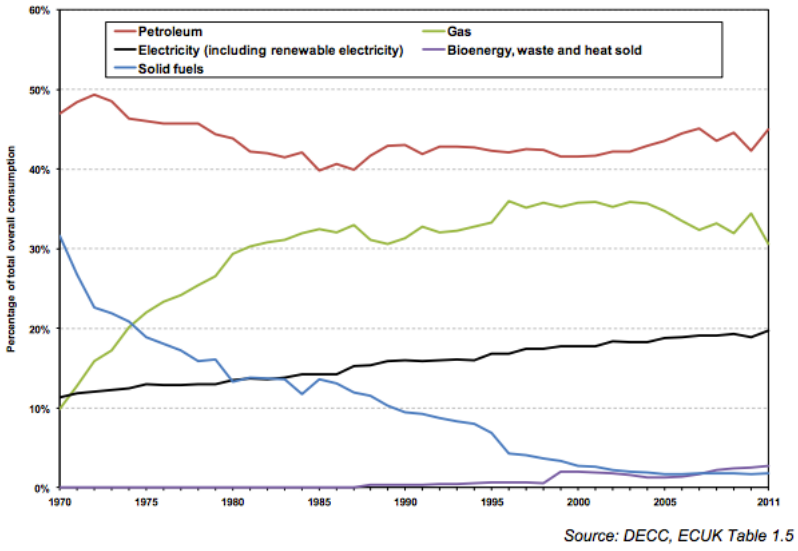

Figure 1.1: Energy consumption from 1970 to 2011 in UK

1.1 Advanced compression-ignition engine technology

In the transport industry, considerable improvement to the internal combustion engine has been made in this regard. Particularly, compression ignition engines have been the object of significant improvement efforts over the last few decades due to their ability to use fuel in order to reach a higher thermal efficiency than the spark ignition engines. This group of engines includes the conventional diesel engine and, more recently, a family of engine technologies that approach approximate to Homogeneous Charge Compression Ignition (HCCI).

The greater efficiency, torque and the durability of the diesel engine have been among the reasons for compression ignition engine technology to be adopted for heavy-duty trucks across the world, and, particularly in Europe, also for light-duty cars. However, engine noise and emissions of pollutants, historically including visible emissions of smoke, have caused diesel engines to become regarded as less environmentally benign. Combustion in a diesel engine is responsible for significant sources of soot particulates and Nitric Oxides (NOx). While after-treatment systems are available and applied to lessen these undesirable effects, additional methods for reducing production of these pollutants have been sought. Many improvements have been facilitated by adoption of the common rail injection system which enables recent models to perform multiple pulses injections. By appropriately choosing the amount of fuel, the number of injections and the injection schedule, numerous injection strategies are possible which may be tailored in order to achieve desirable effects, such as noise and emissions reduction (Ehleskog, 2007) (Barro, Tschanz, & al., 2012) (O'Connor and Musculus, 2013), (Barro, Pandurangi, & al., 2015). However, emissions reduction is a challenging technical problem due to the trade-off between the soot, produced more in richer and colder combustion processes, and NOx, produced more in leaner and hotter combustion processes, which restricts the possibilities of decreasing one pollutant over the other. Multiple injections are a way to circumvent the trade-off by allowing the combustion process to develop in the Low-Temperature Combustion regime (LTC) which enable ultra-low emissions. For soot reduction, post injections (i.e. additional fuel injection events after the main combustion process) have been extensively studied as a means to encourage soot burn out, with one objective of such studies being to identify the appropriate dwell times and to identify the underlying mechanisms reducing soot. Operation in the LTC regime relies upon use of exhaust gas recirculation (EGR) into the intake air, causing a decrease of oxygen in the engine cylinders, thus causing the

combustion to result in lower temperature. However, while extreme levels of EGR tend to continue to reduce soot emissions, the fuel efficiency was found to be impaired. Rather than employing excessive EGR to the detriment of fuel economy, fuel injection profiles may be shaped in order to achieve near-zero NOx emissions and smoke (Sarangi & al., 2013).

Alternative methods for achieving high combustion engine efficiency in combination with low emissions include recent developments of the HCCI engine concept. In these engines, a nominally-premixed mixture of air and fuel (which could be chosen as gasoline, diesel fuel or alternative fuel) undergoes compression ignition. Application of this approach has been hampered by the difficulty of controlling ignition timing, which if too early and rapid can damage the engine. This complication is attributed to the difficulty of controlling the time of autoignition indirectly through the thermal and mixing state of the fluid, unlike the ignition of spark-ignition engines which is controlled directly by the spark timing imposed. Particularly in the low load limit of HCCI combustion, which tends to involve more dilute fuel mixtures, there is insufficient time during the cycle for autoignition to occur. Possible solutions involve using multiple injections to achieve inhomogeneous mixture in which some fluid locally has conditions so that it will undergo autoignition (Yun, Wermuth, and Najt, 2009).

In light of the above discussion, a fundamental understanding of the turbulent chemistry interactions associated with multiple injections in engines is important to the development of strategies for increasing efficiency and reducing emissions. Strategies include exhaust gas recirculation, multiple injections and other combustion approaches that involve multiple streams. While modern common rail technology with piezo electric injectors is capable of producing up to 8 separated pulses, automotive engineers find that the understanding of the chemical, mixing and fluid dynamics of split injection and the available modelling tools are inadequate for the purposes of predictive design, or for understanding engine test data.

1.2 Turbulent combustion in engines

Two limiting combustion regimes have been traditionally defined. In premixed combustion, the fuel and oxidizer are mixed prior to reaction. An external source of energy (spark) triggers the combustion giving place to flame propagation. Examples include lean premixed gas turbine burners and spark-ignition engines. In the case of the fuel and oxidiser being initially separated, the reaction takes place at the location they meet, giving rise to a flame also called a diffusion flame. For example in a diesel en-

gine, a liquid fuel is injected inside a hot oxidizer medium. Combustion is initiated by autoignition, followed by a propagation process that establishes a largely non-premixed flame that envelopes the continuing jet of diesel fuel. In practical devices these combustion processes take place within a turbulent flow, which enhances mixing and can thereby alter the chemical processes taking place.

In turbulence combustion research, the emphasis is often on the fully-developed combustion which is found in steady-flow burners such as gas turbines and industrial furnaces. However, the transition between unreacted, or slowly reacting flow, to fully burning flow through ignition is important for several applications. Autoignition occurs in a slowly reacting mixture without an external source of energy. It is the controlling phenomenon in diesel engine ignition. In Lean Pre-vaporised Premixed (LPP) gas turbines (a technology being developed for low-emission aircraft engines) autoignition may happen in a place not designed for the flame to sit, which can cause structural damage through excessive heating or explosion.

Autoignition in a non-premixed turbulent flow has been characterised in terms of the mixture fraction ξ, which is defined as the fraction of mass at a given location that originated from the fuel stream. Mixture fraction is a conserved scalar that takes values between zero (in pure oxidiser) and unity (in pure fuel). A second key parameter for characterising autoignition is the mixture fraction dissipation rate (also called the scalar dissipation rate), defined as $N_\xi = D(\nabla\xi)^2$ [1] where D is the diffusivity of mixture fraction. The mixture fraction dissipation rate accounts for the rate of mixing. In a non-premixed flow, it is found that autoignition occurs preferentially at one mixture fraction, depending on the composition and thermodynamic state of the fuel and oxidiser, and this is called the most reactive mixture fraction ξ_{mr} (Mastorakos, Baritaud, and Poinsot, 1997). In turbulent flow, ignition tends to occur preferentially in fluid with a history of low scalar dissipation rate, which favours the accumulation of radicals and heat (Mastorakos, 2009). In contrast to autoignition, forced ignition takes place due to an external source of energy such as a spark-ignition engines.

Although combustion systems are frequently classified in terms of one combustion mode or another, in reality, a combination of combustion modes may be present. The intersection of premixed and non-premixed modes has been traditionally referred to as partially premixed combustion (Peters, 2000). In a diesel engine the transition from autoignition towards a fully-established diffusion flame goes through a propagating

[1] The scalar dissipation rate is written N_ξ in the Conditional Moment Closure modelling whereas χ_ξ which is $N_\xi/2$ is usually employed in the flamelet context. N_ξ and χ_ξ are both used in this thesis interchangeably.

flame phase which has partially premixed features (Domingo and Vervisch, 1996; Mastorakos, 2009). The speed of the propagation is larger than the conventional flame propagation through unreacted mixture due to the accumulation of radicals and heat in the mixture that has not yet ignited. In a diesel engine, further partial premixing continues during fuel injection in the region close to the injector where the flow velocity is too high for the flame to stabilise, resulting in a lifted flame structure, in which the diffusion flame is stabilised some way downstream of the injector through a process of autoignition and/or turbulent flame propagation (Reveillon and Vervisch, 2005). The complexity of the interaction between the various combustion modes is expected to increase in a multiple injection system. If the injections occur before ignition, partial premixing arises before ignition. Injecting after the ignition event might result in a strong propagation phase driven by premixed or turbulent autoignition mechanisms. As mixing is enhanced following an injection, local extinction might manifest. Overall, engine combustion is a complex process that cannot be classified or modelled using a single one of the classical premixed or non-premixed descriptions.

1.3 The role of simulation

Simulation plays a key role in the design of modern engines. Prior to prototyping and testing an engine, simulations are a valuable means for informing design of the engine. Once an engine is tested, simulation still has a role in explaining the experimental measurements, since simulations provide access to additional information that cannot be measured directly. A robust predictive model can provide insights about the tests to perform. Simulations in industries are based on a compromise between accuracy and cost, thus, although their role is to assist rather than replace experiments, they significantly reduce the cost and time of the development cycle.

Turbulent combustion is a physical process featuring a wide range of length scales and time scales. Computing the flow evolution by numerical integration of the Navier-Stokes equations is described as Direct Numerical Simulation (DNS) but, due to the range of length and time scales present in a real size engine flow, this is computationally too time consuming for practical use. Averaging processes are necessary to reduce computational cost. If the objective is to obtain improved flow predictions or to access time-resolved features of a turbulent flow, one can use the Large Eddy Simulation (LES) method. LES resolves large structures while the model equations are spatially-filtered at a length scale in the inertial range of turbulence, resulting in modelling of smaller-scale processes that are not resolved at the filter-scale. On the other hand,

Reynolds Average Navier-Stokes (RANS) methods provide an ensemble averaged prediction of a flow, and RANS turbulence models have been validated and/or tuned in order to be able to simulate many flows of practical importance (Poinsot, Veynante, & al., 2005). In this latter method, the averaging process is applied over all scales, and since the computational mesh only needs to resolve the variation of averaged quantities, which vary at length scales greater than or equal to the scales over which the same properties vary instantaneously, this significantly reduces the computational cost. In both methods, unclosed terms that result from the averaging or filtering approach require models, and the accuracy of these models affects the usefulness of the prediction.

In particular, in turbulent combustion involving flames, some flame structures generally have smaller length scales than the turbulence motions, and hence models are required in order to describe the flame processes in both the LES and RANS frameworks. A vast literature of combustion models exists, and an overview of the modelling approaches is given by Veynante and Vervisch (2002). In a first class of approaches that Veynante and Vervisch (2002) describe as *geometrical*, assumptions are made about the structure of the flame. In the flamelet model (Peters, 1988) the flame is considered smaller than the smallest of the flow scales. Therefore, the flame is seen as a thin interface between fresh and burnt gases in premixed combustion or fuel and oxidizer in non-premixed combustion. Because the flame structure is approximately one-dimensional, it is feasible to identify a small number of reference variables (such as mixture fraction or a reaction progress variable, which is a variable that changes monotonically through a premixed flame) which can be used to map the evolution of the composition through the flame, allowing turbulent flames to be described in terms of the statistics of a small number of these reference variables (Peters, 2000). In the statistical approach, the assumption that the flame has a particular structure is removed. Instead, the evolution of either moments or full probability distributions of the composition is modelled and simulated. Approaches that model and transport the full probability density function of composition tend to be computationally expensive, and they require models especially for molecular mixing processes, which are difficult to model accurately since they must account for the diffusive mixing associated with the presence of flame structures, without having access to full information about the geometrical structure of the flames. Because the combustion behaviour in combustion engines is not characterised simply as either premixed or non-premixed, it is not necessarily appropriate to assume a particular flame structure (e.g. premixed or non-premixed) for the flames that are present. The challenge is then to develop

modelling that can account for a range of different flame behaviours while remaining computationally affordable.

1.4 Objective

This thesis is motivated by the need for combustion models to give improved predictive accuracy across several combustion regimes together with low computational cost. The focus of the modelling development is combustion problems involving mixing between multiple fuel injections.

A literature review is presented in Chapter 2 concerning simulation of turbulent reacting flows, which motivates adoption of a class of combustion model referred to as the Conditional Moment Closure (CMC) and, in particular, the double conditional moment closure (DCMC) approach. The formulation of the DCMC is presented and extended in order to consider a more general set of reference (or conditioning) variables in Chapter 3. Chapter 4 presents direct numerical simulations involving autoignition in a configuration involving multiple fuel injection events. The DNS is performed in order to obtain clear information about how to model split injection processes. In chapter 5 the coupling of the DCMC with a CFD solver has been successfully achieved. Simulation of spray in diesel-like engine conditions were performed. In chapter 6, a spray with split fuel injection is simulated. This thesis ends with a conclusion in chapter 7, in which recommendations are provided for future work.

1.5 Summary of novel contributions in this thesis

- A more general formulation of the Double Conditional Moment Closure that accounts for non-conserved conditioning variables with time-varying and inter-dependent normalisations is developed. The derivation is given in Appendix A.

- In Chapter 4, direct numerical simulations with up to three separate fuel injections are presented, allowing analysis of the interactions between more than two fuel injections, and of their modelling.

- An algorithm to increase the speed of the numerical method used to solve the DCMC has been developed (Operator Splitting with Interpolation). It is presented in Chapter 3. The results are shown in Chapter 5.

- Coupling of the DCMC with the CFD solver has been developed and has been demonstrated in diesel engine-like conditions with and without split fuel injection. The method is presented in chapter 3 and the results are presented in chapter 5 without split-fuel injection and chapter 6 with split-fuel injection.

Chapter 2

Theory and modelling

This Chapter introduces mathematical modelling for turbulent reacting flows and for fuel sprays in four sections. First, a set of equations governing single-phase chemically-reacting flow of a compressible fluid are presented, and these equations form the basis of the Direct Numerical Simulations (DNS) in Chapter 4. Second, general modelling approaches for turbulent combusting flows are introduced. Third, a mathematical model describing the transport and evaporation of a fuel spray is discussed and presented. Last, reference variables are introduced that will be considered as a basis for development of Conditional Moment Closure modelling in subsequent Chapters are introduced, and their governing equations are developed.

2.1 Governing equations

The governing equations for single-phase chemically reacting compressible flow written in a conservative form, read:

$$\frac{\partial \rho}{\partial t} + \frac{\partial}{\partial x_i}(\rho u_i) = 0 \tag{2.1}$$

$$\frac{\partial}{\partial t}(\rho u_i) = \frac{\partial}{\partial x_i}(\rho u_i u_j) + \frac{\partial}{\partial x_i}\tau_{ij} - \frac{\partial p}{\partial x_i} + \rho \sum_{k=1}^{N_{species}} Y_k f_{ik} \tag{2.2}$$

$$\frac{\partial}{\partial t}(\rho e_0) = -\frac{\partial}{\partial x_i}\left[u_i(\rho e_0 + p)\right] + \frac{\partial}{\partial x_i}(\tau_{ij} u_j) - \frac{\partial q_i}{\partial x_i} + \rho \sum_{k=1}^{N_{species}} Y_k f_{ki}(V_{i,k} + u_i) \tag{2.3}$$

$$\frac{\partial}{\partial t}(\rho Y_k) = -\frac{\partial}{\partial x_i}\left[\rho Y_k(u_i + V_{i,k})\right] + W_k \dot{\omega}_k \tag{2.4}$$

The index i indicates the direction (x, y, z) in a Cartesian coordinate system. ρ is the density, u is the velocity. Y_k is the mass fraction of the species k. The stress tensor is denoted τ_{ij}, the volumetric forces on the species k is f_{ik}, the heat flux is q_i, the species mass diffusion velocity is V_{ik}. For the k^{th} species, W_k is the molecular weight and $\dot{\omega}_k$ is the molar production rate. The specific total energy is e_0 and is equal to $\frac{u_i^2}{2} - \frac{p}{\rho} + h$. The effects of radiation are not included for the present study.

Thermodynamic properties

The density is related to the pressure and temperature through the equation of state, under the assumption of ideal gas mixture :

$$p = \rho R_u T / W \tag{2.5}$$

where R_u is the universal gas constant and W is the mean molar mass of the gas mixture. Using thermodynamics relationships, the temperature is obtained from the enthalpy and the mixture heat capacity expressed in following way:

$$h = Y_k h_k \tag{2.6}$$

$$h_k = \Delta h^0_{f,k} + \int_{T_0}^{T} c_{p,k} dT \tag{2.7}$$

For the k^{th} species, h_k is the enthalpy, $\Delta h^0_{f,k}$ is the enthalpy of formation at temperature T_0 and $c_{p,k}$ is the heat capacity at constant pressure.

Diffusion velocities

Fick's law is used to compute the diffusion velocities :

$$V_{i,k} = -\frac{D_k}{X_k}\frac{\partial X_k}{\partial x_i} \tag{2.8}$$

The molar fraction X_k is related to the mass fraction using : $Y_k = W_k \frac{X_k}{W}$ Three non-dimensional parameters are used to compute the diffusion coefficient and the viscosity. Their expressions read :

$$Le_k = \frac{\lambda}{\rho C_p D_k} \qquad Pr = \frac{\mu C_p}{\lambda} \qquad Sc_k = \frac{\mu}{\rho D_k} \tag{2.9}$$

The diffusion coefficient D_k is obtained through the Schmidt (Sc_k) number, by prescribing the Lewis (Le_k) numbers for each species, Prandtl (Pr) number and the thermal conductivity λ, which reads (Smooke, 1991).

$$\lambda = A.C_p \left(\frac{T}{T_0}\right)^r \tag{2.10}$$

A is equal to 2.58e-4 g/cm.s, and r is 0.7. The viscosity is obtained by using the Prandtl number by computing the thermal conductivity.

The assumption of equal diffusivity and unity Lewis number has been employed throughout the thesis. The equation 2.4 using the above mentioned simplifications reads :

$$\frac{\partial \rho Y_k}{\partial t} + \frac{\partial \rho Y_k u_i}{\partial x_i} = \frac{\partial}{\partial x_i}\left(\rho D \frac{\partial Y_k}{\partial x_i}\right) + \dot{\omega}_k \tag{2.11}$$

Stress tensor

The stress tensor in the previous equations is obtained from the following relation:

$$\tau_{ij} = \tau_{ji} = \mu\left(\frac{\partial u_i}{\partial x_j} + \frac{\partial u_j}{\partial x_i}\right) - \delta_{ij}\left(\frac{2}{3}\mu\right)\frac{\partial u_i}{\partial x_i} \tag{2.12}$$

where μ is the mixture viscosity with the effect of bulk velocity usually neglected. δ_{ij} is the Kronecker delta. It takes the value of 0 if $i = j$ and 1 otherwise. It is noticed that the momentum equation (2.2) is the same for non-reactive flows, however the effect of the combustion is included in the viscosity and density which responds to chemical heat release and the variation of composition.

Heat flux

The heat flux vector reads:

$$q_i = -\lambda\frac{\partial T}{\partial x_i} + \rho \sum_{k=1}^{N_{species}} h_k Y_k V_{ik} \tag{2.13}$$

The first term on the right-hand side represents the diffusion of heat due to temperature gradients and the term next corresponds to the diffusion of heat due to mass diffusion. Few approximations in the equations above have been adopted as employed in the code s3d. These terms are the gradients in pressure called also the "barodiffusion" and the "Soret" effect accounting for the mass flux due to temperature gradient in the expression of the mass diffusion velocity (Chen, Choudhary, & al., 2009). The inverse effect called "Dufour" has also been neglected in 2.13.

2.2 Modelling of turbulent combustion

In most combustion devices the flow is turbulent. Eddies of different sizes constitute the turbulent flow from eddies scaling with the size of the burner L_T to the smallest

scale referred as the Kolmogorov length scale η_k (Kolmogorov, 1991) :

$$\eta_k = \left(\frac{\nu^3}{\epsilon}\right)^{1/4} \tag{2.14}$$

where ν is the kinematic viscosity, ϵ the dissipation of the kinetic energy. The theory of energy cascade gives a description of the interaction between the different scales. That is, the largest eddies are unstable therefore break-up, subsequently transferring energy to smaller scales which undergo the same process down to the smallest where energy dissipates due to viscous effects. The turbulent Reynolds number Re_T can be related to these scales through the following relation :

$$\eta_k / L_T \sim 1/Re_T^{3/4} \tag{2.15}$$

As the ratio between the two scales increase, Re_T increases. A Direct Numerical Simulation (DNS) is a simulation in CFD that solves numerically the equations 2.1 to 2.4 without any further modelling except the diffusion coefficients and thermodynamic relations. This implies that all the turbulent length scales from the Kolmogorov length scale to the largest flow structures in the domain are resolved. The larger the Re_T is, the larger the ratio becomes in 2.15, such that the smallest grid cell and the time step have to be small enough to capture the motion of η_k. This results in a higher computational cost. As of today, the high value of Re_t in most industrial burners is prohibitive for DNS.

DNS of non-reactive turbulent flows differs greatly from DNS of reactive flows. When chemically reactive species are added in a turbulent medium, the chemical time scales of some species can be smaller than the time scale of the Kolmogorov eddies. Hence, the computational cost becomes more expensive, not only because the number of equations increase due to the added species, but also because the ratio between the turbulent time scale to the fastest chemical time scale increases.
DNS is a powerful tool to investigate the physics of flames and is adopted for the present work to investigate modelling of split fuel injection as discussed in Chapter 4.

The prohibitive cost of DNS gave rise to models simplifying the turbulent flow field. Ensemble averaging methods such as the Reynolds Average Navier-Stokes (RANS) and Large Eddy Simulation (LES) are methods applied in non-reactive and reactive flows. For these latter cases, turbulent combustion models have to be developed.

Reynolds Average Navier Stokes (RANS)

Properties in a turbulent flow may be decomposed into an ensemble mean $\overline{\theta}$ and a fluctuation, where the ensemble mean may vary with time and space.

$$\theta = \bar{\theta} + \theta' \tag{2.16}$$

After including the preceding relation into the governing equations and then averaging, one can obtain the mean equation. The advantage lies on the isolation of the fluctuating terms that have steep gradients from the mean terms that have shallow gradients, hence resulting in a much lower resolution requirement, therefore faster computation of the mean flow.
In flows with important density variations, it is more convenient to include the density in the decomposition such that:

$$\theta = \widetilde{\theta} + \theta'' \tag{2.17}$$

where the operator $\widetilde{(.)}$ denotes the Favre averaging, with:

$$\widetilde{\theta} = \frac{\overline{\rho\theta}}{\overline{\rho}} \tag{2.18}$$

In turbulent combustion, the principal modelling difficulties can be revealed by Favre averaging the mass fraction transport equations (2.11):

$$\frac{\partial \bar{\rho}\widetilde{Y_k}}{\partial t} + \frac{\partial \bar{\rho}\widetilde{u_i}\widetilde{Y_k}}{\partial x_i} = \frac{\partial}{\partial x_i}\left(\bar{\rho}\bar{D}\frac{\widetilde{\partial Y_k}}{\partial x_i}\right) - \underbrace{\frac{\partial \bar{\rho}\widetilde{u_i'Y_k'}}{\partial x_i}}_{\substack{\text{Turbulent} \\ \text{diffusion}}} + \underbrace{\overline{\dot{\omega}_k}}_{\substack{\text{Average reaction} \\ \text{source term}}} \tag{2.19}$$

The exponential dependence of the reaction source term implies that the mean of the reaction source term is not equal to the reaction source terms for the mean thermochemical state.

$$\overline{\dot{\omega}_k} \neq \dot{\omega}_k(\overline{Y_k}, \overline{T}) \tag{2.20}$$

The closure of this term is the main problem in turbulent combustion. The arduous task of modelling the mean reaction source terms lead to the emergence of various approaches that model or circumvent the modelling of the average reaction source term. Several classes of models are presented in the next section. The second term requiring modelling is the turbulent diffusion, and this is commonly modelled using the gradient diffusion assumption, where D_t is a modelled turbulent diffusivity:

$$\widetilde{u_i'Y_k'}| = -\frac{\mu_t}{Sc_{kt}}\frac{\partial \widetilde{Y_k}}{\partial x_i} \tag{2.21}$$

μ_t is the turbulent viscosity which depends on the turbulent model and Sc_{kt} is a turbulent Schmidt number for species k, although it is not always correct (in premixed flames, countergradient transport has been observed Veynante, Trouvé, & al. (1997))

Large Eddy Simulations (LES)

In LES the objective is to achieve improved flow prediction by resolving the large structures of the flow while the smaller ones are modelled. Hence as in RANS, the interaction between mixing and chemical source terms at small scales needs closure. However, the advantage of LES is that the largest structures in the flow depend generally on the geometry whereas the small structures feature more universal properties. LES is potentially more accurate than RANS, because LES requires modelling only for the effects of the unresolved small-scales structures. It can be noted that most of the RANS combustion models can be modified and adapted to LES modelling. A review of turbulent combustion modelling applied to LES has been discussed by Pitsch (2006).
Although the model developed in this thesis has been applied to RANS modelling, it could equally be applied to LES. Key models are next reviewed.

Eddy Break-up model

This simple model (Spalding, 1977) assumes that the reactions are completed at the moment of mixing, thus the reaction rate depends on the rate at which turbulent mixing proceeds. Although, the model provides simplicity and reliable convergence; over predictions of some species concentration and temperature are observed (Veynante and Vervisch, 2002). The model is often used to obtain a first estimate of a sophisticated problem.

Transport pdf model

The model consists of transporting the one-point, one-time joint-pdf of the composition variable and enthalpy. One major advantage is that the reaction source terms do not require any closure. However, in pdf modelling for turbulent combustion, a fundamental challenge is the modelling of the molecular mixing term in a manner which enforces the physical constraint that fluid can only mix locally in composition space. Other constraints include the conservation of the mean through the mixing process, the variance should decay at the correct rate, and finally that the composition remains

bounded between zero and unity.
The interaction by exchange with the mean (IEM) satisfies the conditions, but do not perform well for high ratio of the mixing time scale to a chemical time scale (called Damköhler number, Da) according to Subramaniam and Pope (1998). The Euclidean Minimum Spanning Tree (EMST) and stochastic Multiple Mapping Conditioning (MMC) are mixing models which have been developed from the concept of mapping closure in order to account for the strong localness of mixing by the previous authors.The EMST is general in the sense that it is not necessary to specify any reference variables.
An alternative PDF method which has shown promising results for turbulence-chemistry interaction is the stochastic fields method developed by Valiño (1998). The method is attractive because the stochastic field are continuous and differentiable in space and only continuous in time. This results in no sampling error in the evaluation of the stochastic fields.

Presumed pdf models

The flamelet model has been widely used for non-premixed and premixed flow due to the relatively low computational cost with complex chemistry. The key idea is to assume that the flame is thin such that it is smaller than the Kolmogorov scales, hence the flame can be considered to have a laminar structure. This assumption is possible for high D_a as observed in the classical diagrams regime (Poinsot, Veynante, & al., 2005). The flamelet equations are obtained by a coordinate transformation of the governing equations using the mixture fraction as an independent coordinate along the stoichiometric isosurface (Peters, 1988). It can be noted that the model provides the ability to include detailed finite-rate chemistry. The flamelet model was extended by introduction of another mixture fraction for the simulation of split-injection configuration using an asymptotic analysis (Hasse and Peters, 2005). In the Conditional Moment Closure (CMC), the empirical observation that the temperature and the species mass fractions in a non-premixed flame depend on the mixture fraction is exploited in order to close the reaction rate source term. The CMC equations can be derived by conditionally averaging the equations 2.3 and 2.4. However, contrary to the flamelet model, the CMC method does not assume a flame structure. The CMC equations account for spatial variations of conditional quantities in a way that the standard flamelet method cannot. This method has been adopted for the present study, and is discussed more extensively in the next Chapter.

2.3 The liquid phase

In diesel engine the fuel is liquid at the exit of the injector. Added complexity in the modelling of turbulent combustion arises from the interaction between the liquid phase, turbulence and the combustion. Two main classes of method exist to account for the interaction between the liquid and gas phase.
In a Euler-Euler approach both the liquid and the gas phase are solved in the Eulerian sense (2.13 to 2.1). Such method involves tracking the interface between the liquid and gas phase in order to account for the mass, momentum energy transfer. In DNS, this has been achieved using level-set method (Osher and Sethian, 1988) or Volume of Fluid (VOF) (Hirt and Nichols, 1981). The high Reynolds and Weber number in practical configurations yield very small scales. As a result the full resolution of the primary and secondary breakup process is intractable. In RANS or LES, methods such as ELSA (Eulerian Lagrangian Spray for Atomization) aim to capture the whole spray atomisation through the introduction of a parameter accounting for the density of the liquid surface (Lebas & al., 2005). Challenge comes from the modelling of the interaction of the droplets such as coalescence or collision and heat transfer between the two phases. The model has been successfully applied to cases with turbulent combustion (Desportes & al., 2011).
In a Euler-Lagrange approach the liquid phase is modelled as spherical droplets. Balance of mass, momentum and energy can be readily applied to each droplet. DNS of droplets interacting with turbulent combustion medium have been simulated (Reveillon and Vervisch, 2005). The latter authors proposed turbulent-combustion-spray diagrams using key combustion parameters (flame thickness, flammability limit etc.). The number of droplets can be very large in a simulation, therefore parcel which contains a prescribed number of droplets undergoing the same physical processes rather than a single droplet are used in practice.

In the present work, the liquid phase is not taken into account in the DNS of split-fuel injection presented in the chapter 4, whereas, in chapter 5 an Euler-Lagrange method is adopted. The governing equations as computed in the CFD solver STAR-CD are presented in the following.The motion of the dispersed phase will be influenced by that of the continuous and conversely via displacement and interphase momentum.

Concerning the Eulerian phase, the mass transport equation (2.1) with spray source

term included reads :

$$\frac{\partial \rho}{\partial t} + \frac{\partial}{\partial x_i}\left(\rho u_i\right) = \dot{S}_d \tag{2.22}$$

$$\dot{S}_d = \frac{1}{V}\sum_k \dot{\omega_v^k} \tag{2.23}$$

The subscript d is used for the droplet in the following. The mass equation reads :

$$\frac{dm_d}{dt} = -A_d \dot{mt}_d \tag{2.24}$$

where A_d corresponds to the surface area of the droplet and $\dot{mt}_d$ the mass transfer rate per unit of surface area. The mass transfer rate for evaporation, and, condensation reads:

$$\dot{mt}_d = K_g p_g \ln\left(\frac{p_g - p_v}{p_g - p_{v,s}}\right) \tag{2.25}$$

The pressures p_g, p_v, $p_{v,s}$ correspond respectively to the pressure of the gas phase, the partial pressure of the vapour in the droplet surrounding, and, at its surface. K_g is the mass transfer coefficient, its expression involves (Ranz, 1952a), (Ranz, 1952b):

$$S_h = 2\left(1 + 0.3 Re_d^{1/2} S_c^{1/3}\right) \tag{2.26}$$

where S_h is the Sherwood number, $Re_d = \frac{\rho|\mathbf{u}-\mathbf{u}_d|d_d}{\mu}$ is the Reynolds number for a given droplet, S_c is the Schmidt number. Using the previous relation K_g is defined as

$$K_g = \frac{S_h D_m}{R_m T_m d_d} \tag{2.27}$$

where D_m is the diffusion coefficient of the mixture, R_m the mixture gas constant, T_m is the temperature of the mean film where a 1/3 rule is applied $T_m = \frac{2T_d + T_g}{3}$, d_d is the droplet diameter. In eq. 2.25 the surface vapour pressure is assumed to be equal to the saturation pressure at the droplet temperature T_d.

The momentum balance is discussed next. The droplet momentum is a balance of the drag force F_{drag}, pressure force $F_{pressure}$ and virtual mass F_{vm} force, and body forces (neglected here) :

$$m_d \frac{d\mathbf{u}_d}{dt} = F_{drag} + F_{pressure} + F_{vm} \tag{2.28}$$

The F_{drag} expression reads :

$$F_{drag} = \frac{1}{2} C_d \rho A_{cd} |\mathbf{u} - \mathbf{u}_d|(\mathbf{u} - \mathbf{u}_d) \tag{2.29}$$

where C_d is a drag coefficient, the standard model in the commercial code used in this thesis, STAR-CD, is the following :

$$C_d = \begin{cases} 24(1 + 0.15Re_d^{0.687})/Re_d, & \text{if} \quad Re_d \leq 10^3, \\ 0.44, & \text{otherwise.} \end{cases} \tag{2.30}$$

A_{cd} corresponds to the droplet cross-sectional area. $F_{pressure}$ is given by :

$$F_{pressure} = -V_d.grad(p) \tag{2.31}$$

V_d corresponds to a droplet volume and $grad(p)$ is the total pressure gradient in the carrier fluid.

The added mass or virtual mass F_{vm} is the momentum added to the carrier phase due to the acceleration or deceleration of a given droplet as it moves the volume of fluid that surrounds it, the expression reads (with ρ of the carrier phase) :

$$F_{vm} = 0.5\rho V_d \frac{d(\mathbf{u}_d - \mathbf{u})}{dt} \tag{2.32}$$

The energy equations are addressed next.

The droplet energy balance takes into account the processes of heat transfer through the surface of the droplet and the phase change. The equation reads:

$$m_d c_{p,d} \frac{dT_d}{dt} = -A_d \dot{q_{sd}} + h_{f,g} \frac{dm_d}{dt} \tag{2.33}$$

$c_{p,d}$ is the droplet specific heat and $h_{f,g}$ is the latent heat of phase change. $\dot{q_{sd}}$ corresponds to the surface heat transfer rate, its expression reads:

$$\dot{q_{sd}} = h_t(T_d - T) \tag{2.34}$$

with h_t the heat transfer coefficient obtained using the formulation of El Wakil and Uyehara (1954). In the absence of mass transfer, the heat transfer is obtained from a correlation with a correction factor. The corrected h_t reads:

$$h_t = \frac{\lambda N_u C_H}{(e^{C_H} - 1)d_d} \tag{2.35}$$

The Nusselt number, N_u is obtained using (Ranz, 1952a):

$$N_u = 2(1 + 0.3Re_d^{1/2} Pr^{1/3}) \tag{2.36}$$

C_H is defined as :

$$C_H = \frac{-c_p(\frac{dm_d}{dt})}{\pi d_d \lambda_m N_u} \tag{2.37}$$

As noted earlier the model accounts for the fact that each computational parcel may exchange mass, momentum and energy with the carrier fluid; a loss from a parcel is a gain for the carrier phase and conversely. These exchanges are obtained from the integration of the Lagrangian equations. This implies that additional terms arise in the momentum and energy equation of the carrier phase. These equations are not needed to develop the advanced combustion modelling presented in the next chapter. There are however, employed in the flow solver STAR-CD (the code is used in chapter 5 and 6), but without any modifications due to combustion modelling. Therefore, for a detail of the two-way coupling, the equations, the composition dependences of the thermodynamic and transport coefficients the reader is reffered to the user manual of STAR-CD (STAR-CD, 2004).

The droplets can become unstable due to the action of the interfacial force. The onset of break-up is estimated through a stable droplet diameter $d_{d,stable}$ and a characteristic time scale of the break-up process. The break-up rate is calculated from:

$$\frac{dd_d}{dt} = -\frac{(d_d - d_{d,stable})}{\tau_{stable}} \tag{2.38}$$

The Reitz and Diwakar model is employed. It accounts for the break-up that can result from the non-uniformity of the pressure field around the droplet, and a process in which liquid is sheared from the droplet surface. The former also called the bag break-up occurs when the inertial forces exceeds the surface tension (their ratio corresponds to the Weber number) :

$$We_g = \rho_g(\mathbf{u_d} - \mathbf{u}^2)d_{d,stable}/2\sigma > 6 \tag{2.39}$$

where We_g is the Weber number based on the gas density. The second breakup mechanism referred also as the stripping break-up occurs when:

$$We_g/\sqrt{Re_g} > 0.5 \tag{2.40}$$

Following the previous equations the lifetimes of unstable drops for the bag and stripping modes respectively reads:

$$\tau_{stable,1} = D_1\sqrt{\rho_l d_{d,stable}^3/8\sigma} \tag{2.41}$$

$$\tau_{stable,2} = D_2 \frac{\sqrt{\rho_l/\rho}.d_{d,stable}}{2(\mathbf{u_d} - \mathbf{u})} \tag{2.42}$$

with D_1 and D_2 are of the order of unity (Reitz and Diwakar, 1986).

2.4 Reference variables

2.4.1 Mixture fraction

In non-premixed flames, combustion depends on the mixing and inter-diffusion of fuel and oxidiser. The mixture fraction is used to parameterise the extent of this mixing. It is defined as the mass fraction of fluid at a given point that originated from the fuel stream, and it is therefore a conserved passive scalar with a value equal to unity in pure fuel and zero in pure oxidiser. The mixture fraction ξ can be evaluated by considering the elemental composition and, in flows with preferential diffusion, different definitions arise depending on the choice or the combination of elements used in the definition (Poinsot, Veynante, & al., 2005). For flows in which species are assumed to have equal diffusivities, all of the element-based definitions become equivalent.

In the case of equal Fickian diffusivities, it is also equivalent to define mixture fraction by the following transport equation, including spray terms:

$$\frac{\partial \rho \xi}{\partial t} + \frac{\partial \rho u_i \xi}{\partial x_i} = \frac{\partial}{\partial x_i}\left(\rho D \frac{\partial \xi}{\partial x_i}\right) + \dot{S}_d \tag{2.43}$$

where $\dot{S}_d$ is the mixture fraction source term arising from droplet evaporation.

Additional mixture fractions may be defined in order to describe mixing between fluid from more than two streams. In the case of split fuel injection, transport equation-based definitions of mixture fraction can be used to distinguish mass from different fuel injections by setting initial and boundary conditions appropriately, even though the fuel has the same elemental composition. With two fuel injections corresponding to mixture fractions ξ_1 and ξ_2 respectively, the mixture fraction of the oxidiser stream is given by the requirement that mass fractions sum to unity,

$$\xi_0 = 1 - \xi_1 - \xi_2. \tag{2.44}$$

The equivalence ratio ϕ is generally available in experimental data which is a measure of the fuel-to-air ratio. The mixture fraction which can be seen as a fuel mass fraction is related to the equivalence ratio though the following relation:

$$\phi = \frac{\xi}{1-\xi}\frac{1-\xi_{st}}{\xi_{st}} \tag{2.45}$$

2.4.2 Progress variable

Progress variable Y_c is a scalar reference variable that varies monotonically as fluid proceeds from an unburned to a burned state through a premixed flame, or during autoignition. Its use is not restricted to premixed flames and it has been used to characterise autoignition in gas (Bruel, Rogg, and Bray, 1991) and spray-fuelled combustion (Chang & al., 1996), (Lehtiniemi & al., 2006). In this thesis the progress variable is expressed as a linear combination of the mass fractions with α_k the weight coefficients.

$$Y_c = \sum_{i=k}^{n_{spec}} \alpha_k Y_k \tag{2.46}$$

The choice of the progress variable is still open at this stage and alternative definitions are compared in the results chapters.

Assuming unity Lewis number and equal diffusivities, the transport equation for Y_c reads in a conservative form:

$$\frac{\partial \rho Y_c}{\partial t} + \frac{\partial \rho u_i Y_c}{\partial x_i} = \frac{\partial}{\partial x_i}\left(\rho D \frac{\partial Y_c}{\partial x_i}\right) + \dot{\omega_{Y_c}} + \dot{S_{d,v}} \tag{2.47}$$

The last term arises due to spray evaporation. If the fuel mass fraction is used in the definition of the progress variable, the latter term is not zero. It is not the case in the thesis, therefore, no evaporation source term appears in the latter equation (for detail derivation of the instantaneous equations with spray source term see (Baba and Kurose, 2008), (Mortensen and Bilger, 2009)).

Advantages of defining a normalised progress variable c are discussed extensively in (Bray, Domingo, and Vervisch, 2005). Normalising progress variable so that it varies from zero in reactants to unity in products allows modelling to be formulated in a more general way. For example a number of presumed probability density function models, such as the beta-function apply to variables that span from zero to unity. In the context of DCMC, normalising the progress variable is preferred in order that the equations can be solved on a unit square grid.

Two progress variable normalisations are discussed in this thesis. In the first one, the normalisation involves the extremum values that Y_c reaches for all times, whereas, in the second one the normalisation involves the extremum values that Y_c reaches at each time. The first will be referred to as the normalised progress variable c. It is a well established definition of progress variable (Bray, Domingo, and Vervisch, 2005), and that motivates its choice as the progress variable normalisation use in throughout this thesis. The necessity of accurately defining the boundary conditions in the state space led to the introduction of a second normalisation. It will be referred to as the

temporal normalised progress variable c_t which is presented and motivated in appendix A as an introductory concept.

The maximum and minimum values that Y_c reaches for all times are denoted respectively $Y_{c,maxf}(\xi(x_i,t))$ and $Y_{c,minf}(\xi(x_i,t))$. Chemical equilibrium values $Y_{c,eq}$ are usually used for $Y_{c,maxf}$ and inert solutions $Y_{c,u}$ for $Y_{c,minf}$. The normalised progress variable reads:

$$c(x_i,t) = \frac{Y_c(x_i,t) - Y_{c,u}(\xi(x_i,t))}{Y_{c,eq}(\xi(x_i,t)) - Y_{c,u}(\xi(x_i,t))}. \tag{2.48}$$

The transport equation is obtained after noticing that the equation of Y_c is similar to 2.47 (obtained using the equation of Y_k: 2.11). The spatial and temporal derivatives read:

$$\begin{aligned}
&\frac{\partial \rho Y_c}{\partial t} = Y_{c,\Delta}\frac{\partial \rho c}{\partial t} + \rho c\frac{\partial Y_{c,\Delta}}{\partial \eta}\frac{\partial \xi}{\partial t} + \rho\frac{\partial Y_{c,u}}{\partial \eta}\frac{\partial \xi}{\partial t} \\
&\frac{\partial \rho u_i Y_c}{\partial x_i} = Y_{c,\Delta}\frac{\partial \rho u_i c}{\partial x_i} + \rho u_i c\frac{\partial Y_{c,\Delta}}{\partial \eta}\frac{\partial \xi}{\partial x_i} + \rho u_i\frac{\partial Y_{c,u}}{\partial \eta}\frac{\partial \xi}{\partial x_i} \\
&\frac{\partial}{\partial x_i}\left(\rho D\frac{\partial Y_c}{\partial x_i}\right) = Y_{c,\Delta}\frac{\partial}{\partial x_i}\left(\rho D\frac{\partial c}{\partial x_i}\right) + \left(c\frac{\partial Y_{c,\Delta}}{\partial \eta} + \frac{\partial Y_{c,u}}{\partial \eta}\right)\frac{\partial}{\partial x_i}\left(\rho D\frac{\partial \xi}{\partial x_i}\right) \\
&+ 2\rho\frac{\partial Y_{c,\Delta}}{\partial \eta}N_{\xi,c} + \rho\left(c\frac{\partial^2 Y_{c,\Delta}}{\partial \eta^2} + \frac{\partial^2 Y_{c,u}}{\partial \eta^2}\right)N_\xi
\end{aligned} \tag{2.49}$$

with the dissipation rates:

$$N_\xi = D\left(\frac{\partial \xi}{\partial x_i}\right)^2 \qquad N_{\xi,c} = D\frac{\partial \xi}{\partial x_i}\frac{\partial c}{\partial x_i} \tag{2.50}$$

and with $Y_c = cY_{c,\Delta} + Y_{c,u}$ and $Y_{c,\Delta} = Y_{c,eq} - Y_{c,u}$. Substituting the relations 2.49 into 2.47 one can obtain:

$$\begin{aligned}
&Y_{c,\Delta}\left[\frac{\partial \rho c}{\partial t} + \frac{\partial \rho u_i c}{\partial x_i} - \frac{\partial}{\partial x_i}\left(\rho D\frac{\partial c}{\partial x_i}\right)\right] \\
&+ \left(c\frac{\partial Y_{c,\Delta}}{\partial \eta} + \frac{\partial Y_{c,u}}{\partial \eta}\right)\left[\rho\frac{\partial \xi}{\partial t} + \rho u_i\frac{\partial \xi}{\partial x_i} - \frac{\partial}{\partial x_i}\left(\rho D\frac{\partial \xi}{\partial x_i}\right)\right] = \\
&+ 2\rho\frac{\partial Y_{c,\Delta}}{\partial \eta}N_{\xi,c} + \rho\left(c\frac{\partial^2 Y_{c,\Delta}}{\partial \eta^2} + \frac{\partial^2 Y_{c,u}}{\partial \eta^2}\right)N_\xi \\
&+ \dot{\omega_{Y_c}} + \dot{S_{d,v}}
\end{aligned} \tag{2.51}$$

In the above equation one can see the transport equation of c and ξ explicitly appearing, however, the latter is expressed in the non-conservative form.

Developing the mixture fraction transport equation with spray source term (Eq. 2.43) gives :

$$\rho\frac{\partial \xi}{\partial t} + \rho u_i\frac{\partial \xi}{\partial x_i} + \xi\left(\frac{\partial \rho}{\partial t} + \frac{\partial \rho u_i}{\partial x_i}\right) = \frac{\partial}{\partial x_i}\left(\rho D\frac{\partial \xi}{\partial x_i}\right) + \dot{S}_d \tag{2.52}$$

Replacing the mass equation reads:

$$\rho\frac{\partial\xi}{\partial t}+\rho u_i\frac{\partial\xi}{\partial x_i}=\frac{\partial}{\partial x_i}\left(\rho D\frac{\partial\xi}{\partial x_i}\right)+\dot{S}_d(1-\xi) \tag{2.53}$$

Finally replacing the above relations, one can obtain the final equation which reads:

$$\begin{aligned}\underbrace{\frac{\partial\rho c}{\partial t}+\frac{\partial\rho u_i c}{\partial x_i}}_{\text{Mat. derivative}}&=\underbrace{\frac{\partial}{\partial x_i}\left(\rho D\frac{\partial c}{\partial x_i}\right)}_{\text{Diffusion}}+\underbrace{\frac{\dot{\omega_{Y_c}}}{Y_{c,\Delta}}}_{\text{reaction}}+\underbrace{\rho\frac{2N_{\xi,c}}{Y_{c,\Delta}}\frac{\partial Y_{c,\Delta}}{\partial\eta}}_{T_1}\\&+\underbrace{\rho\frac{N_\xi}{Y_{c,\Delta}}\left(c\frac{\partial^2 Y_{c,\Delta}}{\partial\eta^2}+\frac{\partial^2 Y_{c,u}}{\partial\eta^2}\right)}_{T_2}-\underbrace{\frac{\dot{S}_d}{Y_{c,\Delta}}\left[(1-\xi)\left(c\frac{\partial Y_{c,\Delta}}{\partial\eta}+\frac{\partial Y_{c,u}}{\partial\eta}\right)\right]+\frac{\dot{S_{d,v}}}{Y_{c,\Delta}}}_{\text{Spray source terms}}\end{aligned} \tag{2.54}$$

The equation 2.54 is applicable to all modes of combustion and is not restrained to premixed flames. However, without the dissipation rates no mixing occurs between fluid with different values of mixture fraction, such that molecular transport is associate with perfectly-premixed combustion. Equation 2.54 resembles the equation obtained by Bray, Domingo, and Vervisch (2005). As mentioned by the above authors the term T_2 accounting for non-premixed burning mode is expected to be significantly higher around ξ_{st} due to high curvature of $Y_{c,eq}$ in that region. Note that the additional spray source term arises due to normalisation. It is not equal to zero even if the mass fraction of fuel is not used in the definition of c. In the present work, the equation 2.54 is ensemble averaged, modelling for unclosed terms is applied and the averaged equation is solved in the context of RANS. The DCMC spray combustion simulations in Chapters 5 and 6 of this thesis make a number of simplifying assumptions concerning spray effects, and the spray source terms in the progress variable moment equations are neglected as part of those assumptions as discussed in the relevant chapters.

Chapter 3

Conditional Moment Closure

Conditional Moment Closure (CMC) is studied in this thesis in the context of split fuel injection. As seen in the following, the CMC equations can be rigorously derived from the instantaneous transport equations employed in the DNS, allowing the study of the modelling of split fuel injection through the DNS data in light of the CMC model. This Chapter is structured as follows, first the standard CMC model is presented, next, an advanced CMC model referred as the Doubly-Conditional Moment Closure (DCMC) is discussed in the context of split fuel injection.

3.1 The Conditional Moment Closure model

The CMC is an advanced turbulent reactive flow model which has been initially applied for non-premixed (Smith, Bilger, and Chen, 1992) and later for premixed combustion (Swaminathan and Bilger, 2001). The development of the model was motivated by the need to provide accurate closures for the mean reaction rate source terms. In diffusion flame, this can be achieved by exploiting the dependence between the mixture fraction fluctuations and the temperature and mass fraction species fluctuations. To illustrate the concept a scatter plot of Y_{H_2O} versus the mixture fraction is depicted in Fig. 3.1 during and after autoignition for a statistically homogeneous case in which pockets of fuel evolve in a turbulent oxidiser. The mass fraction Y_k for species k can be decomposed into the conditional average and a conditional fluctuation.

$$Y_k = Q_k(\xi(\mathbf{x},t),\mathbf{x},t) + y_k''(\mathbf{x},t), \tag{3.1}$$

with the conditional mean of the mass fraction of species k defined as:

$$Q_k = \langle Y_k | \xi(\mathbf{x},t) = \eta \rangle \tag{3.2}$$

which corresponds to the average value of Y_k for a given value of the mixture fraction $\xi(x_i, t)$ (depicted in the picture for each value of the mixture fraction). The angled brackets denote an ensemble averaging process and the symbol on the right of the vertical bar denotes the sample-space variable η. The conditional fluctuations of the mass fraction species denoted by y_k'' are the fluctuations with respect to the conditional mean. As noticed in Fig. 3.1(left) the conditional fluctuations are small and, depending on the combustion regime, are generally much smaller than the unconditional fluctuations. This important property justifies simple first order conditional moment closure of the conditional mean of the reaction source terms present in the transport equations of the conditional means of the thermochemical parameters: Using a first order Taylor expansion around the conditional mean of the reaction rate source term yields:

$$\left\langle \dot{\omega^n} | \eta \right\rangle \simeq \dot{\omega}(\mathbf{Q}, P) \tag{3.3}$$

This approximation is quite accurate in high Da flows where the conditional fluctuations tend to be small as illustrated in 3.1 (left) in contrast to the large errors given by using the unconditional first order closure stated in Eq. 2.20. However, the conditional fluctuations are not generally negligible in low Da flows which may display extinction and re-ignition phenomena, or generally in flow with partial-premixing or turbulent autoignition, as illustrated in Fig. 3.1 (right) showing data from a turbulent autoignition process.

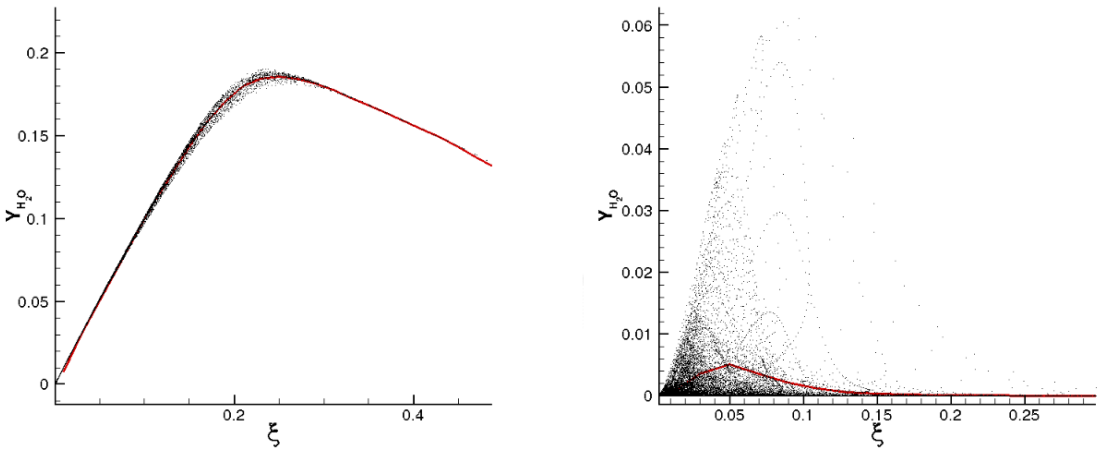

Figure 3.1: Scatter plot of Y_{H_2O} versus ξ from a DNS of auto-igniting mixture (details presented in Chapter 4), the red line is the conditional mean of $\langle Y_{H_2O} | \eta = \xi \rangle$, the left picture is at time $1.52 * \tau_{ign}$ and the right picture at time τ_{ign} during the autoignition process

The solution of the equations along with the modelling for the pdf of the conditioning variable allows evaluation of the unconditional mean values of the thermochemical variables through the following relation:

$$\widetilde{Y_k} = \int Q_k \widetilde{P}(\eta) d\eta. \tag{3.4}$$

The equations for the conditional mean of the species mass fractions are obtained by combining Eq.3.7 with Eq.2.4 assuming equal diffusivities and employing the primary closure hypothesis of Klimenko and Bilger (1999) [1]:

$$\underbrace{\frac{\partial Q_k}{\partial t}}_{\text{Local rate of change}} + \underbrace{\langle u_i|\eta\rangle \frac{\partial Q_k}{\partial x_i}}_{\text{convection}} = \underbrace{\langle N_\xi|\eta\rangle \frac{\partial^2 Q_k}{\partial \eta^2}}_{\text{Transport in the } \eta\text{-space}} + \underbrace{\frac{\langle \dot{\omega}_k|\eta\rangle}{\langle \rho|\eta\rangle}}_{\text{Reaction source term}} + \underbrace{\frac{1}{\langle\rho\rangle P(\eta)} \frac{\partial}{\partial x_i} \left(\langle u_i'' Y_k''|\eta\rangle \langle\rho\rangle P(\eta)\right)}_{\text{Conditional turbulent flux}} \tag{3.5}$$

and the scalar dissipation rate defined as :

$$N_\xi = D \left(\frac{\partial \xi}{\partial x_i}\right)^2 \tag{3.6}$$

The scalar dissipation rate gives an indication of the rate at which local mixing occurs.

In Eq.3.5, the following terms need closures: The conditional velocity $\langle u_i|\eta\rangle$, the conditional scalar dissipation rate $\langle N_\xi|\eta\rangle$, the conditional mean of the reaction rate source term $\langle \dot{\omega}_k|\eta\rangle$, the mixture fraction pdf $P(\eta)$, the conditional turbulent flux $\langle u_i'' Y_k''|\eta\rangle$ and the conditional reaction rate $\langle \dot{\omega}_k|\eta\rangle$ presented earlier.

In flows displaying significant conditional fluctuation the zero dimensional CMC (without the convection term) can be improved in two ways: using the second-order closure which incorporates the conditional variances in the reaction source term, or alternatively the doubly CMC which consists of using an additional conditioning variables which render the first-order closure for the reaction source term valid.

In the second order closure, additional transport equations for the conditional variances of thermochemical parameters have to be solved. More details can be found about the various possibilities in the literature (Mastorakos and Bilger, 1998). Moving to high-order methods changes the modelling issues. The conditional turbulent flux requires closure in the singly first-order CMC to account for the flame expansion phenomena in spark-ignition or other related problems (Mastorakos, 2009). Conversely, the magnitude of the conditional turbulent flux has been found negligible when a

[1] The detail of the derivation is more complex but similar for the DCMC. Hence, the derivation is detailed in the DCMC section

second conditioning variable is adequately chosen by Kronenburg (2004), hence, its modelling could be potentially avoided, although more analyses are required to draw a conclusion. In the following, the doubly CMC approach is investigated.

3.2 Double-conditional moment closure

3.2.1 Selection of conditioning variables

The conditional fluctuations around the conditional means can be significantly reduced by introducing additional conditioning variables. Cha, Kosály, and Pitsch (2001) used the scalar dissipation rate as a second conditioning variable for extinction and re-ignition problem, however, the onset of re-ignition is captured too early, which they explained by the fact that the conditional fluctuations around the mean are over predicted for low values of scalar dissipation rates around the quenching values.
Kronenburg (2004) found that there is not a clear dependence of the reduced temperature on the mixture fraction and the scalar dissipation rates. A temperature-like conditioning variable characterizing the heat transfer responsible for re-ignition should be taken into account. He proposed conditioning on mixture fraction and sensible enthalpy, since using the temperature itself leads to an additional source term in the energy equation for which a closure is not obvious.

Although extinction and reignition are combustion regimes that could manifest in a system that employs multiple injections, neither of the above mentioned authors considered the modelling implications of such injection technique. Later, via the flamelet framework Hasse and Peters (2005) developed an extended flamelet model that involves two mixture fractions. The equations closely resemble the zero-dimensional DCMC equations conditioned on two mixture fractions. The initial method consisting of defining a mixture fraction parameter based on the composition which results from an injection had been extended to account for more than two injections using a lumping method. The composition resulting from two injections can be effectively lumped into one mixture providing that no significant interaction takes place (Felsch & al., 2009). However, this method restricts the time of the injections since the accuracy of the lumping method is time dependent. Conditioning on three or more parameters could be done, however as discussed below, the DCMC brings several terms for which closures are very challenging. There is no restriction on the choice of the conditioning variables, however, the ones satisfying the following criteria will be preferred:

- The conditional fluctuations around the doubly-conditional mean should be small such that the first-order closure remains valid.

- Statistical independence between the conditioning parameters facilitates modelling. Several unclosed terms arise: the dissipation rates N_{ϕ_1}, N_{ϕ_2}, N_{ϕ_1,ϕ_2}, and, the joint-probability density function $P(\phi_1, \phi_2)$ with ϕ_1 and ϕ_2 being the conditioning parameters. For instance, the joint pdf could be closed using the following relation $P(\phi_1, \phi_2) = P(\phi_1)P(\phi_2)$ and the effect of the cross dissipation rate N_{ϕ_1,ϕ_2} could be negligible as observed by Cha, Kosály, and Pitsch (2001).

The DCMC equations are presented for two sets of conditioning parameters. Their choice is motivated by the results of the DNS presented in the next chapter. The two sets of conditioning parameters are:

- The mixture fraction ξ and a progress variable Y_c.

- Two mixture fractions accounting for the mixture of two separated injections ξ_1 and ξ_2.

3.2.2 DCMC for the mixture fraction ξ and normalised progress variable c

The abilities of the mixture fraction to characterize non-premixed combustion and the progress variable for the fully premixed regimes make their combinations through the DCMC a potential regime-less combustion model. That is, the realisation of the species composition should be close to a two dimensional manifold parametrised by these two parameters. Nguyen & al. (2010) through flamelet modelling derived equations describing the trajectories of the composition and temperature in the mixture fraction and progress variable space.

Similar equations can be obtained using the CMC model where additional terms arise. The derivation is presented once for the mixture fraction and a progress variable. In the case of non-reactive scalars the governing equations are a simplification of the ξ–c formulation. Therefore, for clarity, the equations for two mixture fractions as conditioning parameters will be presented subsequently without the derivation being repeated.

Derivation of the mass fraction species DCMC equation

Next the DCMC equation for species the mass fractions is obtained using the decomposition approach. In a similar fashion to the single conditioned CMC, the decomposition reads:

$$Y_k(x_i,t) = Q_k(x_i,t,\xi(x_i,t),c(x_i,t)) + y_k''(x_i,t) \tag{3.7}$$

with Q_k the conditional mean of Y_k which expression reads

$$Q_k(x_i,t,\xi,c) = \langle Y_k|\eta=\xi,\zeta=c\rangle \tag{3.8}$$

The second term y_k'' is the conditional fluctuation. Using the chain rule, the spatial and temporal derivative respectively read:

$$\frac{\partial Y_k}{\partial t} = \frac{\partial Q_k}{\partial t} + \frac{\partial Q_k}{\partial \eta}\frac{\partial \xi}{\partial t} + \frac{\partial Q_k}{\partial \zeta}\frac{\partial c}{\partial t} + \frac{\partial y_k''}{\partial t} \tag{3.9}$$

$$\frac{\partial Y_k}{\partial x_i} = \frac{\partial Q_k}{\partial x_i} + \frac{\partial Q_k}{\partial \eta}\frac{\partial \xi}{\partial x_i} + \frac{\partial Q_k}{\partial \zeta}\frac{\partial c}{\partial x_i} + \frac{\partial y_k''}{\partial x_i} \tag{3.10}$$

$$\begin{aligned}
\frac{\partial}{\partial x_i}\left(\rho D\frac{\partial Y_k}{\partial x_i}\right) &= \frac{\partial Q_k}{\partial \eta}\frac{\partial}{\partial x_i}\left(\rho D\frac{\partial \xi}{\partial x_i}\right) + \rho N_\xi\frac{\partial^2 Q_k}{\partial \eta^2} + \rho D\frac{\partial \xi}{\partial x_i}\frac{\partial}{\partial x_i}\left(\frac{\partial Q_k}{\partial \eta}\right)\\
&+ \frac{\partial Q_k}{\partial \zeta}\frac{\partial}{\partial x_i}\left(\rho D\frac{\partial c}{\partial x_i}\right) + \rho N_c\frac{\partial^2 Q_k}{\partial \zeta^2} + 2\rho N_{\xi,c}\frac{\partial^2 Q_k}{\partial \eta \partial \zeta}\\
&+ \rho D\frac{\partial c}{\partial x_i}\frac{\partial}{\partial x_i}\left(\frac{\partial Q_k}{\partial \zeta}\right) + \frac{\partial}{\partial x_i}\left(\rho D\frac{\partial Q_k}{\partial x_i}\right) + \frac{\partial}{\partial x_i}\left(\rho D\frac{\partial y_k''}{\partial x_i}\right)
\end{aligned} \tag{3.11}$$

After inserting relation 3.7 in the transport equation of the mass fraction species (2.11, replacing the transport equation of the mixture fraction and the normalised progress variable and conditionally averaging the resulting expression, one can obtain the doubly conditioned species mass fraction equation:

$$\begin{aligned}
\frac{\partial Q_k}{\partial t} + \langle u_i|\eta,\zeta\rangle\frac{\partial Q_k}{\partial x_i} &= \underbrace{\langle N_\xi|\eta,\zeta\rangle\left[\frac{\partial^2 Q_k}{\partial \eta^2} - \underbrace{\frac{1}{Y_{c,\Delta}}\left(\zeta\frac{\partial^2 Y_{c,\Delta}}{\partial \eta^2} + \frac{\partial^2 Y_{c,u}}{\partial \eta^2}\right)\frac{\partial Q_k}{\partial \zeta}}_{QT_1}\right]}_{QT_{1f}}\\
&+ \underbrace{2\langle N_{\xi,c}|\eta,\zeta\rangle\left(\frac{\partial^2 Q_k}{\partial \eta\partial\zeta} - \underbrace{\frac{1}{Y_{c,\Delta}}\left(\frac{\partial Y_{c,\Delta}}{\partial \eta}\right)\frac{\partial Q_k}{\partial \zeta}}_{QT_2}\right)}_{QT_{2f}} + \underbrace{\langle N_c|\eta,\zeta\rangle\frac{\partial^2 Q_k}{\partial \zeta^2}}_{QT_{3f}} + \underbrace{\frac{\langle \dot\omega_k|\eta,\zeta\rangle}{\langle \rho|\eta,\zeta\rangle}}_{QT_{4f}}\\
&- \underbrace{\frac{\langle \dot\omega_{Y_c}|\eta,\zeta\rangle}{Y_{c,\Delta}\langle \rho|\eta,\zeta\rangle}\frac{\partial Q_k}{\partial \zeta}}_{QT_{5f}} + \frac{e_{y_k''}}{\langle \rho|\eta,\zeta\rangle} + \frac{e_{Q_k}}{\langle \rho|\eta,\zeta\rangle}
\end{aligned} \tag{3.12}$$

with

$$
\begin{aligned}
e_{Q_k} &= \left\langle \rho D \frac{\partial \xi}{\partial x_i} \frac{\partial}{\partial x_i} \left(\frac{\partial Q_k}{\partial \eta} \right) + \rho D \frac{\partial c}{\partial x_i} \frac{\partial}{\partial x_i} \left(\frac{\partial Q_k}{\partial \zeta} \right) \middle| \eta, \zeta \right\rangle \\
&+ \frac{\partial}{\partial x_i} \left(\rho D \frac{\partial Q_k}{\partial x_i} \right) \\
e_{y_k''} &= \left\langle \rho \frac{\partial y_k''}{\partial t} + \rho u_i \frac{\partial y_k''}{\partial x_i} - \frac{\partial}{\partial x_i} \left(\rho D \frac{\partial y_k''}{\partial x_i} \right) \middle| \eta, \zeta \right\rangle
\end{aligned}
\tag{3.13}
$$

with the conditional dissipation rates:

$$
\begin{aligned}
\langle N_\xi | \eta, \zeta \rangle &= \left\langle D \left(\frac{\partial \xi}{\partial x_i} \right)^2 \middle| \eta, \zeta \right\rangle \\
\langle N_{\xi,c} | \eta, \zeta \rangle &= \left\langle D \frac{\partial \xi}{\partial x_i} \frac{\partial c}{\partial x_i} \middle| \eta, \zeta \right\rangle \\
\langle N_c | \eta, \zeta \rangle &= \left\langle D \left(\frac{\partial c}{\partial x_i} \right)^2 \middle| \eta, \zeta \right\rangle
\end{aligned}
\tag{3.14}
$$

$e_{y_k''}$ represents the conditional turbulent flux which is necessary to describe flame propagation in single conditioned CMC. In the DCMC such processes are accounted for through the dissipation terms. It should be noted that $e_{y_k''}$ is not negligible when differential diffusion effects are present and would require modelling. In the case of a statistically homogeneous (i.e zero dimensional) formulation the convection term (second term on the left-hand side) and e_{Qk} are identically equal to zero. Otherwise, it is usually neglected in flows with high Reynolds number. Similarly, the presence of differential effects require its modelling. The temperature equation derivation is detailed in the appendix (see B.9 for the final equation).

Unconditional averages are obtained through integration of the conditional parameters with the pdf using the following relation.

$$
\widetilde{Y_k} = \iint Q_k \widetilde{P}(\eta, \zeta) d\eta d\zeta \tag{3.15}
$$

where the joint pdf $P(\eta, \zeta)$ needs to be modelled.

Limiting cases

The ability of the DCMC equation to characterize different combustion regimes can be studied using the previous simplifications, in zero-dimension, steady state and using c:

$$
\begin{aligned}
\frac{\langle \dot{\omega_{Y_c}} | \eta, \zeta \rangle}{Y_{c,\Delta} \langle \rho | \eta, \zeta \rangle} \frac{\partial Q_k}{\partial \zeta} &= \langle N_\xi | \eta, \zeta \rangle \left[\frac{\partial^2 Q_k}{\partial \eta^2} - \frac{1}{Y_{c,\Delta}} \left(\zeta \frac{\partial^2 Y_{c,\Delta}}{\partial \eta^2} + \frac{\partial^2 Y_{c,u}}{\partial \eta^2} \right) \frac{\partial Q_k}{\partial \zeta} \right] \\
&+ 2 \langle N_{\xi,c} | \eta, \zeta \rangle \left(\frac{\partial^2 Q_k}{\partial \eta \partial \zeta} - \frac{1}{Y_{c,\Delta}} \left(\frac{\partial Y_{c,\Delta}}{\partial \eta} \right) \frac{\partial Q_k}{\partial \zeta} \right) \\
&+ \langle N_c | \eta, \zeta \rangle \frac{\partial^2 Q_k}{\partial \zeta^2} + \frac{\langle \dot{\omega_k} | \eta, \zeta \rangle}{\langle \rho | \eta, \zeta \rangle}
\end{aligned}
\tag{3.16}
$$

Following the analysis carried out by Domingo, Vervisch, and Veynante (2008) the previous equation can be written in terms of Damköhler numbers. $Da_{diff} = \langle \dot{\omega_{Y_c}} | \eta, \zeta \rangle / \langle N_\xi | \eta, \zeta \rangle$, $Da_{pf} = \langle \dot{\omega_{Y_c}} | \eta, \zeta \rangle / \langle N_c | \eta, \zeta \rangle$, $Da_{ppf} = \langle \dot{\omega_{Y_c}} | \eta, \zeta \rangle / (2 \langle N_{\xi,c} | \eta, \zeta \rangle)$ (with diff: diffusion flame, pf: premixed flame, ppf: partially premixed flame). It follows:

$$\begin{aligned} \frac{1}{Y_{c,\Delta}} \frac{\partial Q_k}{\partial \zeta} &= \frac{1}{Da_{diff}} \left[\frac{\partial^2 Q_k}{\partial \eta^2} - \frac{1}{Y_{c,\Delta}} \left(\zeta \frac{\partial^2 Y_{c,\Delta}}{\partial \eta^2} + \frac{\partial^2 Y_{c,u}}{\partial \eta^2} \right) \frac{\partial Q_k}{\partial \zeta} \right] \\ &+ \frac{1}{Da_{ppf}} \left(\frac{\partial^2 Q_k}{\partial \eta \partial \zeta} - \frac{1}{Y_{c,\Delta}} \left(\frac{\partial Y_{c,\Delta}}{\partial \eta} \right) \frac{\partial Q_k}{\partial \zeta} \right) \\ &+ \frac{1}{Da_{pf}} \frac{\partial^2 Q_k}{\partial \zeta^2} + \frac{\langle \dot{\omega_k} | \eta, \zeta \rangle}{\langle \dot{\omega_{Y_c}} | \eta, \zeta \rangle} \end{aligned} \tag{3.17}$$

The well-known combustion regimes are retrieved when the Damköhler numbers are varied. When combustion is driven by chemistry all the Damköhler numbers go to infinity and the equation simplifies to:

$$\frac{1}{Y_{c,\Delta}} \frac{\partial Q_k}{\partial \zeta} = \frac{\langle \dot{\omega_k} | \eta, \zeta \rangle}{\langle \dot{\omega_{Y_c}} | \eta, \zeta \rangle} \tag{3.18}$$

The equation describes autoignition of homogeneous mixtures in the normalised progress variable space. It can be derived starting from the mass fraction species equation for homogeneous mixtures after eliminating the time and using the transport equation of c. Note that in that case the first-order closure for the chemical source term is exact. In the case no mixing occurs between the isolines of ξ such that Da_{ppf} and Da_{diff} tend to infinity. In this limit the DCMC equation describes premixed flames with different equivalence ratios not interacting with each other. The equation reads:

$$\frac{1}{Y_{c,\Delta}} \frac{\partial Q_k}{\partial \zeta} = \frac{1}{Da_{pf}} \frac{\partial^2 Q_k}{\partial \zeta^2} + \frac{\langle \dot{\omega_k} | \eta, \zeta \rangle}{\langle \dot{\omega_{Y_c}} | \eta, \zeta \rangle} \tag{3.19}$$

This latter equation can be obtained starting from the mass fraction species equation written in non-conservative form with the flame speed explicitly appearing to describe freely propagating premix flames.

$$\rho s_l \frac{\partial Y_k}{\partial x_i} = \frac{\partial}{\partial x_i} \left(\rho D \frac{\partial Y_k}{\partial x_i} \right) + \dot{\omega_k} \tag{3.20}$$

The convection term accounting for the moving flame is captured by the zero dimensional form of the CMC. This term along with the diffusion term is related to the reaction source term of the progress variable (see Eq. 2.54). Multi-dimensional CMC is therefore not necessary for freely propagating premixed flame without differential diffusion. The flame thickness δ_l manifests in the state space through N_c. A measure of the flame thickness reads: $\delta_l \simeq \left(max \left(\left| \frac{\partial Y_c}{\partial x_i} \right|^{-1} \right) \right) = max(D/N_c)^{1/2}$. This latter

relation allows to interpret N_c through the flame thickness. That is higher N_c is correlated with thinner flames in premixed flames.

Next the diffusion flame is considered. The term N_c and $N_{c,\xi}$ are finite in a diffusion flame, therefore, the well known zero dimensional CMC equations can not be retrieved from the DCMC equations. N_c does not only dictate the species and temperature trajectories in the c space for premix flames but also for diffusion flames. In the case of one-dimensional counterflow, using the mixture fraction as conditioning parameter would result in no conditional fluctuations. In this particular case adding a second conditioning parameter c would require closures for the dissipation rates N_c and $N_{c,\xi}$. Therefore, introducing c would add unnecessary complexity. Low values of N_c in comparison with N_ξ would correspond to a thin flame front evolving in a non-uniform equivalence ratio (Nguyen & al., 2010). In tabulated methods with mixture fraction and progress variable, generating tables from zero-dimensional CMC would require all the dissipation rates to be included. The modelling of N_c is case dependant and challenging – in unsteady laminar counterflow flames, it is expected to be higher in the mixture fraction region between the most reactive and stoichiometric mixture fraction. In a box with pockets of fuel that evolve in a turbulent medium of oxidiser, mixing between richer and leaner mixtures would result in high N_c across the mixture fraction space (see Chapter 4). Providing models were available for N_c the full DCMC equations would give an improved description of autoigniting mixture that leads to diffusion flames. Influence of models for the conditional dissipation rate of N_c is given in Chapter 5.

The presence of $N_{c,\xi}$ in the case of premix flames implies that interaction takes place between the isomixtures. It characterises a direct measure of the degree of partial premixing and is discussed further in the modelling section. In one-dimensional counterflow diffusion flame $N_{c,\xi}$ is positive for leaner mixture and negative for richer mixtures.

Initial and boundary conditions

All boundaries in $\eta-\zeta$ space have zero diffusive flux on account of the dissipation rates for transport normal to the boundaries being equal to zero at the boundary: the η-space dissipation (and therefore the η-ζ dissipation) is necessarily equal to zero at the $\eta = 0$ and $\eta = 1$ boundaries; the ζ-space dissipation (and therefore the η-ζ dissipation) is necessarily equal to zero at the $\zeta = 0$ and $\zeta = 1$ boundaries. In addition, boundaries corresponding to zero progress variable have their chemical source term set equal to

zero. The DCMC equations are otherwise solved in the conventional manner at the boundaries.

DCMC calculations based on $\xi - c$ conditioning variables are initialised by linear interpolation across ζ space between an equilibrium solution at $\zeta = 1$ and an inert solution at $\zeta = 0$. The DCMC solution then adjusts rapidly to dissipation rates that are imposed. The initialisation of the domain for $\xi_1 - \xi_2$ conditioning variables is presented below.

3.2.3 DCMC for the mixture fraction ξ_1 and ξ_2

The DCMC equation for the mass fraction species can be expressed for a two mixture fractions formulation. The equation is obtained from 3.12 removing the reactive terms ($Q_{T_{5f}}$, $Q_{T_{4f}}$), terms due to the normalisation (Q_{T_2}, Q_{T_1}), and the convection terms (second term on the left-hand side of the equation).

$$\begin{aligned}\frac{\partial Q_k}{\partial t} + \langle u_i|\eta_1,\eta_2\rangle \frac{\partial Q_k}{\partial x_i} &= \langle N_{\xi_1}|\eta_1,\eta_2\rangle \frac{\partial^2 Q_k}{\partial {\eta_1}^2} + 2\langle N_{\xi_1,\xi_2}|\eta_1,\eta_2\rangle \frac{\partial^2 Q_k}{\partial \eta_1 \partial \eta_2} \\ &+ \langle \dot{\omega}_k|\eta_1,\eta_2\rangle + \langle N_{\xi_2}|\eta_1,\eta_2\rangle \frac{\partial^2 Q_k}{\partial {\eta_2}^2} + \frac{e_{y_k''}}{\langle\rho|\eta_1,\eta_2\rangle} + \frac{e_{Q_k}}{\langle\rho|\eta_1,\eta_2\rangle}\end{aligned} \tag{3.21}$$

$$\begin{aligned}\langle N_{\xi_1}|\eta_1,\eta_2\rangle &= \left\langle D\left(\frac{\partial \xi_1}{\partial x_i}\right)^2 \middle| \eta_1,\eta_2 \right\rangle \\ \langle N_{\xi_1,\xi_2}|\eta_1,\eta_2\rangle &= \left\langle D\frac{\partial \xi_1}{\partial x_i}\frac{\partial \xi_2}{\partial x_i} \middle| \eta_1,\eta_2 \right\rangle \\ \langle N_{\xi_2}|\eta_1,\eta_2\rangle &= \left\langle D\left(\frac{\partial \xi_2}{\partial x_i}\right)^2 \middle| \eta_1,\eta_2 \right\rangle\end{aligned} \tag{3.22}$$

The dissipation rates have been studied in the flamelet context. Hasse and Peters (2005) and Felsch & al. (2009) found the contribution of N_{ξ_1,ξ_2} to be small. The reason they provide for its low magnitude is that since the flow field acts identically on all scalar fields, on the small scales there should be no preference for either direction as a result the net contribution of the cross-mixing term should be small. Doran (2011) found that the term is not negligible in the state space. In particular at the boundary $\xi_1 + \xi_2 = 1$ he found that the angle between the gradients of ξ_1 and ξ_2 is -180 degrees. (Felsch & al., 2009) conducted numerical experiments showing that the dissipation rates account for different combustion processes. The dissipation rate of the first mixture N_{ξ_1} requires low values for autoignition to happen, whereas high values of the dissipation rate of the second mixture N_{ξ_2} led to shorter ignition delay of the main ignition. That is, the faster mixing enhanced flame propagation.

In a zero dimensional case and without any differential diffusion effects the term e_{Q_k} is

set to zero. Providing that the set of coordinates reduces the conditional fluctuations around the conditional mean $e_{y_k''}$ is set to zero. With the simplifications the DCMC equation is equivalent to the two-dimensional flamelet equation (Hasse and Peters, 2005).

The state space of the two mixture fractions coordinate is a unit triangle space as depicted in figure 3.2. A transformation can be done in different ways to obtain a unit square domain which is preferred numerically. The transformation is defined by:

$$\xi_1^* = \xi_1 \qquad \xi_s = \frac{\xi_2}{1-\xi_1} \tag{3.23}$$

For the mass fraction species equation reads, after applying the chain-rule transformation, for a zero-dimensional formulation:

$$\begin{aligned}\frac{\partial Q_k}{\partial t} - 2\frac{\langle N_{\xi_1^*,\xi_s}|\eta_1^*,\eta_s\rangle}{1-\xi_1^*}\frac{\partial Q_k}{\partial \eta_s} &= \langle N_{\xi_1^*}|\eta_1^*,\eta_s\rangle \frac{\partial^2 Q_k}{\partial \eta_1^{*2}} + 2\langle N_{\xi_1^*,\xi_s}|\eta_1^*,\eta_s\rangle \frac{\partial^2 Q_k}{\partial \eta_1^* \partial \eta_s} \\ &+ \langle N_{\xi_s}|\eta_1^*,\eta_s\rangle \frac{\partial^2 Q_k}{\partial \eta_2^{2*}} + \frac{\langle \dot{\omega}_k|\eta_1^*,\eta_s\rangle}{\langle \rho|\eta_1^*,\eta_s\rangle}\end{aligned} \tag{3.24}$$

with the transformed scalar dissipation rates expressed as

$$N_{\xi_1} = N_{\xi_1}^*, \qquad N_{\xi_1^*,\xi_s} = \frac{N_{\xi_1^*}\xi_s + N_{\xi_1\xi_2}}{1-\xi_1^*}, \qquad N_{\xi_s} = \frac{N_{\xi_1}\xi_s^2 + 2N_{\xi_1,\xi_2}\xi_s + N_{\xi_2}}{(1-\xi_1^*)^2} \tag{3.25}$$

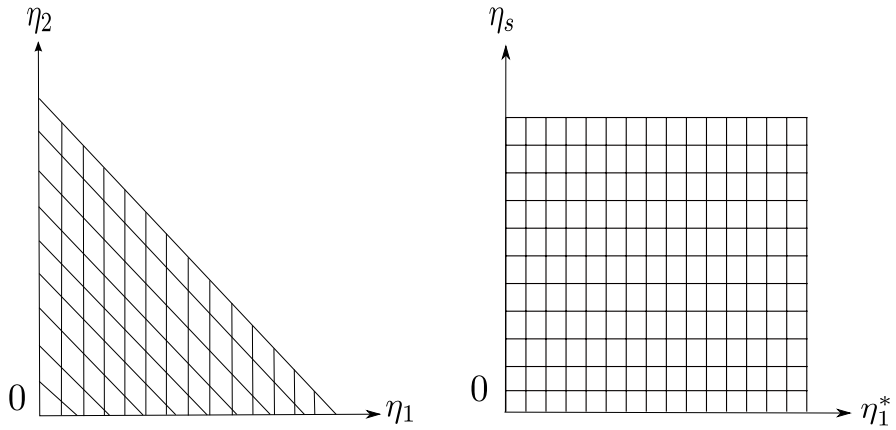

Figure 3.2: Illustration of the two mixture fractions sample space variable domain (left) and the normalised space (right)

Injections in the $\xi_1 - \xi_2$ state space

The second mixture fraction dimension comes in to existence at the time of the second injection at which point the $2D$ solution must be initialised based on the previously singly-conditioned solution. The composition at $\xi_2 = 1$ mixes with all of the compositions along the ξ_1 axis at $\xi_2 = 0$ (see Fig.3.3). This mixing process corresponds to an linear interpolation in the two-mixture fraction space given by the function:

$$Y_k(\eta_1, \eta_2) = \eta_2 Y_k(0,1) + (1-\eta_2) Y_{k,old}\left(\frac{\eta_1}{1-\eta_2}, 0\right) \tag{3.26}$$

where $Y_{k,old}$ corresponds to the composition prior to ignition and Y_k the composition of the new injection. Mapped onto the unit square we obtain:

$$Y_k^{''}(\eta_1^*, \eta_s) = \eta_s(1-\eta_1^*) Y_k(0,1) + (1-\eta_s(1-\eta_1^*))\, Y_{k(old)}\left(\frac{\eta_1^*}{1-\eta_s(1-\eta_1^*)}, 0\right) \tag{3.27}$$

with $\eta_1 * = \eta$ and $\eta_s = \frac{\eta_2}{1-\eta_1}$

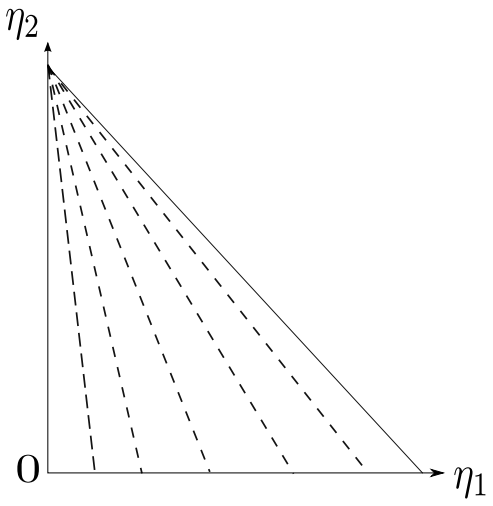

Figure 3.3: Illustration of the injection process. The dashed line represents the mixing line.

Boundary conditions

All boundaries in $\eta_1 - \eta_2$ space have zero diffusive flux on account of the dissipation rates for transport normal to the boundaries being equal to zero at the boundary: the η_1-space dissipation (and therefore the η_1-η_2 dissipation) is necessarily equal to zero

at the $\eta_1 = 0$ and $\eta_1 = 1$ boundaries; the η_2-space dissipation (and therefore the η_1-η_2 dissipation) is necessarily equal to zero at the $\eta_2 = 0$ and $\eta_2 = 1$ boundaries. The DCMC equations are otherwise solved in the conventional manner at the boundaries. Note that the η_1-η_2 dissipation is not zero at the $\eta_1 + \eta_2 = 1$ boundary. In the flamelet context it was found equal to:

$$-\frac{1}{2}\sqrt{N_{\xi_1} N_{\xi_2}} \tag{3.28}$$

(Doran, 2011), and could be used as an approximation in the DCMC formulated with the conditional dissipation rates instead.

3.3 Coupling between DCMC and Computational Fluid Dynamics solutions

The coupling of the DCMC equations with a CFD solver is illustrated in fig. 3.4 for the DCMC ξ-c. This coupling procedure is employed for the simulations in Chapter 5 and 6. The Favre mean transport equations solved within the CFD solver allow the computation of a presumed joint pdf in each CFD cell that is consistent with the moments transported in the CFD, and evaluation of the mean dissipation rates at each point using an algebraic model. Using the joint pdf and the unconditional dissipation rates, a modelling for the conditional dissipation rates in each CFD cell is determined that is consistent with the unconditional mean dissipation rates. A weighted spatial average of the conditonal dissipation rates throughout the domain is then evaluated.

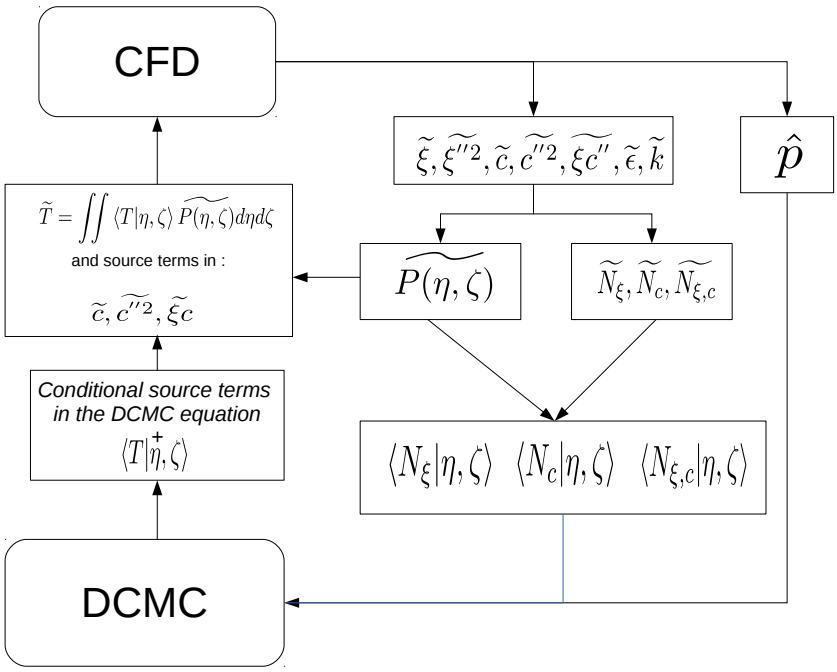

Figure 3.4: Chart illustrating the coupling between the DCMC and the CFD

Two spatial averaging methods have been implemented, a mass-weighted average and a pdf-weighted average. They read respectively:

$$\widehat{\langle q|\eta,\zeta\rangle} = \frac{\int_v \langle q|\eta,\zeta\rangle \, \bar{\rho} dv}{\int_v \bar{\rho} dv} \tag{3.29}$$

and for pdf-weighted averages

$$\langle q|\eta,\zeta\rangle_{pdf} = \frac{\int_v \langle q|\eta,\zeta\rangle \, \bar{\rho} \widetilde{\langle P|\eta,\zeta\rangle} dv}{\int_v \bar{\rho} \widetilde{\langle P|\eta,\zeta\rangle} dv} \tag{3.30}$$

where q is either the dissipation rate or the pressure and the hat denotes mass-average quantities. The pdf-weighted average method should be generally preferred for better representation of the effect of the turbulent flow field in the state space. The mass-weighted averaged method is computationally faster since the joint-pdf does not have to be computed at each CFD cell for that operation. Furthermore, the method may be preferred in the case more stability is required since smoother profiles are obtained. In a zero-dimensional formulation, using 3.29 decreases the contribution of $\langle q|\eta,\zeta\rangle$ for $c > 0$ and $\xi > 0$ as the domain size increases, which is not the case with 3.30.

Along with the mass-averaged pressure $\hat{p}$, obtained to compute its rate of change required in the energy equation, the DCMC equations are solved. In Chapter 4 the DCMC temperature equation is solved due to the constant volume case simulated. That is the pressure rate of change is explicitly accounted for in the temperature

equation. In Chapter 5, the total enthalpy is solved instead. The total enthalpy is linear in the state space using:

$$h(\eta,\zeta) = h(\eta=0,\zeta) + \left[h(\eta=1,\zeta) - h(\eta=0,\zeta)\right]\zeta \tag{3.31}$$

Using iterative methods, the temperature can be obtained. The change of the energy equation is motivated by the necessity of a more stable numerical solution. Indeed, the conditional dissipation rates computed at each time step were found to give instabilities particularly during ignition which resulted in a substantial increase of the CPU time as discussed in Chapter 5. Adding the temperature equation resulted in increased difficulties to obtain convergence. However, the pressure did not affect the temperature and the composition in the state space, but only the density through the ideal gas law. Although, the case presented in Chapter 5 is in a constant volume chamber, for that latter case the spatial and temporal variation of pressure throughout ignition is small.

Source terms in the Favre mean progress variable equations that are presented in the following section are assessed in the DCMC code. Using relation 3.15 the mean parameters needed are returned to the CFD code.

3.3.1 Favre averaged equations

Next the mean, variance and covariance of the equations are discussed. Due to the spray, additional source terms arise in the equations. Spray source terms in the state space have not been included in this study. To obtain the mean equation, the relation 2.16 is included in the transport equation of the parameter, followed by a Favre averaging. The mean equation of ξ reads when the spray source term is included:

$$\frac{\partial\bar{\rho}\widetilde{\xi}}{\partial t} + \frac{\partial\bar{\rho}\widetilde{u}_i\widetilde{\xi}}{\partial x_i} = \frac{\partial}{\partial x_i}\left(\overline{\rho D\frac{\partial\xi}{\partial x_i}} - \bar{\rho}\widetilde{u_i''\xi''}\right) + \overline{\dot{S}_d} \tag{3.32}$$

$$\begin{aligned}\frac{\partial\bar{\rho}\widetilde{\xi''^2}}{\partial t} + \frac{\partial\bar{\rho}\widetilde{u}_i\widetilde{\xi''^2}}{\partial x_i} = &\underbrace{\frac{\partial}{\partial x_i}\left(\overline{\rho D\frac{\partial\xi''^2}{\partial x_i}}\right)}_{\text{molecular diffusion}} - \underbrace{\frac{\partial}{\partial x_i}\left(\bar{\rho}\widetilde{u_i''\xi''^2}\right)}_{\text{turbulent flux}} \\ &\underbrace{-2\bar{\rho}\widetilde{u_i''\xi''}\frac{\widetilde{\partial\xi}}{\partial x_i}}_{\text{production}} \underbrace{-2\bar{\rho}D\widetilde{\frac{\partial\xi''}{\partial x_i}^2}}_{\text{dissipation}}\end{aligned} \tag{3.33}$$

The spray source terms have been neglected in the variance equation since their contribution had been found negligible by Borghesi & al. (2011) for the same experimental setup as in this study. He observed that the differences in ignition delay time and

lift-off height were negligible. Concerning the two mixture fractions formulation the above equations can be applied for both mixtures. The mean equation of the normalised progress variable reads:

$$\begin{aligned}\frac{\partial\bar{\rho}\widetilde{c}}{\partial t}+\frac{\partial\bar{\rho}\widetilde{u}_i\widetilde{c}}{\partial x_i}=\frac{\partial}{\partial x_i}\left(\overline{\rho D\frac{\partial c}{\partial x_i}}-\bar{\rho}\widetilde{u_i''c''}\right)+\underbrace{\frac{\overline{\dot{\omega}_{Y_c}}}{Y_{c,\Delta}}}_{T_1}+\underbrace{\overline{\rho\frac{2N_{\xi,c}}{Y_{c,\Delta}}\frac{\partial Y_{c,\Delta}}{\partial\xi}}}_{T_2}\\ \underbrace{+\overline{\rho\frac{N_\xi}{Y_{c,\Delta}}\left(c\frac{\partial^2 Y_{c,\Delta}}{\partial\xi^2}+\frac{\partial^2 Y_{c,u}}{\partial\xi^2}\right)}}_{T_3}\end{aligned} \tag{3.34}$$

The terms T_1, T_2 and T_3 on the right-hand side of the equation 3.34 are expressed simply as the average of the corresponding terms in the equation 2.54 without any additional approximation. The terms are computed in the DCMC and averaged using the joint pdf through the equation 3.15. Careful consideration has to be taken for the mean reaction source term which is not a Favre averaged quantity, it is obtained using:

$$\overline{\dot{\omega}_c}=\bar{\rho}\iint\frac{\langle\dot{\omega}_c|\eta,\zeta\rangle}{\langle\rho|\eta,\zeta\rangle}\widetilde{P}(\eta,\zeta)d\eta d\zeta \tag{3.35}$$

The variance equation reads:

$$\begin{aligned}\frac{\partial\bar{\rho}\widetilde{c''^2}}{\partial t}+\frac{\partial\bar{\rho}\widetilde{u}_i\widetilde{c''^2}}{\partial x_i}=\frac{\partial}{\partial x_i}\left(\overline{\rho D\frac{\partial c''^2}{\partial x_i}}\right)-\frac{\partial}{\partial x_i}\left(\bar{\rho}\widetilde{u_i''c''^2}\right)\\ -2\bar{\rho}\widetilde{u_i''c''}\frac{\widetilde{\partial}c}{\partial x_i}+\underbrace{2\overline{c''\frac{\dot{\omega}_{Y_c}}{Y_{c,\Delta}}}}_{T_1}-2\bar{\rho}D\widetilde{\frac{\partial c''}{\partial x_i}}^2\\ \underbrace{+\overline{4\rho c''\frac{N_{\xi,c}}{Y_{c,\Delta}}\frac{\partial Y_{c,\Delta}}{\partial\xi}}}_{T_2}+\underbrace{2\overline{\rho c''\frac{N_\xi}{Y_{c,\Delta}}\left(c\frac{\partial^2 Y_{c,\Delta}}{\partial\xi^2}+\frac{\partial^2 Y_{c,u}}{\partial\xi^2}\right)}}_{T_3}\end{aligned} \tag{3.36}$$

Again T_1, T_2 and T_3 in 3.36 are computed from the state space except that the following relation is used for a given parameter γ:

$$\widetilde{c''\gamma}=\iint(\zeta-\widetilde{c})\,\langle\gamma|\eta,\zeta\rangle\,\widetilde{P}(\eta,\zeta)d\eta d\zeta \tag{3.37}$$

In order to obtain a model for the cross scalar dissipation term a mean transport

equation for the covariance equation has to be solved. It reads:

$$\begin{aligned}\frac{\partial\bar{\rho}\widetilde{\xi''c''}}{\partial t}+\frac{\partial\bar{\rho}\widetilde{u}_i\widetilde{\xi''c''}}{\partial x_i}&=\frac{\partial}{\partial x_i}\left(\overline{\rho D\frac{\partial\xi''c''}{\partial x_i}}\right)-\frac{\partial}{\partial x_i}\left(\bar{\rho}\widetilde{u_i''\xi''c''}\right)\\&-\bar{\rho}\widetilde{u_i''\xi''}\frac{\widetilde{\partial c}}{\partial x_i}-\bar{\rho}\widetilde{u_i''c''}\frac{\widetilde{\partial\xi}}{\partial x_i}+\underbrace{\overline{\xi''\frac{\dot{\omega_{Y_c}}}{Y_{c,\Delta}}}}_{T_1}-2\bar{\rho}D\frac{\widetilde{\partial\xi''c''}}{\partial x_i}\\&+\underbrace{2\overline{\rho\xi''\frac{N_{\xi,c}}{Y_{c,\Delta}}\frac{\partial Y_{c,\Delta}}{\partial\xi}}}_{T_2}+\underbrace{\overline{\rho\xi''\frac{N_\xi}{Y_{c,\Delta}}\left(c\frac{\partial^2Y_{c,\Delta}}{\partial\xi^2}+\frac{\partial^2Y_{c,u}}{\partial\xi^2}\right)}}_{T_3}\end{aligned}\tag{3.38}$$

The terms T_1, T_2 and T_3 are evaluated in the state space using $\widetilde{\xi}$ instead of $\widetilde{c}$ in relation 3.37. No covariance transport equation is solved for the two mixture fractions formulation.

In addition to the source terms arising due to the normalisation, it was observed in Eq. 2.54 that spray source terms are present. The equations of $\widetilde{Y}_c$ and $\widetilde{Y_c''^2}$ have a simpler expressions without spray source terms if the mass fraction of fuel is not used in the definition of the progress variable. They read:

$$\frac{\partial\bar{\rho}\widetilde{Y}_c}{\partial t}+\frac{\partial\bar{\rho}\widetilde{u}_i\widetilde{Y}_c}{\partial x_i}=\frac{\partial}{\partial x_i}\left(\overline{\rho D\frac{\partial Y_c}{\partial x_i}}-\bar{\rho}\widetilde{u_i''Y_c''}\right)+\overline{\dot{\omega_{Y_c}}}\tag{3.39}$$

$$\begin{aligned}\frac{\partial\bar{\rho}\widetilde{Y_c''^2}}{\partial t}+\frac{\partial\bar{\rho}\widetilde{u}_i\widetilde{Y_c''^2}}{\partial x_i}&=\frac{\partial}{\partial x_i}\left(\overline{\rho D\frac{\partial Y_c''^2}{\partial x_i}}\right)-\frac{\partial}{\partial x_i}\left(\bar{\rho}\widetilde{u_i''Y_c''^2}\right)\\&-2\bar{\rho}\widetilde{u_i''Y_c''}\frac{\widetilde{\partial Y_c}}{\partial x_i}+\overline{2Y_c''\dot{\omega_{Y_c}}}-2\bar{\rho}D\frac{\widetilde{\partial Y_c''}^2}{\partial x_i}\end{aligned}\tag{3.40}$$

This method has not been tested, instead the equations involving $\widetilde{c}$ are computed in this thesis. If statistical independence between the conditioning parameters is assumed, $\widetilde{c}$ can be related to $\widetilde{Y}_c$ (Bruel, Rogg, and Bray, 1991):

$$\langle c|\eta\rangle=\widetilde{c}\tag{3.41}$$

It follows that:

$$\langle Y_c|\eta\rangle=\widetilde{c}\left(Y_{c,eq}(\eta)-Y_{c,u}(\eta)\right)+Y_{c,u}(\eta)\tag{3.42}$$

The integration with the pdf yields:

$$\widetilde{c}=\frac{\widetilde{Y}_c-\widetilde{Y_{c,u}}}{\widetilde{Y_{c,eq}}-\widetilde{Y_{c,u}}}\tag{3.43}$$

where the Favre averaged $Y_{c,eq}$ and $Y_{c,u}$ are expressed using the pdf $\widetilde{Y_{c,u}} = \int_0^1 Y_{c,u}(\eta)P(\eta)d\eta$ and $\widetilde{Y_{c,eq}} = \int_0^1 Y_{c,eq}(\eta)P(\eta)d\eta$
Similarly an expression for the variance can be obtained, starting by taking the average of the square of c and noticing that $\langle c^2|\eta\rangle = \widetilde{c^2}$ (due to the statistical independence) we can obtain:

$$\left\langle {Y_c}^2|\eta\right\rangle = \widetilde{c^2}\left(Y_{c,eq}(\eta) - Y_{c,u}(\eta)\right)^2 + 2\left\langle Y_c|\eta\right\rangle Y_{c,u}(\eta) - {Y_{c,u}}^2(\eta) \tag{3.44}$$

Taking the square of Eq. 3.42 gives :

$$\langle Y_c|\eta\rangle^2 = \widetilde{c}^2\left(Y_{c,eq}(\eta) - Y_{c,u}(\eta)\right)^2 + 2\widetilde{c}\left(Y_{c,eq}(\eta) - Y_{c,u}(\eta)\right)Y_{c,u} + Y_{c,u}^2(\eta) \tag{3.45}$$

Subtracting equation 3.44 with 3.45 using 3.42 one can obtain:

$$\left\langle Y_c^2|\eta\right\rangle - \langle Y_c|\eta\rangle^2 = \widetilde{Y_c''^2}\left(Y_{c,eq}(\eta) - Y_{c,u}(\eta)\right)^2 \tag{3.46}$$

Integrating over the PDF yields:

$$\widetilde{c''^2} = \frac{\widetilde{Y_c''^2}}{\widetilde{Y_{c,eq}}^2 - 2\widetilde{Y_{c,eq}}\widetilde{Y_{c,u}} + \widetilde{Y_{c,u}}^2} \tag{3.47}$$

The models are next discussed, first in the state space, next in the physical space.

3.4 DCMC sub-models

The modelling of the conditional reaction source term $\langle\dot{\omega}_k|\eta,\zeta\rangle$, the conditional dissipation rates and the joint pdf are next discussed.

3.4.1 Conditional reaction source terms

Providing that the conditioning parameters correlate well with the composition fluctuation, the first-order closure is employed:

$$\langle\dot{\omega}_\phi|\eta,\zeta\rangle \simeq \dot{\omega}_k(Q_T, Q_k, P) \tag{3.48}$$

Zero conditional fluctuations means perfect correlation, which is a condition hardly possible to satisfy for all combustion regimes. It is reminded that the study of the DCMC is motivated by the use of this closure which becomes justifiable when appropriate conditioning parameters are chosen for a given regime.

3.4.2 Conditional dissipation rates

The modelling of the conditional dissipation rates is a challenging task, and models in the context of DCMC are not available. New models are not presented in this thesis. In the following the simple extension to two conditioning parameters of the current available models are discussed.

Modelling of $\langle N_\xi|\varphi_1,\varphi_2\rangle$

The AMC (Amplitude Mapping Closure) (Gao and O'Brien (1991)) allows the closure of the conditional dissipation rate $\langle N|\xi\rangle$. Its validity for two conditioning parameters will depend on the choice of the conditioning parameters. It follows:

$$\langle N_\xi|\varphi_1,\varphi_2\rangle = A.G(\varphi_1) \tag{3.49}$$

Where A is the amplitude which is known after double integration of the previous relation, hence:

$$\langle N_\xi|\varphi_1,\varphi_2\rangle = \frac{\widetilde{N_\xi}.G(\varphi_1)}{\iint G(\varphi_1)P(\widetilde{\varphi_1,\varphi_2})d\varphi_1 d\varphi_2} \tag{3.50}$$

with $G(\varphi_1) = \exp\left(-2\left[\text{erf}^{-1}(2\varphi_1-1)^2\right]\right)$.
This model is generally expected to be accurate for the two mixture fractions formulation, although Doran (2011) discusses the modelling implications for possible dependencies when strong inhomogeneities invalidate the assumption of independence.

For the DCMC ξ-c the uniform A across the c space is not a trend which is desired since unburned mixtures are expected to experience a higher N_ξ. The dependency of A with φ_2 is discussed assuming G is a function of φ_1 only, such that:

$$\langle N_\xi|\varphi_1,\varphi_2\rangle = A(\varphi_2).G(\varphi_1) \tag{3.51}$$

Integrating the above relation gives:

$$\widetilde{N_\xi} = \int A(\varphi_2)\widetilde{P(\varphi_2)}F(\varphi_2)d\varphi_2 \tag{3.52}$$

where $F(\varphi_2) = \int G(\varphi_1)P(\widetilde{\varphi_1|\varphi_2})d\varphi_1$. The conditional mean can be expressed as:

$$\widetilde{N_\xi} = \iint \langle N_\xi|\varphi_1,\varphi_2\rangle\, \widetilde{P(\varphi_2)}P(\widetilde{\varphi_1|\varphi_2})d\varphi_1 d\varphi_2 \tag{3.53}$$

From the two above relations it is found that:

$$\langle N_\xi|\varphi_2\rangle = A(\varphi_2)F(\varphi_2) \tag{3.54}$$

Providing that $\langle N_\xi|\varphi_2\rangle$ is known, 3.51 is closed. Unfortunately information about $\langle N_\xi|\varphi_2\rangle$ is not available, however, attempting to close the term would be easier to close $\langle N_\xi|\eta,\zeta\rangle$ directly.

Without A depending on c, the choice of the averaging method will significantly affect the results as variation of N_ξ with c is accounted for with the pdf weighted average method only. Note that the approximation: $\widetilde{P(\varphi_1,\varphi_2)} \simeq \widetilde{P(\varphi_2)}\widetilde{P(\varphi_1|\varphi_2)}$ has been employed in the previous equations following previous work (Bondi and Jones, 2002), (Landenfeld, Sadiki, and Janicka, 2002), (Schneider & al., 2008).

Modelling of $\langle N_c|\eta,\zeta\rangle$

Next the conditional dissipation rate of the progress variable $\langle N_c|\eta,\zeta\rangle$ is discussed. Modelling have been discussed in the context of premixed flames. Nguyen & al. (2010) developed a model in the flamelet context by studying one-dimensional freely propagating premixed flamelets for various equivalence ratios. They looked at the distribution of the gradient of Y_c versus the ratio of Y_c to its value at equilibrium conditions $Y_{c,eq}$. In their definition $Y_{c,u}$ was set to zero. If the progress variable is defined by a linear combination of the intermediate or major species (as done in this study) their model is applicable. Furthermore, they assume that the coupling of the flow field with the flame manifests as a external strain rate affecting the flame, such as:

$$\begin{aligned}\langle N_{Y_c}|\eta,\zeta\rangle &= B.G\left(\frac{\eta}{2\eta_{st}}\right)G(\zeta)\\ B &= \frac{\widetilde{N_c}}{\iint G\left(\frac{\eta}{2\eta_{st}}\right)G(\zeta)P(\eta,\zeta)d\eta d\zeta}\end{aligned} \tag{3.55}$$

However, the conditional dissipation rate of the normalised progress variable $\langle N_c|\eta,\zeta\rangle$ is needed. Relations between the different dissipation rate terms can be obtained starting from :

$$\frac{\partial Y_c}{\partial x_i} = \frac{\partial c}{\partial x_i}Y_{c,eq} + c\frac{\partial Y_{c,eq}}{\partial \eta}\frac{\partial \xi}{\partial x_i} \tag{3.56}$$

Multiplying the above relation respectively by $2D\frac{\partial Y_c}{\partial x_i}$, $2D\frac{\partial c}{\partial x_i}$, or $2D\frac{\partial \xi}{\partial x_i}$ and taking the conditional average give the following relations :

$$\langle N_{Y_c}|\eta,\zeta\rangle = \langle N_{c,Y_c}|\eta,\zeta\rangle\, Y_{c,eq} + \left(\zeta\frac{\partial Y_{c,eq}}{\partial \eta}\right)\langle N_{Y_c,\xi}|\eta,\zeta\rangle \tag{3.57}$$

$$\langle N_{c,Y_c}|\eta,\zeta\rangle = \langle N_c|\eta,\zeta\rangle\, Y_{c,eq} + \left(\zeta\frac{\partial Y_{c,eq}}{\partial\eta}\right)\langle N_{c,\xi}|\eta,\zeta\rangle \tag{3.58}$$

$$\langle N_{Y_c,\xi}|\eta,\zeta\rangle = \langle N_{c,\xi}|\eta,\zeta\rangle\, Y_{c,eq} + \left(\zeta\frac{\partial Y_{c,eq}}{\partial\eta}\right)\langle N_{\xi}|\eta,\zeta\rangle \tag{3.59}$$

Including relation 3.59 and 3.58 in 3.57 yields :

$$\begin{aligned}\langle N_{Y_c}|\eta,\zeta\rangle = &\langle N_c|\eta,\zeta\rangle\left[\left(\zeta\frac{\partial Y_{c,eq}}{\partial\eta}\right)Y_{c,eq^2} + Y_{c,eq}\right]\\ &+\langle N_{c,\xi}|\eta,\zeta\rangle\left(\zeta\frac{\partial Y_{c,eq}}{\partial\eta}\right)Y_{c,eq}\\ &+\langle N_{\xi}|\eta,\zeta\rangle\left(\zeta\frac{\partial Y_{c,eq}}{\partial\eta}\right)^2\end{aligned} \tag{3.60}$$

This equation relates the key dissipation rates parameter involved in the problem. If $\langle N_c|\eta,\zeta\rangle$ was known the conditional cross scalar dissipation term could be obtained. Unfortunately, N_c has not been computed in their study.

The above relation is applicable in premix flames where strong gradients of c are expected in the stoichiometric region. However, in turbulent autoignition where gradients of c are influenced by mixing, richer mixtures are likely to experience strong gradients. Since the AMC model accounts for mixing due to the turbulence, its use as a first approximation seems more justified :

$$\langle N_c|\eta,\zeta\rangle = C.G(\zeta) \tag{3.61}$$

$$\langle N_c|\eta,\zeta\rangle = \frac{\widetilde{N_c}.G(\zeta)}{\iint G(\zeta)\widetilde{P(\eta,\zeta)}d\eta d\zeta} \tag{3.62}$$

Modelling of $\langle N_{c,\xi}|\eta,\zeta\rangle$

The conditional cross scalar dissipation terms can be written using the unit normal vectors:

$$\langle N_{\xi,c}|\eta,\zeta\rangle = \left\langle \mathbf{n_\xi}.\mathbf{n_c}\sqrt{N_\xi N_c}|\eta,\zeta\right\rangle \tag{3.63}$$

The following model is suggested for the conditional cross scalar dissipation terms $\langle N_{\xi,c}|\eta,\zeta\rangle$:

$$\langle N_{\xi,c}|\eta,\zeta\rangle \simeq \mathbf{n_\xi}.\mathbf{n_c}\sqrt{\langle N_\xi|\eta,\zeta\rangle\,\langle N_c|\eta,\zeta\rangle} \tag{3.64}$$

Where the following assumption has been used $\left\langle\sqrt{N_\xi N_c}|\eta,\zeta\right\rangle \simeq \sqrt{\langle N_\xi|\eta,\zeta\rangle\,\langle N_c|\eta,\zeta\rangle}$. It is noted that 3.64 is exact using the flamelet notations. It is not clear how the conditional mean approximation affect the results and require further consideration. The

direction of unit normal vectors to the isosurfaces are discussed for Y_c by Nguyen & al. (2010):

1. $\mathbf{n}_\xi.\mathbf{n}_{\mathbf{Y_c}} \simeq 0$ corresponds to weakly stratified to mostly premixed flame. There is no cross conditional dissipation rates in that case.

2. $\mathbf{n}_\xi.\mathbf{n}_{\mathbf{Y_c}} \pm 1$ is likely to occur in a moderately curved diffusion flame. In a one-dimensional counterflow flame $+1$ is expected for the lean region, whereas -1 for the rich region.

3. $-1 < \mathbf{n}_\xi.\mathbf{n}_{\mathbf{Y_c}} < +1$ would occur in partially premixed combustion regimes.

Since $\mathbf{n}_{\mathbf{Y_c}}$, $\mathbf{n_c}$ aligns, the above explanation is valid also for the normalised progress variable. An estimation of the scalar product of the unit vectors normal to the isosurfaces is obtained, using similar relation than 3.63 but for N_{Y_c} and using relation 3.55 and 3.49:

$$\mathbf{n}_\xi.\mathbf{n}_{\mathbf{Y_c}} \simeq \frac{\widetilde{N_{\xi,Y_c}}}{\iint \left(B.A.G(\eta)G\left(\frac{\eta}{2\eta_{st}}\right)G(\zeta)\right)^{1/2} P(\eta,\zeta;x_i,t)d\eta d\zeta} \tag{3.65}$$

Again for the normalised progress variable the above relation does not hold. A possible avenue to model $\mathbf{n}_\xi.\mathbf{n_c}$ would be to use the correlation coefficient:

$$\mathbf{n}_\xi.\mathbf{n_c} = \frac{\widetilde{\xi c}}{\sqrt{\widetilde{\xi''^2}\widetilde{c''^2}}} \tag{3.66}$$

Modelling of $\langle N_{\xi_1,\xi_2}|\eta_1,\eta_2\rangle$

Hasse and Peters (2005) argues that since that in a isotropic turbulent flow the unit normals should not align in a specific direction, on average the contribution of this term is likely to be negligible. As mentioned above Doran (2011) argues that the term in the state space cannot be negligible at the boundary $\xi_1 + \xi_2 = 1$, otherwise, conservation is not enforced (3.28). Note that $\langle N_{\xi_1,\xi_2}|\eta_1,\eta_2\rangle$ does not require any modelling in this thesis since in Chapter 3 the term is taken from the DNS.

3.4.3 Joint pdf

The pdf provides information about the local state of mixing of the fluid. In the DCMC the joint pdf is necessary in order to obtain mean quantities from the state space. However, similar to the conditional dissipation rates their modelling is an active

field of research especially for the joint pdf of ξ and c. Approaches using stochastic particle method (Monte Carlo) are possible avenues which are very costly, alternatively, the use of presumed pdf based on moments of each parameter provides a simple and straightforward way to compute the pdf. As observed in Chapter 5 the DCMC is an expensive model, therefore, the case of presumed-pdf are considered for the present study.

Prior to discussing the modelling of the joint pdf, the modelling of the marginal pdf of key parameters are reviewed.

Modelling of $\widetilde{P(\xi)}$

The β-pdf is a widely used model in system with two-feed combustion systems which is a function of the mean and the variance of the mixture fraction. The model reads:

$$\widetilde{P}(\eta; u, v) = \frac{\eta^{u-1}(1-\eta)^{v-1}}{B(u,v)} \tag{3.67}$$

$$u = w\widetilde{\xi} \tag{3.68}$$

$$v = w(1-\widetilde{\xi})\widetilde{\xi} \tag{3.69}$$

$$w = \frac{\widetilde{\xi}(1-\widetilde{\xi})}{\widetilde{\xi''^2}} \geq 0 \tag{3.70}$$

$$B(u,v) = \frac{\Gamma(u)\Gamma(v)}{\Gamma(u+v)} \tag{3.71}$$

The β-pdf give singularities at $\eta = 0$ and $\eta = 1$. Wright, De Paola, & al. (2005) uses a Clipped-Gaussian pdf at the boundary, which reads:

$$\widetilde{P}(\eta) = \gamma_1\delta(\eta) + (1-\gamma_1-\gamma_2)\frac{H(\eta)}{I_g} + \gamma_2\delta(1-\eta) \tag{3.72}$$

$$H(\zeta) = \frac{1}{\sqrt{2\pi\widetilde{\xi''^2}}}\exp\left(-\frac{(\eta-\widetilde{\xi})^2}{2\widetilde{\xi''^2}}\right) \tag{3.73}$$

$$I_g = \int_0^1 H(\eta)d\eta \tag{3.74}$$

$$\gamma_1 = \int_{-\infty}^0 H(\eta)d\eta \tag{3.75}$$

$$\gamma_2 = \int_1^{\infty} H(\eta) d\eta \tag{3.76}$$

Their model is used for the present study.

Modelling of $\widetilde{P(c)}$

The pdf of reacting scalars are more complicated to model due to mixing and added effect of chemical reactions where the coupling of these two effects depends on the combustion regime. Bray, Domingo, and Vervisch (2005) discusses the modelling of $P(c; x, t)$ in partially premixed combustion in the case of sufficiently high Damköhler number. The thin reaction zone leads to $c = 0$ outside the flame and $c = 1$ within, hence, for such regime the pdf is strongly bimodal.
In turbulent autoignition c varies during pre-ignition as observed in Chapter 4. The bimodal distribution for such case is valid only when the flame is fully established. Beta distribution has been tested in DNS with added regimes of extinction and reignition (Cha and Pitsch, 2002). It has been found that the beta pdf incorporated into the CMC framework accurately predicted the conditional mean. However, it could not describe the case of extinction and reignition were the pdf becomes unimodal or bimodal.

Modelling of $\widetilde{P(\xi, c)}$

In the DCMC the joint pdf is required. Its modelling is particularly challenging since c can be a strong function of ξ.
Ihme and Pitsch (2008a) uses the Statistically-Most-Likely-Distribution (SMLD) for the marginal pdf $P(c|\xi)$ following Bayes' decomposition $P(\xi, c) = P(\xi)P(c|\xi)$. The model consists of maximizing the entropy which can be interpreted as using the minimum amount of information. In other words, no additional information about the shape of the distribution is required, only the moments are used. Improved agreement was obtained in flows with extinction, reignition and shear flows. However, the β-pdf was observed to outperform the SMLD in regions where unmixed scalar distribution are present such as the fuel inlet. In RANS information about $P(c|\xi)$ is not available unlike in LES where the pdf can be approximated by the unconditional one. Such approximation is possible since most of the scalar variance within a computational cell is resolved Ihme and Pitsch (2008b).
An alternative way is to account for the dependency of the sample space variables through the Copulas. There are functions relating multivariate distribution to the marginal distributions of the variables.

Darbyshire and Swaminathan (2012) tested the model by simulating V-flames using RANS. They compared the improved model with a model assuming independence between the conditioning parameters:

$$\widetilde{P}(\xi, c) \simeq \widetilde{P(\xi)}\widetilde{P(c)} \tag{3.77}$$

When simulating V-flames using RANS the differences between the two models were marginal which they attribute to low turbulence and stratification levels.
Matheson (2016, PhD thesis) employs the model first for a lifted flame with ethylene chemistry where differences where also found to be marginal. Next, he studied the Sandia constant volume chamber (studied in the Chapter 5) where the lift-off length and the ignition delay time were found to be under-predicted. Using the Copula resulted in minor changes for the lift-off length and improvement of the ignition delay time. However, the comparison was performed for one case only, therefore more cases need to be run in order to draw conclusions.

The *a priori* analyses using DNS and experimental carried out by the previous authors clearly motivate the use of Copula. However, in simulations with RANS the small differences observed between the models motivate the use of relation 3.77 for the present work.

Modelling of $P(\widetilde{\xi_1, \xi_2})$

The statistical independence between two non-reactive scalars facilitate modelling since relation 3.77 can be used. Doran (2011) discusses advance modelling of the joint pdf of $P(\widetilde{\xi_1, \xi_2})$. He compares two models for the joint pdf with the SMLD. The first is the Dirichlet distribution which is an extension of the beta distribution to the multivariate case (Girimaji, 1991). The restricted set of moments (two means and one overall variance) was found to be the principal limitation of the model. In order to account for more moments he developed the second model called bivariate beta distribution which has a shape related to the beta distribution and satisfy all the first and second moments. The different models predicted the same trends in the case isotropic with equal means for both injections were employed whereas when inhomogeneities were introduced (by varying the equivalence ratios) the SMLD and especially the bivariate distributions where found to perform better. Note that this term does not to be modelled in the current thesis since its values are taken from the DNS in the next chapter.

3.4.4 Models in the physical space

Turbulent flux

$$\bar{\rho}\widetilde{u_i''\xi''} = -\bar{\rho}\frac{\nu_t}{S_{ct}}\frac{\partial\widetilde{\xi}}{\partial x_i} \tag{3.78}$$

A gradient assumption has been used to model the term where ν_t is the turbulent viscosity and S_{ct} is the turbulent Schmidt number which is of the order of unity (set to 0.8 for the present study).

The same model was used for the turbulent flux of the c. Depending on the combustion regime this assumption is not always valid. For instance, in the case of a premixed flame, a counter gradient transport has been observed which causes the effective turbulent diffusivity for progressive variable become negative (Veynante, Trouvé, & al., 1997). This term requires a specific attention in the case of "flame expansion" problems (Echekki and Mastorakos, 2011), as in autoignition, spark-ignition, and, multiple-injection problems. For example, after the occurrence of an autoignition spot, the reaction-front propagates with a speed that may be orders of magnitude greater than the laminar flame speed under those conditions since, away from the spots, the mixture is partially reacted. In the context of spark-ignition (Richardson, Chakraborty, and Mastorakos, 2007) analysed the term. The modelling of this term has not been studied at the current stage in the context of split fuel injection.

The gradient assumptions were employed also for $\widetilde{\xi''^2}$, $\widetilde{c''^2}$ and $\widetilde{\xi c''}$.

Production terms

A gradient assumption has been used to model $\bar{\rho}\widetilde{u_i''\xi''}$ in the production term.

$$\bar{\rho}\widetilde{u_i''\xi''}\frac{\partial\widetilde{\xi}}{\partial x_i} = -\bar{\rho}\frac{\bar{\nu}_t}{S_{ct}}\frac{\partial\widetilde{\xi}}{\partial x_i}\frac{\partial\widetilde{\xi}}{\partial x_i} \tag{3.79}$$

The similar term term appearing in the equation of $\widetilde{c''^2}$ and $\widetilde{\xi c''}$ have been modelled using also the gradient assumption.

Dissipation rate of ξ

The decay of the mean dissipation rates corresponding to the decay of the scalar fluctuations fluctuations are estimated by the variance of the scalar. They have been modelled using the variance and the inverse turbulence timescale:

$$\widetilde{\chi}_\xi = C_\phi\frac{\widetilde{\epsilon}}{\widetilde{k}}\widetilde{\xi''^2} \tag{3.80}$$

$$\widetilde{\chi_c} = C_\phi \frac{\widetilde{\epsilon}}{\widetilde{k}} \widetilde{c''^2} \tag{3.81}$$

$$\widetilde{\chi_{\xi,c}} = C_\phi \frac{\widetilde{\epsilon}}{\widetilde{k}} \widetilde{\xi c''} \tag{3.82}$$

The constant C_ϕ was set to 2. Although, the previous model has been found to be valid for non-reactive scalars it is found to over-predict the mean dissipation rate for reactive scalars in premix flames. Extensions accounting for equivalence ratio in the context of premixed flames have been developed (Darbyshire, Swaminathan, and Hochgreb, 2010). No models have been developed/adapted for turbulent autoignition. However, Ruan & al. (2012) compared 3.81 with the advanced model developed for premixed flame in a lifted flame, he found that the former performed significantly better than the latter model. He attributed the discrepancies to the presence of several combustion modes and not solely the premixed mode. This motivates the use of 3.81 in this study. Similarly, he found that relation 3.82 was a good approximation for $\widetilde{\chi_{\xi,c}}$

3.5 Numerical methods

The eq.3.12 is discretised using a finite difference method. Second order central difference method for the second order derivatives are used. An upwind left-sided difference method is used if the convection term is negative, otherwise, a right-sided derivative is employed.

Because of the intricate coupling of the chemistry with the dissipation rate, standard numerical methods to solve the equations are not always applicable. The solver used is VODPK (Brown, Byrne, and Hindmarsh, 1989), (Brown, Byrne, and Hindmarsh, 1994). It is based on a linear multistep method using the backward differentiation formula. It is implicit with good stability properties and can be set for stiff and non-stiff solvers. The Operator Splitting (OS) method is a reference method used in this study (Wright, De Paola, & al., 2005).

The operator splitting method reads:

$$\begin{aligned}
\frac{\partial Q_k^{(1)}}{\partial t} &= QT_{1f} + QT_{2f} + QT_{3f} \\
& t \in [t_0, t_0 + \frac{t_0}{2}] \\
\frac{\partial Q_k^{(2)}}{\partial t} &= QT_{5f} + QT_{4f} \\
& t \in [t_0, t_0 + \Delta t] \\
\frac{\partial Q_k^{(3)}}{\partial t} &= QT_{1f} + QT_{2f} + QT_{3f} \\
& t \in [t_0 + \frac{t_0}{2}, t_0 + \Delta t]
\end{aligned} \tag{3.83}$$

The second step of the method can be computationally very expensive. An alternative method has been investigated which consists of integrating only the conditional reaction source term and interpolating the new solution back onto the previous grid. The method reads:

1. $\int_0^{t+dt} QT_{5f} dt$ is computed to find the new conditional mean of the composition denoted $Q_k^{''}(t + dt)$. The results are not correct yet due to the absence of the convection term in the state space (QT_{4f}).

2. At this stage plotting ζ versus $(Y_c - Y_{c,u}) / Y_{c,\Delta}$ results in a line deviating from a straigtht line. This new ζ is referred as $\zeta^{''}$ and is computed at every point in the state space. A straight line in that space corresponds to the solution prior using the method in step 1.

   The correction which accounts for the missing convection term consist of for each ζ to replace the composition by a linear interpolation of the newly obtained composition between the point on the L.H.S ($\zeta_L^{''}$) and R.H.S ($\zeta_R^{''}$) of ζ. This reads:

$$Q_k(\eta, \zeta) = Q_k(\eta, \zeta_L^{''}) + \frac{(\zeta - \zeta_L^{''})}{(\zeta_R^{''} - \zeta_L^{''})} \big(Q_k(\eta, \zeta_R^{''}) - Q_k(\eta, \zeta_L^{''}) \big) \tag{3.84}$$

The advantage of the method $\zeta^{''}$ is that the second step of the OS is faster and that the condition $(Y_c - Y_{c,u}) / Y_{c,\Delta} = \zeta$ is enforced.

Chapter 4

Results - I DNS analysis of multi-stream ignition

A range of combustion applications involve mixing between multiple streams such as recirculated exhaust gas (EGR), streams of different fuels in dual-fuel engines, and between fuel streams injected at different times in split-injection engines. Modelling of autoignition in multi-stream systems had been carried out by Doran, Pitsch, and Cook (2013) who used Direct Numerical Simulation (DNS) to study the interaction of an autoigniting flow with additional freshly injected fuel. Their extended flamelet model employed two mixture fractions and was tested by comparison with the DNS. Good agreement was observed between DNS and predictions of the model for the pressure and the heat release.

Using a similar DNS configuration, the objective of this chapter is to identify a set of conditioning parameters that accurately characterise the thermochemical states occurring during various injection strategies in the context of single and double conditional moment closure modelling (CMC and DCMC). The conditioning parameters investigated are based on mixture fractions and progress variables. The effect of the choice of conditioning parameters is assessed using two approaches:

1. In an *a priori* approach, the DNS data is conditionally averaged using alternative sets of conditioning variables, and the accuracy of the first-order reaction-rate closure is assessed in each case.

2. In an *a posteriori* approach, the CMC and DCMC equations are integrated numerically, using information about conditional dissipation rates taken from the DNS, in a fashion analogous to Doran, Pitsch, and Cook (2013), Kronenburg (2004), and, Cha, Kosály, and Pitsch (2001).

This section proceeds by presenting the details of the DNS setup, followed by an analysis on the effect of the injection time on the ignition. Subsequently the *a priori* analysis approach is outlined and the *a priori* results are discussed for several selected cases. Last, the *a posteriori* analysis and results are discussed, leading to recommendations of conditioning variables that are used further in the subsequent chapters.

4.1 DNS configuration

The DNS configuration employed in this section is designed to show the effects of turbulence-like flow fluctuations on mixing and chemical reaction as fuel goes through the process of autoignition in a hot oxidiser. In particular, the effect of introducing additional fuel at different times is investigated. The configuration is modelled on the one used by Doran, Pitsch, and Cook (2013), and extended to consider cases where fuel is injected at three different times. The DNS configuration consists of a two dimensional square domain with periodic boundary conditions. Fuel is introduced as "blobs" of fuel randomly generated in a background of air which mix and autoignite in a velocity field initialised with homogeneous isotropic velocity fluctuations. Subsequent fuel injections are accounted for by overlaying "blobs" of fuel at a later time.

The fuel stream is composed of 65% of H_2 with 35% of N_2. The focus of the study is not specifically on hydrogen combustion technology or on the chemistry of hydrogen autoignition, rather, hydrogen is adopted because it is a fuel whose ignition physics share several features with more complex fuels and which can be described by a relatively simple chemical model. In numerous combustion devices, combustion is initiated by injecting cold fuel into an ambient hot air. The temperature of the fuel is set equal to 400K, and the temperature of the oxidizer is 1050K, with a pressure of 1bar. Numerous analyses of turbulent autoignition were conducted in the past with DNS using diluted hydrogen as a fuel (Hilbert and Thévenin, 2002), (Im, Chen, and Law, 1998).

4.1.1 Numerical simulation

The code used for the present study is s3d which was developed at the Sandia National Laboratories (Chen, Choudhary, & al., 2009). The governing equations presented in chapter 2 for compressible and reacting flow are integrated numerically on a structured Cartesian mesh. Several degrees of simplifications can be made in DNS depending on whether effects of compressibility are significant. The code s3d solves

the fully compressible formulation of the Navier-Stokes equations allowing study of combustion including the interactions between flames and pressure waves. The numerical schemes used are high-order finite difference schemes due to their accuracy and their efficiency in massively parallel computation: a six-stage fourth-order explicit Runge-Kutta method is used for time integration (Kennedy and Carpenter, 1994) and an eighth-order central differencing scheme is used for the spatial terms. A tenth-order filter is used periodically to remove spurious high wave number oscillations in the solution (Kennedy, Carpenter, and Lewis, 2000).
Using an explicit time advancement scheme in this case restricts the time step such that the Courant-Friedrichs-Lewy number (CFL), defined by $CFL = a\frac{\Delta t}{\Delta x}$ with a the speed of the sound, should be less than unity, prescribing that an acoustic wave cannot move more than one computational grid step during one computational time step.

The 1.2cm $\times$ 1.2cm domain is discretised with 360^2 grid points and the time step chosen is 4ns. The resolution was shown to give sufficient resolution of the reaction zone. Several simulations with 720^2 indicated that increasing resolution does not show different results.

The Fuel-air chemistry is modelled using a 9 species hydrogen mechanism (Li & al., 2004). Molecular diffusion is modelled using the unity Lewis number approximation. Differential diffusion is important in hydrogen combustion technology, due to the high diffusivity of hydrogen. However most split-injection engines use hydrocarbon fuels, for which differential diffusion is not a leading-order phenomenon. The goal of the thesis is to develop modelling for practical split-injection systems, for which it is justifiable to simplify modelling by assuming unity Lewis number. For this reason, unity Lewis number assumptions are used in the DNS and in the model development, while acknowledging that this is not a correct description of hydrogen combustion physics.

4.1.2 Generating the initial distribution of fuel mass fraction

The mixture fraction is initialised by generating random "blobs" in the domain, giving a bimodal distribution of fuel mass fraction that is statistically homogeneous and isotropic. The procedure starts by generating a continuous reference scalar field with a characteristic length scale based on a model spectrum for turbulent flow. The continuous scalar field is then binarised using a threshold, and regions of the domain where the reference scalar is above the threshold are set to pure fuel, and the thermochemical state in the remainder of the domain is left unchanged. The threshold is adjusted in order to obtain the desired fuel-air ratio following injection. The mathematical detail

of this procedure is given below.

The reference scalar field in generated in Fourier space using a distribution which has a similar form to the Passot-Pouquet distribution (Chen, Hawkes, & al., 2006).

$$\phi(\boldsymbol{\kappa}) = \frac{2\pi}{L}\sqrt{\frac{f_\phi(\kappa)}{2\pi\kappa}}exp\left[2\pi i\theta(\boldsymbol{\kappa})\right] \tag{4.1}$$

where κ is the magnitude of the wavenumber $\boldsymbol{\kappa}$, and, the parameter θ is a random number distributed uniformly between 0 and 1. The width of the $f_\phi(\kappa)$ profile is κ_0 and it is centred on the most energetic wavenumber κ_e :

$$f_\phi(\kappa) = \begin{cases} 1, & \text{if } \kappa_e - \kappa_0/2 \leq \kappa \leq \kappa_e + \kappa_0/2 \\ \frac{32}{3}\sqrt{\frac{2}{\pi}}\frac{u'^2}{\kappa_e}\left(\frac{\kappa}{\kappa_e}\right)^4 exp\left(-2\left(\frac{\kappa}{\kappa_e}\right)^2\right) & \text{otherwise} \end{cases} \tag{4.2}$$

The reference scalar field in physical space is obtained by applying an inverse Fourier transformation. At this stage, the field contains values with a continuous variation of positive and negative values and zero mean (see Fig 4.1(a)). In their study of two-stream scalar mixing, Eswaran and Pope (1988) obtained a bi-modal scalar distribution by resetting the negative values to -1 and the positive values to 1. However, here we want to set physically-realisable values of fuel mass fraction, and to obtain a specified averaged equivalence ratio φ_f in the domain. If the equivalence ratio in the oxidiser stream, before any fuel is injected is φ_o, the final equivalence ratio after all fuel injections have been performed is to be φ_g, and the proportion of the total fuel injection to be added in the first injection is X_1, then the target equivalence ratio for the first fuel addition is equal to

$$\varphi_{f1} = \varphi_o + (\varphi_g - \varphi_o)X_1 \tag{4.3}$$

The threshold is adjusted iteratively until the target equivalence ratio φ_f is obtained.

Finally the field is filtered in physical space such that it can be resolved on a computational mesh. A box filter is applied:

$$\hat{\xi}_{ijk} = \frac{1}{(2m+1)^3}\sum_{i-m}^{i+m}\sum_{j-m}^{j+m}\sum_{k-m}^{k+m}\xi_{ijk} \tag{4.4}$$

with m the number of grid points inside the filter stencil. In this study m is set equal to at least 9, so that the filtered scalar field is smooth across the 8^{th}-order stencil used for finite differences. The physical size of the filter is dependent on m and the grid spacing, however the grid spacing is constant for all of the final simulations presented in this chapter, so that $m = 9$ gives a constant filter length scale equal to 300μm. The resulting initial mixture fraction field is shown in Fig. 4.1(c)).

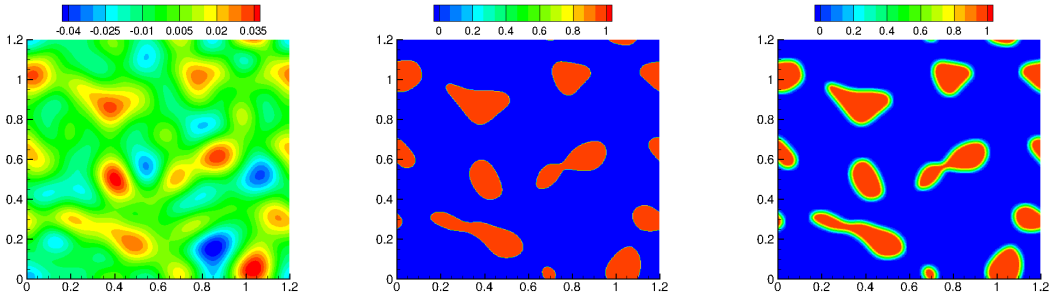

(a) Field after inverse Fourier transform (b) Binarised mixture fraction field (c) Filtered mixture fraction field

Figure 4.1: Mixture fraction field respectively before binarisation procedure, after binarisation, and after applying filtering for $X_1 = 100\%$ and $\varphi_g = 0.8$

4.1.3 Generating the mixture fraction field for subsequent fuel injection events

For subsequent fuel injection events, random blobs within the DNS solution domain are instantaneously replaced with fresh fuel mixture. The approach is similar to the approach taken for the first injection described above. The regions that get replaced with fresh fuel are determined by generating a new homogeneous isotropic reference scalar field and binarising it using a threshold. The mixture fraction ξ_n for the nth injection is set to unity in the region where the reference scalar exceeds the threshold value. The enthalpy (h) and mass fraction vector ($\mathbf{Y}$) fields are obtained from the values in the existing DNS solution (subscript old) and in the fuel stream (subscript fu) by assuming a linear relation with the mixture fraction of the n^{th} injection:

$$\mathbf{Y}_{new} = \mathbf{Y}_{fu}\xi_n + \mathbf{Y}_{old}(1 - \xi_n) \tag{4.5}$$

$$h_{new} = h_{fu}\xi_n + h_{old}(1 - \xi_n) \tag{4.6}$$

The equivalence ratio ϕ_{fn} immediately following the nth injection event is then calculated and the threshold is adjusted iteratively in order to achieve a target equivalence ratio. For multiple injections the target equivalence ratio after the n^{th} injection is given by the following relation:

$$\varphi_{f_n} = \varphi_o + (\varphi_g - \varphi_o) \sum_{i=1}^{n} X_i \tag{4.7}$$

where X_i is the proportion of the total fuel addition that is added during the ith injection event.

Because the pressure increases during the DNS calculation, the fuel injection temperature is taken as a function of pressure, assuming that the fuel undergoes an isentropic expansion from its initial temperature.

A figure of the initial field, and the solution at the time of the subsequent injection is depicted in Fig 4.2. It can be seen that the number and size of the blobs vary depending on the percentage of fuel being added.

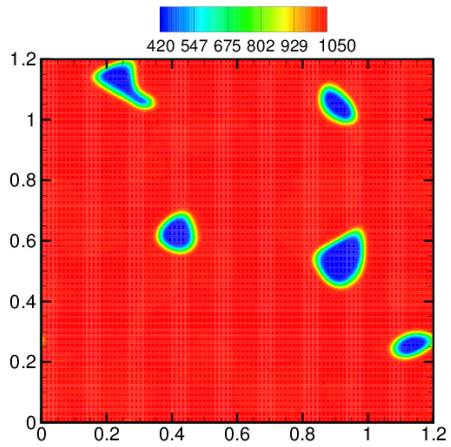

(a) Initial temperature field

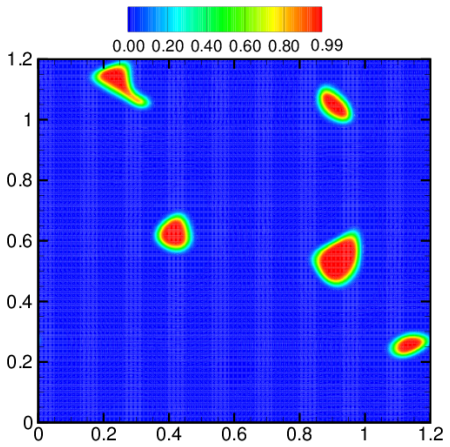

(b) Initial mixture fraction field

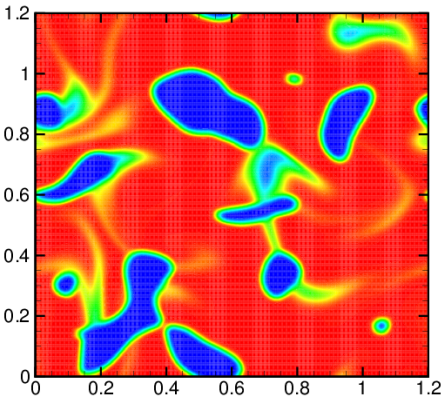

(c) Temperature field at the time of the second injection

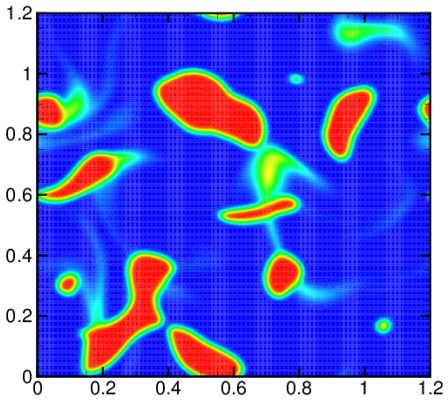

(d) Mixture fraction field at the time of the second injection

Figure 4.2: Temperature and mixture fraction fields in the physical space (x, y) at the initial time and the time of the second injection with $X_1 = 20\%$, and, $X_2 = 80\%$.

4.1.4 Initialisation of the velocity field

The velocity field is initialised with zero mean plus fluctuations with an r.m.s value u' and a characteristic length scale. The Passot-Pouquet model turbulence spectrum is adopted (Passot and Pouquet, 1987):

$$E(\boldsymbol{\kappa}) = C\left(\frac{\boldsymbol{\kappa}}{\kappa_e}\right)^4 \exp\left(-2\left(\frac{\boldsymbol{\kappa}}{\kappa_e}\right)^2\right) \tag{4.8}$$

with κ_e the most energetic wavenumber and C a constant which is defined below. This model is widely used for its good compromise between accuracy and simplicity, however, it does not take into account the effect of the small scales. The spectral characteristics of isotropic turbulence are :

$$k = \int_0^\infty E(\boldsymbol{\kappa}) d\boldsymbol{\kappa} \tag{4.9}$$

$$\epsilon = 2\nu \int_0^\infty \boldsymbol{\kappa}^2 E(\boldsymbol{\kappa}) d\boldsymbol{\kappa} \tag{4.10}$$

$$L_{11} = \frac{3\pi}{4k} \int_0^\infty \frac{E(\boldsymbol{\kappa})}{\boldsymbol{\kappa}} d\boldsymbol{\kappa}, \tag{4.11}$$

where k denotes the turbulent kinetic energy, ϵ is the dissipation rate and L_{11} is the auto-correlation integral length scale. Substituting relation (4.8) into (4.9), (4.10) and (4.11) gives the following relations:

$$C = \frac{32}{3}\frac{k}{\kappa_e}\sqrt{\frac{2}{\pi}} \tag{4.12}$$

$$\epsilon = \frac{10}{4} k \kappa_e^2 \nu \tag{4.13}$$

$$L_{11} = \frac{\sqrt{2\pi}}{\kappa_e} \tag{4.14}$$

The size of the domain is taken equal to eight times the auto-correlation integral length scale L_{11}. The size of the domain was taken large enough to take into account the energy-containing motions, and the grid spacing is small enough to resolve the Kolmogorov length scale according to criteria given in Pope, 2000.

For this simulation configuration, a relevant Damköhler number can be defined as $D_a = (l_e/u')/\tau_{ign}$, with l_e the most energetic length scale and τ_{ign} the ignition delay. l_e and u' were selected in order to obtain D_a equal to unity. The ignition delay time characterising ignition of non-premixed fluid with the stated fuel and oxidiser compositions, temperatures and pressure in a quiescent environment is found to be $0.37ms$, via laminar simulation Case 1 introduced below. Setting D_a to unity ensures that the intensity of decaying velocity fluctuations remains high up to the ignition time.

The turbulent Reynolds number is $Re_T = \frac{u' L_T}{\nu}$, with L_T being the turbulent length scale. All of the non-dimensional parameters reported are based on the initial values in the flow field. Selecting values for Damköhler number, turbulent Reynolds number, viscosity and a characteristic ignition delay time, and setting $\epsilon = u'^3/L_T$, fully specifies the initial flow field. From these parameters, the corresponding rms velocity for a Passot Pouquet spectrum is given by,

$$u' = (10 Re_T)^{1/4} \sqrt{\frac{\pi \nu}{D_a \tau_{ign}}}. \tag{4.15}$$

L_T is related to L_{11} through the following relation:

$$L_T = \frac{1}{5} \frac{L_{11}^2 u'^3}{\pi k \nu} \tag{4.16}$$

4.1.5 Simulation cases

The effects of different injection schedules are investigated in this study by varying the number, timing, and proportions ($\mathbf{X}$) of the injections, while keeping the final global equivalence ratio ϕ_g equal to 0.8. The different cases studied are summarised in Table 4.1. The first case is a single injection case and is the reference case for the Chapter. Cases 2 and 2a include a second injection at 70% of the ignition time that is observed in Case 1. Case 2 has a 20:80 split of fuel mass between the two injections and Case 2a has a 5:95 split in order to investigate the effects of pilot injection. Case 3 involves three injections, with the amount of fuel added split evenly, and with the injection times occurring before the ignition delay time to mimic the behaviour of most strategies used in practice.

Cases	X_i (%)	$t_i(ms)$
1	$X_1 = 100\%$	-
2	$X_1 = 20\%, X_2 = 80\%$	$t_2 = 0.7\tau_{ign}$
2a	$X_1 = 5\%, X_2 = 95\%$	$t_2 = 0.7\tau_{ign}$
3	$X_1 = 33\%, X_2 = 33\%, X_3 = 33\%$	$t_2 = 0.54\tau_{ign}, t_3 = 0.7\tau_{ign}$

Table 4.1: DNS cases with $\tau_{ign} = 0.37ms$

4.2 Observations from split-fuel injection simulations

4.2.1 Effect of split-fuel injection

In the present study for the one injection Case 1, the heat release peaked initially at mixture fraction $\xi = 0.05$. Defining ignition as the occurrence of OH mass fraction greater than a threshold value of 0.0001, it is determined that $\xi = 0.05$ is the most reactive mixture fraction, ξ_{mr}. The subsequent reaction fronts propagate towards richer mixture and ultimately non-premixed combustion is established with the maximum temperature observed at the stoichiometric mixture fraction, $\xi_{st} = 0.195$.

Keeping ϕ_g constant for one and two injections (Case 1 and Case 2 respectively) allows investigation of effects of the injection schedule while keeping the overall heat release and pressure rise constant. Figure 4.3 confirms that the differences in injection schedules cause differences in the heat release profile, but not in the final pressure. Although, the chemical kinetics employed are different from hydrocarbon kinetics, the elementary kinetics involving H, O, OH, HO_2 and H_2O_2 determine the composition of the radical pool in these systems (Kreutz, Nishioka, and Law, 1994). The maximum value of the heat released is higher in Case 1, whereas the heat release spreads over a longer period of time in Case 2. In that latter case the second injection partly quenches the accumulation of some radicals that are required for autoignition to happen, therefore, less mixture ignites at an early time, resulting in a lower heat peak release. However the pockets of fuel from the second injection ignite faster than the fuel from the first injection due to mixing with the more reacted mixture, resulting in a smooth continuation of the heat release.

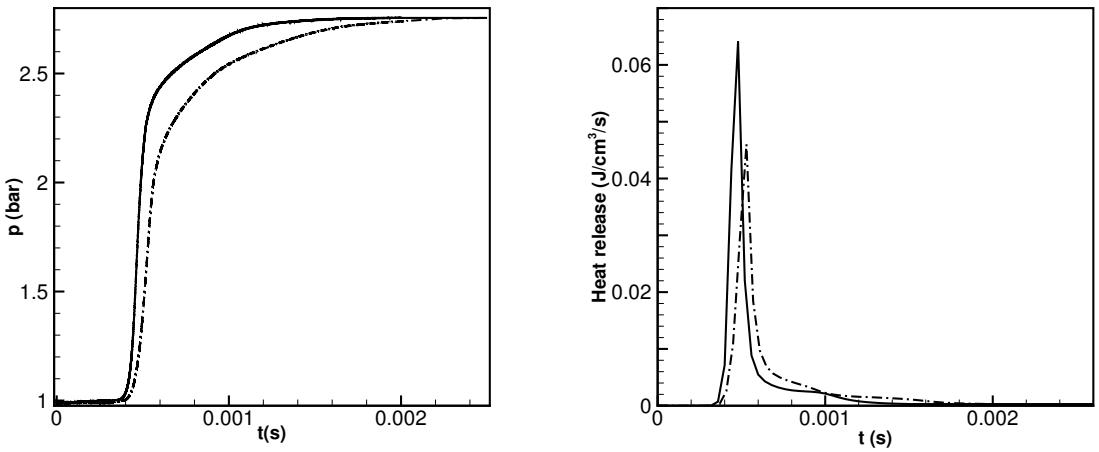

(a) Pressure trace

(b) Heat release

Figure 4.3: Pressure traces and heat release for the one injection case 1 (solid line) and two injections case 2 (dashed line)

4.2.2 Conditional statistics of dissipation rate

Modelling for double-conditionally-averaged scalar dissipation rates is a key ingredient for application of the DCMC approach. However there is a lack of information from autoigniting flows about the double-conditional statistics of (cross-)dissipation rates of mixture fraction and progress variable. Laboratory measurements of scalar dissipation rates and cross-dissipation rates in turbulent flows are especially challenging, however the present DNS provides complete information about joint statistics of dissipation and composition, albeit in a simple two-dimensional flow. Scatter plots of the scalar dissipation rates during simulation of Case 1 are shown in mixture fraction-progress variable space in Fig. 4.4. The un-normalised progress variable Y_c used in this analysis is based on the product of hydrogen combustion, $Y_c = Y_{H2O}$.

The scatter plots illustrate the ignition process, starting around the most reactive mixture fraction $\xi = 0.05$, followed by propagation through mixture fraction space, and evolution towards a one-dimensional manifold corresponding to the fully-burned state. During ignition there are very substantial fluctuations around the conditional mean composition, which cannot be described using the first-order single-conditional CMC approach. Although not visible on the linear colour map shown in Fig. 4.4, third column, the first instances of ignition arise in fluid with moderate and low mixture fraction dissipation rates, relative to the critical scalar dissipation rate above which

ignition does not occur Mastorakos and Bilger (1998), and, in this single-injection case, the conditional scatter can be attributed primarily to the effects of the variation in scalar dissipation rate through the flow.

The dissipation rate of Y_c shown in the first column of Fig. 4.4 increases during ignition as the conditional variance of Y_c grows, however it continues to increase between the second and third rows of Fig. 4.4. This further steepening of gradients after ignition indicates an increasing contribution of quasi-premixed flame propagation leading to diffusive flux aligned with gradients of Y_c after the formation of ignition kernels.

The cross-dissipation rate N_{ξ,Y_c} generally changes sign from positive values in fluid that is leaner than the mixture fraction where maximum Y_c occurs, to negative values in richer fluid. During ignition, the location of maximum Y_c is in lean fluid and, once burning, the maximum occurs close to the stoichiometric mixture fraction ($\xi_{st} = 0.195$). The sign of the cross dissipation rate indicates the direction of alignment between mixture fraction and Y_c gradients. Figure 4.5 shows the solutions of zero-dimensional singly-conditional CMC calculations involving autoignition with fixed dissipation rate amplitudes (using the AMC model for conditional dissipation rate), plotting the conditional average of Y_c across mixture fraction sample-space at many times. The figure indicates that the peak value of Y_c migrates from the most-reactive mixture fraction value towards the stoichiometric value and that the physical process of autoignition in the inhomogeneous mixture fraction field leads to a positive dependence of Y_c on ξ in mixture leaner than this maximum, and a negative dependence in richer mixture. Although the 0D-CMC calculations do not include the physics of flame propagation in progress variable space, it is shown that the general form of the N_{ξ,Y_c} evolution seen in the unsteady 2D flow can be explained by the physical processes (i.e. ignition and mixture fraction-space transport) represented by the 0D-CMC model.

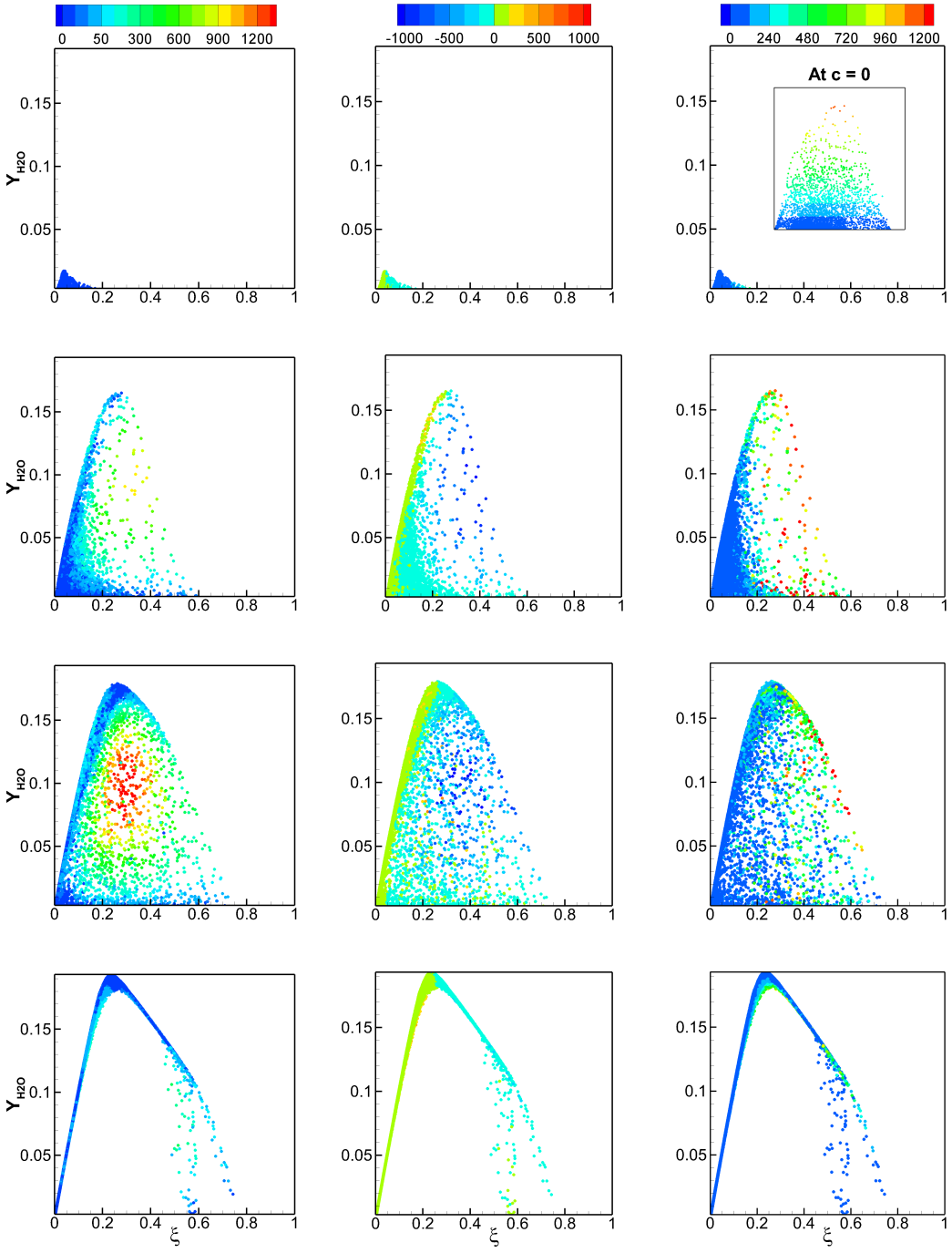

Figure 4.4: Y_{H_2O} versus ξ coloured by N_{Y_c} (first column), N_{ξ,Y_c} (second column), N_{ξ} (third column) at τ_{ign} (first row), $1.15\tau_{ign}$ (second row), $1.26\tau_{ign}$(third row), 1.57 τ_{ign}(fourth row). (For the subplot at c=0, the dissipation rate of ξ versus ξ is plotted)

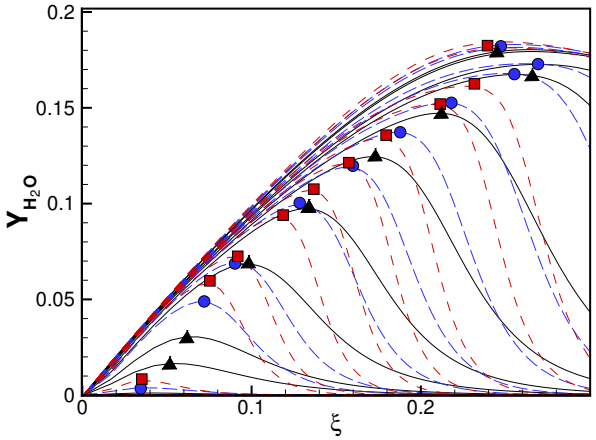

Figure 4.5: 0D-CMC solutions using $N_0 = 50$ (dashed line), $N_0 = 100$ (long dashed line), $N_0 = 200$ (solid line) at fixed time intervals. The symbols denote the maximum value $N_0 = 50$ (square), $N_0 = 100$ (circle), $N_0 = 200$ (triangle).

4.3 A Priori assessment of the first-order conditional moment closure for the reaction rate

Insight about modelling of split injection processes is obtained by looking at the statistics of the DNS for several cases. The quantities of interest are the conditional fluctuations around the conditional mean. The set of conditioning parameters that best accounts for the variation of the composition should give the smallest error in unconditional reaction rate. Plots similar to the one showed in Fig. 3.1 could be plotted in two dimensions, however, it can be visually difficult to assess the magnitude of the conditional fluctuations. Instead, in this work their impact on prediction of the mean reaction rate is assessed using the first-order closure for the reaction rate (Eq. 3.48), which neglects the fluctuations around the conditional mean.

Two approaches are used to assess the first-order closure in this and the following section. In this section, an *a priori* approach is used. This involves evaluating conditional averaged mass fractions and temperature from the DNS data, and using these in order to evaluate the reaction source terms using the first-order closure. It is called a priori because it depends directly on information from the supposedly exact DNS solution. In the subsequent section, an *a posteriori* approach is used. This involves solving the DCMC equations independently from the DNS, but using the same initial conditions and employing the first order closure. It is called a posteriori because it

does not obtain the conditional average composition directly from the DNS, rather it is obtained from the solution of the DCMC equations. This DNS-based a posteriori investigation does take the conditional scalar dissipation rates and joint pdfs from the DNS in order to remove any uncertainty due to modelling of those terms from the discussion of the reaction rate closure and choice of conditioning variables. Full a posteriori validation tests, with modelling applied also for joint pdfs and conditional dissipation rates, is presented in the subsequent chapters.

Kronenburg (2004) used DNS simulations of a turbulent flame undergoing local extinction and reignition to suggest that first-order DCMC modelling conditioned on mixture fraction and *sensible* enthalpy (which may be considered a reaction progress variable) provided an accurate closure for the mean reaction rate. Salehi & al. (2014) used the DCMC approach for the modelling of HCCI (Homogeneous Charge Compression Ignition) with temperature inhomogeneity by conditioning on mixture fraction and *total* enthalpy (which is a passive scalar and may be considered as a mixture fraction-like variable that tracks fluids with different unburned temperatures). Significant discrepancies were observed between the exact mean reaction rate and the modelled mean reaction rate using the total enthalpy as a conditioning parameter, although their *a posteriori* evaluation of this conditioning parameter showed very good agreement. Doran, Pitsch, and Cook (2013) used two mixture fractions in a two-dimensional flamelet approach to model autoignition following split injection, obtaining good predictions in a posteriori tests, even though the same method gives poor predictions in a priori tests below. This indicates that a lack of agreement between the first order closure evaluated from the DNS data with the conditional average reaction rate evaluated from the DNS does not necessarily imply that the same closure will not be useful when applied in an a posteriori test. A posteriori tests may be more forgiving because the chemical state is able to adjust according to the errors in the closure by rapidly driving the chemical state towards the correct slow-manifold in state space, whereas conditionally averaging DNS data can result in compositions away from the slow chemical manifolds that are not likely to be realised in practice, leading to much larger errors in reaction rate predictions.

The unclosed DCMC equations (Eq. 3.12) are exact, prior to modelling of the unclosed terms, and all of the terms can be evaluated from the DNS. The mean reaction source terms $\overline{\dot{\omega}_k}$ obtained from the DNS simulations can be computed in two different ways, either through simple spatial averaging of the DNS reaction rate, which corresponds to the exact solution, or by evaluating the conditional average state mass

fraction and temperature and integrating over the joint-pdf :

$$\overline{\dot{\omega}_k(T,\mathbf{Y})} = \iint \dot{\omega}_k\left(\langle T|\varphi_1^*,\varphi_2^*\rangle, \langle \mathbf{Y}|\varphi_1^*,\varphi_2^*\rangle\right) \widetilde{P(\varphi_1^*,\varphi_2^*)} d\varphi_1^* d\varphi_2^* \tag{4.17}$$

The pdf's and the conditional averages are obtained from the DNS for different sets of conditioning variables $\xi_1 - \xi_2$, $Y_{H_2O} - \xi$, $h_s - \xi$, and using one single conditioning parameter ξ. In order to do this a new post processing tool has been added to the s3d code in this project. The implementation of the pdf integration was verified comparing the unconditional mean temperature obtained by pdf-integration of conditional means (Eq. 4.17) with the unconditional mean obtained directly from the DNS data. Excellent accuracy is achieved with 100 uniformly space points for each conditioning variable.

The analysis of the first-order CMC for the reaction rate has been applied to cases 1, 2, and 3. In Fig. 4.6 the data for the one injection case (case 1) are plotted. It is observed that the mean reaction rates are significantly over predicted for all the species when conditioning only on the mixture fraction ξ, with the trends not captured for the intermediate species. It seems to indicate that single conditioning is not suitable for the modelling of the studied case. Using a progress variable, Y_{H_2O}, or h_s, as a conditioning parameter decreases the predicted mean reaction source terms. For Y_{H_2O} as a conditioning parameter the agreement suffers for intermediate species such as $Y_{H_2O_2}$, Y_{HO_2}, Y_O, Y_H, whereas for h_s excellent agreement is observed for all species.

The results for the two-injection case (Case 2) are plotted in Fig.4.7. In a similar fashion to the previous case, prediction suffers when using the mixture fraction ξ as the only conditioning parameter. The two mixture fraction conditioning parameters result in little improvement compared to single-conditioning on the mixture fraction ξ, in contrast to the conclusions of Doran, Pitsch, and Cook (2013). Again, similar trends were observed for double conditioning using a progress variable, where employing the sensible enthalpy yields better prediction compared to using a progress variable based on water vapour.

The results for a three injection case (Case 3) are plotted in Fig.4.8. Analyses are similar to the other cases. It has been generally observed that for up to three injections and for varying injection times, using the sensible enthalpy as the second conditioning variable leads to excellent agreement.

The advantage of using total mixture fraction and sensible enthalpy does not come only from the increased accuracy but also through the reduction of the dimensionality for increased number of injections over the multiple mixture fractions formulation. Next more insights about modelling is obtained through the coupling of the DCMC/CMC with the DNS.

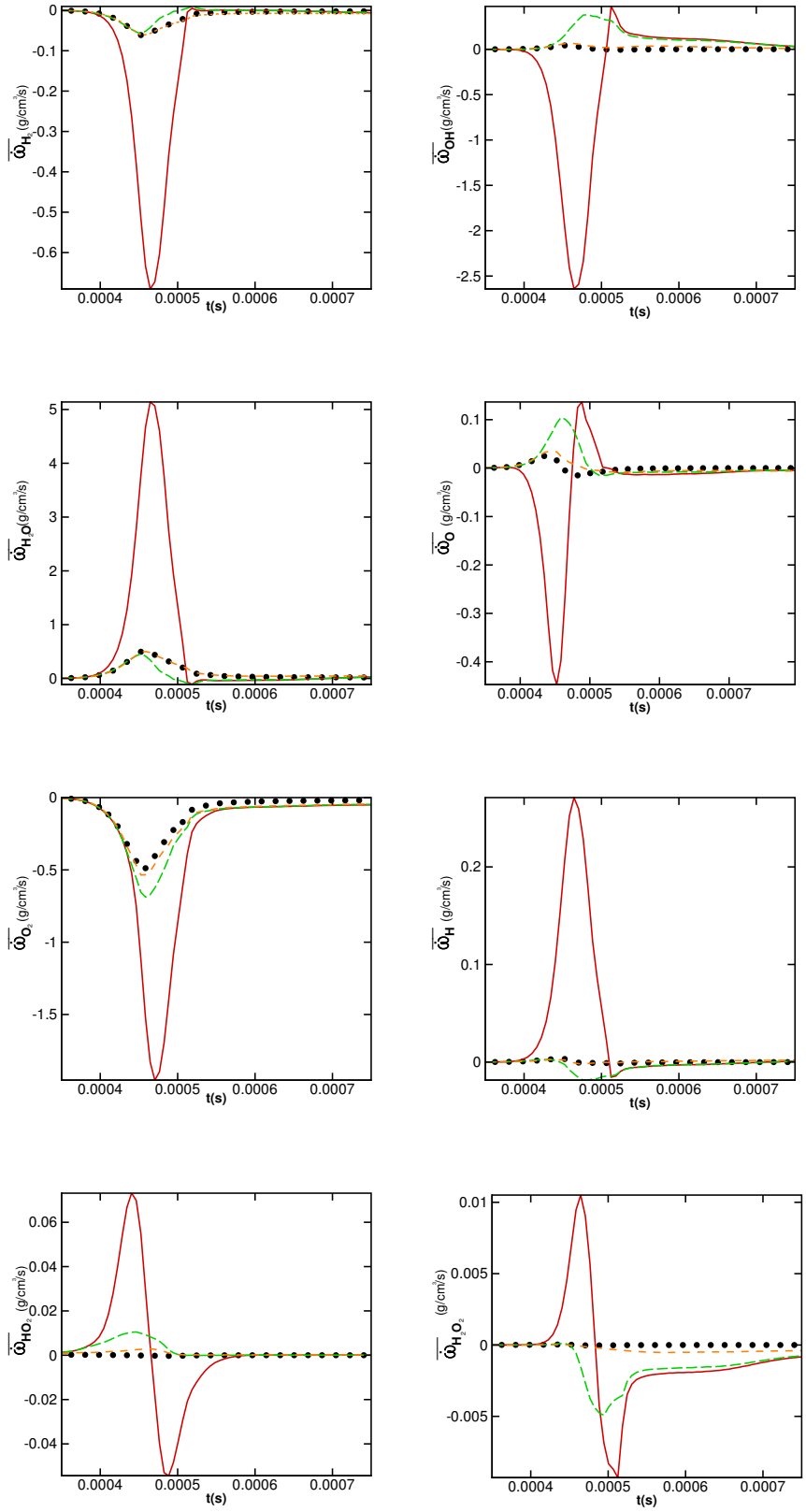

Figure 4.6: Mean reaction rate for several species for the case 1; symbols : DNS, lines : conditioned on ξ and Y_{H_2O} (dashed line), ξ and h_s (small dash), ξ (solid line)

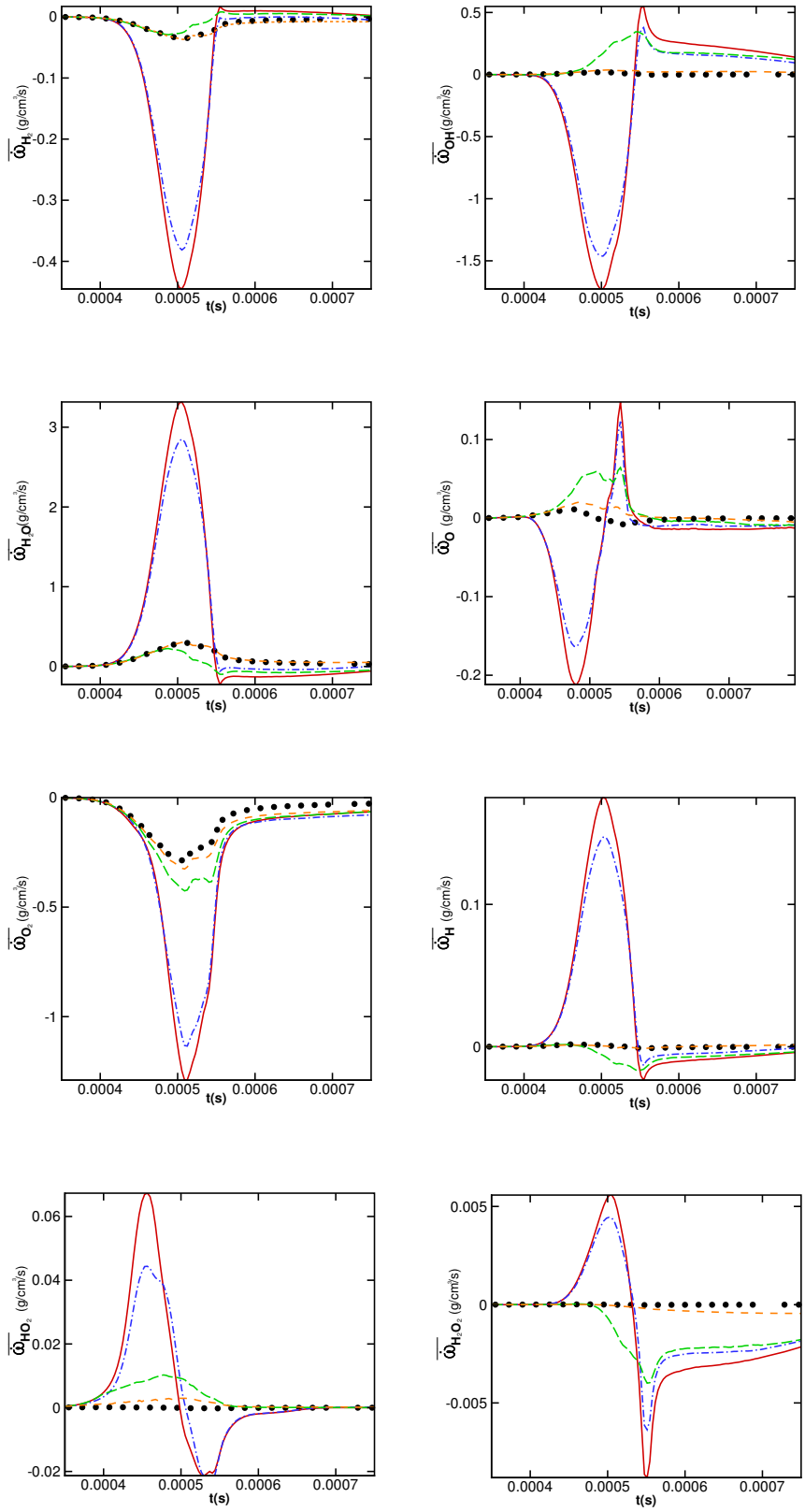

Figure 4.7: Mean reaction rate for several species for the case 2; symbols : DNS, lines: conditioned on ξ and Y_{H_2O} (dashed line), ξ and h_s (small dash), ξ (solid line), ξ_1 and ξ_2 (dash-dot)

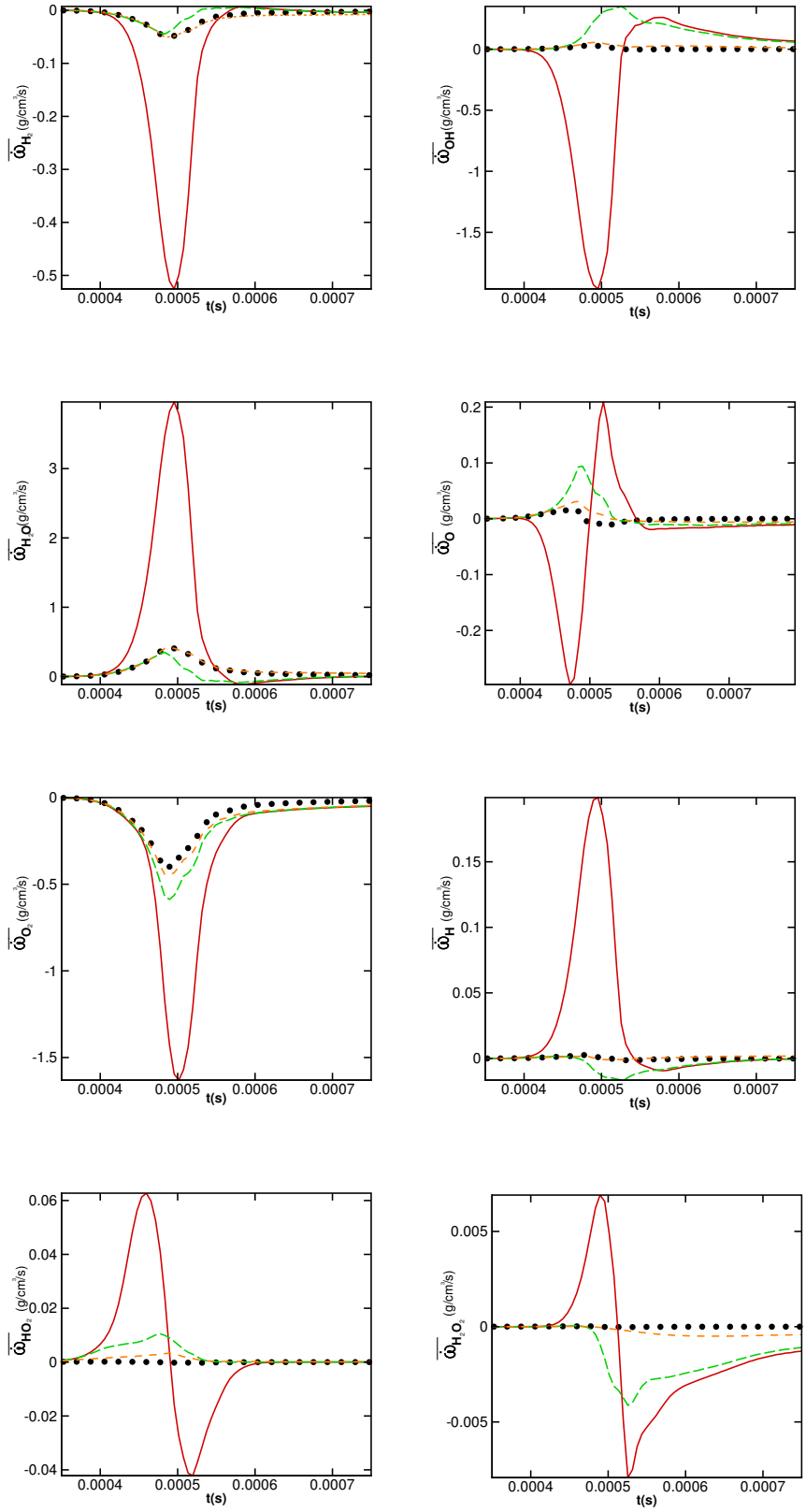

Figure 4.8: Mean reaction rate for several species for the case 3, symbols : DNS, dashed line : DCMC ξ – Y_{H_2O}, solid line : CMC ξ, case A3, small dash : DCMC ξ – h_s

4.4 A posteriori assessment of the DCMC

4.4.1 One-way coupling between the DNS and the CMC solution

In the *a posteriori* analysis the DCMC equations were coupled with the DNS using a one-way coupling (see Fig. 4.9). The equations were solved using the method of lines with the implicit solver VODPK (Brown, Byrne, and Hindmarsh, 1994). The DCMC equations presented in Chapter 3 were solved with the DCMC temperature equation B.9. The constant density ρ_0 was initially computed in the DCMC using the Favre pdf ($\widetilde{P}(\varphi_1, \varphi_2)$) obtained from the DNS :

$$\frac{1}{\rho_0} = \iint \frac{\widetilde{P}(\varphi_1^*, \varphi_2^*)}{\langle \rho | \varphi_1^*, \varphi_2^* \rangle} d\varphi_1^* d\varphi_2^* \tag{4.18}$$

Knowing the constant density the pressure is obtained by integrating the ideal gas law expressed in the state space:

$$p = \rho_0 \iint \langle RT | \varphi_1^*, \varphi_2^* \rangle \, \widetilde{P}(\varphi_1^*, \varphi_2^*) d\varphi_1^* d\varphi_2^* \tag{4.19}$$

Two approaches were investigated :

- The only submodels used to close the DCMC equations are for the conditional dissipation rates. By providing the conditional dissipation rates from the DNS in the 0D-DCMC, accurate set of conditioning parameters can be identified such that they minimise errors in the prediction of reaction rate.
- In addition to the conditional dissipation rates the conditional reaction source terms and the conditional heat release are computed from the DNS to validate the coupling method.

All the inputs needed from the DNS were obtained using a post-processing tool written within s3d parallelised using MPI. It was found that a uniform grid in the mixture fraction state space was not appropriate as a converged solution was not obtained with a practical number of grid points. Instead, a grid refined around the stoichiometric mixture fraction and in the region of $\eta = 0$ and 1 (see Fig. 4.11 which shows the non-uniform η grid combined a uniform grid in ζ). Additional routines in s3d were added to compute the pdf and the conditional dissipation rates for any grid provided by the user. It was found that 101 points for η were sufficient (see Fig. 4.10). Noisy distributions for the dissipation rates were observed for certain conditioning parameters due to the

absence of samples in a given bin. However, the noise did not affect the stability of the solution.

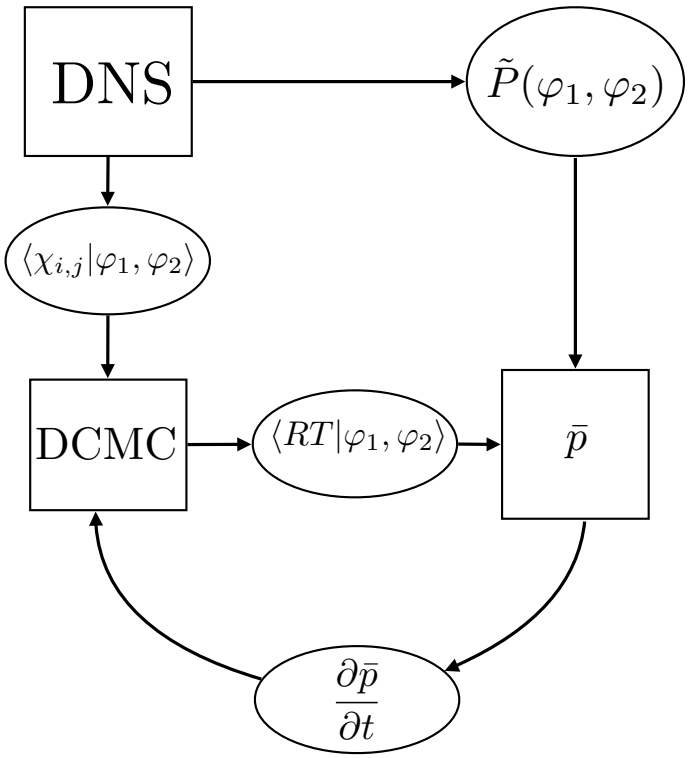

Figure 4.9: One-way coupling between CMC and DNS

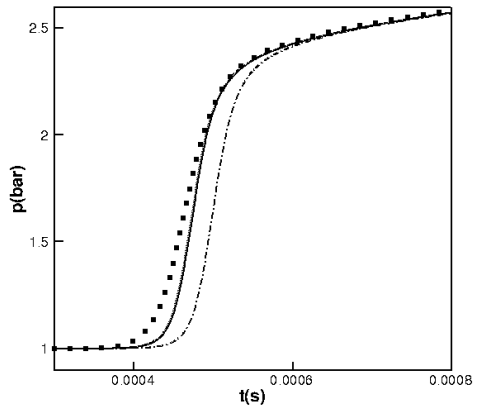

Figure 4.10: Pressure trace for the one injection Case 1: 60 points (dashed-dots), 100 points (solid), 120 points (dots).

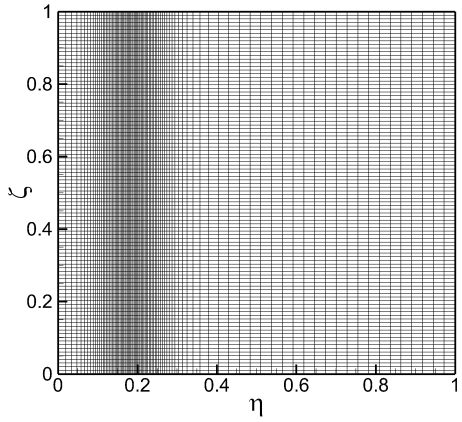

Figure 4.11: Illustration of the refined mesh along stoichiometric mixture fraction for 101 points in $\varphi_1 = \eta$ and uniform along $\varphi_2 = \zeta$ with 101 points for a generic conditioning parameter.

4.4.2 Single conditioning parameter

In Fig. 4.12 the pressure traces are shown for the cases 1, 2 and 3. The pressure obtained from the DNS is compared with the one obtained from the 0D-CMC code where first the conditional dissipation rates and pdf were used as an input, and in the second case the conditional reaction rates and heat releases were added.

For a single injection (case 1), the trend was reasonably captured with discrepancies from autoignition to the flame establishment which was observed for different input parameters. Adding the conditional mean reaction rates shows a perfect agreement with the DNS indicating that the first-order closure is responsible for the error.

Concerning the two and three injections case it is seen that the first-order CMC performs reasonably well. The discrepancies are again attributed to the first-order assumption where additional conditional fluctuations arise due to the injections of unreacted fuel in the domain. Generally it was observed that the time of the onset of ignition was underpredicted. The heat release plots reveal that the good pressure agreement in certain regions can be misleading. For the case 1 around $0.5ms$ the heat release obtained from the CMC is overpredicted yet the pressure agrees well. However, the comparison between the two parameters is not straightforward as the pressure depends on the cumulative heat release up to that point, not the instantaneous one. It was also observed that the heat release was generally overpredicted during ignition, which reflects the overprediction of the first-order closure for the reaction source term as observed in the *a priori* section (for instance 4.6).

Considering the results in the *a priori* analysis, where significant discrepancies were observed it is remarkable that such good results are obtained. In Fig. 4.13 the $\langle T''^2 | \xi_{mr} \rangle$ versus the time is computed. It is observed that the conditional variance increases and spreads for a longer period of time for the cases with injections due to combined effect of autoignition and the multiple injections. As a result, the pressure trace prediction for Case 2 and Case 3 suffers for a longer period of time than for a single injection.

The conditional mean temperature is illustrated in Fig. 4.14 for the two injection case 2. As discussed previously, autoignition occurs around the lean region $\xi_{mr} = 0.05$ from which the flame propagates towards slightly richer mixture up to $\xi_{st} = 0.195$. The conditional mean of the temperature is successfully predicted at the start and until the flame is established, however it is underpredicted at the onset of autoignition and overpredicted during intermediate times which is reflected in the pressure trace.

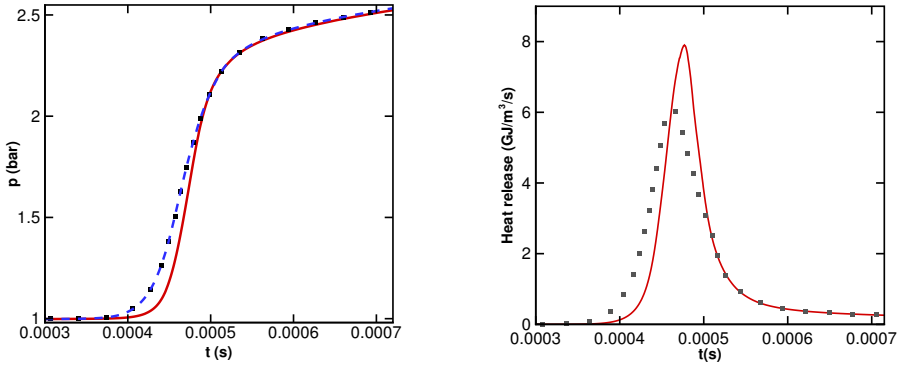

(a) Case 1

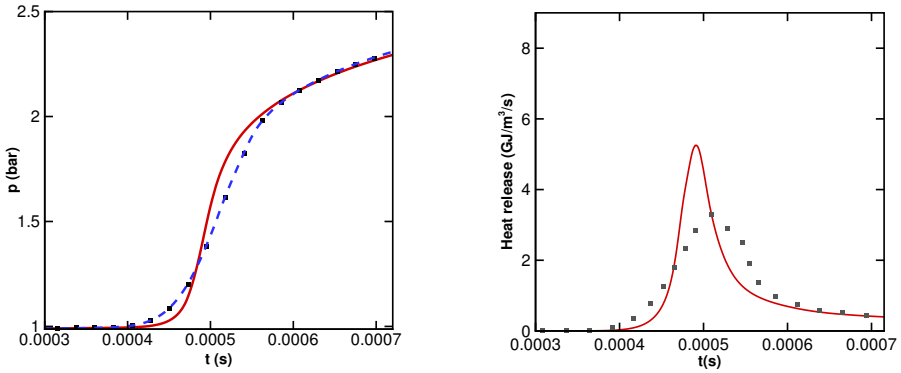

(b) Case 2

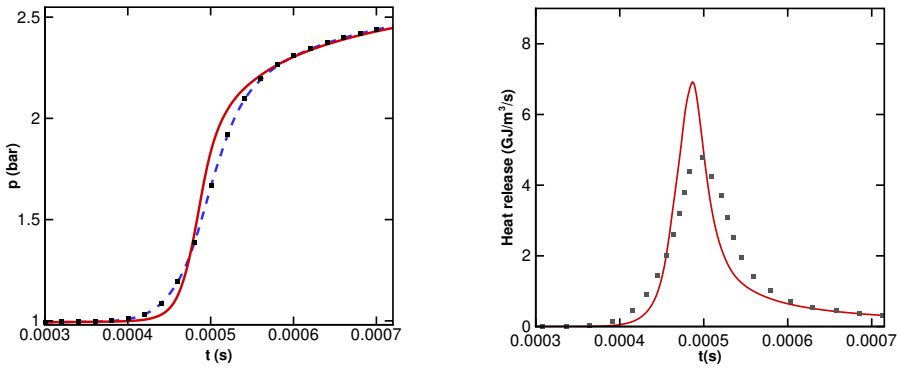

(c) Case 3

Figure 4.12: Comparison of the pressure traces for case 1, 2 and 3 between DNS and CMC, symbol : DNS; solid line : Conditional scalar dissipation rates (CSDR) from DNS only; dashed line : CSDR + conditional reaction rates and heat release from DNS

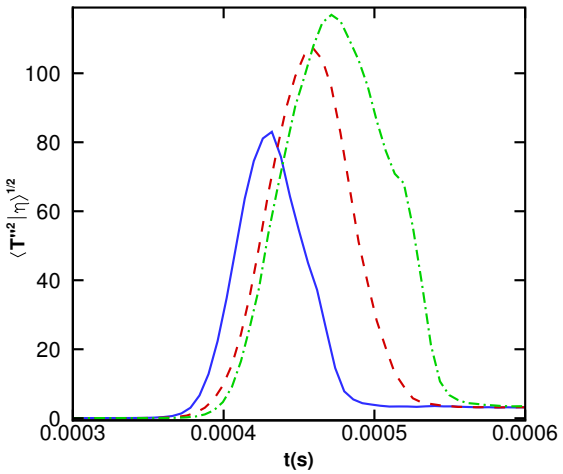

Figure 4.13: Comparison of the conditional variances for case 1 : solid line, case 2 : dash-dot and case 3 : dashed line obtained from the DNS at the most reactive mixture fraction $\xi_{mr} = 0.05$

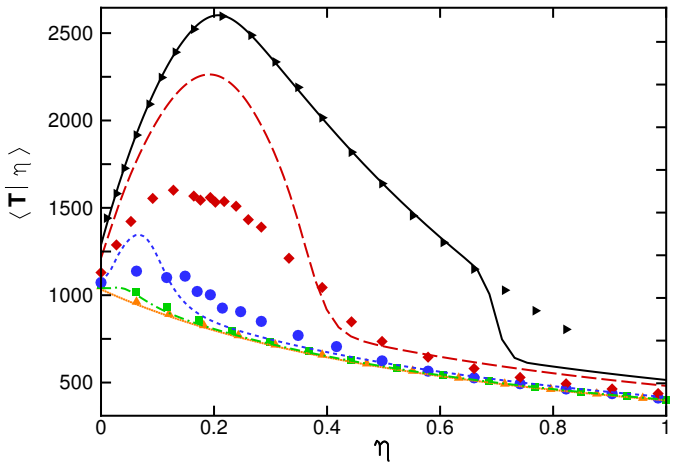

Figure 4.14: Comparison of the conditional mean of the temperature obtained from the DNS and the 0D-CMC for the case2; symbols : DNS (triangle = 0.5e-6s, square = 0.42e-3s, circle = 0.45e-3s, diamond = 0.52e-3s left triangle = 0.69e-3s), lines : CMC ξ

4.4.3 DCMC $\xi_1 - \xi_2$

Cases where the conditional fluctuations resulting from injections are more significant were investigated. This was achieved through injections of small amount of fuel followed by the bulk injection (cases 2a and 3a). First the case 2a is studied. The

autoignition occurring in the regions where ξ_1 is present subsequently ignites the surrounding mixture containing fuel from other injections. That localised process for small amount of fuel, generates more conditional fluctuation in the composition versus mixture fraction space.

The pressure trace is depicted in Fig. 4.15 for the cases 2 and 2a obtained using DCMC $\xi_1 - \xi_2$, the CMC ξ and the DNS data with the conditional dissipation rates only taken from the DNS. It was generally observed that the DCMC is necessary to account for more accurate exchange of mass and heat where very good agreement was obtained for the case 2, and improved for the case 2a than the CMC counterpart. In Fig. 4.16 a scatter plot of the temperature obtained from the DNS (black circles), DCMC $\xi_1 - \xi_2$ (red circles) and the conditional mean of the temperature obtained from the CMC (blue circles) are depicted for the case 2a. Although, autoignition occurs at preferential mixture, the surrounding mixtures which ignites first depend on the location of the first injected 'blobs' of fuel. Different random numbers, might result in different flame response in the mixture fraction space shortly after ignition, however, for small amount of fuel injected followed by a bulk injections, richer mixtures ignite at later times (the (c) picture in 4.16). It is observed that the DCMC model captures more information that leads to an improved prediction of the pressure trace, particularly at $t = 0.52ms$ ignition is still happening at lean mixtures whereas the CMC ξ is unable to describe the process. Discrepancies can arise due to the unpopulated regions where the dissipation rates have been set to zero, rapid diffusion in these regions accelerate heat and mass exchanges, hence the occurrence of autoignition. While, that latter effect had minor contribution in the case 2, the small amount of fuel injected in the case 2a results in faster unpopulated regions.

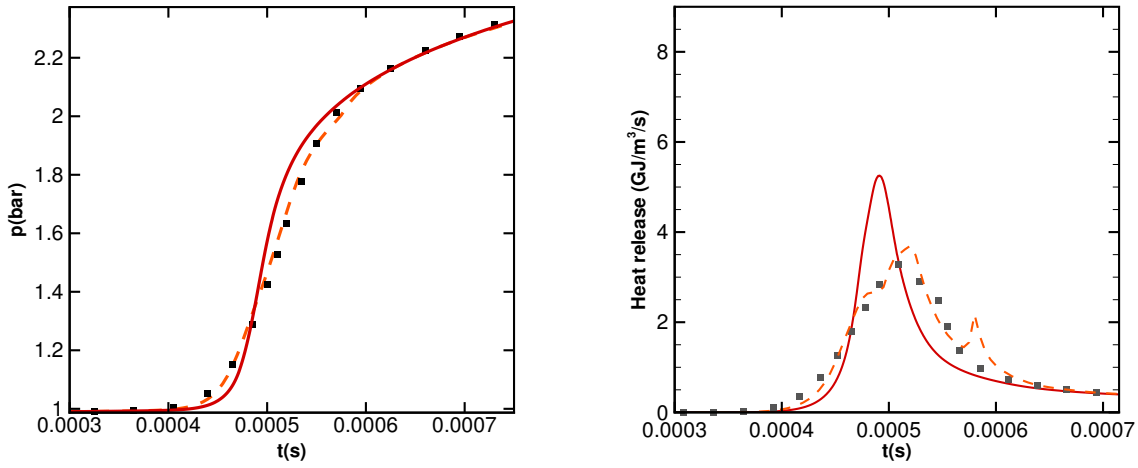

(a) Case 2

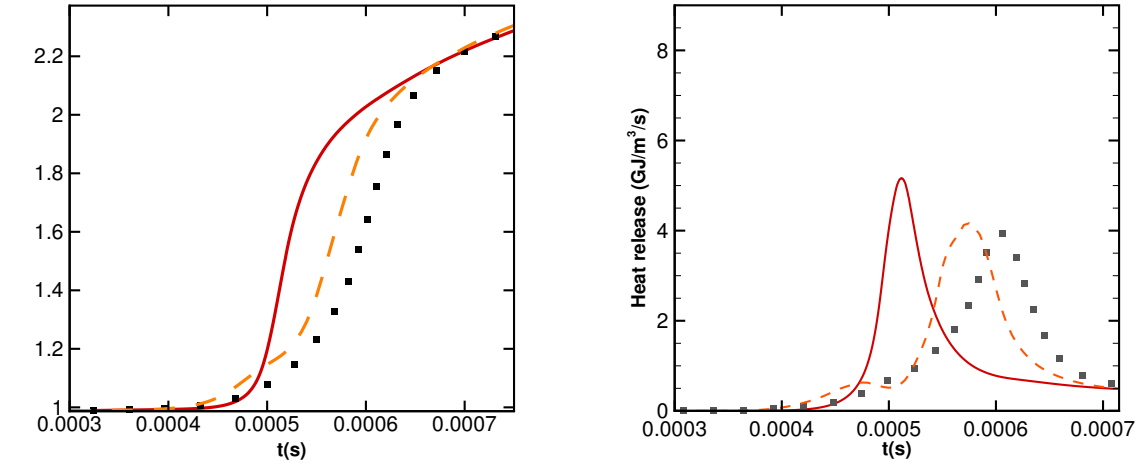

(b) Case 2a

Figure 4.15: Comparison pressure traces for case 2 and 2a between DCMC, CMC and DNS, symbol : DNS, dashed line : DCMC ξ_1 – ξ_2, solid line : CMC

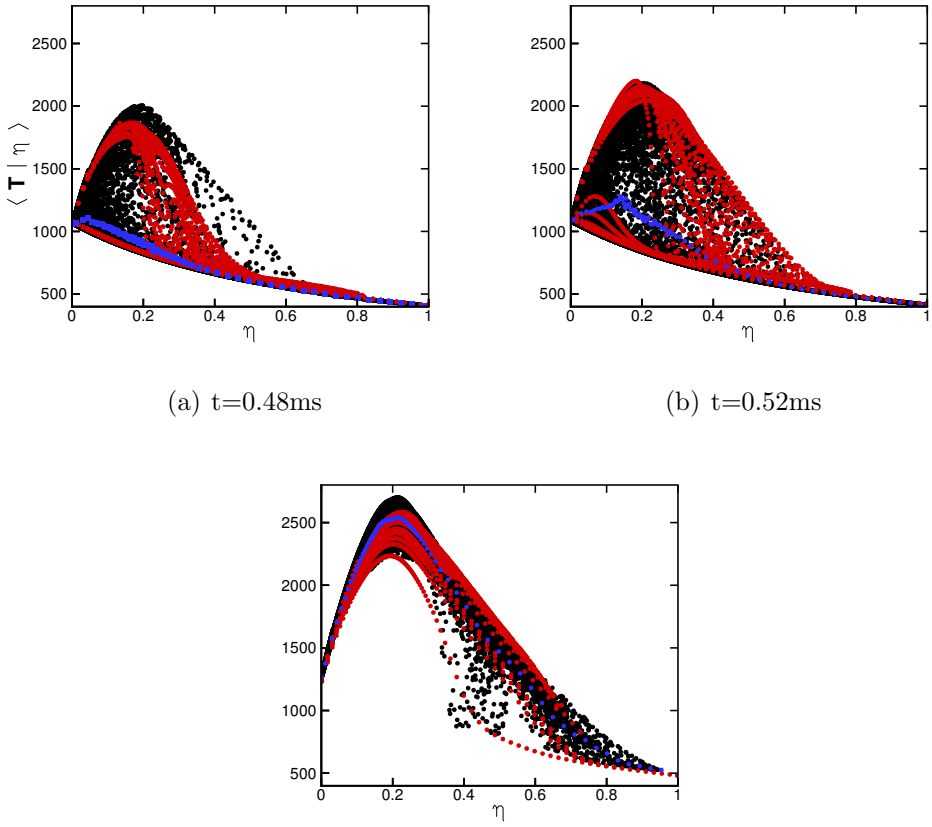

(a) t=0.48ms

(b) t=0.52ms

(c) t=0.665ms

Figure 4.16: Temperature comparison from DNS, CMC, and DCMC for the case 2a. black circles : DNS, red circles : DCMC ξ_1–ξ_2, blue circle : CMC ξ

4.4.4 DCMC $\xi - c$

The *a priori* analysis indicated that the first-order for the reaction source term is a good model when the conditioning parameters are ξ and h_s or Y_{H_2O}. The DCMC $\xi - c$ formulation developed in Chapter 3 was attempted using the *a posteriori* method. Although, the sensible enthalpy *hs* as a progress variable yield better results, the mass fraction of Y_{H_2O} was chosen for simplicity. Indeed, additional terms arise in the DCMC $\xi - h_s$ equations (Kronenburg, 2004). The objective was to observe whether using Y_{H_2O} in addition to ξ resulted in improved accuracy during ignition in a *a posteriori* fashion over using ξ only. A normalised progress variable was defined as $\frac{Y_{H_2O}}{Y_{eq(\xi)}}$ in order to have a unit square domain. The sample space variables were chosen respectively as η and ζ. A uniform grid was employed for ζ and similarly to the other formulations, a refined grid along $\xi = \xi_{st}$ was employed for η. The number of points were chosen

as 100 in η and ζ directions. The equilibrium solution was obtained by prescribing a Burke-Schumann solution as an input to a constant pressure 0D-CMC code. The dissipation rate was set to zero, hence, a thermo-equilibrium solution was obtained. The obtained composition was prescribed at $c = 1$. The state space was populated by linearly interpolating between $c = 1$ and $c = 0$. The conditional dissipation rates computed in the DNS are obtained using the maximum value of Y_{H_2O} ($Y_{H_2O}(\max)$) and not Y_{eq}. The reading of the conditional dissipation rates is done in a following manner : after interpolation of the conditional dissipation rates on the DCMC grid, Y_{H_2O} is computed using c as defined in the DCMC. The $Y_{H_2O}(\max)$ being saved prior to the calculation is then used to compute the c defined in the DNS in order to look up the conditional dissipation rates. It is noted that $Y_{H_2O}(\max)$ above $\eta = 0.45$ has no samples therefore the solution is interpolated up to $\eta = 1$.

The pressure and the heat release were found to be better captured around ignition using the DCMC than the CMC. The trend was in in agreement with the *a priori* analysis, however, the prediction suffers at later time where it is observed that the pressure and the heat release are overpredicted. Increasing the number of points in c and η did not result in an improvement indicating that the spatial resolution is sufficient. Grid refined at $c = 1$ with varying from number of points varying up to 180 points resulted in the same results. The error can come from the inconsistency of closures for the conditional reaction source term. The Favre joint-pdf $\widetilde{P(\eta, \zeta)}$ is a strong function of the combustion in contrast with the one employed in the other CMC/DCMC formulations where passive scalars are used. $\widetilde{P(\eta, \zeta)}$ obtained from the DNS is the result of exact values of the conditional reaction source term whereas in the DCMC the first-order closure is employed. Isolating the effects of the first-order closure in a manner that has been done in the previous sections is not possible with the current methodology. In Fig. 4.17 a scatter plot of the DNS coloured by the temperature and OH is compared with a scatter plot obtained from the DCMC $\xi - c$ coloured by the conditional mean of the temperature and conditional mean of OH in the $Y_{H_2O} - \xi$ space and η for the DCMC. In the DCMC the composition is available in the entire space from the beginning. Cells in which there are no samples are not displayed. Therefore, the shape of the DCMC space is similar to the DNS space and the effect of the combustion on the pdf is not accounted for. Unlike in the mixture fractions formulations the shape of the space is correlated with the progress of combustion. Higher, values of H_2O is associated with higher values of the temperature and OH, especially around stoichiometry. Up to 1.37 τ_{ign} the joint-pdf progressively unveils the existing state space in the DCMC. For these times variation of the composition

and temperature is characterized by lines, which is the result of the initial linear interpolation. At 1.8 τ_{ign} it is observed that the flame propagates in the state space towards the lean region. Higher values of OH were obtained in the DCMC. It was found that the overall trend was well captured with the overestimation of some intermediate species which is reflected on the pressure and the heat release. Due to the nature of the coupling with the current methodology which does not allow to isolate the reasons of discrepancies the split-injection cases were not investigated further.

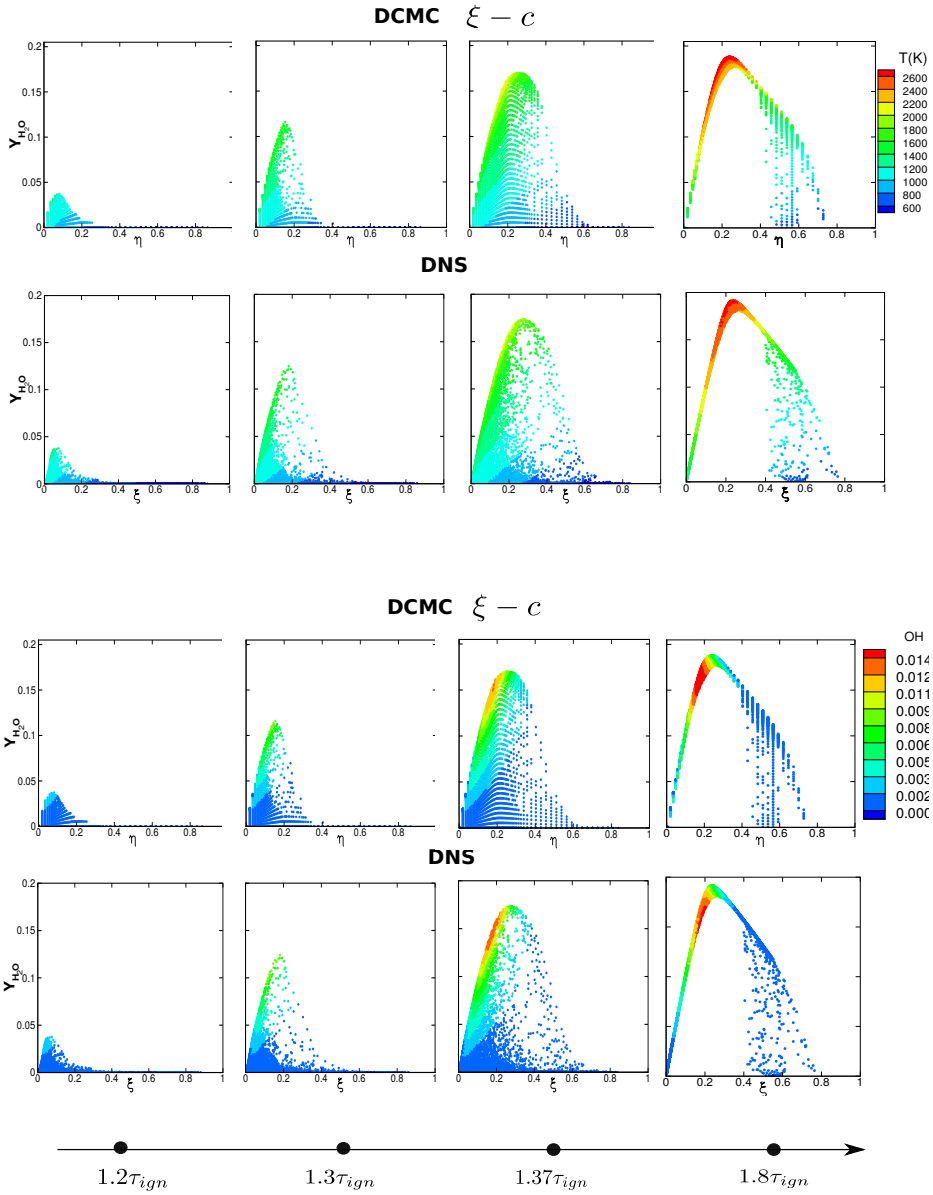

Figure 4.17: Scatter plot of Y_{H_2O} versus η (and ξ in the DNS) coloured by the conditional mean of the temperature (DCMC) and temperature (DNS) in the $\xi - c$ space (first two row), and similar for Y_{OH} (next two other rows) and coloured by the temperature for the case 1.

4.4.5 Conclusions

Direct numerical simulations have been performed for a configuration involving up to three separate fuel injections. The simulations use a multi-step chemistry model

and are well resolved numerically. In the case with a single injection, fluctuations around the mixture fraction-conditioned mean arise due to variation in mixture fraction dissipation rate affecting the progress of ignition differently at different points. In cases with multiple injections, the repeated addition of unreacted fuel also adds to fluctuations around the conditional mean. The high level of conditional fluctuations lead to large errors when employing singly-conditioned first-order conditional moment closure.

Alternative doubly conditional moment closure approaches are tested using two different approaches. First, in an a priori approach, the unconditional mean reaction rates are modelled using the first order closure using conditional averages taken from the DNS solution. Second, in an a posteriori approach, the transport equations for the double conditional moments are solved using the first order closure, and the results compared to the DNS. The a priori analysis indicates that single conditioned first order closure gives extremely poor agreement with the DNS, and that for multiple injection cases, conditioning on two mixture fractions provides little improvement. Reasonable agreement is given by double conditioning on mixture fraction and a progress variable. Sensible enthalpy serves as a superior progress variable than water vapour in this instance, however this result may be chemistry specific, and other combinations of species mass fractions may give superior resolution of progress variable space. Results of the a posteriori tests indicate that the DCMC may in practice be more tolerant of the choice of conditioning variables than indicated by the a priori analysis, however, conditioning on two mixture fractions outperforms conditioning on a single mixture fraction coordinate only. Conditioning on the mixture fraction and water vapour did not result in overall improved prediction. This was attributed to the one-way coupling method used rather than the inability of these two parameters to better characterise the combustion process. On the other hand, it may be noted that modelling for presumed joint-pdfs and conditional scalar (cross-)dissipation rates for progress variables is generally less well developed than for mixture fractions, and modelling for these quantities is investigated further in the subsequent chapters.

Chapter 5

Results - II Sandia constant-volume chamber

The analysis in Chapter 4 has indicated the suitability of double conditional moment closure (DCMC) using mixture fraction and progress variable for modelling autoignition in non-premixed flows in which the composition exhibits fluctuations around the mixture fraction-conditioned mean. The objective of Chapter 5 is to implement and test the double conditional moment closure approach formulated in Chapter 3 for modelling spray combustion in autoigniting fuel sprays, and to validate this approach by comparison with spray ignition in well-characterised laboratory flames. The validation test cases selected are from the so-called Sandia-H series, measured in a constant-volume test chamber at Sandia National Laboratories, and comparison can be made in terms of ignition delays and lift-off lengths. Previous attempts to model the Sandia-H flames (Borghesi & al., 2011; Bolla & al., 2013) using CMC have used multi-dimensional singly-conditioned CMC, and have indicated that thousands of CMC control volumes are required in order to solve even the two-dimensional single-conditioned CMC equations accurately. Here, a like-for-like comparison is made between the multi-dimensional singly-conditional CMC, the zero-dimensional singly-conditional CMC and the new zero-dimensional DCMC formulation developed in this thesis. The comparison is made in terms of the accuracy of predictions and the corresponding computational cost. This chapter starts by setting out the numerical approach and set up for simulating the Sandia-H spray experiments, proceeds to verify the numerical accuracy of the implementation, and finishes with validation of the DCMC and comparison with alternative CMC formulations.

5.1 Experimental configuration

This numerical study is based on simulation of previously-published laboratory experiments involving spray ignition performed by (Idicheria and Pickett, 2007). Spray ignition was studied in a cubic combustion chamber with 108 mm sides, giving optical access through side-port sapphire windows(Idicheria and Pickett, 2007), (Idicheria and Pickett, 2005). A fuel injector was mounted in a metal side-port and n-heptane spray was injected into the center of the chamber. A common-rail fuel injector was employed. The experimental conditions were chosen to replicate the conditions expected near the top-dead-center (TDC) in an engine. In order to raise the pressure and temperature prior to the start of fuel injection, flammable premixture was burned in the chamber, leaving an amount of excess oxygen as required for the spray combustion experiment. The specified initial thermochemical state for the spray experiment was achieved as the burnt mixture cools, and a mixing fan was used to ensure that the composition and temperature in the region of the spray injector were homogeneous. An illustration of the vessel is given in Fig. 5.1 and the experimental conditions are given in table 5.1. These conditions correspond to an initial pressure of the order of 40 bars.

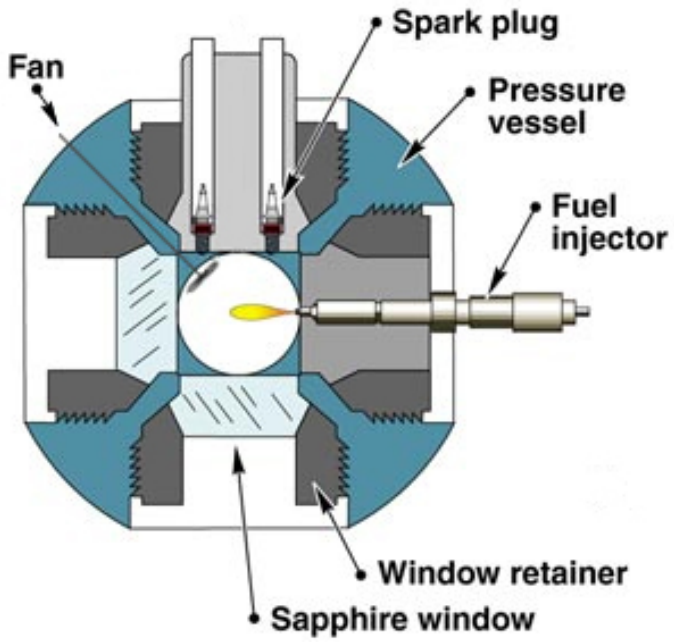

Figure 5.1: Schematic of a cross-section of the Sandia constant volume chamber

This numerical study makes comparison with experimental data for five experimental test conditions (A1-A5 in table 5.2) in which the percentage of oxygen in the ambient mixture prior to fuel injection varies from 0% (inert) to 21% (approximat-

Table 5.1: Ambient and injector conditions

Ambient temperature T	$1000K$
Ambient density ρ	14.8 kg/m^3
Fuel injection pressure	150 MPa
Orifice diameter	100 μm

Table 5.2: Case studied

Case	O_2 (% by vol.)	Mol. Weight
A1	**21**	**29.47**
A2	15	29.24
A3	12	29.13
A4	10	29.06
A5	0	28.68

ing combustion in undiluted air). The intermediate oxygen levels are representative of diesel engine conditions involving various amounts of dilution with recirculated exhaust gas. Case A1 is taken as the reference case for the present chapter.

The Sandia spray-bomb experiments have been carried out for a range of operating parameters such as the fuel type, temperature, density and dilution for an injection duration of 6ms. The results available include the vapour and liquid length penetrations for non-reactive conditions, and lift-off length and ignition delay time for reactive conditions. Schlieren imaging has been used to identify the vapour boundary of a penetrating jet. The boundary of the spray was obtained from image analysis where the penetration distance is defined as the distance along the spray axis to the boundary of the spray. Analysis of Mie-scattered images allowed to extract the liquid length by determining the maximum axial distance in the spray where the light intensity was above a threshold equal to 3% of the light intensity range measurable with the camera. The definition of liquid length was found to be relatively insensitive to large changes in parameters such as the laser power and the camera gain. Following ignition, the flame stabilised at a length referred to as the lift-off length. Chemiluminescence from the excited-state of OH (OH^*) was used as a marker to determine that length. An optical method was used also to compute the ignition delay time. 50% of the high-temperature chemiluminescence level was the reference metric.

5.2 Numerical simulation

The simulations start at the beginning of fuel injection, with uniform initial temperature, pressure and compositions given by Tables 5.1 and 5.2. The fuel mass flow rate is prescribed based on the reported experimental measurements, as given in Fig.5.2.

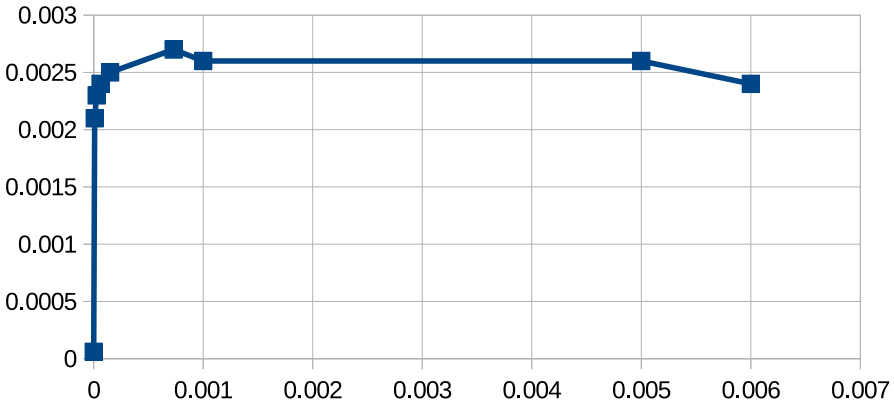

Figure 5.2: Fuel mass flow rate profile used in the simulation [g/ms] versus time [s]

5.2.1 DCMC implementation

The DCMC equations and requisite submodels have been discretised and integrated numerically using a Fortran code. In order to apply the DCMC approach to the simulation of practical combustion systems, eventually including engines with moving pistons, valves and spray fuel injection, the DCMC code is coupled with a Computational Fluid Dynamics code which solves equations for momentum, mass, and energy conservation, for spray properties, and for selected moments of the DCMC conditioning variables. In general, the spatial scales of the properties solved by the CFD code are smaller than or equal to the spatial scales over which the conditional moments vary, allowing a coarser spatial discretisation to be used for the conditional moment equations in some applications, which potentially affords a saving of computational effort, at the expense of some added complexity in the coupling between the CFD and DCMC codes.

The starting point for the implementation of the zero-dimensional DCMC modelling in this project is a three-dimensional singly-conditioned CMC code developed at the ETH Zurich and at the University of Cambridge that is coupled with the commercial CFD code STAR-CD, which is a popular CFD code for internal combustion engine simulation. While the experimental configuration simulated in this chapter is statistically axisymmetric, allowing a two-dimensional axisymmetric CMC-CFD calculation

in this case, we still refer to the multi-dimensional single conditional approach as *3D-CMC*, reflecting the generality of the code's implementation. The CMC–STAR-CD has been developed and used in a number of previous research studies, including (Wright, De Paola, & al., 2005; Borghesi & al., 2011; Bolla & al., 2013). The CMC-CFD coupling accounts for the use of different computational meshes for the CMC and CFD discretisation. The CMC grid is structured and Cartesian, although not necessarily uniformly spaced. A goal of the zero-dimensional DCMC code development has been to maintain compatibility with the three dimensional singly-conditioned CMC code, and to facilitate future extension of the DCMC approach to multiple spatial dimensions. Zero-dimensional operation of the (D)CMC code is then achieved by specifying only one control volume in physical space, and retaining the usual approach for coupling between CMC and CFD cells that is outlined below.

The DCMC–STAR-CD is set up for zero-dimensional DCMC modelling, and therefore the implementation and options for modelling and numerical solution of the DCMC equation set is identical to that described in Chapter 3. Here, a summary is given of only the main features of the DCMC implementation and of the numerical and modelling options that are investigated in this Chapter. The fully-three dimensional singly-conditional CMC code remains unchanged from studies such as Bolla & al., 2013, and the zero-dimensional singly-conditional CMC is given by a trivial simplification of the spatial CMC (by selecting only one CMC control volume), or equivalently simplification of the zero-dimensional DCMC (by specifying only one point in the direction of the second conditioning variable).

The DCMC equations for doubly-conditionally averaged species mass fractions and for temperature are discretised using first order upwind differences for first order derivatives and second-order central differences for second derivatives. Thermochemical properties are evaluated using the semi-perfect gas approximation (ideal gas law and temperature-dependent heat capacities) based on NASA polynomials. Where required, temperature is evaluated from the mixture enthalpy using a Newton iteration. Chemical reaction rates are obtained by supplying a reaction rate subroutine that can be arbitrarily detailed. Because the chemical reactions are numerically stiff (involving a wide range of physical time scales) the equation set is integrated with a stiff ordinary differential equation (ODE) solver called DVODE. For the DCMC, the number of coupled ODEs to be solved, equal to the number of DCMC partial differential equations solved multiplied by the total number of grid points in the two-dimensional sample space, is even larger than for the singly-conditional CMC, and using the *method of lines* to integrate the full equation set including detailed chemical models can be im-

practically time consuming. In order to reduce the computational time, alternative operator splitting approaches are tested in this chapter.

The 0D-CMC simulations were performed with the same code as the 3D-CMC and 0D-DCMC calculations, but using one CMC node. One core was used for the DCMC calculation and 16 cores for the 3D-CMC where an efficient parallelisation method was implemented (Wright, De Paola, & al., 2005). Although not pursued in this study, parallelisation of the DCMC calculation is expected to be straightforward because the operator-split solution method leads to many independent chemistry integration calculations that can be distributed among multiple processors.

Following previous singly-conditioned CMC modelling (Bolla & al., 2013), the spray evaporation terms appearing in the DCMC equations have been neglected. This removes the need for modelling of spray conditional source terms for which modelling is not well established, and simplifies the treatment of the energy equation. In particular, if radiative heat transfer is also neglected and pressure changes slowly relative to dissipation timescales, the total enthalpy remains a linear function of mixture fraction(s), and solution of the energy equation becomes unnecessary. For consistency with the previous CMC modelling studies concerning Sandia Spray H, the spray source terms are removed from the equations, however, the conditional mean of the temperature is solved unlike in the DCMC where no energy equation is solved, and the conditional enthalpy is updated only to account for changes in pressure.

Chemistry modelling: The chemistry is modelled using the reduced n-heptane mechanism by Liu & al., (2004). The mechanism was derived from a 43 species and 185 reactions. It contains 22 non-steady-state species reacting according to 18 global steps. The mechanism is known to be very stiff during autoignition due to the strong coupling between the conditional dissipation rates and the chemistry. The decoupling of mixing and chemistry terms is achieved through the Operator Splitting (OS) methods which resulted in significant decrease of the CPU time with very little loss of accuracy (Paola, 2007, PhD thesis). Bolla & al. (2013) obtained very good agreement of the lift-off length and the ignition delay time using the OS. In this work, an OS method has been developed for the DCMC and presented in the chapter 3. Its validation is presented in the following section.

5.2.2 CFD set-up

The flow field is modelled using the Reynolds-Averaged Navier-Stokes (RANS) approach, coupled with a Lagrangian-particle approach for describing the fuel spray. The turbulence model employed is the k-ϵ model with the standard coefficients provided

by STAR-CD.

Initial and boundary conditions: Cyclic boundary conditions were used for the planes in the azimuthal directions, inlet boundary where the spray was injected and impermeable wall boundaries otherwise. As mentioned earlier for the inlet condition a mass flow rate profile has been prescribed (see Figure 5.2). STAR-CD offers two forms of wall functions for high Reynolds number to represent the distribution of the parameters within the boundary layers, the standard form and the non-equilibrium form. The standard form (Launder and Spalding, 1974) with the default constant values was employed. As the spray flame remains far from the chamber walls, heat transfer (including radiation) is neglected. For the mass fraction species a Newman boundary conditions (zero-diffusive flux) were employed at the wall.
Initial temperature, density and molecular weight were prescribed as specified in the table 5.1. The background turbulence was initialised with $k = 1.25\ m^2/s^2$ and $\epsilon = 125\ m^2/s^3$.

Spray model: The Reitz-Diwakar model discussed in the chapter 2 is used to model the spray, both for atomization and secondary break up. The number of numerical spray parcels (each representing a large number of physical droplets) per injection was set to 2×10^7 with a cone angle of 10 degrees. The properties of the droplets were calculated internally by STAR. More details of the constants used are discussed in the validation of the turbulent-spray section.

CFD grid: A quasi-2D CFD grid with one degree angle was used with three zones in which the mesh differ as illustrated in Fig. 5.3. An homogeneous resolution of 0.5x0.5 mm^2 was employed for the first 15 mm in the radial direction (first zone) then doubled each time in the next zone. The mesh has been used for the same conditions simulated in this study by Bolla & al. (2013) and is line with the recommendations of the ECN (Pickett, 2016). The CFL number was set to 0.35 and the time step to 1.10^{-6} s as recommended by the ECN (Pickett, 2016).

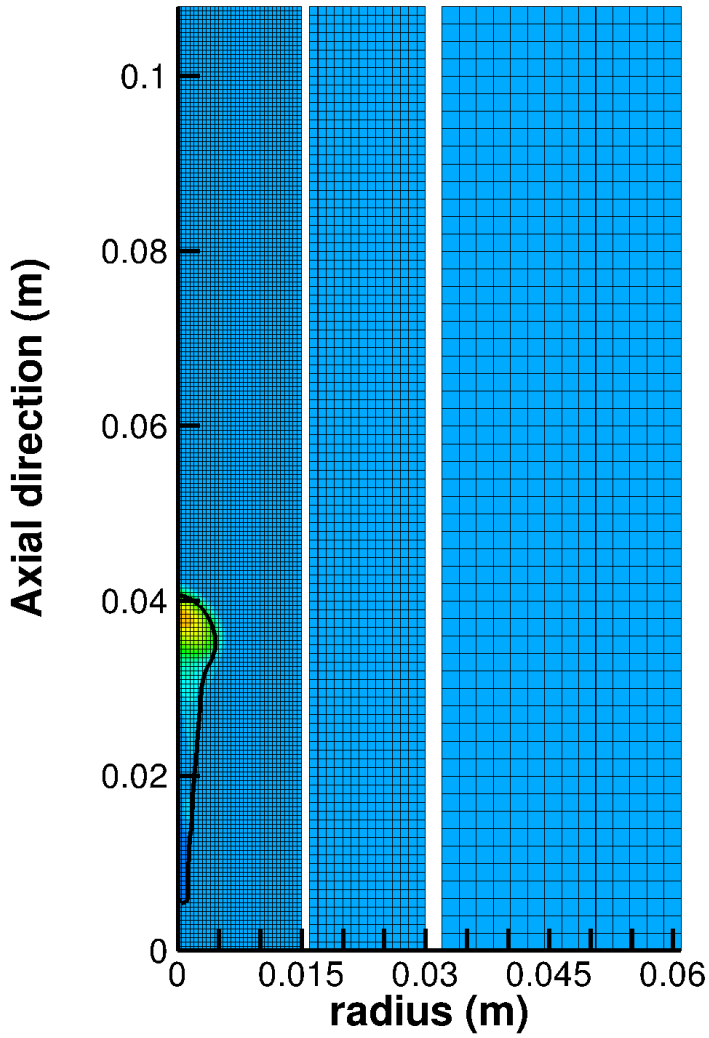

Figure 5.3: Mesh used for the simulation of the n-heptane spray

5.2.3 Coupling of the (D)CMC and CFD

CMC grid: The lift-off length predicted by the singly-conditioned CMC approach has previously been shown to be very sensitive to the CMC resolution. 54 uniformly-spaced CMC nodes in the axial direction, with 30 nodes in the radial direction and 1 node in the statistically-homogeneous azimuthal direction has been found to give grid-independent results. Whereas simulations with half the number of nodes in the axial direction resulted in the flame becoming attached to the nozzle. A $54 \times 30 \times 1$ grid is used in the following calculations.

Due to the *fractional step* numerical approach (also called *operator splitting*) used

for integrating the CMC and DCMC equations, the numerical error due to the fractional stepping approach depends on the time-step for the (D)CMC integration. It is established below that, for the 1.10^{-6} s used for the CFD, two (D)CMC sub-steps are sufficient to give time-step independent results, and the ratio of two (D)CMC sub-steps for every CFD time step is used in the following simulations.

Initialisation of the (D)CMC solution: The unity mixture fraction composition is defined as pure n-heptane fuel, and the zero mixture fraction composition is defined by the composition of the ambient fluid. The initial unburned composition (i.e. zero progress variable, $c = 0$) is obtained by linear mixing of mass fractions and enthalpy between the compositions at the limiting mixture fraction values (zero and unity). Where needed for DCMC modelling, the burnt composition (i.e. unity progress variable, $c = 1$) for each mixture fraction is set equal to an equilibrium composition – obtained by the integrating the chemical mechanism for a sufficiently long time until the composition ceases to change, keeping the total enthalpy and pressure constant. For each value of mixture fraction, the composition for intermediate values of progress variable is given by linear interpolation of mass fractions and enthalpy between the $c = 0$ and $c = 1$ states.

5.2.4 Post processing

The lift-off length and ignition delay time have been determined using a temperature threshold as done in previous studies (Borghesi & al., 2011). The threshold was set to 1100 K, therefore for the ignition delay time corresponds to the time when temperature exceeds that threshold, and the lift-off length is the length at which the temperature exceeds that threshold. Due to the steep temperature gradients, both temporally and spatially, the choice of the threshold had a marginal influence.

5.3 Assessments of numerical methods

Alternative operator splitting approaches were introduced in Chapter 3. This section presents results that demonstrate their accuracy and evaluate their relative computational cost. These results are also used to determine the timestep. The validity of the spray modelling provided by STAR-CD is also confirmed, leaving assessment of the validity of the new DCMC modelling aspects for the subsequent section.

5.3.1 Operator splitting methods

Two distinct operator splitting approaches for solving the DCMC equation were introduced in Chapter 3. The first approach referred to as plain Operator Splitting (OS) is given in Eq. 3.83, involving integration of convection in progress variable space (due to the chemical source term of progress variable) for all points in progress variable space. The second approach, referred to as Operator Splitting/Interpolation (OSI) given in Eq.3.84 involves point-wise integration of the chemical source terms, followed by an interpolation procedure to shift the data back on to the regular progress variable grid. The later approach is expected to be faster and to enforce the correct values of progress variable at the corresponding grid points in ζ-space.

The accuracy and cost of the two operator splitting methods is compared in an uncoupled zero-dimensional DCMC simulation with initial composition conditions corresponding to Sandia spray case A1 in Table 5.3 – the resulting pressure is 42.5 bar. Temporally-constant conditional scalar dissipation rates $\langle N_\xi|\eta,\zeta\rangle$ and $\langle N_c|\eta,\zeta\rangle$ are imposed following the amplitude mapping closure model (Eqs. 3.49 and 3.61). The amplitude (maximum value) of the mixture fraction conditional dissipation rate is denoted by A and the maximum value of the progress variable conditional dissipation rate is denoted by C. A range of values for A and C are tested, with upper and lower bounds selected based on the values encountered in the CFD simulations of case A1 presented in the subsequent section. The time step chosen is $0.5\mu s$. The number of points in the state space are 101 points in η and 51 points in ζ space. The choice of the number of grid points and timestep is discussed further below. The conditionally-averaged cross dissipation $\langle N_{c,\xi}|\eta,\zeta\rangle$ is set equal to zero, and the effect of this parameter is discussed below also.

	T(K)	Y_{O_2}	Y_{N_2}	Y_{CO_2}	Y_{H_2O}	$Y_{C_7H_{16}}$
Oxidiser stream	1000	0.22809	0.65891	0.09125	0.02175	-
Fuel stream	373	-	-	-	-	1

Table 5.3: Composition used for the parametric study

In Fig. 5.4, the conditional average progress variable Q_c is plotted against the sample space variable ζ. The aim is to reveal the discrepancies due to the numerical methods which manifest through evolution of c that differs from a linear one in the ζ space. An advantage of the OSI is the enforcement of the linear evolution during its second step. However, deviations can arise following its third step, but these are generally much smaller than errors that arise within the OS approach. It is generally

observed that error given by the OS approach becomes more pronounced as C increases. Particularly, for high values of C around the lean regions. For both methods, the linear evolution is not conserved at the stoichiometric mixture around $\zeta = 1$. Variations of the composition and temperature are more pronounced around that region, therefore, they are more influenced by the dissipation rates during the third step of OS and OSI. In Fig. 5.5 contour plots of the species that are used to define c are plotted. It is observed that the overall trends are similar in the state space with more pronounced differences around $\zeta = 1$.

In Fig. 5.6 the CPU time is plotted for the case with low dissipation rates for the two methods employed. The OSI was observed to be faster than the OS. Profiling the code indicated that the step during which the reaction source term is computed is the most expensive due to the stiff solutions. Increasing the size of the array given to the solver during that step significantly increases the CPU time. The advantage of OSI does not lie only in a better conservation of c with respect to ζ but also its speed. OS was found to be impractical while coupling it with a CFD solver. OSI is therefore the method of reference used for all the following analysis.

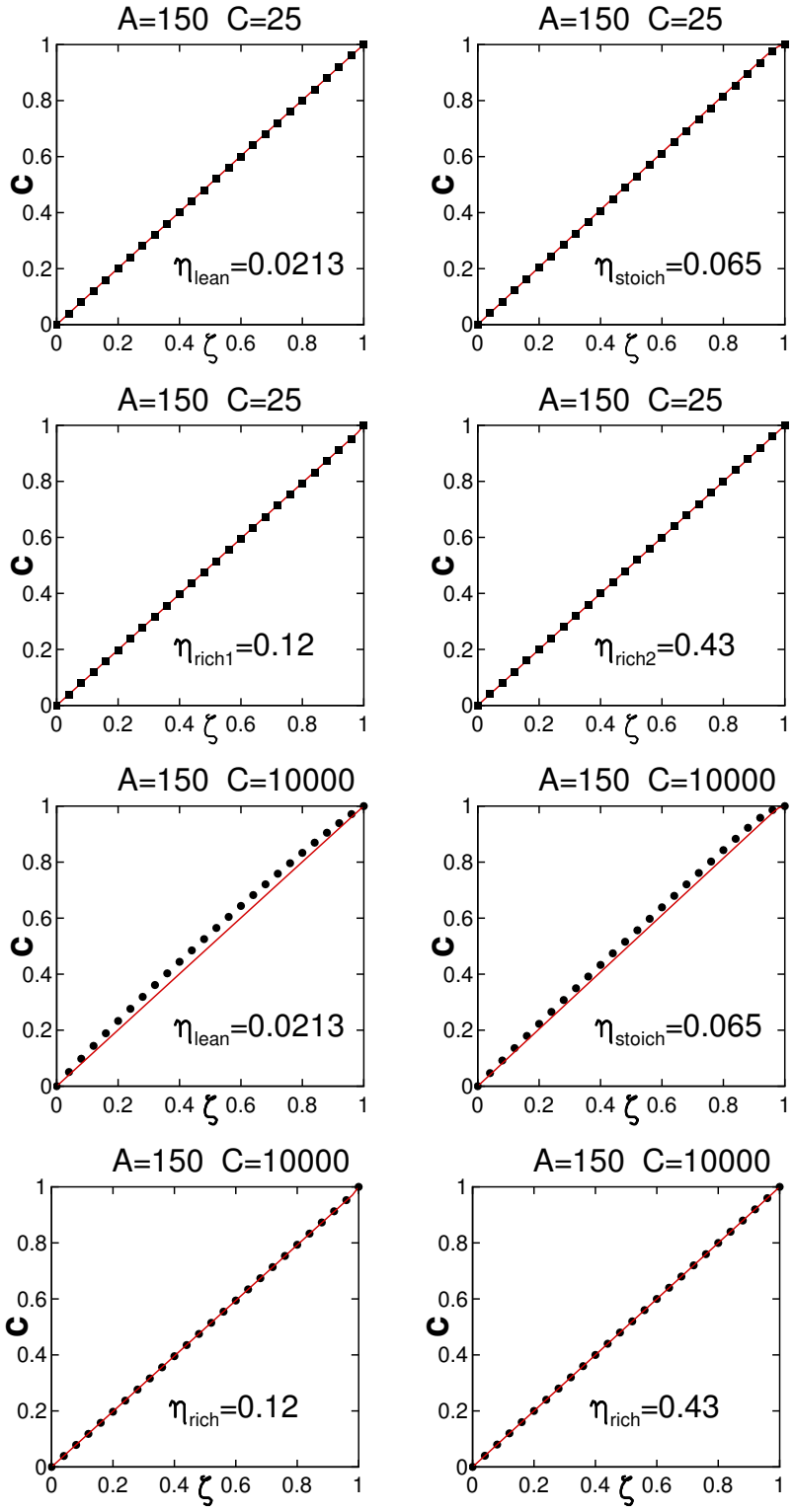

Figure 5.4: Normalised conditional average progress variable Q_c versus its sample space variable ζ, symbols: OS, line: OSI. Four mixture fraction values are plotted as indicated on the figures.

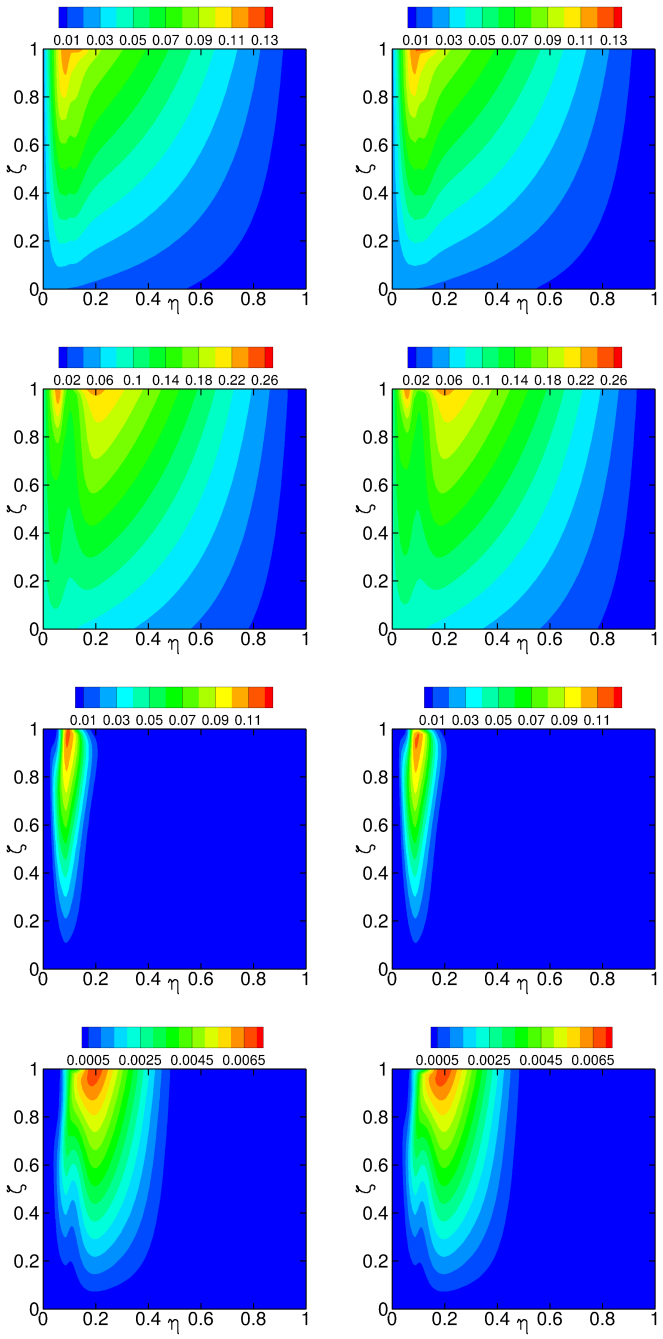

Figure 5.5: Contour plots of the conditional average of H_2O (first line), CO_2 (second line), CO (third line), H_2(fourth line) for OS (first column) and OSI (second column)

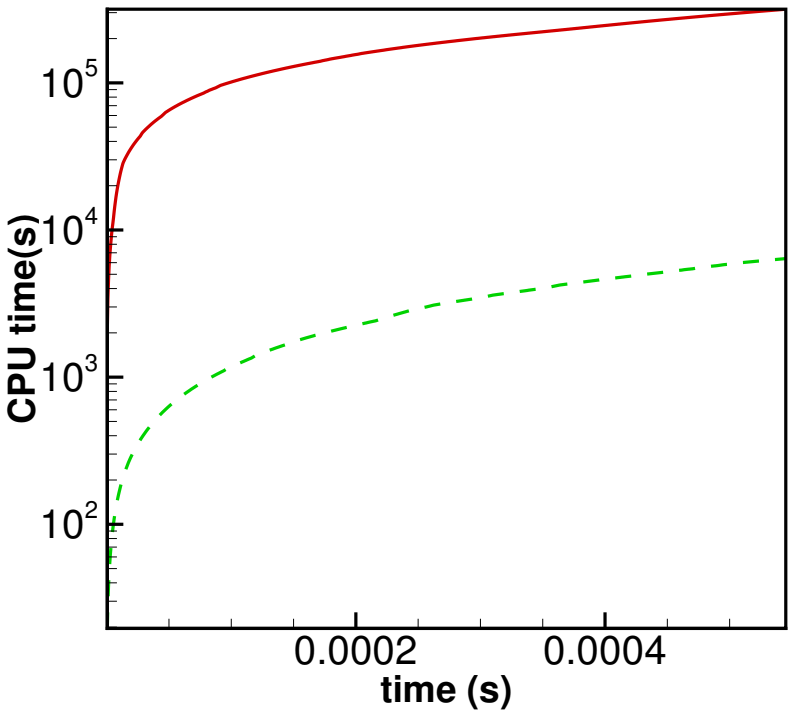

Figure 5.6: CPU time for the OS (red solid line) and the OSI (green dashed line)

5.3.2 Influence of the operator splitting time step

Having adopted the OSI operating splitting approach, the time step required in order to obtain accurate calculations under the experimental conditions is investigated by repeating the stand-alone DCMC calculation with time steps equal to $\Delta_t = 1.10^{-5}s$, $\Delta_t = 1.10^{-6}s$ and $\Delta_t = 5.10^{-7}s$. The stand alone calculation is repeated for a range of conditional scalar dissipation rate amplitudes, A and C, and for three different profiles of conditional cross-dissipation rate $\langle N_{c,\xi}|\eta,\zeta\rangle$. The three cross-dissipation rate profiles are given by setting the cross dissipation rate equal to zero; to the maximum possible value, $\sqrt{\langle N_c|\eta,\zeta\rangle\,\langle N_c|\eta,\zeta\rangle}$; or the minimum possible value $-\sqrt{\langle N_c|\eta,\zeta\rangle\,\langle N_c|\eta,\zeta\rangle}$. The corresponding results are presented in Figs. 5.7, 5.8 and 5.9. High values of C resulted in increased temperature diffusion down to $\zeta = 0.2$ with marginal differences for the chosen values of A. Varying the sign of $\langle N_{c,\xi}|\eta,\zeta\rangle$ resulted in faster diffusion for the lean side (when the alignment is negative) or rich side (when it is positive).

The results presented in Figs. 5.7, 5.8 and 5.9 indicate that the temperature solutions are time-step independent for time steps less than or equal to $\Delta_t = 1.10^{-6}s$. Small differences in the predictions of minor species and reaction rates (not shown) however are observed between $\Delta_t = 5.0^{-7}s$ and $\Delta_t = 1.10^{-6}s$, and $\Delta_t = 5.0^{-7}s$ is

adopted as the operator splitting time step in the subsequent simulations.

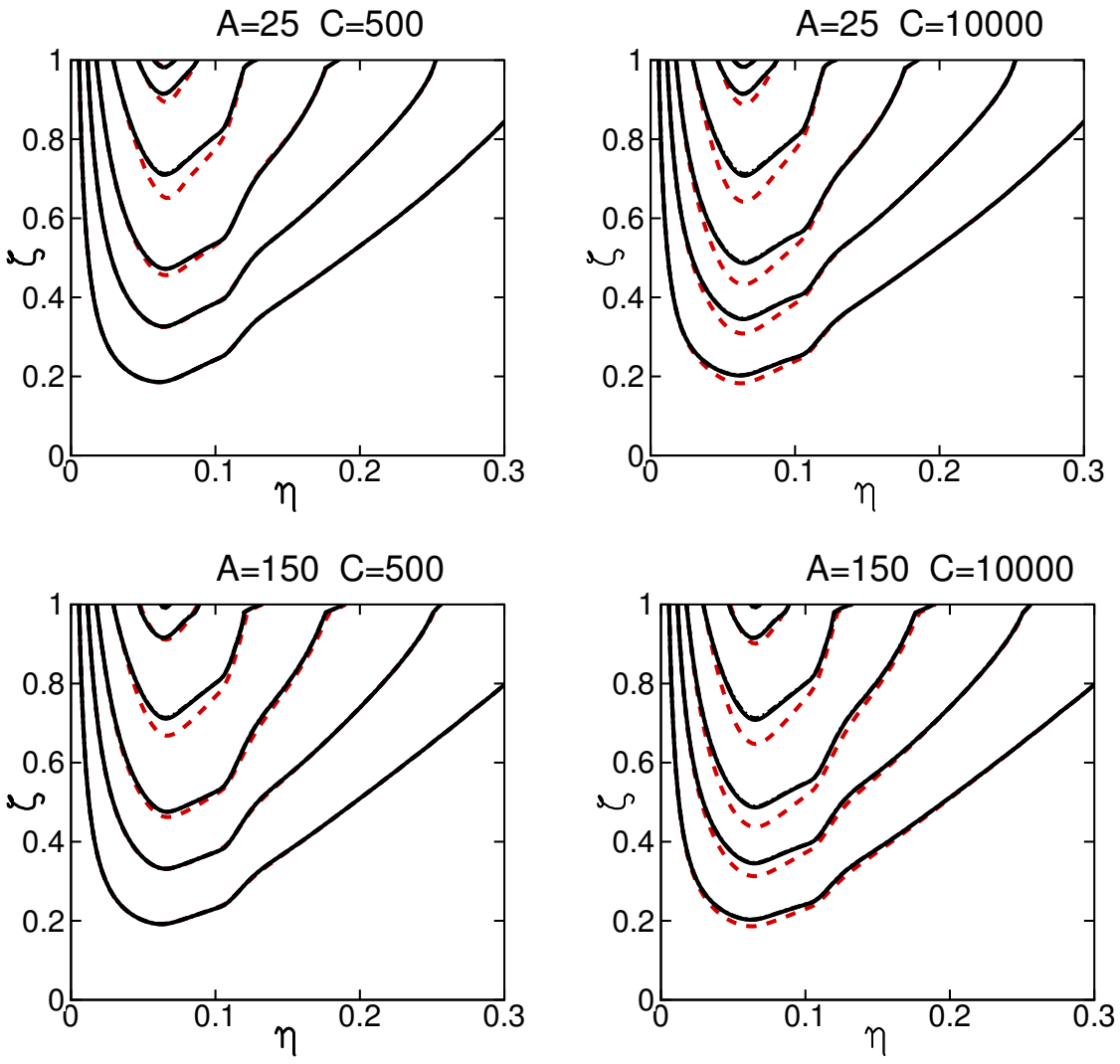

Figure 5.7: Contour lines of temperature in the state space for different time step. Dashed line : $\Delta_t = 1.10^{-5}s$, Solid line $\Delta_t = 1.10^{-6}s$, Dashed-dot : $\Delta_t = 5.10^{-7}s$. $\langle N_{c,\xi}|\eta,\zeta\rangle = 0$

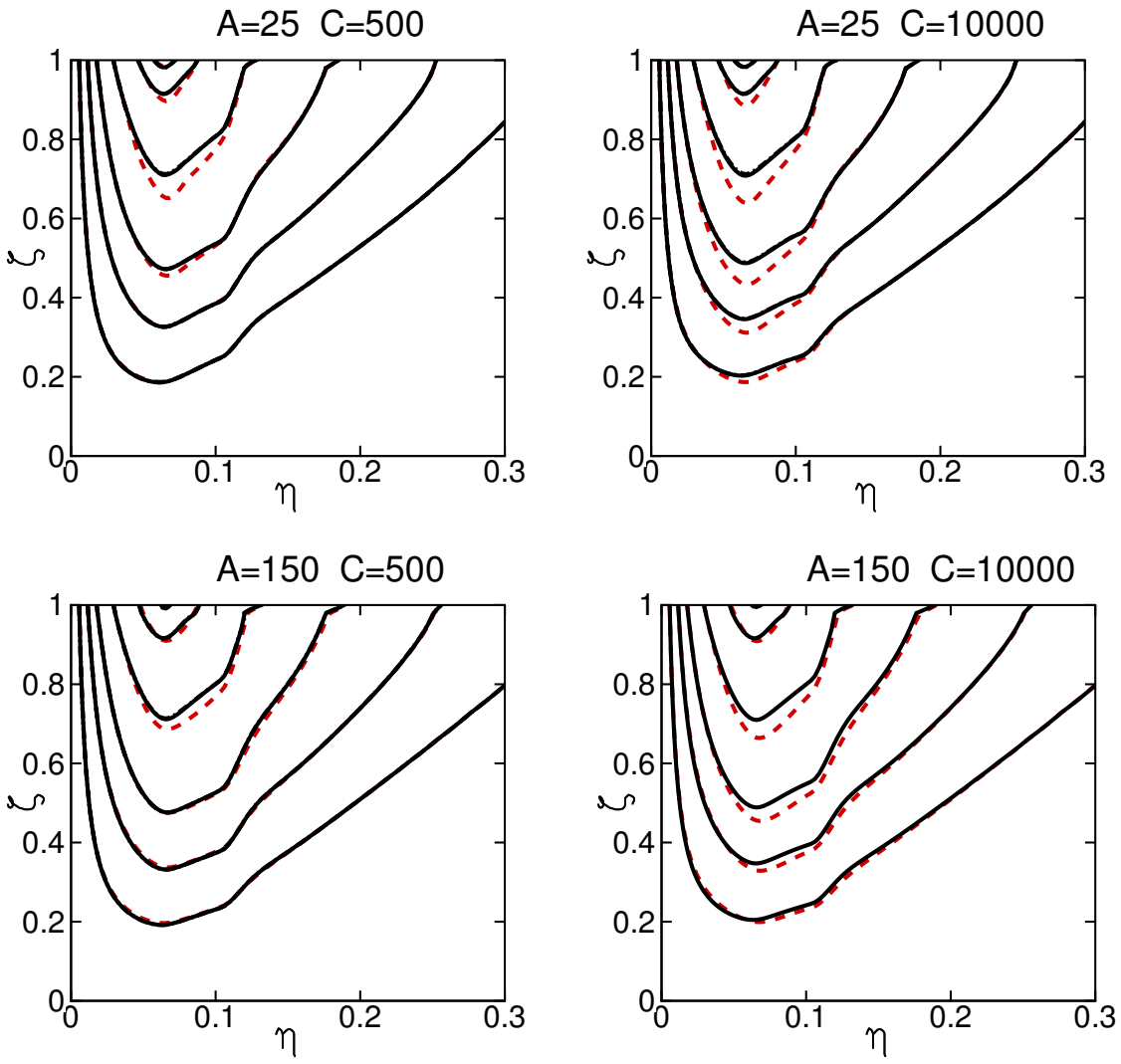

Figure 5.8: Contour lines of temperature in the state space for different time step. Dashed line : $\Delta_t = 1.10^{-5}s$, Solid line $\Delta_t = 1.10^{-6}s$, Dashed-dot : $\Delta_t = 5.10^{-7}s$. $\langle N_{c,\xi}|\eta,\zeta\rangle = \sqrt{\langle N_c|\eta,\zeta\rangle \langle N_c|\eta,\zeta\rangle}$

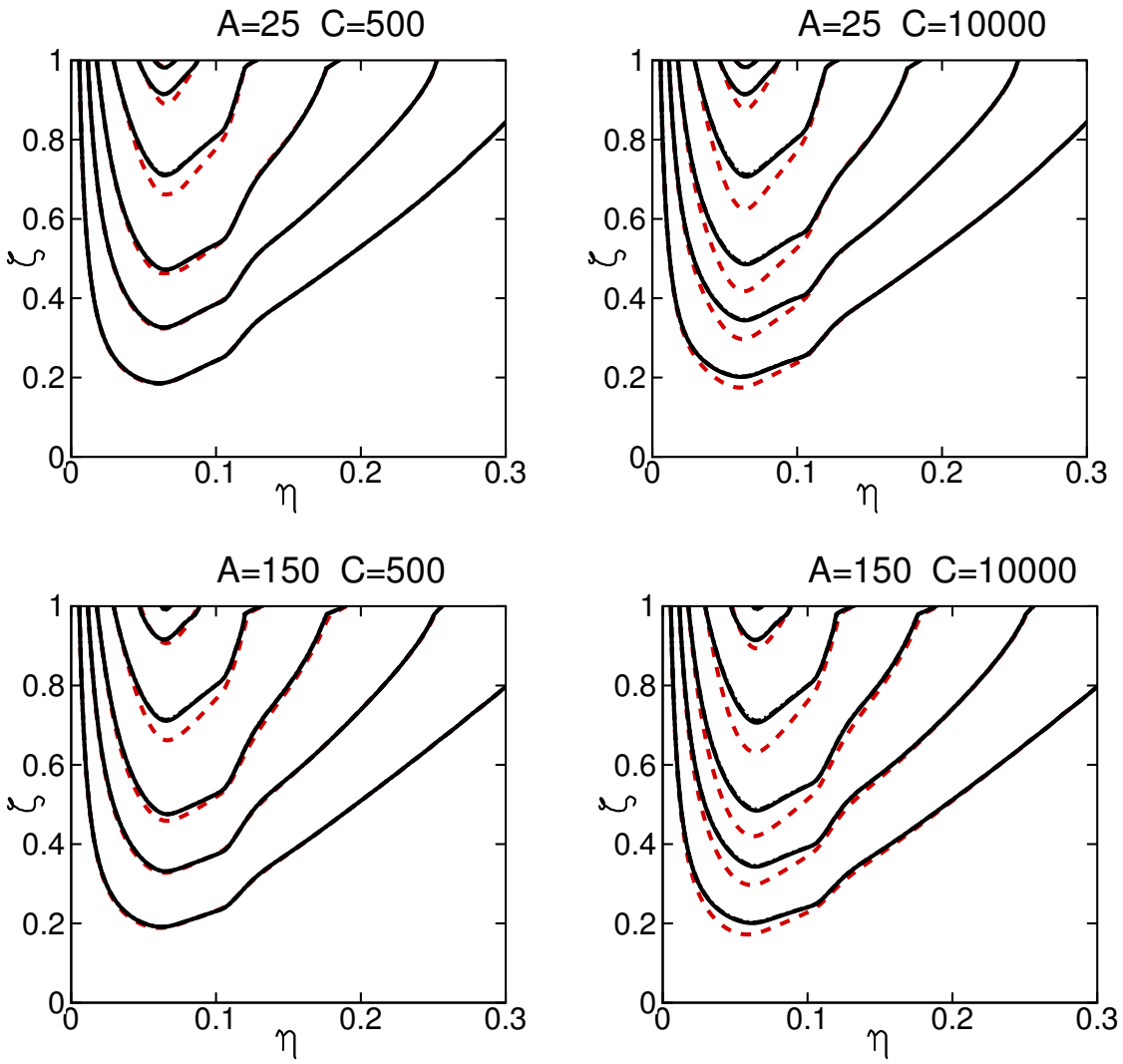

Figure 5.9: Contour lines of temperature in the state space for different time step. Dashed line : $\Delta_t = 1.10^{-5}s$, Solid line $\Delta_t = 1.10^{-6}s$, Dashed-dot : $\Delta_t = 5.10^{-7}s$. $\langle N_{c,\xi}|\eta,\zeta\rangle = -\sqrt{\langle N_c|\eta,\zeta\rangle\,\langle N_c|\eta,\zeta\rangle}$

5.3.3 Verification of the progress variable space implementation

Verification of the new progress variable-space implementation, and investigation of the number of points needed in progress variable space was carried out by comparison with freely propagating planar flame simulations conducted with (PREMIX) (Kee & al., 1985) adapted to use constant unity Lewis number. The scalar dissipation rates from the laminar premixed flame solutions were used as the model for the conditional scalar dissipation rate in the progress-variable space CMC calculations. The composi-

tion and temperature obtained from the code can then be plotted against the progress variable, allowing the comparison with the CMC solution. The unburned temperature was set to $300K$ and pressure set to 1bar. The equivalence ratio was varied. Figure 5.10 illustrates the method for the temperature, CO_2, H_2O and OH with different equivalence ratio ($\phi = 1$, $\phi = 1.27$). Very good agreement is observed for the temperature and major species with small discrepancies for intermediate species. It was found that, starting from an initial condition found by linear interpolation, the composition and the temperature converge to the steady state values in couple of time steps (chosen equal to $50\mu s$). The CMC solution was run until the following condition is lower than 1.10^{-5} :

$$\Delta T^n = \frac{|T(\eta,\zeta)^{n+1} - T(\eta,\zeta)^n|}{T(\eta,\zeta)^n} \tag{5.1}$$

The number of points in ζ-space is varied from 20 points to 80 points in Fig. 5.11. Differences are minor and 20 points is found to be sufficient for the temperature and major species. However 50 points were needed for the intermediate species as seen by the OH profile. Similar analysis have been carried out with methane chemistry by Nguyen & al. (2010) where discrepancies were observed for some species. The overall good agreement and the similarities with previous analysis give confidence on the numerics used in the code.

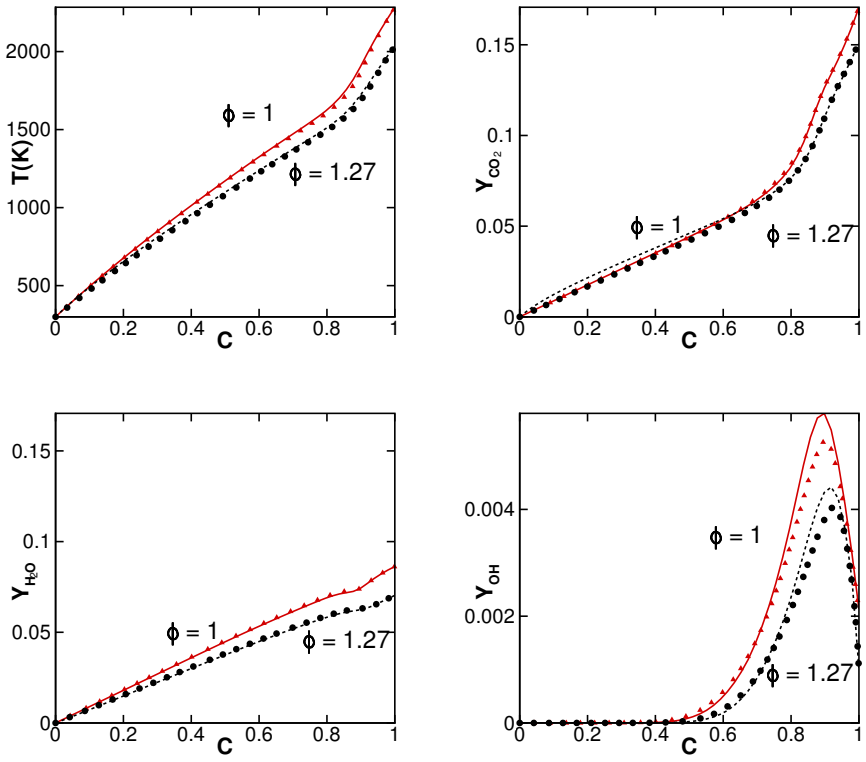

Figure 5.10: Temperature, Y_{CO_2}, Y_{H_2O}, Y_{OH} versus normalised progress variable c. Solutions from PREMIX (triangles: $\phi = 1$, circles: $\phi = 1.27$), and CMC (solid line: $\phi = 1$, dashed: $\phi = 1.27$)

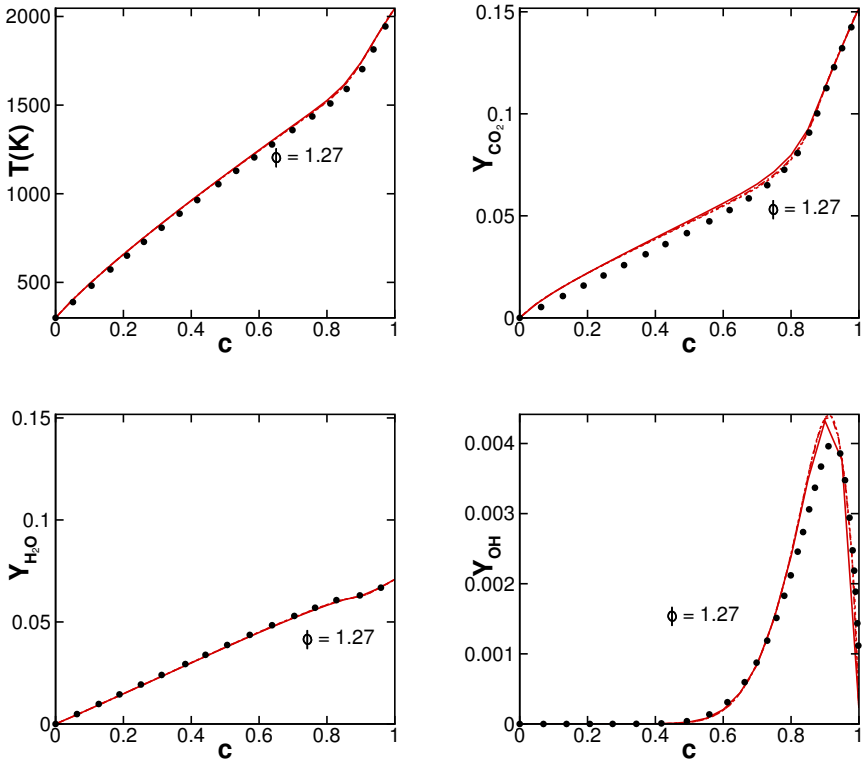

Figure 5.11: Temperature, Y_{CO_2}, Y_{H_2O}, Y_{OH} versus normalised progress variable c. symbols : Solutions from PREMIX, line : CMC (solid line : 20 points, dashed dot : 50 points, dashed : 80 points in c)

5.3.4 Spray sub model validation

Experimental data for the vapour and spray penetration are available for the non-reactive case A5. The liquid penetration length is shown in Fig. 5.12 and the vapour penetration in Fig. 5.13. The liquid penetration has been defined as the distance from the nozzle outlet to the farthest axial position encompassing 99% of the injected mass. The vapour penetration in the simulation has been determined from the leading spray boundary. The threshold has been set as the location where 0.1% of the fuel mass fraction remains.

The liquid penetration was significantly underestimated with the default break-up constants in STAR-CD (STAR-CD, 2004). Details of the break up models are given in the Chapter 2. Varying the coefficients had little effects on the vapour penetration length and the initial evolution of the liquid penetration length for the Reitz-Diwakar break-up model.

Concerning the vapour penetration, the correct trend with underprediction arising

from 1.5ms are observed. Overall these latter inaccuracies have been observed in previous work (Wright, De Paola, & al., 2005). Sensitivity of the mass flow rate profile has not been investigated and could influence the results as mentioned by the latter authors. Summary of the simulations on the n-heptane spray discussed by the ECN (Pickett, 2016) revealed that the vapour length penetration was generally underpredicted after 0.6ms.

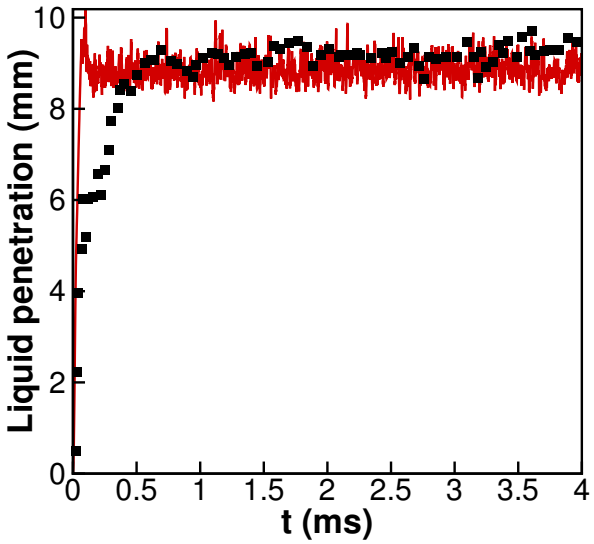

Figure 5.12: Liquid penetration for case A5 with 0% oxygen, line: simulation, symbols: experiment

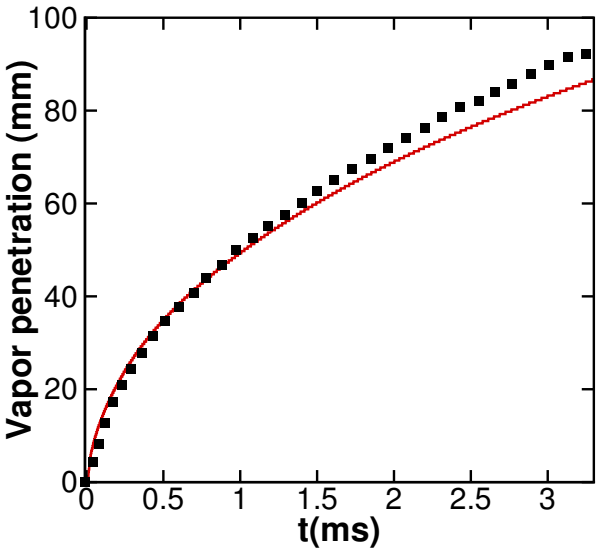

Figure 5.13: Vapor penetration for case A5 with 0% oxygen, line : simulation, symbols: experiment

5.4 Evaluation of the DCMC approach

5.4.1 Prediction of lift-off length and ignition delay time

Cases A1 to A4 have been simulated with three coupled CFD-CMC approaches: 0D-CMC, 3D-CMC and 0D-DCMC. Due to the lack of evidence concerning how the conditionally-averaged cross dissipation rate $\langle N_{\xi,c}|\eta,\zeta\rangle$ should be modelled in general flows, three limiting cases are considered for its modelling: setting the cross dissipation rate equal to zero; to the maximum possible value, $\sqrt{\langle N_c|\eta,\zeta\rangle\,\langle N_c|\eta,\zeta\rangle}$; or the minimum possible value $-\sqrt{\langle N_c|\eta,\zeta\rangle\,\langle N_c|\eta,\zeta\rangle}$. All of the simulations apply the same CFD and spray modelling set up, and the same assumptions regarding neglect of spray source terms in all of the CMC approaches. The predictions of lift-off length and ignition delay time are presented in Fig. 5.14.

Correct trends are observed with the zero dimensional DCMC formulation, with better agreement as the level of dilution decreases (i.e. more oxygen). Differences in lift-off length may be partly due to the different definition of flame location between the experiment and simulation which may result in a systematic difference between the two measures, however it is fair to compare the trends shown by the experiment and simulations. This same trend was found in previous studies employing the same chemical mechanism (Pei, Hawkes, and Kook, 2013), (Bolla & al., 2013). Allowing for an offset that may partly be due to the chemistry modelling errors and neglect of

spray terms, the trend predicted for lift-off length is in closer agreement than for the 3D-DCMC, and the magnitude of the ignition delay times predicted by the DCMC is closer to the experimental values than for the 3D-CMC.

Although the 0D-CMC was found to predict the ignition delay time reasonably well, the flame was found to be attached to the nozzle for all cases, resulting in no lift-off length. Here the 3D-CMC resulted in better agreement, compared to the 0D-CMC. Discrepancies given by the 3D-CMC as the level of dilution decreases are attributed to the absence of spray source terms in the state space. Indeed, very good agreement was found for the same conditions simulated by Bolla & al. (2013) with the 3D-CMC and the spray source term included. The DCMC captured the trend correctly, although, the values were overpredicted. The previous authors observed a propagation phase upstream following ignition.(Wright, De Paola, & al., 2005) simulated the autoignition of an n-heptane spray at high pressure (p=50 bars) and intermediate oxidiser temperature (T_a=783-823 K) in an open reactor and they found that the combined effect of pre-ignition and gas expansion were responsible for the apparent propagation. Borghesi & al. (2011) simulated the same cases as in this study with advanced spray modelling and suggested that a turbulent flame propagation mechanism was the driving mechanism. The discrepancies could result from an inappropriate modelling of $\langle N_c|\eta,\zeta\rangle$. Models for $\langle N_c|\eta,\zeta\rangle$ including corrections for premixed flame effects would have to be considered (Nguyen & al., 2010). It is recalled that the spray source term has not been included in the transport equation of c, which could have an effect. Advanced model of spray source terms yielded better prediction of the lift-off length (Borghesi & al., 2011). The effect of the sign of the conditional cross dissipation rates was found to be minor.

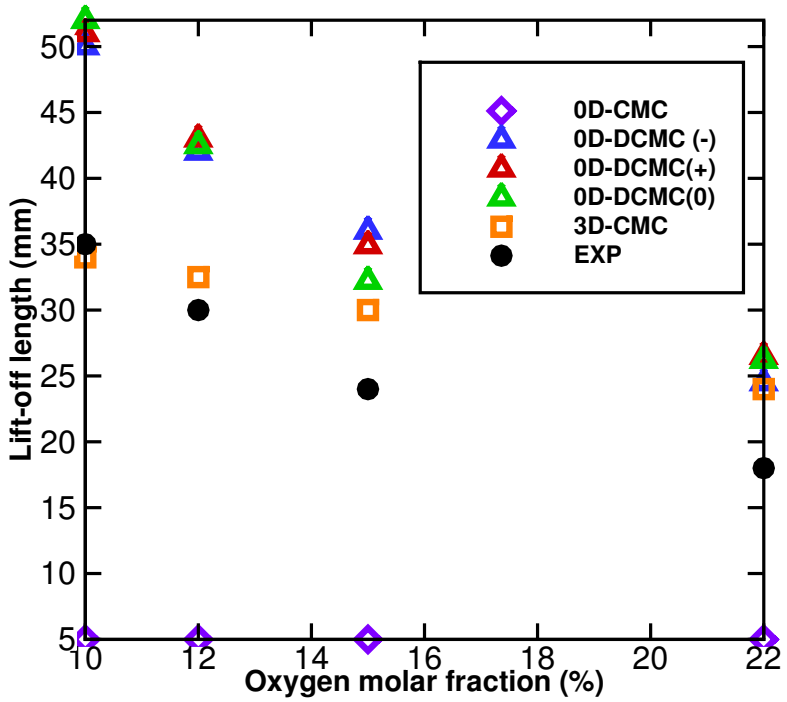

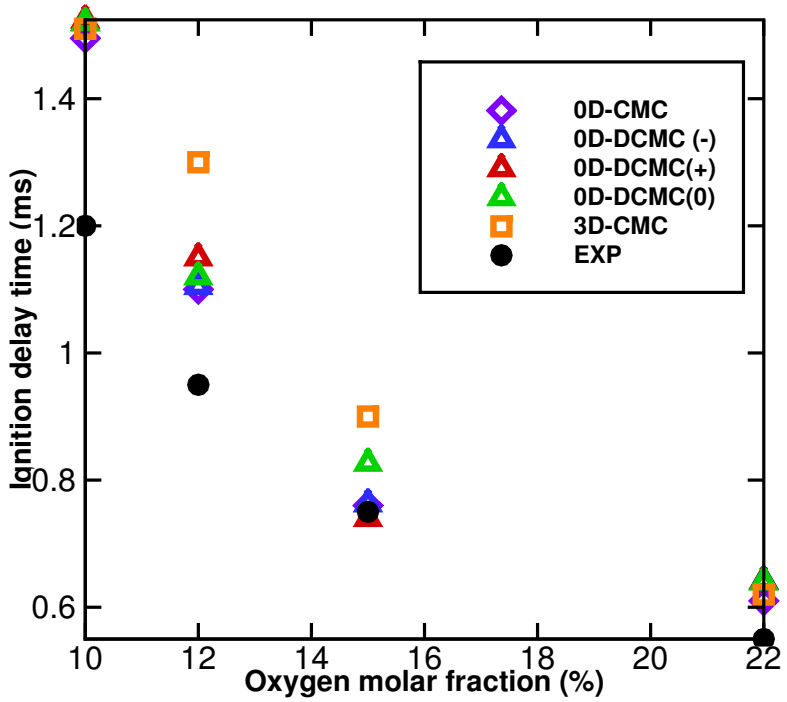

Figure 5.14: Lift-off length and ignition delay time for various level of dilution. For the 0D-CMC (purple diamond), 0D-DCMC (-) (blue triangle), 0D-DCMC (+) (ref triangle), 0D-DCMC (0) (green triangle), 3D-CMC (orange square), EXP (black filled circle)

5.4.2 Evolution of the flame structure

The evolution of the flame structure predicted for case A1 is investigated further in this subsection. Direct laboratory observations of the transient flame structure are not available, and the discussion compares the flame structures predicted by the three CMC approaches: 0D-CMC, 3D-CMC, and 0D-DCMC. Results for 0D-DCMC are shown for the case where the conditionally-averaged cross dissipation rate is modelled by its limiting minimum value, $-\sqrt{\langle N_c|\eta,\zeta\rangle \langle N_c|\eta,\zeta\rangle}$. Negative cross-dissipation arises when there is a tendency for fluid with low values of mixture fraction to be more reacted. Because, in this case, reaction is instigated by autoignition at a *most reactive mixture fraction* which is on the lean-side of stoichiometric, and the stoichiometric mixture fraction has a small magnitude, it is reasonable to expect negative values of cross-dissipation across the majority of mixture fraction space. Supporting evidence for the tendency of lifted autoigniting jet flames to exhibit negative mixture fraction-normalised progress variable cross-dissipation rates is presented in Chapter 6.

The evolution of the unconditional Favre averages of temperature, H_2O mass fraction, and mixture fraction is presented as a sequence of contour plots in Figs. 5.14-5.14 for the three CMC approaches. The times reported are the time after the start of injection.Fig. 5.14 indicates that the 3D-CMC and 0D-DCMC approaches predict ignition occurring close to the tip of the spray first, but that ignition occurs throughout the fuel jet for the 0D-CMC approach. The same features are indicated by plots of mean water vapour mass fraction in Fig. 5.14. Gopalakrishnan and Abraham (2002) who simulated a similar diesel spray using the laminar flamelet model found that ignition occurred at the tip of the spray as observed here. Following ignition the flame spreads upstream until the flame stabilises, in what is conventionally described as the *premixed propagation* phase in diesel engine combustion. The process of flame spread towards the tip and downstream of the tip however is due to combined effects of convection, which is driven both by the momentum of the fuel jet and thermal expansion in the flame, sequential autoignition of the fluid in different locations, and also turbulent flame propagation through flammable mixture. The temperature in the established flame is seen to peak at the stoichiometric mean mixture fraction isoline, as expected for a turbulent diffusion jet flame. The shape of the stoichiometric mean mixture fraction isoline however differs substantially between the three different simulation approaches. The mean mixture fraction contour plots in Fig. 5.14 show at all times that the peak value of mean mixture fraction near to the injector is highest in the case of the 0D-CMC, followed by the 3D-CMC, with the lowest near-injector peak values for mean mixture fraction observed in the 0D-DCMC simulation. There is a

corresponding difference in the penetration of mixture fraction. After ignition, the jet of mean mixture fraction in the 0D-DCMC case penetrates further into the domain, with the two singly-conditioned approaches showing more similar penetration lengths, as judged by the locus of the stoichiometric mean mixture fraction.

The 0D-CMC provides an unsatisfactory description of the flame stabilisation process because it assumes that composition follows the same functional dependence on mixture fraction throughout the whole domain, and thereby predicts that the fuel ignites throughout the domain simultaneously, without the possibility of flame propagation (as opposed to flame spread through mixture fraction space). The simulations confirm that, as may be expected, this leads to unsatisfactory predictions of the flame evolution, and to the flame stabilising too close to the injector.

The 3D-DCMC formulation admits the possibility of different extents of reaction progress at different locations in the flow, and accounts for transport of differently-reacted conditionally-averaged compositions through conditional turbulent transport and conditional convection terms, as well as allowing for the possibility of sequential ignition at different locations. The modelling of conditional transport terms employed is analogous to the unconditional modelling used for the transport of progress variable in the 0D-DCMC simulation however, in contrast to the modelling for unconditional transport of the mean progress variable, there is relatively little direct evidence for the validity of the conditional transport terms in the presence of premixed flame propagation. The 3D-CMC approach (singly-conditioned on mixture fraction) neglects one-point fluctuations of progress variable. In the case of perfectly-premixed combustion at low to moderate Karlovitz numbers, neglecting one-point fluctuations of progress variable is known to be an unacceptable approximation: for low to moderate Karlovitz numbers, premixed combustion occurs in thin flame fronts, giving a relatively bi-modal distribution of progress variable involving mostly reacted and unreacted mixture in which the reaction rate is generally low. Neglecting the one-point fluctuations of progress variable results in an intermediate composition in which the reaction rate is potentially much greater than the averaged reaction rate expected from the true, relatively bi-modal distribution. This *well-mixed* assumption for conditional progress variable in the singly-conditioned CMC approach is in principle only suitable for distributed flame propagation, but sufficiently high Karlovitz numbers to achieve distributed combustion are not expected in internal combustion engines. This conditional-well-mixed assumption is expected to lead to an overprediction of mean reaction rates during the flame propagation phase, and consequently to cause a reduction in the predicted lift-off length. This may be a factor contributing to the more rapid up-

stream propagation and shorter lift-off position predicted by the 3D-CMC, compared to the 0D-CMC. However the overall approximate agreement between the two methods, and the successes of the 3D-CMC approach across many previous compression-ignition diesel engine modelling studies suggests that deficiencies caused by neglect of conditional fluctuations of progress variable during the propagation phase might not affect predictions of some global engine performance parameters too much.

The 0D-DCMC approach accounts for the flame propagation process through the unconditional transport equations for the mean and variance of the progress variable. The resulting flame evolution is quantitatively similar to that in the 3D-CMC, despite substantially different assumptions in the two formulations of the model. The 0D-DCMC formulation accounts for the effect of the joint-distribution of progress variable and mixture fraction on the reaction rates and therefore has potential to overcome the deficiency due to the assumption of well-mixed of progress variable in the 3D-CMC approach and thereby to model flame propagation at low and moderate Karlovitz numbers, provided that an acceptable model for the joint mixture fraction-progress variable pdf is available. Being zero-dimensional however, the 0D-DCMC approach cannot account for factors that give rise to spatial variation in double conditional moments. The unconditional scalar dissipation rates vary over several orders of magnitude through the fuel spray and are known to be an important factor for the prediction of autoignition by the CMC approach. The pdf-weighted averaging procedure used to obtain the conditionally-averaged scalar dissipation rates used for the DCMC solution retains the important feature that mixture fraction dissipation rate is high in the unreacted fluid (which, spatially is near to the injector), and low in the more reacted fluid (which is further from the injector). The distribution of dissipation rates is discussed further below.

The near field of the flow reaches steady-state by 3ms after the start of injection and the flow in the full domain shown in Figs. 5.14-5.14 is in steady state by 5ms. After reaching steady-state, there remains a substantial difference between the mixture fraction fields given by the 3D-CMC and 0D-DCMC approaches. Mean and variance of mixture fraction and progress variable, and mean temperature and O_2 mass fraction are shown at 5 ms after the start of injection in Fig. 5.15. The 3D-CMC indicates higher peak values of mixture fraction in Fig. 5.14 in the near-field of the injector and that the stoichiometric mean mixture fraction isoline approaches closer to the injector. Given that the nominal liquid length in the non-reacting case is around 10 mm, and the lift-off length for case A1 reported for the 3D-CMC in Fig. 5.14 is 24 mm, it is remarkable that the combustion modelling has an effect on the fuel evaporation.

Close examination of the temperature field indicates that, despite the lift-off lengths reported in Fig. 5.14, the temperature increases upstream of 20 mm from the injector in the 3D-CMC simulation. The temperature upstream of and around the flame base may tend to both enhance evaporation and, through thermal expansion, affect the near-field mixing of fuel. This appears to have a substantial knock-on effect on the downstream mixing out of the mixture fraction field.

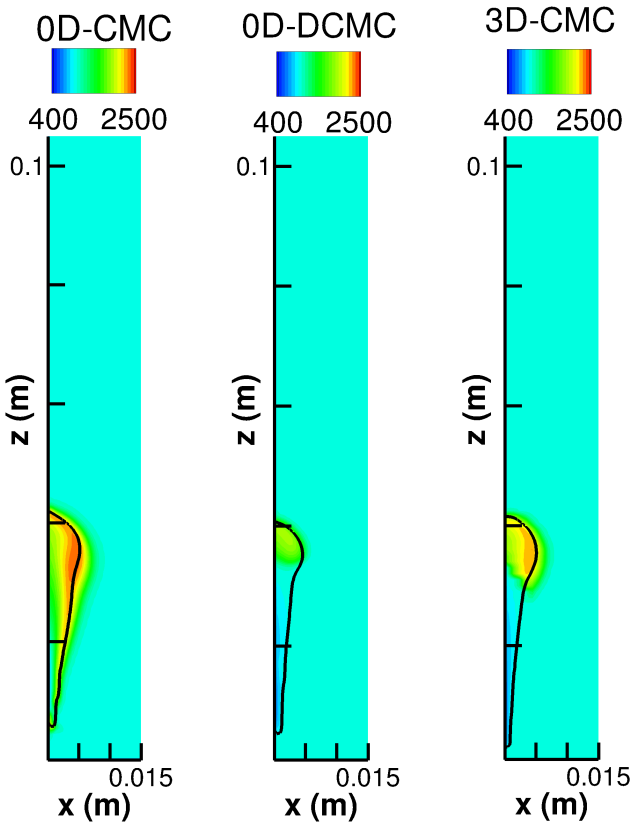

(a) $t = 0.7ms$

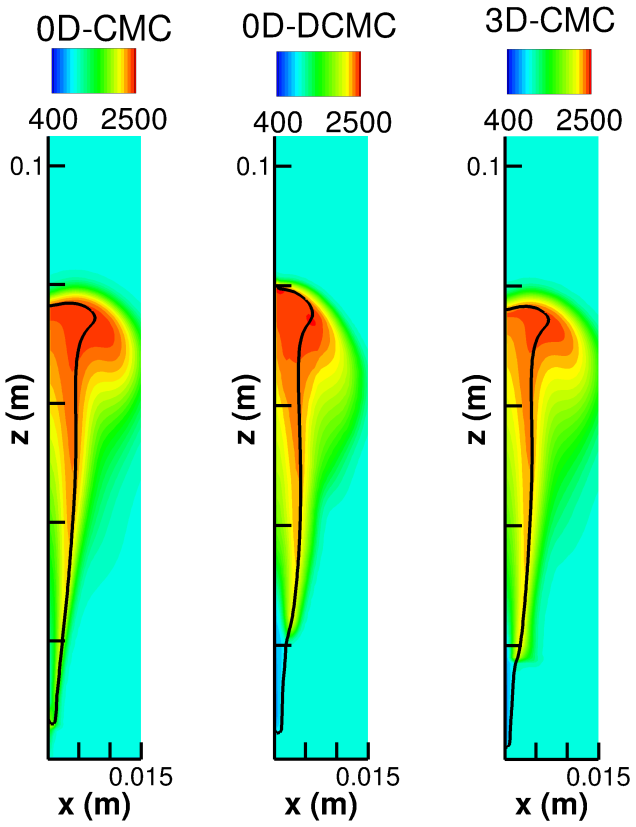

(b) $t = 3ms$

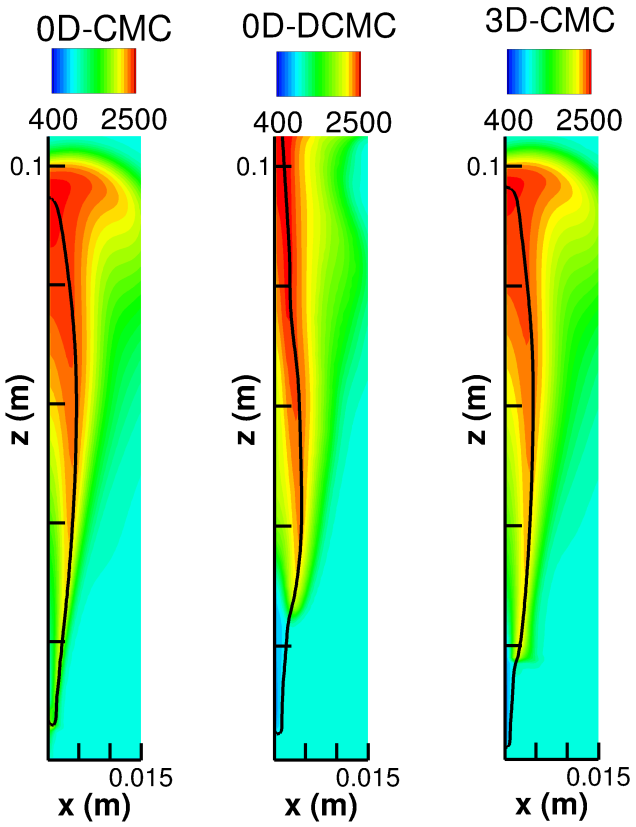

(c) $t = 5ms$

Figure 5.14: $\widetilde{T}$ at three different times, during ignition ($t = 0.7ms$), after ($t = 3ms$) and at steady state conditions ($t = 5ms$), for the 0D-CMC (left), 0D-DCMC (center), 3D-CMC (right). The stoichiometric mean mixture fraction isoline is shown in black.

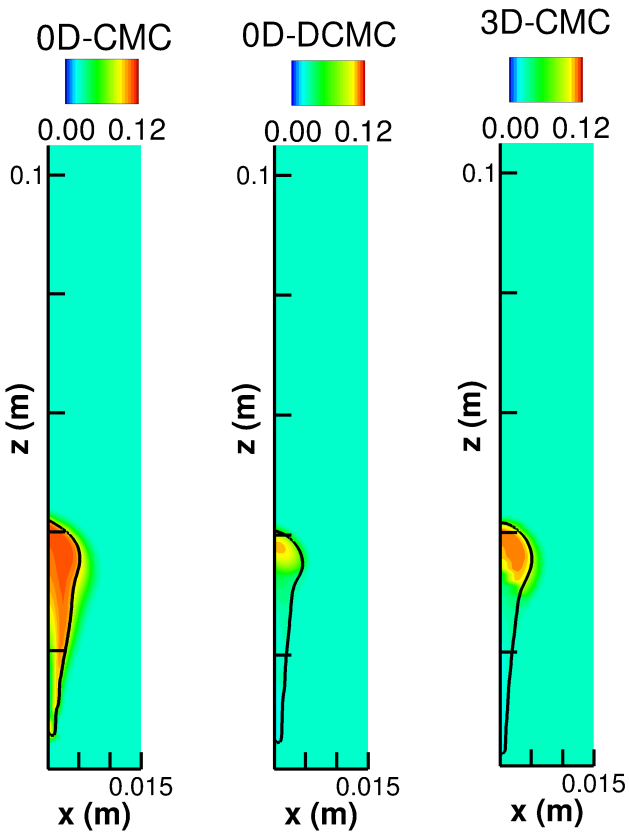

(d) $t = 0.7ms$

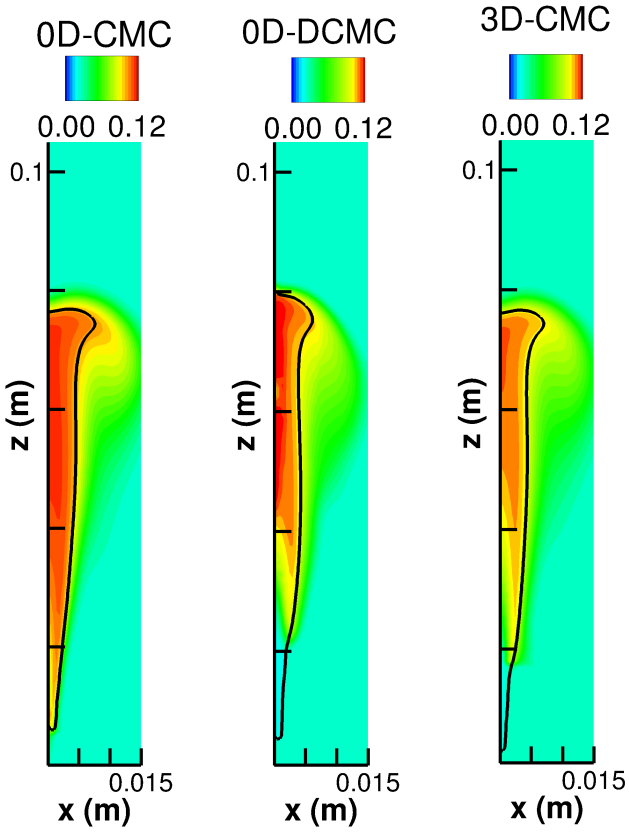

(e) $t = 3ms$

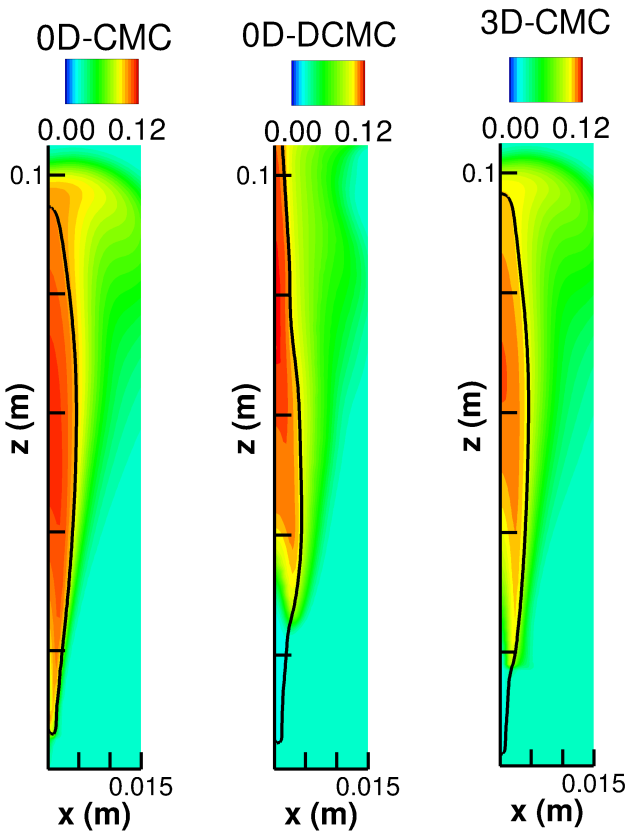

(f) $t = 5ms$

Figure 5.14: $\widetilde{Y_{H_2O}}$ at three different times, during ignition ($t = 0.7ms$), after ($t = 3ms$) and at steady state conditions ($t = 5ms$), for the 0D-CMC (left), 0D-DCMC (center), 3D-CMC (right). The stoichiometric mean mixture fraction isoline is shown in black.

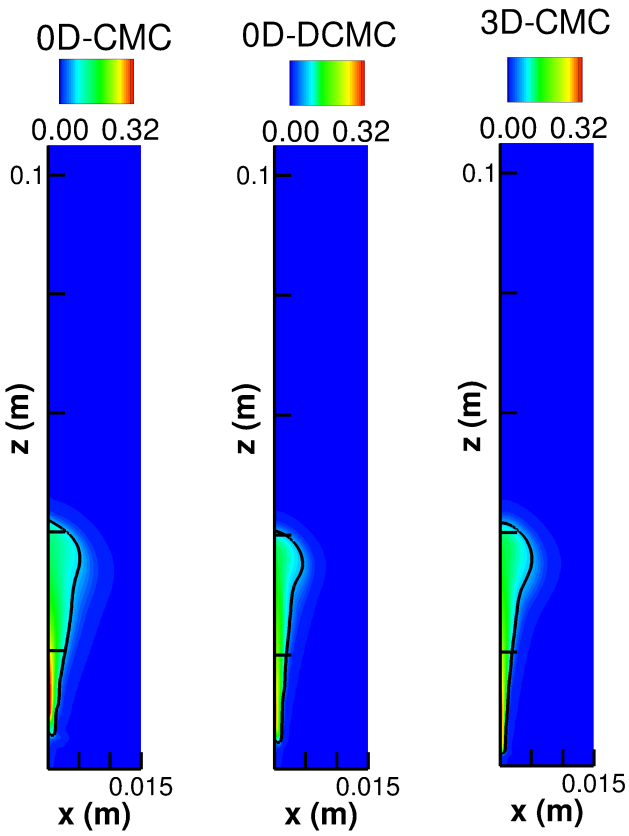

(g) $t = 0.7ms$

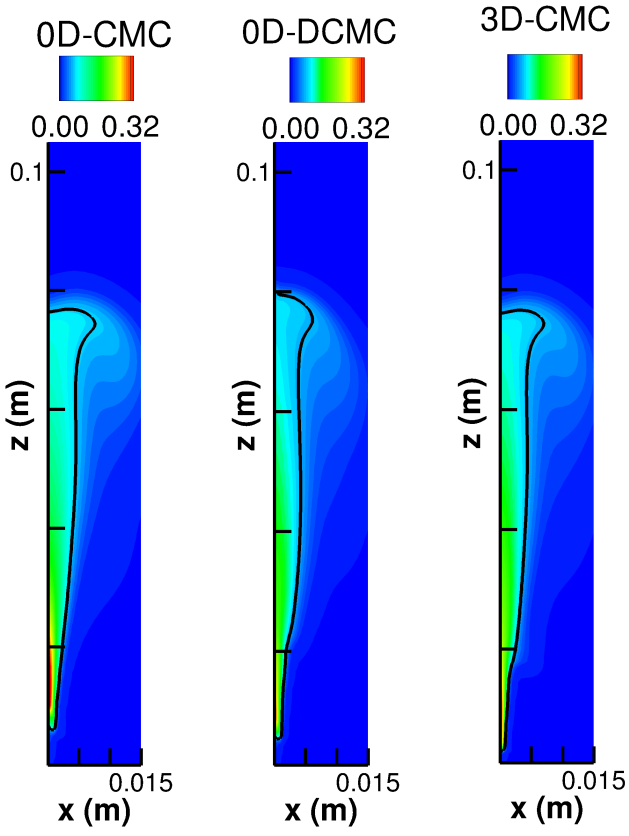

(h) $t = 3ms$

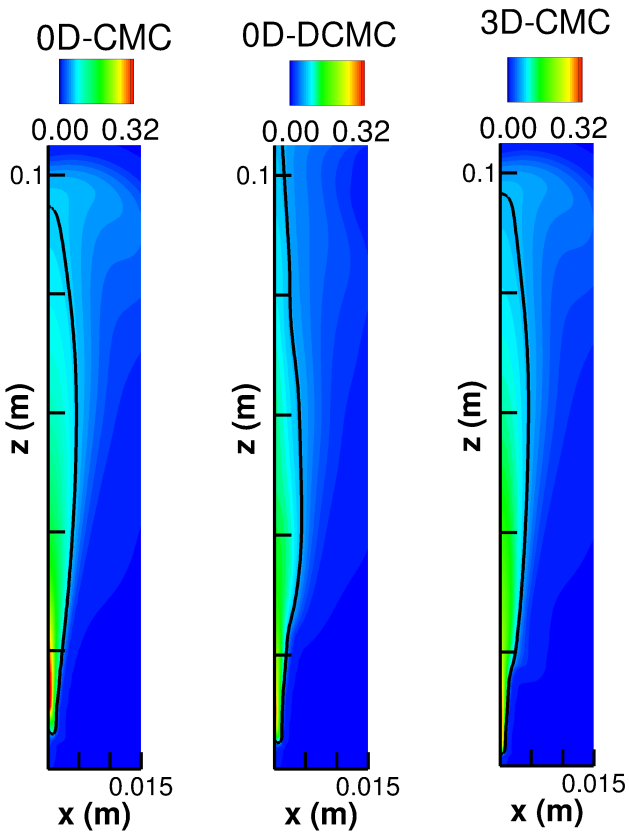

(i) $t = 5ms$

Figure 5.14: $\widetilde{\xi}$ at three different times, during ignition ($t = 0.7ms$), after ($t = 3ms$) and at steady state conditions ($t = 5ms$), for the 0D-CMC (left), 0D-DCMC (center), 3D-CMC (right). The stoichiometric mean mixture fraction isoline is shown in black.

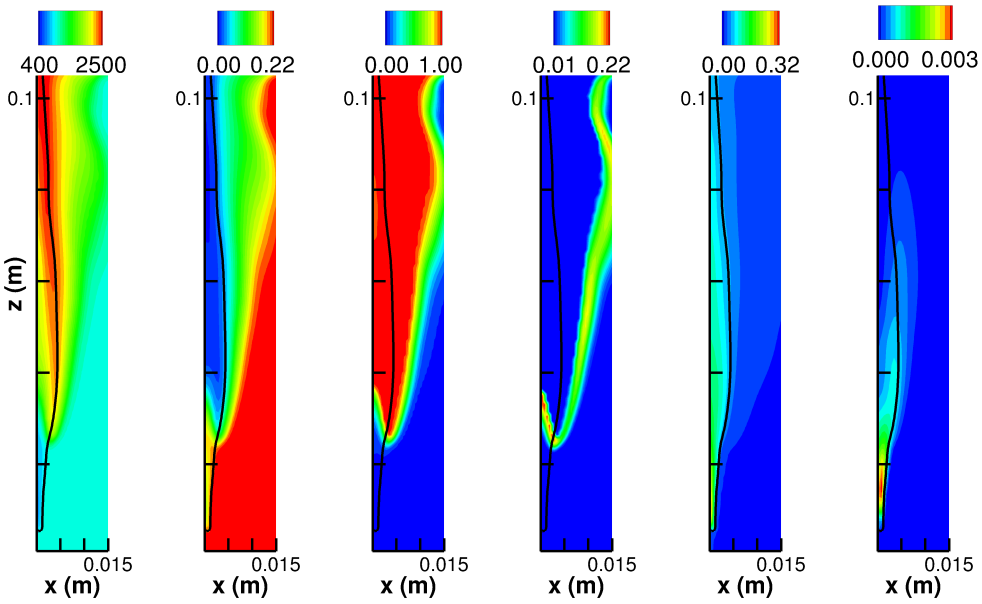

Figure 5.15: Contour of $\widetilde{T}$, $\widetilde{YO_2}$, $\widetilde{c}$, $\widetilde{c''^2}$,$\widetilde{\xi}$ and its $\widetilde{\xi''^2}$ at steady-state conditions $5ms$ for the case A1, solid line : ξ_{st} (0.065) in the DCMC with $\langle N_{\xi,c}|\eta,\zeta\rangle = -\sqrt{\langle N_\xi|\eta,\zeta\rangle \langle N_c|\eta,\zeta\rangle}$

5.4.3 Conditional dissipation rates

The modelled conditional dissipation rates from the 0D-DCMC simulations of case A1 with $\langle N_{\xi,c}|\eta,\zeta\rangle = -\sqrt{\langle N_\xi|\eta,\zeta\rangle \langle N_c|\eta,\zeta\rangle}$ are presented in Fig. 5.16 (η-space variation) and in Fig. 5.17 (ζ-space variation). Using the amplitude mapping closure gives $\langle N_\xi|\eta,\zeta\rangle$ at each CFD cell as a function of only η, and $\langle N_c|\eta,\zeta\rangle$ at each CFD cell as a function of only ζ, however the procedure of pdf-weighted averaging of the conditional scalar dissipation rates across the domain introduces variation in both η and ζ space. At early times, before ignition, regions of ζ space corresponding to more-reacted conditions have negligible probability, and the pdf-weighted average for the conditional dissipation rates cannot be determined numerically. In regions where the conditional dissipation rate cannot be determined, the conditional dissipation rates are set equal to zero.

The high turbulence intensity generated by the spray motion and steep mixture fraction gradients generated by evaporation leads to increased turbulent dissipation of mixture fraction close to the injector and, due to the pdf-weighted averaging procedure, this trend is reflected in the high values of conditional scalar dissipation rate of mixture fraction at low values of progress variable (up to $\zeta \approx 0.02$). Fig. 5.17 shows that the pdf-weighted conditional scalar dissipation rate of mixture fraction varies lit-

tle with progress variable in the range ($0.02 < \zeta < 0.98$), which may be explained by the observation that the mean progress variable transitions from unburned to burnt over a small distance and, since mixture fraction dissipation rate statistics vary over longer length scales, the conditional dissipation rate is nearly constant during this transition. The conditional mixture fraction dissipation rate close to $\zeta = 1$ is then lower, since this is an average across all of the fully-reacted mixture in the domain, including fluid far from the injector in which the mixture fraction dissipation rate is lower. The pdf-weighted averaging procedure therefore is able to convey information about the spatial variation of scalar dissipation rates into the zero-dimensional DCMC calculation. In order to resolve the important pre-ignition transport processes occurring close to the injector and the steep variation of the conditional dissipation rate it is therefore necessary to have high resolution close to the $\zeta = 0$ boundary.

The variation of the conditional average of progress variable dissipation rate also represents the variation of flow conditions throughout the spray. Fig. 5.16 plots conditional averages at given values of ζ. Isolines of mean progress variable shown in Fig. 5.15 track the edge of the flame from richer mixture at the centreline near the stabilisation point towards leaner mixture at the exit of the domain. Noting that the progress variable dissipation rates are expected to be highest near to the stabilisation point (due to relatively higher turbulence intensity and steeper gradients of mean progress variable), isolines of mean progress variable and, by analogy, averages conditioned on progress variable are expected to follow a transition from high progress variable dissipation rates at higher η (corresponding to fluid near the jet centreline close to the injector) to low values of dissipation rate at lower η (corresponding to radially-outer fluid further from the injector).

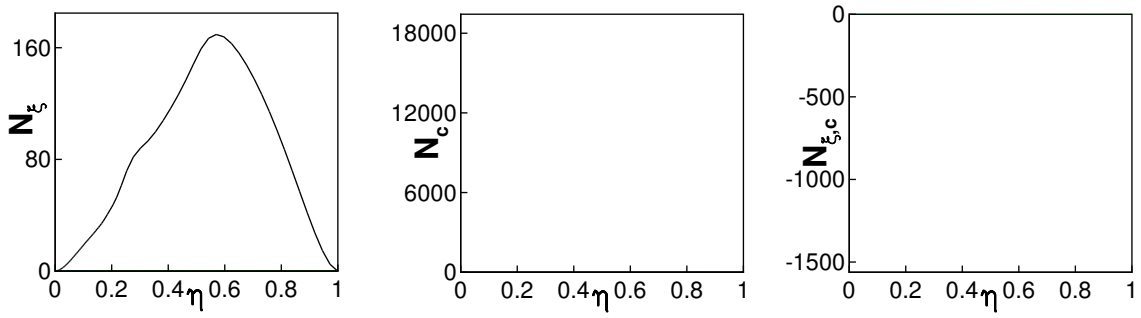

(a) $t = 0.3ms$

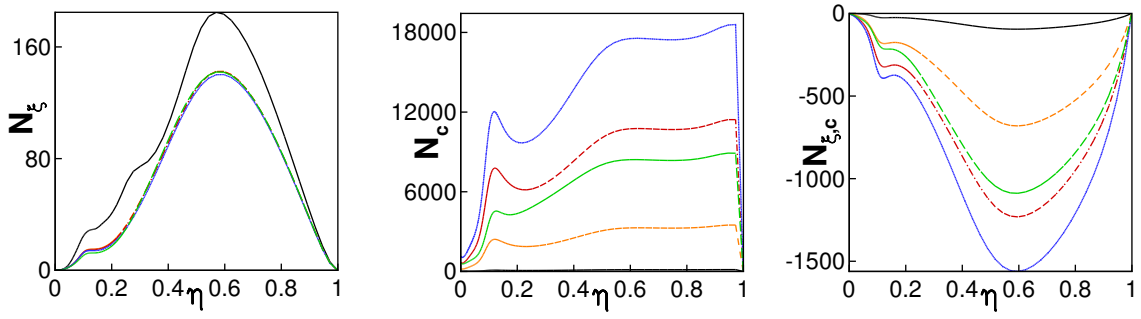

(b) $t = 3ms$

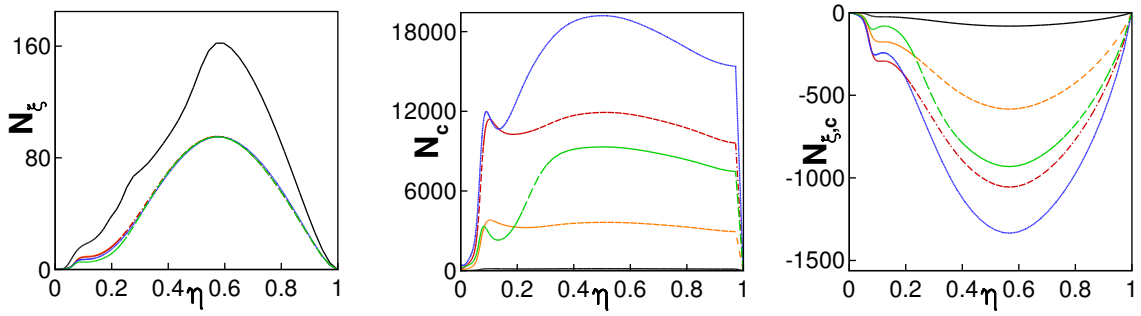

(c) $t = 5ms$

Figure 5.16: $\langle N_\xi|\eta,\zeta\rangle$ (first column), $\langle N_c|\eta,\zeta\rangle$(second column), $\langle N_{\xi,c}|\eta,\zeta\rangle$ (third column) versus η for different ζ, black solid line: $\zeta = 0.01$; orange dashed line: $\zeta = 0.1$; red dash-dotted line: $\zeta = 0.25$; blue dotted line: $\zeta = 0.5$; green long dash line: $\zeta = 0.8$

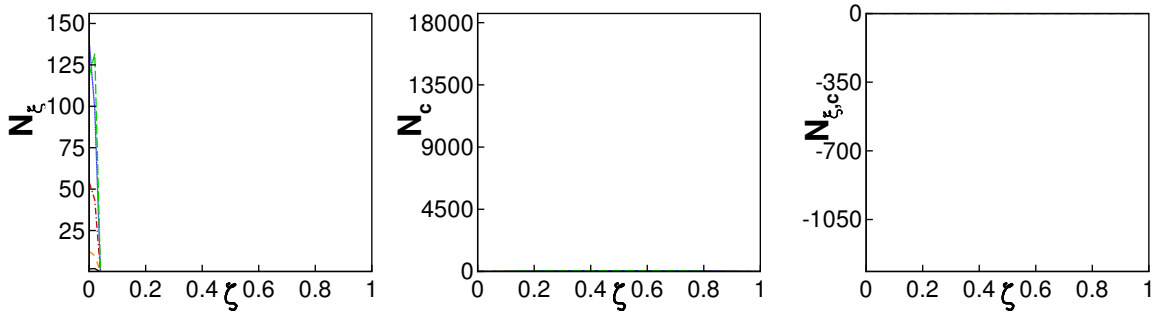

(a) $t = 0.3ms$

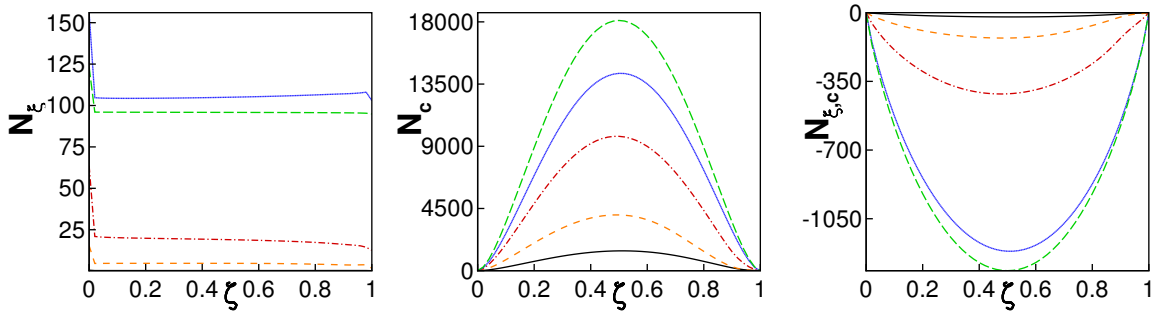

(b) $t = 3ms$

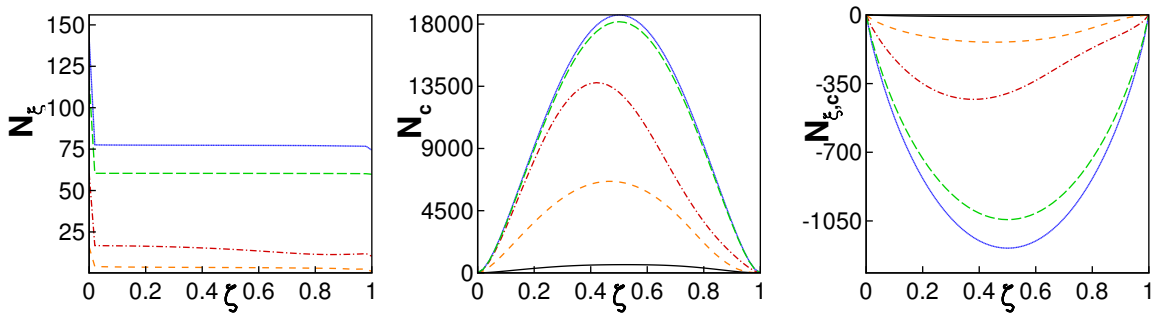

(c) $t = 5ms$

Figure 5.17: $\langle N_\xi|\eta,\zeta\rangle$ (first column), $\langle N_c|\eta,\zeta\rangle$(second column), $\langle N_{\xi,c}|\eta,\zeta\rangle$ (third column) versus ζ for different η, black solid line: $\eta = 0.0212$, orange dashed line: $\eta = 0.065(\eta_{stoi})$, red dash-dot line: $\eta = 0.2$, blue line: $\eta = 0.43$ green long dash line: $\eta = 0.8$

The higher values of the conditional dissipation rates in richer regions is reflected in the temperature and composition which are plotted on Fig. 5.18 and Fig. 5.19 for several values of η, ζ and for three times: before ignition, after and at steady-state conditions ($5ms$). The temperature and major species vary markedly in the richer regions as combustion proceeds. Minor variations for the temperature is observed at $3ms$ whereas CO_2 decreases throughout the simulation. Intermediate species increase

significantly around the rich and stoichiometric region following ignition. At steady-state conditions it is seen that further species are created in richer regions. These results indicate that the unconditional composition is expected to vary more markedly at the centreline and upstream where the mixture is richer.

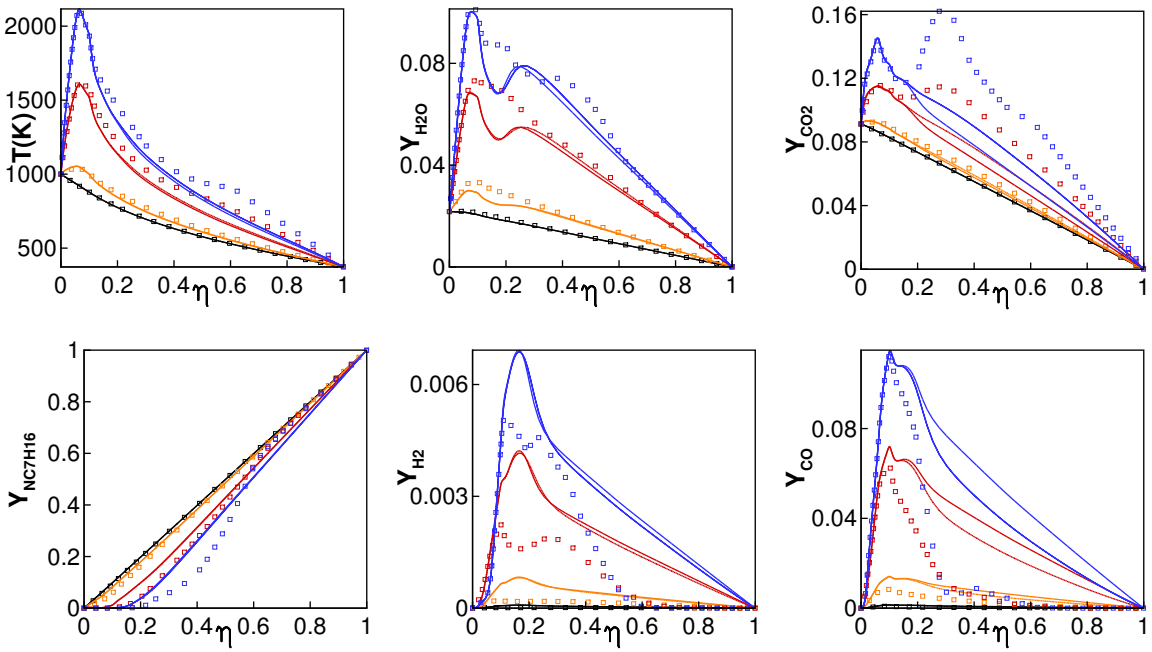

Figure 5.18: $T(K)$, H_2O, CO_2, NC_7H_{16}, H_2, CO versus η for different ζ; black lines : $\zeta = 0.01$; orange lines : $\zeta = 0.1$; red lines : $\zeta = 0.5$; blue lines : $\zeta = 0.8$ for time $t = 0.3ms$ (square symbols), $t = 3ms$ (dotted lines), $t = 5ms$ (solid lines). Case A1

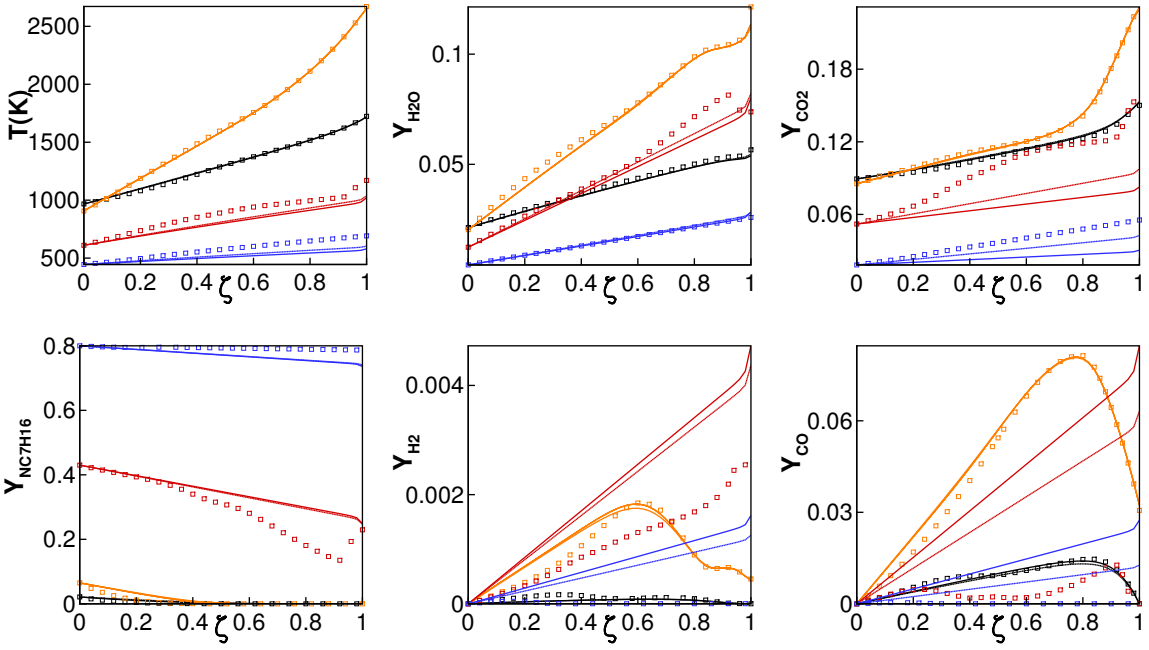

Figure 5.19: $T(K)$, H_2O, CO_2, HO_2, H_2, CO versus η for different η, black lines : $\eta = 0.0212$; orange lines : $\eta = 0.065$; red lines : $\eta = 0.43$; blue lines : $\eta = 0.8$, for time $t = 0.3ms$ (square symbols), $t = 3ms$ (dotted lines), $t = 5ms$ (solid lines). Case A1.

5.4.4 Computational efficiency

The cumulative simulation time for case A2 is plotted in Fig. 5.20 for the 3D-CMC and 0D-DCMC approaches. The cumulative time for the first one millisecond of simulation using one processor is 9 CPU hours for the 0D-DCMC and 18 hours for the 3D-CMC approach, making the 0D-DCMC faster by a factor of two in this instance. The 0D-DCMC calculation is currently only implemented for serial computation, whereas the 3D CMC implementation is parallelised by domain decomposition, allowing calculations to be completed in a shorter wall-time. Efficient parallelisation of the chemistry calculations in the DCMC approach through a task farming approach (either with shared memory or message passing, e.g. open-MP or MPI respectively) is relatively straightforward and can be expected to provide a near-linear speed up with the number of processors used.

Both the 0D-DCMC and 3D-CMC implementations use operator splitting such that the integration of chemical processes at each point in CMC space is an independent calculation. Due to the numerical stiffness of the chemical mechanism, integration of the chemistry is expected to represent a substantial portion of the overall computational time for the CMC approach. One might expect that the computational

cost would therefore scale with the number of chemistry integrations. The number of chemical integrations per time step in the 0D-DCMC approach is 5,000 (given by 100 points in $\eta\times$ 50 points in ζ), compared to 162,000 in the 3D-CMC simulation ($54\times$ 30 CMC nodes $\times$ 100 η points). Although the 0D-DCMC simulation involves a factor of 30 fewer chemical evaluations each time step, the computational time for each chemical evaluation is not the same, and the chemical evaluations for the DCMC-0D take longer on average. In particular, the computational time increases by orders of magnitude as composition goes through high-temperature ignition ($0.4 < c < 0.95$). In the 3D-CMC approach, the majority of CMC nodes are in regions of the flow that are either unburned or fully-burnt, with a small proportion in the stabilisation region with $0.4 < c < 0.95$. In the DCMC approach using progress variable as one of the conditioning variables, a substantial proportion of the grid points are located in the numerically-stiff range of progress variables ($0.4 < \zeta < 0.95$) throughout the simulation. A further reason for the disproportionately higher cost of this DCMC calculation is the time taken for convolution of conditional averages with the two-dimensional pdf of the conditioning variables, compared to the corresponding one-dimensional calculation in the singly conditional approach.

The computational time for convolution of the conditional means with the presumed joint-pdf is compared with the cost for the DCMC step in Fig. 5.21. In order to reduce the computational time, the convolution is performed for every CFD cell in which there is a non-negligible variance of mixture fraction, and the number of cells meeting this criterion increases as the fuel jet penetrates into the solution domain. The computational time for each DCMC step changes relatively little by contrast, and from 0.6ms after the start of injection the convolution operation consumes more computational time than than the DCMC step.

A number of strategies for reducing the computational cost of the DCMC calculation may be considered. In order to address the greatest computational costs, priorities are to

1. optimise the numerical convolution of the joint-pdf, and use approximations to the full numerical convolution where appropriate,

2. parallelise the chemistry integration,

3. reduce the number of grid points for the DCMC solution, especially within the stiffer region of progress variable space by for example using variable or adaptive grid spacing.

In the present test case the conditional average composition is unsteady throughout the calculation. Figure 5.19 shows that the conditional carbon monoxide profile continues to evolve up to 5 ms, suggesting that assumptions of steady-state for doubly-conditional conditional statistics is not appropriate. However, in many classes of combustion simulation, treating double conditional statistics as stationary can be a useful approximation even though the singly-conditional statistics are time-dependent. In such cases the DCMC solution can be performed off-line, allowing entirely removing the cost of the DCMC from the CFD (although the cost of the convolution step remains). In some cases with gradual evolution of the conditional dissipation rates, a quasi-steady-state approximation might be also be applicable, allowing the DCMC solution to be updated only intermittently (rather than through fully-coupled integration through time.)

Despite the scope for improving the computational efficiency of the DCMC, the fact remains that the approach is already a factor of two faster than the 3D-CMC approach for this axi-symmetric problem involving only 30×54 CMC nodes, and the advantage of the DCMC approach is expected to be orders of magnitude greater in truly 3-D configurations that require a truly-3D CMC grid with more CMC nodes.

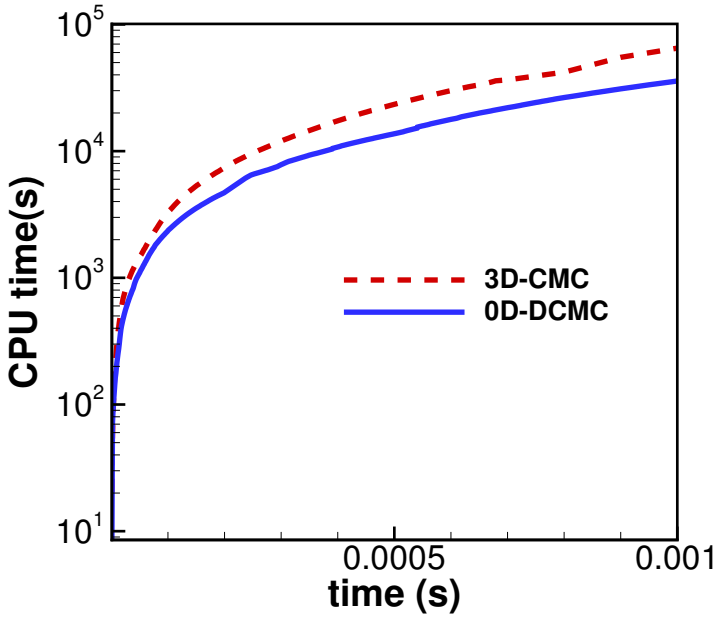

Figure 5.20: Total CPU time vs time for the 0D-DCMC (solid line) and 3D-CMC (dashed-line) using one core for the case A2

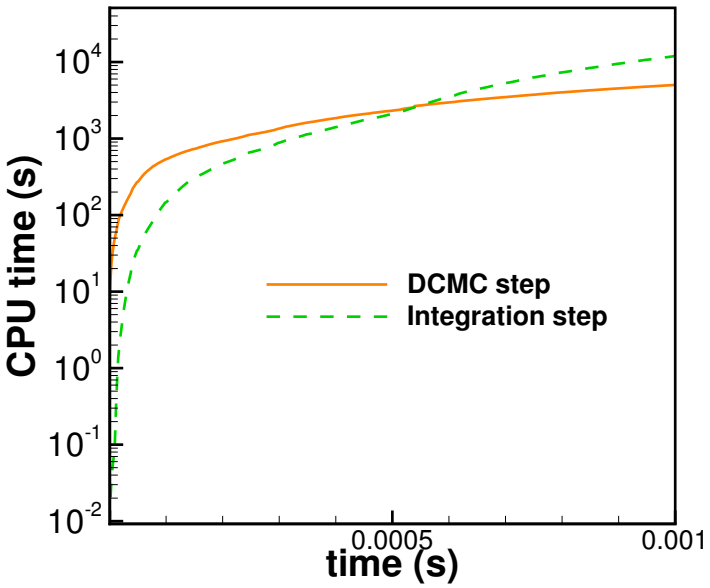

Figure 5.21: CPU time vs time for the 0D-DCMC solver and the integration. Case A2

5.5 Conclusion

This chapter demonstrated the feasibility of the zero-dimensional DCMC approach coupled with a CFD solver. The temperature and composition dynamically responded to the flow field and combustion. The model was found to predict the correct trend for lift-off length and ignition delay with less computational expense than for the singly-conditioned 3D-CMC. This increase could be particularly beneficial for the simulation of 3D burners involving complex multi-mode combustion phenomena, since the turbulent combustion can be described in a 2D space characterised by the mixture fraction and progress variable.

The results of this chapter encourage further development of the zero-dimensional DCMC approach and indicate a number of areas for further improvement:

- Spray source term in the equation of c still need to be added. In RANS or LES context, the later term could be assessed from the state space, providing a model for the doubly conditioned mean of the evaporation source term was available.
- The covariance transport equation could be solved, or an algebraic model employed, in order to provide a model for the sign (or coefficient) pre-multiply

$\langle N_{\xi,c}|\eta,\zeta\rangle$.

- Model of $\langle N_c|\eta,\zeta\rangle$ that account for several combustion regimes has to developed.

Chapter 6

Results - III Modelling of split-fuel injection under diesel engine conditions

The analysis in Chapter 4 has indicated the suitability of double conditional moment closure (DCMC) using mixture fraction and progress variable for modelling of split-injection processes. The double conditional moment closure formulated in Chapter 3 was implemented and tested for single-injection test cases in Chapter 5. The objective of Chapter 6 is to evaluate the performance of the mixture fraction-progress variable DCMC implementation in simulation of combustion of split-injection fuel sprays at engine-like conditions.

Detailed experimental measurements of split-injection combustion processes in laboratory set-ups with well documented boundary conditions are relatively scarce. In this Chapter, laboratory experiments concerning split-injection of n-heptane sprays reported by Cung & al. (2015) are simulated using the DCMC approach, and the performance of the DCMC is evaluated in terms of the global parameters that are available from the experimental measurements. The DCMC predictions however provide information on the full transient evolution of the split-injection ignition process that is not available from the current state-of-the-art measurements, and the prediction of this evolution is presented and discussed. Previous predictions concerning these laboratory measurements based simply on characteristic time ignition models (Cung & al., 2015) do not lead to values for lift off length. Other very recent publications concerning singly-conditioned CMC-based simulations of split-injection of dodecane fuel sprays (Blomberg & al., 2016) focussed on the relative merits of Reynolds-averaged and large eddy simulation approaches, indicating that large numbers of CMC control

volumes are needed in order to achieve acceptable predictions of the ignition and flame behaviour. The DCMC approach is motivated by the possibility of massively reducing the number of CMC control volumes required in order to describe the combustion process. This Chapter represents the first application of the DCMC approach to the simulation of split-injection spray ignition and combustion processes.

6.1 Configuration

6.1.1 Experimental Configuration

The analysis in this Chapter is based on previous split-injection spray ignition and combustion measurements reported previously by Cung & al. (2015). The experiments take place in a constant volume chamber in the Alternative Energy Research Building at Michigan Technological University. The combustion chamber geometry and operation is based on the Sandia National Laboratories (Nesbit & al., 2011) chamber that produced the measurements analysed in Chapter 5. The chamber is capable of operation at high temperature and pressures that are representative of diesel engine combustion conditions. The high temperature and pressures required ahead of fuel injection are obtained by spark ignition and premixed combustion of a fuel-lean mixture of light hydrocarbon gases. The test conditions are summarised in Table 6.1.

In order to investigate the spray transport and vaporisation process independently from the ignition and combustion process, a set of measurements was first performed in an oxygen-free environment, involving an ambient gas volumetric composition approximately equal to O_2 (0.0%), N_2 (89.7%), CO_2 (6.5%), and H_2O (3.8%) (Cung & al., 2015). The combustion cases have 15% O_2 by volume. The measurements in the non-reacting case consist of simultaneous shadowgraphy and Mie scattering, whereas flame luminosity is recorded in the combustion cases.

A single-hole solenoid injector was used to perform split-fuel injection. 15% of the total fuel mass is injected in the first *pilot* injection, and 85% is injected in the main injection. This corresponds to a nominal pilot injection duration of 0.26 ms, and a main injection duration of 0.95 ms. After filtering the measured mass flow rate signal, the rate of injection (ROI) used as input for CFD modelling are shown in Fig. 6.1. The effect of varying the dwell time (the interval between the end of the pilot injection and the start of the main injection) is investigated by setting it to 0.17, 0.77 or 1.37 ms.

The bulk temperature T_b in the chamber equals 950 K prior to injection. The bulk temperature is calculated from the pressure measurement and from the known density

in the chamber, assuming that the temperature is uniform. Since the chamber wall temperature is only 453 K, there is a significant temperature variation in the thermal boundary layers, and it is recognised that the ambient temperature T_a in the region of the spray is higher than the bulk temperature value (Idicheria and Pickett, 2007). Empirically-derived corrections for the difference between T_a and T_b have been suggested for other constant volume spray ignition studies (Idicheria and Pickett, 2007), but are not available for the present case.

Table 6.1: Summary of test conditions

Parameter	Value
Fuel	n-Heptane
Nozzle diameter	100 μ m
Injection Pressure	120 MPa
Injection durations for 15 : 85% mass split	0.26 ms : 0.95 ms
Dwell time	0.17, 0.77, 1.37 ms
Gas density	23 kg/m^3
Oxygen level	0%, 15%
Chamber temperature	453 K
Bulk temperature at injection	950 K

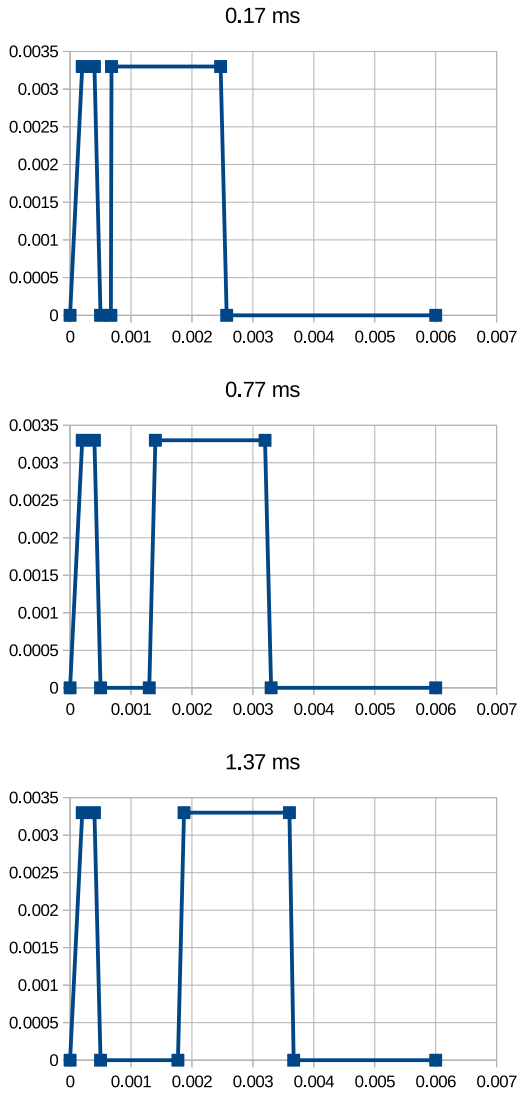

Figure 6.1: Rate of injection (ROI) [g/ms] versus time [s] used for short, medium and long dwell time

6.1.2 Summary of the experimental observations of (Cung & al., 2015)

The flame evolution observed by (Cung & al., 2015) for cases B1-B3 is visualised in Fig. 6.2 as a false colour rendering of the flame luminosity. Case B1 has a short dwell time, and the flame kernel from the pilot injection survives until the time that it is engulfed by the main fuel injection. The flame base then moves further towards the injector, establishing a quasi-steady lifted flame during the main injection. For cases B2 (with a dwell time of 0.77 ms) and B3, the pilot luminosity fades away, due to dilution of the pilot flame with ambient oxidiser and consequent burn out of soot, before the main

injection ignites. The pilot has a decreasing influence on ignition of the main injection in cases B2 and B3, resulting in a longer ignition delay for the main fuel injection and in the main injection igniting at a location further downstream, before propagating back towards the fuel injector.

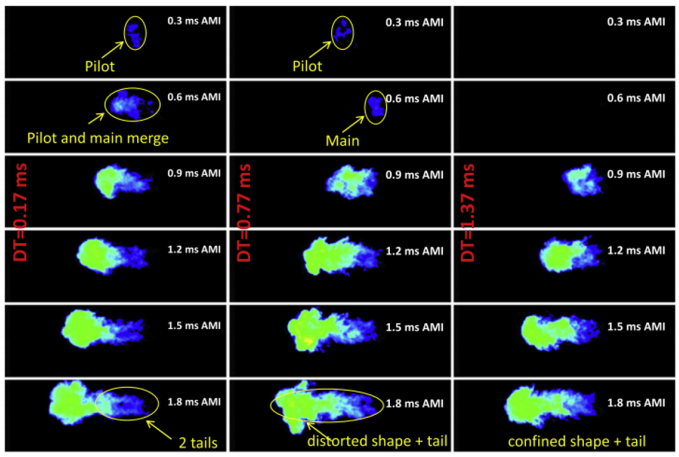

Figure 6.2: Pilot and main flame luminosities (false color) after main injection (AMI) for dwell time = 0.17 ms/Case B1 (left column), dwell time/Case B2 = 0.77 ms (middle column), and dwell time/Case B3 = 1.37 ms (right column), direction of the jet is from right to left, from Ref. (Cung & al., 2015).

The temporal evolution of the combustion process in the experiments is further illustrated by (Cung & al., 2015) in plots of the axial variation of the radially-integrated luminosity during the whole combustion event, reproduced in Fig. 6.3. This presentation of the experimental observation serves to emphasise the separation between the pilot combustion and the main fuel combustion in case B3, such that the ignition delay for the main injection shows a large reduction in case B1 compared to the pilot ignition delay, but a much smaller reduction in case B3. Following the ignition transient, the most upstream location showing significant luminosity is approximately 30 mm from the injector in all cases, and this is indicative of the lift-off length in the experiments.

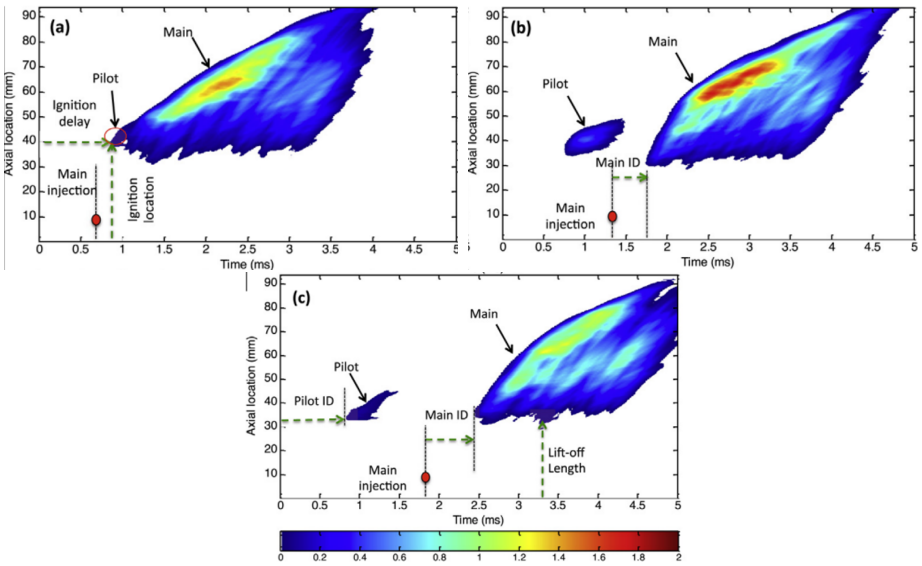

Figure 6.3: Instantaneous axial integration of flame luminosity for (a) dwell time = 0.17 ms/Case B1, (b) dwell time = 0.77 ms, (c) dwell time = 1.37 ms/Case B3.

6.1.3 Numerical setup

The numerical setup is identical to the set up verified in the previous chapter. This involves coupling of the double conditional moment closure code with the commercial computational fluid dynamics (CFD) code STAR-CD. The same numerical discretisation and numerical methods are employed as in Chapter 5: the mesh, the time step in the CFD and the DCMC (respectively $\Delta T = 1.10^{-6}$ and $\Delta T = 5.10^{-7}$), the turbulence model (k-ϵ for high Reynolds number), the spray and atomisation model (Reitz-Diwakar), the n-heptane chemical mechanism, the conditional dissipation rate models, and the number of points in the respective sample-space directions are identical. For more information about the numerical setup, the reader is referred to the previous chapter.

The cases studied are summarised in Table 6.2. Three non-reactive and two reactive cases are analysed. Since the focus of this chapter is to address the ability of the DCMC to model turbulent combustion in split-fuel injection configuration, the first three cases are studied only in order to validate the spray and turbulence models in non-reactive conditions, as discussed in the next section.

Table 6.2: Cases studied

Case	Gas T(K)	Gas density (kg/m^3)	O_2 (% by vol.)	Dwell (ms)
A1	980	23	0	0.17
A2	980	23	0	0.77
A3	980	23	0	1.37
B1	980	23	15	0.17
B3	980	23	15	1.37

6.1.4 Conditional cross-dissipation rate modelling

Three approaches for modelling the conditional scalar cross-dissipation rate are considered, corresponding mixture fraction–progress variable correlations of +1, 0 and -1, denoted by DCMC(+1), DCMC(0), and DCMC(-1) respectively, as set out in Chapter 5.

The modelling of $\langle N_{\xi,c}|\eta,\zeta\rangle$ was found to have a strong effect on the predictions. The ignition location was found to be very close to the injector for the DCMC(+) and DCMC(0) modelling, corresponding to mixture fraction-progress variable correlations equal to unity and zero respectively. The DCMC(-) modelling, corresponding to negative correlation, does yield a flame that is lifted and that behaves similarly to the experimental observations. The mixture fraction–progress variable correlation is expected to be related to the timing, location and stoichiometry within the flow. For example, Fig. 6.4 shows the correlation between mixture fraction and progress variable in a lifted autoignitive ethylene-air jet flame from (Matheson, 2016, PhD thesis), showing that in an autoignitive fuel jet the rich mixture shows a negative correlation, and the lean mixture a negative correlation. This effect arises because mixture around the most-reactive mixture fraction (which is close to stoichiometric in many cases) tends to ignite first (leading to positive correlation for leaner mixture and negative correlation for richer mixture), and because the leaner mixture fractions have a lower convection velocity, and therefore a longer cumulative residence time up to a given axial distance, which tends to give greater ignition progress in leaner mixture (promoting negative correlation). In the present case involving split-injection, it is expected that the older fluid from the first injection will be more reacted and also have a lower mixture fraction, due to mixing with oxidiser, while freshly injected fuel arriving at the same location will tend to be less reacted and to have undergone less mixing with oxidiser – and this contributes to a negative correlation. While the mixture fraction–progress variable correlation and cross-dissipation clearly have a complicated

dependence on the flow and reaction processes, there is a tendency for negative correlation to be dominant within the fuel jet, and, while it is just one limiting case, the simple DCMC(-) model may be closer to representing the dominant physics than the other two modelling approaches (DCMC(0) and DCMC(+)) in this case.

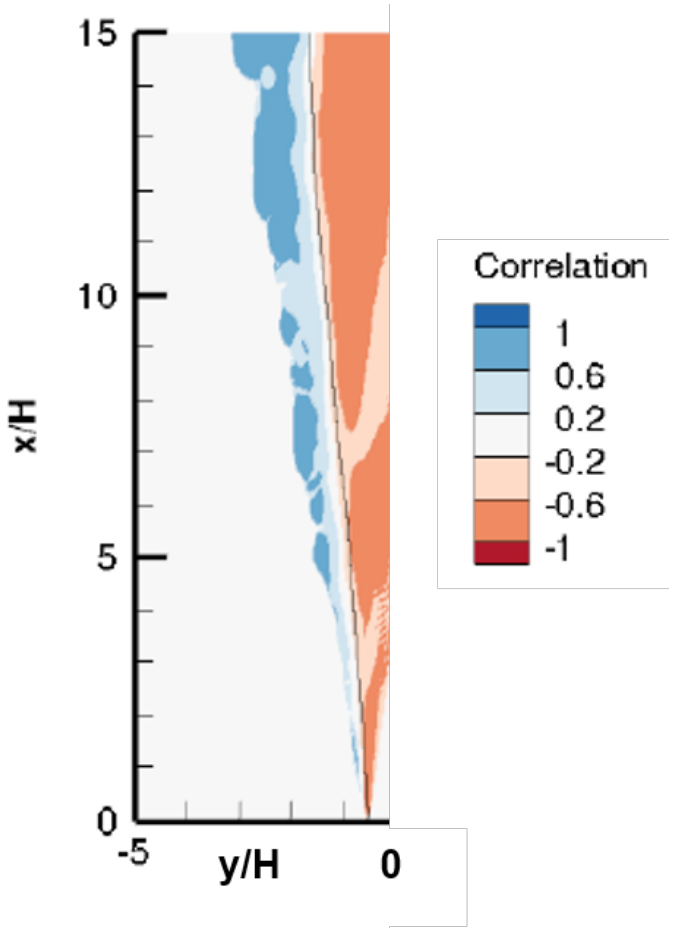

Figure 6.4: Mixture fraction-progress variable correlation in a statistically-stationary autoignitive lifted ethylene-air slot jet direct numerical simulation. The solid line is the isocontour of stoichiometric mean mixture fraction (Matheson, 2016, PhD thesis).

6.2 Vapour penetration in non-reacting flow

Before investigating the performance of the combustion modelling, the spray penetration predictions are compared with the experimental data in order to ensure that the underlying flow solution is of acceptable accuracy. The default values in the break up models were found to give satisfactory agreement as observed in Fig. 6.5. For shorter dwell time the error increases and fine tuning of the spray constants for each case might

potentially lead to better agreement, but this is not done here. It was observed that the shorter injection case resulted in faster penetration. This observation is explained by the fact that the main injection sees less resistance as it travels closely in the wake of the pilot injection, and rapidly catches the pilot injection. The combined main and pilot injection travels faster than pilot injection does independent of the main injection. This effect is illustrated in Figs. 6.6 and 6.7 that show the mixture fraction from the second injection ($\widetilde{\xi_2}$) catching that from the pilot in case B1. This observation is in agreement with previous observations by (Skeen, Manin, and Pickett, 2015), who studied injections with equal duration and suggested that the main injection sees a lower pressure in the wake of the pilot injection. The CFD however shows that differences in thermodynamic pressure are very small between case B1 and B3, and it may be more useful to explain the catch up effect in terms of the higher axial velocity that the main injection sees, due to the presence of the wake behind the pilot injection.

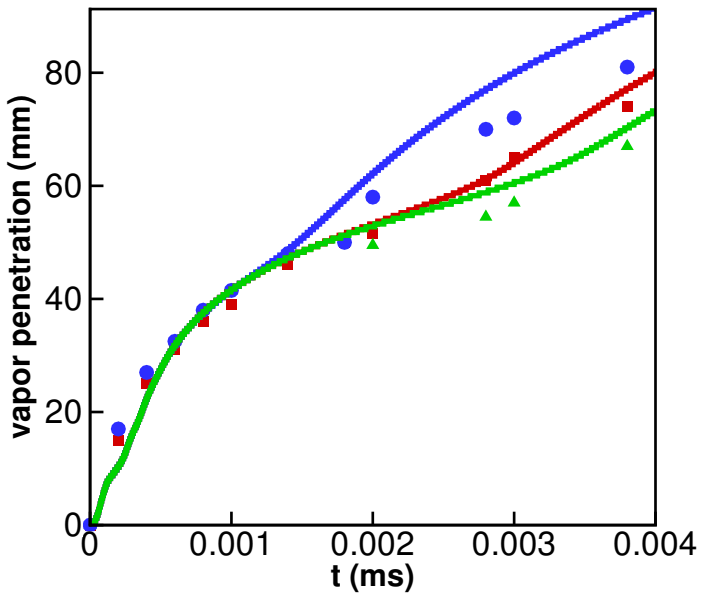

Figure 6.5: Vapour penetration versus time for several injection strategies. Symbols : experiment, solid lines : simulation. A1 (blue circles and line) , A2 (red square and line), A3 (green triangle and line)

6.3 Reacting cases

Because ignition delay time has a high sensitivity to temperature, the difference between the nominal bulk temperature and the ambient temperature around the spray

can significantly affect how ignition takes place. In addition, the modelling of n-heptane ignition kinetics is subject to considerable uncertainty. The uncertainty about the initial temperature in the simulations is a common problem and was discussed in previous studies. (Wright, Margari, & al., 2010) found that the ignition delay was significantly influenced by small variations in T_a. Due to these two sources of uncertainty, which both affect ignition timing, the a range of values for ambient temperature between 950 and 1000 K have been compared using the simulations. T_a was then chosen such that the ignition delay time of the pilot injection in the simulation is the closest to the experimental value for the B1 case, while ensuring good agreement of the vapour penetration lengths for the non-reactive cases A1, A2, A3 is retained. For $T_a = 1000$ K, the pilot ignition delay was 0.48 ms, which is too short in comparison with 0.6 ms in the experiment. $T_a = 950$ K gave poor predictions of the vapour penetration lengths when using the values of the spray constants recommended by STAR-CD (STAR-CD, 2004). Ultimately $T_a = 980K$ yielded an ignition delay time of the pilot injection equal to 0.55ms, while giving good prediction of the vapour penetration as observed in Fig. 6.5, and this value is adopted for the simulations presented below.

6.3.1 Ignition delay times

The ignition time for the main injection reported for the simulations was found from the time when the value of the $\widetilde{Y_{OH}}$ exceeded 1.10^{-4} in the region containing fuel from the second injection, whereas the experimental value is determined from the radially-averaged value of the luminosity. The ignition delay time of the pilot and main injection are reported in table 6.3. The latter was the elapsed time from the start of the main injection. The ignition delay for the main injection was generally shorter than for the pilot injection due to heat and mass transfer from the remains of the pilot flame accelerating ignition. The presence of additional heat, combustion products and intermediate species is expected to both accelerate ignition and potentially flame propagation after ignition. The effect of the pilot kernel reduces as the dwell time increases since the concentration of products and intermediate species consequently reduces. Longer ignition time of the pilot injection would have resulted in a longer ignition time of the main ignition, as the ignition location of the main ignition would have been located further downstream. Note that for the DCMC(+) and DCMC(0) the ignition delay time of the main injection occurs following the injection as a flame attached to the nozzle was observed.

Table 6.3: Ignition delay times for the case B1 and B3

	Short dwell time B1	Long dwell time B3
Exp	Pilot : 0.6 ms Main : 0.35-0.525 ms	Pilot : 0.6 ms Main : 0.6-0.66 ms
Simulation	Pilot : 0.55 ms (-), 0.53 (+), 0.555 (0) Main : 0.13 ms (-), 0 ms (+), 0 ms (0)	Pilot : 0.55 ms (-), 0.53 (+), 0.555 (0) Main : 0.41 ms (-), 0 ms (+), 0 ms (0)

6.3.2 Temporal evolution of the split-injection combustion process

The temporal evolution of the combustion event is shown in contour plots of $\widetilde{\xi_1}$, $\widetilde{\xi_2}$, $\widetilde{c}$, T for cases B1 and B3 for the DCMC(-) in Figs. 6.6-6.13 with iso-lines of $\widetilde{\xi_{st}}$ (dashed), $\widetilde{\xi_{1,st}}$ (dashed-dot) $\widetilde{\xi_{2,st}}$ (solid). The combustion process in both cases is seen to begin with ignition of the pilot fuel, resulting in values of progress variable close to unity at the tip of the fuel jet at around 0.55 ms. The mean temperature remains low however because the most reacted mixture is on the rich side of the stoichiometric mean mixture fraction. The head of the pilot injection forms a mushroom-shaped vortex ring structure which propagates along the axis of the injector. The injection duration of the pilot injection is sufficient for the jet to leave behind a wake, that contains fuel-rich mixture. By 0.75 ms, combustion has propagated back to the tail of the pilot jet, and through mixture fraction space across the stoichiometric value, resulting in mixture temperatures close to the temperature of stoichiometric burned mixture. The flame base propagates back to around 20 mm from the fuel nozzle, which compares with a lift off length of approximately 30 mm in the experimental observations. By 1.50 ms, the main fuel injection in the short dwell B1 case begins to interact visibly with the tail of the pilot injection, pushing the reacting pilot fuel radially outwards so that the main fuel jet is enveloped by reacting mixture. In neither the short dwell B1 or long dwell B3 case does the main injection jet develop the mushroom-shaped leading vortex ring structure, presumably on account of the main jet fluid seeing the wake of the pilot injection rather than running in to fluid with no mean velocity. After the main fuel jet comes into contact with the unity-progress variable residual fluid from the pilot injection, a diffusion/edge flame front is established rapidly, which propagates upstream approximately along the mean stoichiometric iso-line, stabilising at a lift-off length of around 20 mm until the end of the main fuel injection.

Comparing the plots of mean progress variable and the mean temperature for cases B1 and B3 shows that although the dwell period in B3 is sufficient for the

unconditional mean temperature to drop before arrival of the main fuel jet, the mean progress variable remains close to unity. The drop in temperature is therefore because the mixture becomes lean, rather than because products are convected away. This explains why fuel from the main injection is ignited so rapidly, suggesting that what (Cung & al., 2015) call the *ignition delay* of the main injection is not an ignition delay in the sense of an autoignition event. Rather, it is a delay associated with the time for the evaporation of fuel from the main fuel injection and for convection of that vapour to the region where it interacts with the residual gas from the pilot fuel combustion, and followed by, perhaps a much smaller delay associated with turbulent mixing with the residual pilot fluid and ignition. If this physical description is a correct explanation for the ignition delay of the main fuel jet, then the predicted value of the main ignition delay will be sensitive to the predicted location of the residual gas from the pilot fuel combustion. The DCMC modelling presented here has a tendency to under-predict the lift-off length, and a consequence of this is that the convection and mixing time delays before the main injection interacts with the pilot fuel residuals is similarly underpredicted – providing one reason for the underprediction of the main injection delay time in Table 6.3.

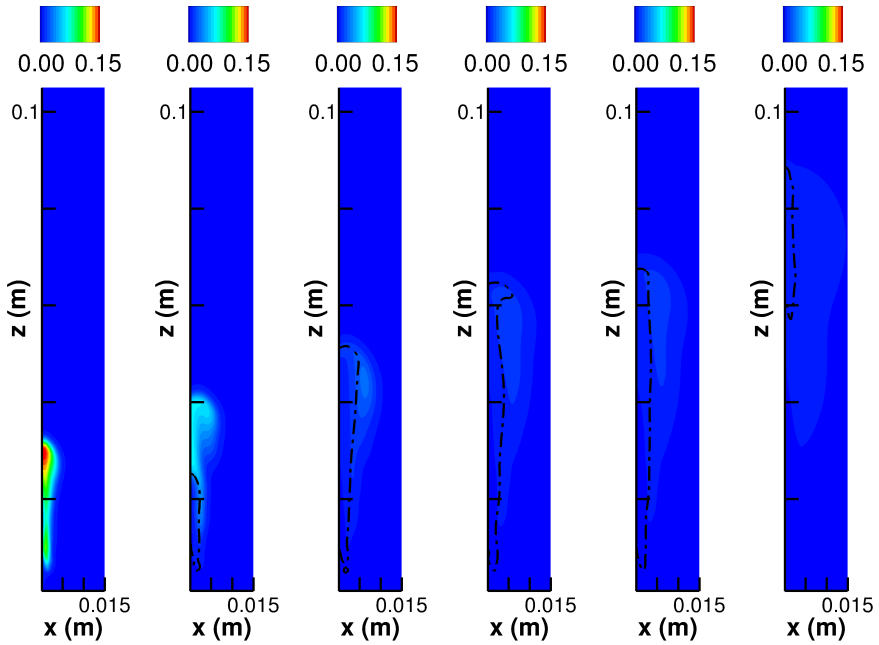

Figure 6.6: Contour plots of $\widetilde{\xi_1}$ at time $t = 0.55ms$, $t = 0.95ms$, $t = 1.50ms$, $t = 2.10ms$, $t = 2.30ms$, $t = 3.50ms$, solid line : $\xi_{2,st}$ with $t = 0ms$ corresponding to the start of the pilot injection. Short injection case B1

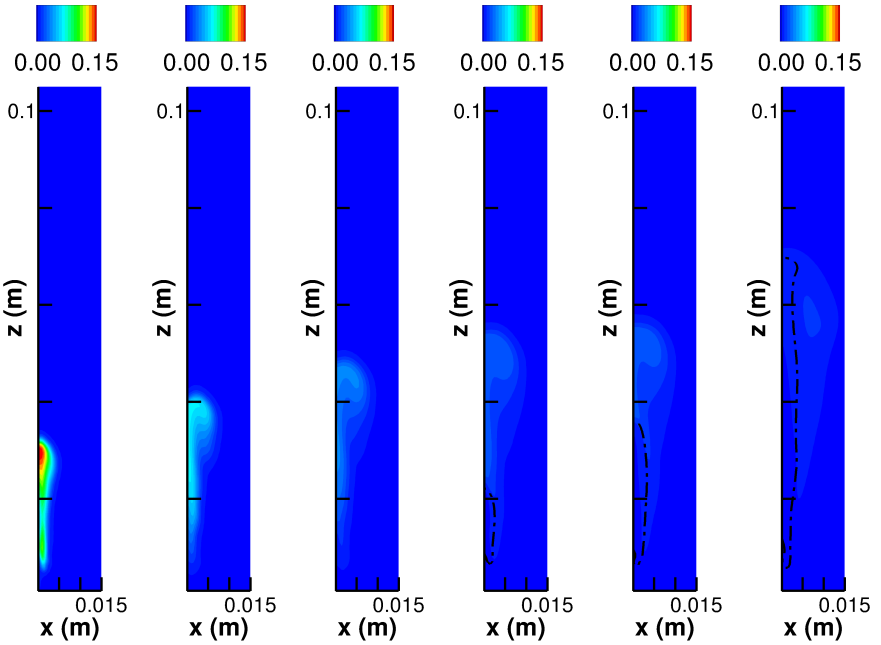

Figure 6.7: Contour plots of $\widetilde{\xi_1}$ at time $t = 0.55ms$, $t = 0.95ms$, $t = 1.50ms$, $t = 2.10ms$, $t = 2.30ms$, $t = 3.50ms$, solid line : $\xi_{2,st}$, solid line : ξ_{st} with $t = 0ms$ corresponding to the start of the pilot injection. Long injection case B3

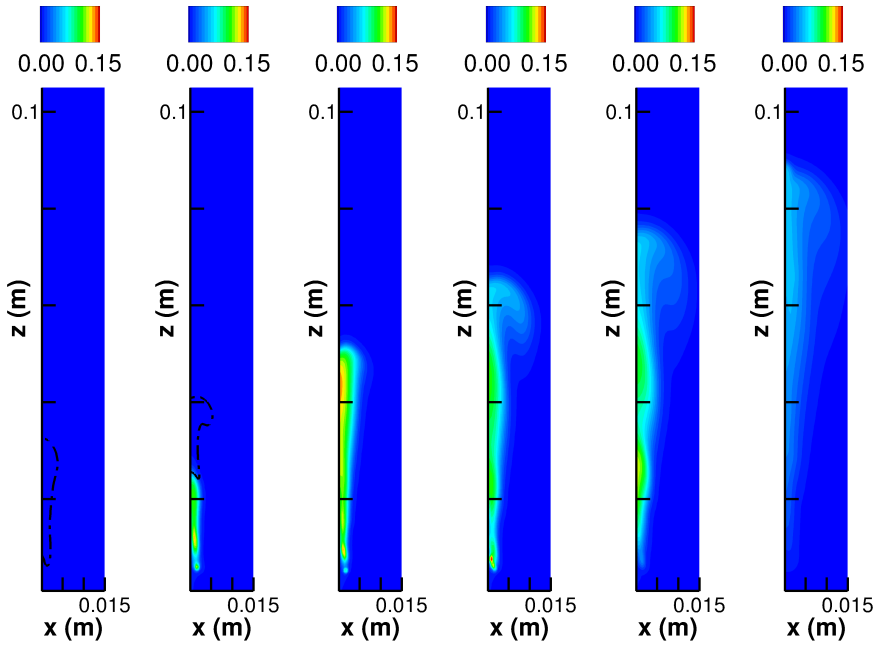

Figure 6.8: Contour plots of $\widetilde{\xi_2}$ at time $t = 0.55ms$, $t = 0.95ms$, $t = 1.50ms$, $t = 2.10ms$, $t = 2.30ms$, $t = 3.50ms$, dashed-dot : $\xi_{1,st}$ with $t = 0ms$ corresponding to the start of the pilot injection. Short injection case B1

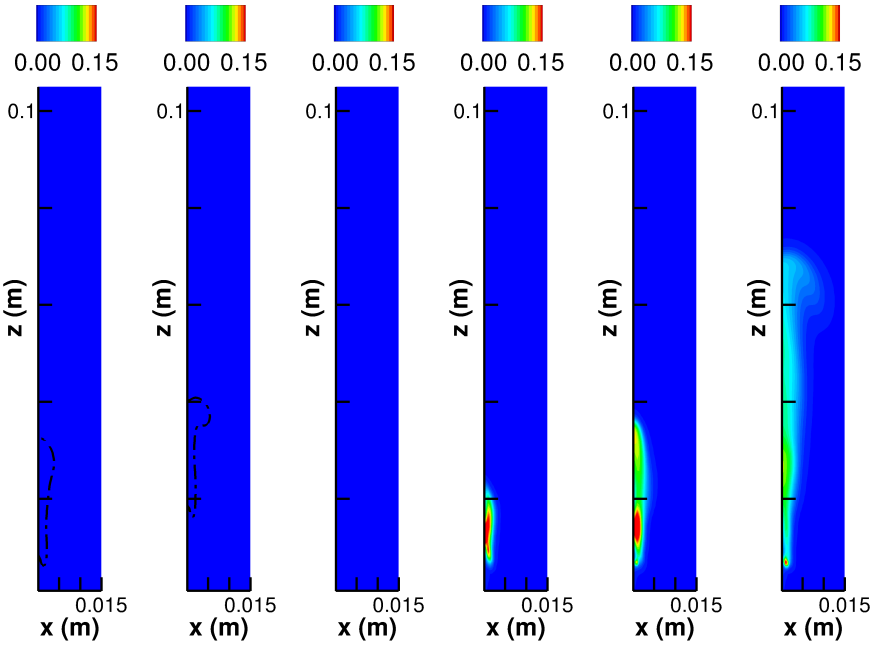

Figure 6.9: Contour plots of $\widetilde{\xi_2}$ at time $t = 0.55ms$, $t = 0.95ms$, $t = 1.50ms$, $t = 2.10ms$, $t = 2.30ms$, $t = 3.50ms$, solid line : $\xi_{2,st}$, solid line : ξ_{st} with $t = 0ms$ corresponding to the start of the pilot injection. Long injection case B3

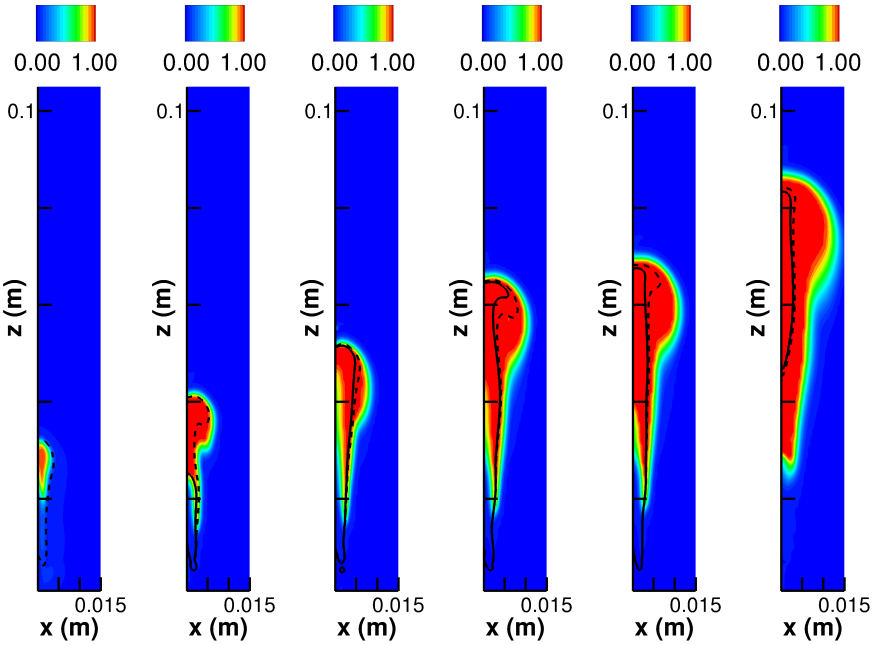

Figure 6.10: Contour plots of $\widetilde{c}$ at time $t = 0.55ms$, $t = 0.95ms$, $t = 1.50ms$, $t = 2.10ms$, $t = 2.30ms$, $t = 3.50ms$, solid line : $\xi_{2,st}$, solid line : ξ_{st} with $t = 0ms$ corresponding to the start of the pilot injection. Short injection case B1

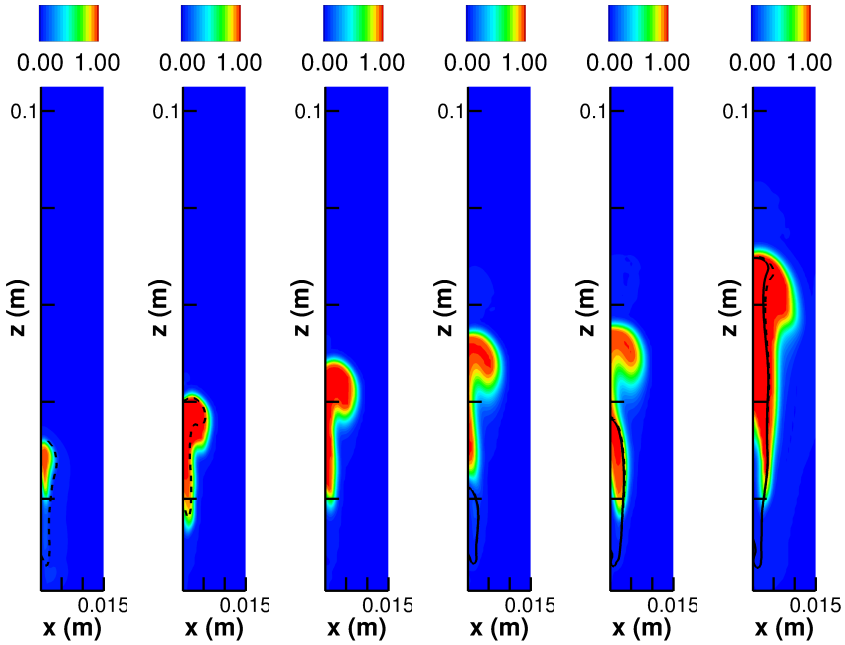

Figure 6.11: Contour plots of $\widetilde{c}$ at time $t = 0.55ms$, $t = 0.95ms$, $t = 1.50ms$, $t = 2.10ms$, $t = 2.30ms$, $t = 3.50ms$, solid line : $\xi_{2,st}$, solid line : ξ_{st} with $t = 0ms$ corresponding to the start of the pilot injection. Long injection case B3

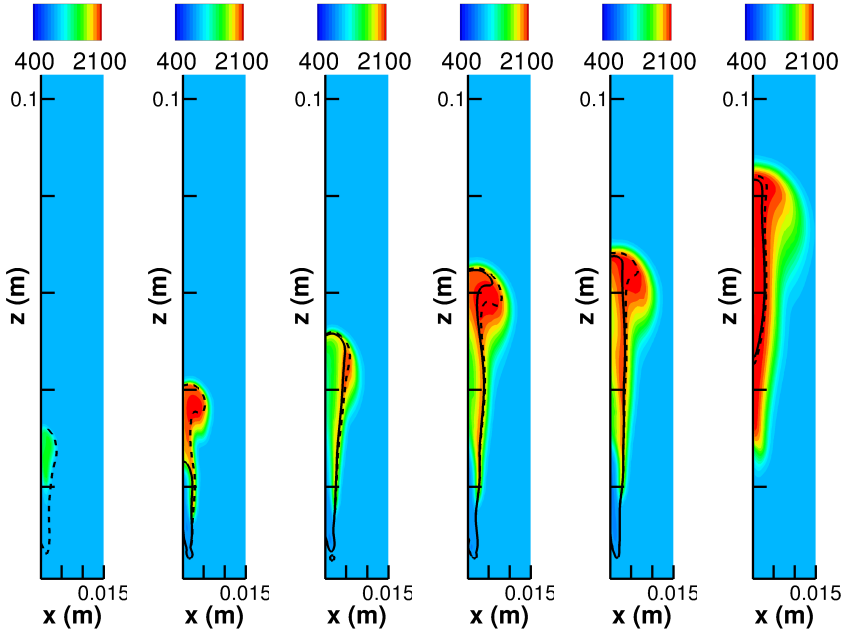

Figure 6.12: Contour plots of $\widetilde{T}$ at time $t = 0.55ms$, $t = 0.95ms$, $t = 1.50ms$, $t = 2.10ms$, $t = 2.30ms$, $t = 3.50ms$, solid line : $\xi_{2,st}$, solid line : ξ_{st} with $t = 0ms$ corresponding to the start of the pilot injection. Short injection case B1

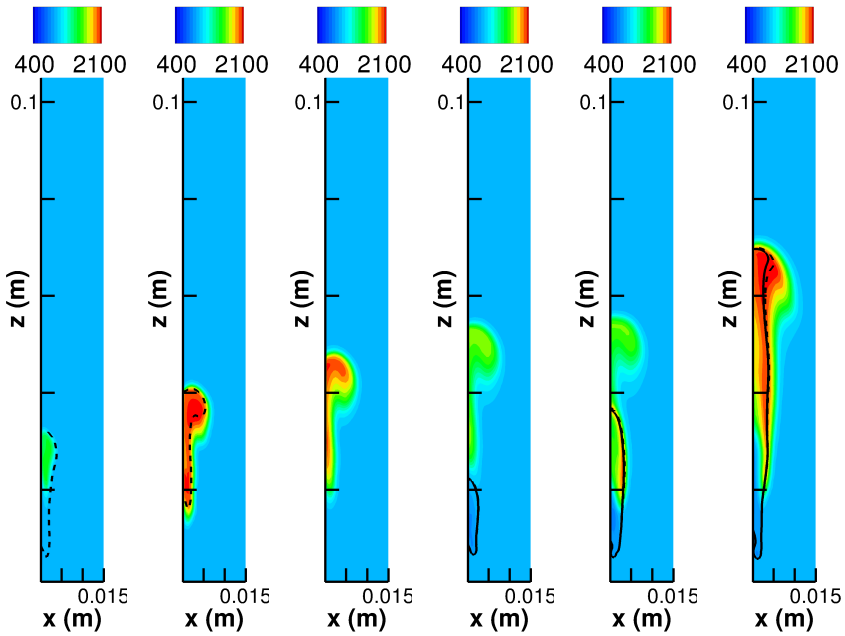

Figure 6.13: Contour plots of $\widetilde{T}$ at time $t = 0.55ms$, $t = 0.95ms$, $t = 1.50ms$, $t = 2.10ms$, $t = 2.30ms$, $t = 3.50ms$, solid line : $\xi_{2,st}$, solid line : ξ_{st} with $t = 0ms$ corresponding to the start of the pilot injection. Long injection case B3

6.4 Conclusion

The mixture fraction–progress variable DCMC implementation developed in this thesis has been applied to simulation of split-injection in a high pressure combustion vessel. The predictions show the same trends as the experimental observations, however ignition delays and lift off lengths agree with the measurements only approximately. Reasons for the discrepancies can include the uncertainty in the chemical modelling as well as in the ambient temperature surrounding the spray in the experiment. The modelling of conditional cross-scalar dissipation rate is also found to have a significant influence on the flame evolution, with the limiting cases of modelling corresponding to zero correlation or unity correlation between mixture fraction and progress variable giving unrealistic predictions. Conditional cross-dissipation rate modelling corresponding to negative unity correlation gives reasonable predictions, and an argument for why negative mixture fraction–progress variable correlation is expected to be dominant in autoignitive lifted jet flames involving multiple fuel injections is presented. Other aspects of modelling uncertainty with regard to conditional dissipation rates, presumed joint mixture fraction-progress variable probability density functions and first order source term closures will also contribute to the model error, and further development of models suitable for spray autoignition cases would be beneficial. Not withstanding the imperfect predictions, the ability of the zero-dimensional DCMC to describe the whole split-injection process and to provide new insight into the mechanisms involved is encouraging: this implies that only a few DCMC control volumes may be needed in order to model a wide range of flows involving very complex physics, such as split-injection, and the DCMC approach is therefore recommended for further development.

Chapter 7

Conclusions

The aim of this thesis was to investigate the modelling of turbulent autoignition in systems with multiple streams. Such processes are expected in burners with split-fuel injection and/or EGR techniques which allow cleaner emissions. In the context of split-fuel injection the models developed during the last decade using the flamelet framework has been successfully applied in engine-like conditions for restricted injection strategies. With the capabilities of the current injectors an accurate and fast general model for any injection time and any numbers of injection is still required. The double conditional moment closure (DCMC) approach is developed in this thesis, and its performance assessed by analysis of direct numerical simulations (DNS) and through validation against laboratory measurements.

The formulation of the DCMC approach is extended to accommodate a general set of conditioning variables in Chapter 3, and numerical approaches are devised for coupling the solution of the DCMC with computational fluid dynamics (CFD) simulations of engine-relevant flows. The choice of the most suitable conditioning variables is investigated in Chapter 4 through analysis of DNS data of a configuration involving up to three separate fuel injections. In the case with a single injection, fluctuations around the mixture fraction-conditioned mean arise due to variation in mixture fraction dissipation rate affecting the progress of ignition differently at different points. In cases with multiple injections, the repeated addition of unreacted fuel also adds to fluctuations around the conditional mean. The high level of conditional fluctuations lead to large errors when employing singly-conditioned first-order conditional moment closure.

Alternative doubly conditional moment closure approaches are tested using two different approaches. First, in an a priori approach, the unconditional mean reaction rates are modelled using the first order closure using conditional averages taken from

the DNS solution. Second, in an a posteriori approach, the transport equations for the double conditional moments are solved using the first order closure, and the results compared to the DNS. The a priori analysis indicates that single conditioned first order closure gives extremely poor agreement with the DNS, and that for multiple injection cases, conditioning on two mixture fractions provides little improvement. Reasonable agreement is given by double conditioning on mixture fraction and a progress variable. Sensible enthalpy serves as a superior progress variable than water vapour in this instance, however this result may be chemistry specific, and other combinations of species mass fractions may give superior resolution of progress variable space. Results of the a posteriori tests indicate that the DCMC may in practice be more tolerant of the choice of conditioning variables than indicated by the a priori analysis. The encouraging results obtained with the mixture fraction and water vapour in the a priori analysis motivated their study through the a posteriori analysis. Ignition was better captured, however, discrepancies were observed following combustion. This was attributed to the one-way coupling used rather to the inability of the conditioning parameters to capture combustion. The feasibility of the zero-dimensional DCMC approach for practical predictive design calculations is then assessed further through simulations of spray ignition in constant volume research vessels in Chapters 5 and 6.

In Chapter 5 a spray of n-heptane at diesel engine conditions was successfully simulated by coupling the zero-dimensional first order double conditional moment closure (0D-DCMC) with a commercial CFD code using the coupling approach and modelling developed in this thesis. An efficient Operator Splitting method was developed which resulted in increased accuracy and a significant improvement of the CPU time. Correct trends of the lift-off length and ignition delay was obtained. Indeed, the model was found to predict a lift-off length unlike the 0D-CMC model. Overestimation was observed in comparison with the well established 3D-CMC which was attributed to simplified models employed and lack of spray source terms. Furthermore, the flame propagation downstream was seen to preferentially increase along the centreline, which was again attributed to the simplified modelling. In comparison with the 3D-CMC, the 0D-DCMC model is a promising approach which is expected to be substantially faster than the 3D-CMC approach in most problems of engineering interest.

In Chapter 6 the mixture fraction–progress variable DCMC implementation developed in this thesis has been applied to simulation of split-injection in a high pressure combustion vessel. The predictions show the same trends as the experimental observations, however ignition delays and lift off lengths agree with the measurements only approximately. Reasons for the discrepancies include the uncertainty in the chem-

ical modelling as well as in the ambient temperature surrounding the spray in the experiment. The modelling of conditional cross-scalar dissipation rate is also found to have a significant influence on the flame evolution, with the limiting cases of modelling corresponding to zero correlation or unity correlation between mixture fraction and progress variable giving unrealistic predictions. Conditional cross-dissipation rate modelling corresponding to negative unity correlation gives reasonable predictions, and an argument for why negative mixture fraction–progress variable correlation is expected to be dominant in autoignitive lifted jet flames involving multiple fuel injections is presented. Other aspects of modelling uncertainty with regard to conditional dissipation rates, presumed joint mixture fraction-progress variable probability density functions and first order source term closures will also contribute to the model error, and further development of models suitable for spray autoignition cases would be beneficial. Not withstanding the imperfect predictions, the ability of the zero-dimensional DCMC to describe the whole split-injection process and to provide new insight into the mechanisms involved is encouraging: this implies that only a few DCMC control volumes may be needed in order to model a wide range of flows involving very complex physics, of which split-injection is just one example, and the DCMC approach is therefore recommended for further development.

Appendices

Appendix A

The temporal normalised progress variable c_t

The advantages and disadvantages of using a temporal normalised progress variable is discuss in the following. Minimum and maximum values are defined for each time denoted respectively by $Y_{c,min}(\xi(x_i,t),t)$ and $Y_{c,max}(\xi(x_i,t),t)$. Using the latter parameters the temporal normalised progress variable reads:

$$c_t(x_i,t) = \frac{Y_c(x_i,t) - Y_{c,min}(\xi(x_i,t),t)}{Y_{c,max}(\xi(x_i,t),t) - Y_{c,min}(\xi(x_i,t),t)} \tag{A.1}$$

The time dependency on ξ accounts for its own variation in time but not the variation of Y_c. As observed in Fig. 3.1 in a turbulent autoigniting case Y_c (there chosen as Y_{H_2O}) is a strong function of time as combustion proceeds. The temporal normalised progress variable $c_t(x_i,t)$ allows the realisation of a unit square domain at each time as illustrated in fig. A.1 for the mixture fraction and the temporal normalised progress variable sample space variables respectively noted η and ζ'' (The double prime is removed in the following for clarity). The boundary conditions are applied on a non-moving mesh, where the terms accounting for the moving boundaries of the domain are included in the transport equation of c_t as presented in the following. The transformed space includes singularites on the axis $\eta = 0$ and $\eta = 1$.

The introduction of c_t is motivated by the necessity of easily specifying the boundary conditions on the DCMC domain. However, c_t introduces further complexity in the DCMC since unclosed terms function of c_t have to be adressed for which modelling are not available. The modelling of the terms function of c_t (pdf, dissipation rates) have not been adressed.
Instead, the well-established normalised progress variable c (2.48) has been employed

throughout the thesis.

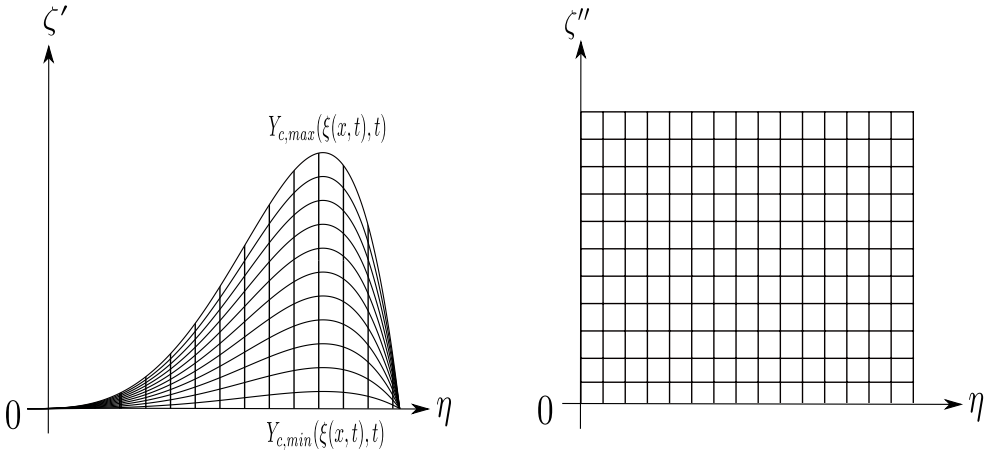

Figure A.1: Illustration of ξ and Y_c sample space variable domain (left) and ξ and c_t (right)

Its transport equation reads :

$$\begin{aligned}\underbrace{\frac{\partial \rho c_t}{\partial t} + \frac{\partial \rho u_i c_t}{\partial x_i}}_{\text{Mat. derivative}} &= \underbrace{\frac{\partial}{\partial x_i}\left(\rho D \frac{\partial c_t}{\partial x_i}\right)}_{\text{Diffusion}} + \underbrace{\frac{\dot{\omega_{Y_c}}}{Y_{c,\Delta}}}_{\text{reaction}} + \underbrace{\rho \frac{2N_{\xi,c_t}}{Y_{c,\Delta}} \frac{\partial Y_{c,\Delta}}{\partial \xi}}_{T_1} \\ &+ \underbrace{\rho \frac{N_\xi}{Y_{c,\Delta}}\left(c_t \frac{\partial^2 Y_{c,\Delta}}{\partial \xi^2} + \frac{\partial^2 Y_{c,min}}{\partial \xi^2}\right)}_{T_2} - \underbrace{\frac{\rho}{Y_{c,\Delta}}\left(c_t \frac{\partial Y_{c,\Delta}}{\partial t} + \frac{\partial Y_{c,min}}{\partial t}\right)}_{T_3}\end{aligned} \tag{A.2}$$

with the dissipation rates :

$$N_\xi = D\left(\frac{\partial \xi}{\partial x_i}\right)^2 \qquad N_{\xi,c_t} = D\frac{\partial \xi}{\partial x_i}\frac{\partial c_t}{\partial x_i} \qquad N_{c_t} = D\left(\frac{\partial c_t}{\partial x_i}\right)^2 \tag{A.3}$$

The additional term T_3 is present in the equation accounting for the moving boundaries. The DCMC equation reads :

$$
\begin{aligned}
\frac{\partial Q_k}{\partial t} + \langle u_i|\eta,\zeta\rangle \frac{\partial Q_k}{\partial x_i} = & \underbrace{\langle N_\xi|\eta,\zeta\rangle \left[\frac{\partial^2 Q_k}{\partial \eta^2} - \underbrace{\frac{1}{Y_{c,\Delta}} \left(\zeta \frac{\partial^2 Y_{c,\Delta}}{\partial \eta^2} + \frac{\partial^2 Y_{c,min}}{\partial \eta^2} \right) \frac{\partial Q_k}{\partial \zeta}}_{QT_1} \right]}_{QT_{1f}} \\
& + \underbrace{2 \langle N_{\xi,c_t}|\eta,\zeta\rangle \left(\frac{\partial^2 Q_k}{\partial \eta \partial \zeta} - \underbrace{\frac{1}{Y_{c,\Delta}} \left(\frac{\partial Y_{c,\Delta}}{\partial \eta} \right) \frac{\partial Q_k}{\partial \zeta}}_{QT_2} \right)}_{QT_{2f}} \\
& + \underbrace{\langle N_{c_t}|\eta,\zeta\rangle \frac{\partial^2 Q_k}{\partial \zeta^2}}_{QT_{3f}} + \underbrace{\frac{1}{Y_{c,\Delta}} \left(\zeta \frac{\partial Y_{c,\Delta}}{\partial t} + \frac{\partial Y_{c,min}}{\partial t} \right) \frac{\partial Q_k}{\partial \zeta}}_{QT_{4f}} + \underbrace{\frac{\langle \dot{\omega_k}|\eta,\zeta\rangle}{\langle \rho|\eta,\zeta\rangle}}_{QT_{5f}} \\
& - \underbrace{\frac{\langle \dot{\omega_{Y_c}}|\eta,\zeta\rangle}{Y_{c,\Delta} \langle \rho|\eta,\zeta\rangle} \frac{\partial Q_k}{\partial \zeta}}_{QT_{6f}} + \frac{e_{y_k''}}{\langle \rho|\eta,\zeta\rangle} + \frac{e_{Q_k}}{\langle \rho|\eta,\zeta\rangle}
\end{aligned}
\tag{A.4}
$$

with

$$
\begin{aligned}
e_{Q_k} &= \left\langle \rho D \frac{\partial \xi}{\partial x_i} \frac{\partial}{\partial x_i} \left(\frac{\partial Q_k}{\partial \eta} \right) + \rho D \frac{\partial c_t}{\partial x_i} \frac{\partial}{\partial x_i} \left(\frac{\partial Q_k}{\partial \zeta} \right) \middle| \eta, \zeta \right\rangle \\
&+ \frac{\partial}{\partial x_i} \left(\rho D \frac{\partial Q_k}{\partial x_i} \right) \\
e_{y_k''} &= \left\langle \rho \frac{\partial y_k''}{\partial t} + \rho u_i \frac{\partial y_k''}{\partial x_i} - \frac{\partial}{\partial x_i} \left(\rho D \frac{\partial y_k''}{\partial x_i} \right) \middle| \eta, \zeta \right\rangle
\end{aligned}
\tag{A.5}
$$

Again the term QT_{4f} accounts for the moving boundary. Similarly the mean transport equations read :

$$
\begin{aligned}
\frac{\partial \bar{\rho} \widetilde{c}}{\partial t} + \frac{\partial \bar{\rho} \widetilde{u_i} \widetilde{c}}{\partial x_i} = & \frac{\partial}{\partial x_i} \left(\overline{\rho D \frac{\partial c}{\partial x_i}} - \bar{\rho} \widetilde{u_i'' c''} \right) + \underbrace{\frac{\overline{\dot{\omega_{Y_c}}}}{Y_{c,\Delta}}}_{T_1} + \underbrace{\overline{\rho \frac{2 N_{\xi,c}}{Y_{c,\Delta}} \frac{\partial Y_{c,\Delta}}{\partial \xi}}}_{T_2} \\
& + \underbrace{\overline{\rho \frac{N_\xi}{Y_{c,\Delta}} \left(c \frac{\partial^2 Y_{c,\Delta}}{\partial \xi^2} + \frac{\partial^2 Y_{c,u}}{\partial \xi^2} \right)}}_{T_3} - \underbrace{\overline{\frac{\rho}{Y_{c,\Delta}} \left(c \frac{\partial Y_{c,\Delta}}{\partial t} + \frac{\partial Y_{c,min}}{\partial t} \right)}}_{T_4}
\end{aligned}
\tag{A.6}
$$

The variance equation reads :

$$\begin{aligned}\frac{\partial\bar{\rho}\widetilde{c''^2}}{\partial t}+\frac{\partial\bar{\rho}\widetilde{u}_i\widetilde{c''^2}}{\partial x_i}&=\frac{\partial}{\partial x_i}\left(\overline{\rho D\frac{\partial c''^2}{\partial x_i}}\right)-\frac{\partial}{\partial x_i}\left(\bar{\rho}\widetilde{u_i''c''^2}\right)\\&-2\bar{\rho}\widetilde{u_i''c''}\frac{\widetilde{\partial}c}{\partial x_i}+\underbrace{\overline{2c''\frac{\dot{\omega_{Y_c}}}{Y_{c,\Delta}}}}_{T_1}-2\bar{\rho}D\widetilde{\frac{\partial c''}{\partial x_i}}^2\\&+\underbrace{\overline{4\rho c''\frac{N_{\xi,c}}{Y_{c,\Delta}}\frac{\partial Y_{c,\Delta}}{\partial\xi}}}_{T_2}+\underbrace{\overline{2\rho c''\frac{N_\xi}{Y_{c,\Delta}}\left(c\frac{\partial^2Y_{c,\Delta}}{\partial\xi^2}+\frac{\partial^2Y_{c,u}}{\partial\xi^2}\right)}}_{T_3}\\&-\underbrace{\overline{2c''\frac{\rho}{Y_{c,\Delta}}\left(c\frac{\partial Y_{c,\Delta}}{\partial t}+\frac{\partial Y_{c,min}}{\partial t}\right)}}_{T_4}\end{aligned}\tag{A.7}$$

$$\begin{aligned}\frac{\partial\bar{\rho}\widetilde{\xi''c''}}{\partial t}+\frac{\partial\bar{\rho}\widetilde{u}_i\widetilde{\xi''c''}}{\partial x_i}&=\frac{\partial}{\partial x_i}\left(\overline{\rho D\frac{\partial\xi''c''}{\partial x_i}}\right)-\frac{\partial}{\partial x_i}\left(\bar{\rho}\widetilde{u_i''\xi''c''}\right)\\&-\bar{\rho}\widetilde{u_i''\xi''}\frac{\widetilde{\partial}c}{\partial x_i}-\bar{\rho}\widetilde{u_i''c''}\frac{\widetilde{\partial\xi}}{\partial x_i}+\underbrace{\overline{\xi''\frac{\dot{\omega_{Y_c}}}{Y_{c,\Delta}}}}_{T_1}-2\bar{\rho}D\widetilde{\frac{\partial\xi''c''}{\partial x_i}}\\&+\underbrace{\overline{2\rho\xi''\frac{N_{\xi,c}}{Y_{c,\Delta}}\frac{\partial Y_{c,\Delta}}{\partial\xi}}}_{T_2}+\underbrace{\overline{\rho\xi''\frac{N_\xi}{Y_{c,\Delta}}\left(c\frac{\partial^2Y_{c,\Delta}}{\partial\xi^2}+\frac{\partial^2Y_{c,u}}{\partial\xi^2}\right)}}_{T_3}\\&-\underbrace{\overline{\xi''\frac{\rho}{Y_{c,\Delta}}\left(c\frac{\partial Y_{c,\Delta}}{\partial t}+\frac{\partial Y_{c,min}}{\partial t}\right)}}_{T_4}\end{aligned}\tag{A.8}$$

The temporal terms can be obtained after expressing the DCMC equation at $\zeta=1$ and $\zeta=0$

$$\frac{\partial Y_{c,max}}{\partial t}=\langle N_\xi|\eta,\zeta=1\rangle\frac{\partial^2Y_{c,max}}{\partial\eta^2}+\frac{\langle\dot{\omega_{Y_c}}|\eta,\zeta=1\rangle}{\langle\rho|\eta,\zeta\rangle}\tag{A.9}$$

$$\frac{\partial Y_{c,min}}{\partial t}=\langle N_\xi|\eta,\zeta=0\rangle\frac{\partial^2Y_{c,min}}{\partial\eta^2}\tag{A.10}$$

Since linear mixing is used to initialise the composition eq. A.10 reduces to :

$$\frac{\partial Y_{c,min}}{\partial t}=0\tag{A.11}$$

Therefore the following term appearing in the above equations reduces to:

$$\zeta\frac{\partial Y_{c,\Delta}}{\partial t}+\frac{\partial Y_{c,min}}{\partial t}=\zeta\left(\langle N_\xi|\eta,\zeta=1\rangle\frac{\partial^2Y_{c,max}}{\partial\eta^2}+\frac{\langle\dot{\omega_{Y_c}}|\eta,\zeta=1\rangle}{\langle\rho|\eta,\zeta\rangle}\right)\tag{A.12}$$

Appendix B

Derivation of the DCMC temperature equation

In the following the DCMC temperature equation is derived for the mixture fraction and the progress variable. The temperature equation can be written for unity Lewis number, equal diffusivity, the viscous term neglected and the spatial variation of the pressure are neglected (Low Mach number approximation) such as :

$$\rho cp\frac{\partial T}{\partial t} + \rho cpu_i\frac{\partial T}{\partial x_i} = \frac{\partial}{\partial x_i}\left(\rho cpD\frac{\partial T}{\partial x_i}\right) + \sum_{k=1}^{N}\rho cp_k D\frac{\partial Y_k}{\partial x_i}\frac{\partial T}{\partial x_i} + \frac{\partial p}{\partial t} - \sum_{k=1}^{N}h_k\dot{\omega}_k \quad \text{(B.1)}$$

Using the decomposition approach:

$$T(x_i,t) = Q_T(\xi(x_i,t), c(x_i,t), x_i, t) + T''(x_i,t)$$

$$\frac{\partial T}{\partial t} = \frac{\partial Q_T}{\partial t} + \frac{\partial Q_T}{\partial \eta}\frac{\partial \xi}{\partial t} + \frac{\partial Q_T}{\partial \zeta}\frac{\partial c}{\partial t} + \frac{\partial T''}{\partial t}$$

$$\frac{\partial T}{\partial x_i} = \frac{\partial Q_T}{\partial x_i} + \frac{\partial Q_T}{\partial \eta}\frac{\partial \xi}{\partial x_i} + \frac{\partial Q_T}{\partial \zeta}\frac{\partial c}{\partial x_i} + \frac{\partial T''}{\partial x_i}$$

$$\begin{aligned}
&\frac{\partial}{\partial x_i}\left(\rho cpD\frac{\partial T}{\partial x_i}\right) = cp\frac{\partial}{\partial x_i}\left(\rho D\frac{\partial Q_T}{\partial x_i}\right) + \frac{\partial cp}{\partial x_i}\left(\rho D\frac{\partial Q_T}{\partial x_i}\right) \\
&+ \left[cp\frac{\partial}{\partial x_i}\left(\rho D\frac{\partial \xi}{\partial x_i}\right) + \frac{\partial cp}{\partial x_i}\left(\rho D\frac{\partial \xi}{\partial x_i}\right)\right]\frac{\partial Q_T}{\partial \eta} \\
&+ \rho cpD\frac{\partial \xi}{\partial x_i}\left(\frac{\partial^2 Q_T}{\partial x_i \partial \eta} + \frac{\partial^2 Q_T}{\partial \eta^2}\frac{\partial \xi}{\partial x_i} + \frac{\partial^2 Q_T}{\partial \eta \partial \zeta}\frac{\partial c}{\partial x_i}\right) \\
&+ \left[cp\frac{\partial}{\partial x_i}\left(\rho D\frac{\partial c}{\partial x_i}\right) + \frac{\partial cp}{\partial x_i}\left(\rho D\frac{\partial c}{\partial x_i}\right)\right]\frac{\partial Q_T}{\partial \zeta} \\
&+ \rho cpD\frac{\partial c}{\partial x_i}\left(\frac{\partial^2 Q_T}{\partial x_i \partial \zeta} + \frac{\partial^2 Q_T}{\partial \eta \partial \zeta}\frac{\partial \xi}{\partial x_i} + \frac{\partial^2 Q_T}{\partial \zeta^2}\frac{\partial c}{\partial x_i}\right) \\
&+ cp\frac{\partial}{\partial x_i}\left(\rho D\frac{\partial T''}{\partial x_i}\right) + \frac{\partial cp}{\partial x_i}\left(\rho D\frac{\partial T''}{\partial x_i}\right)
\end{aligned} \tag{B.2}$$

Replacing the terms above into equation B.1 yields :

$$
\begin{aligned}
&\rho cp\frac{\partial Q_T}{\partial t} + \rho cp\frac{\partial Q_T}{\partial x_i} - cp\frac{\partial}{\partial x_i}\left(\rho D\frac{\partial Q_T}{\partial x_i}\right) \\
&+ cp\frac{\partial Q_T}{\partial \eta}\left[\rho\frac{\partial \xi}{\partial t} + \rho u_i\frac{\partial \xi}{\partial x_i} - \frac{\partial}{\partial x_i}\left(\rho D\frac{\partial \xi}{\partial x_i}\right)\right] \\
&+ cp\frac{\partial Q_T}{\partial \zeta}\left[\rho\frac{\partial c}{\partial t} + \rho u_i\frac{\partial c}{\partial x_i} - \frac{\partial}{\partial x_i}\left(\rho D\frac{\partial c}{\partial x_i}\right)\right] \\
&= \rho cpD\frac{\partial \xi}{\partial x_i}\frac{\partial^2 Q_T}{\partial x_i \partial \eta} + \rho cpD\frac{\partial c}{\partial x_i}\frac{\partial^2 Q_T}{\partial x_i \partial \zeta} \\
&+ \rho cpN_\xi\frac{\partial^2 Q_T}{\partial \eta^2} + 2\rho cpN_{\xi,c}\frac{\partial^2 Q_T}{\partial \eta \partial \zeta} + \rho cpN_c\frac{\partial^2 Q_T}{\partial \zeta^2} \\
&+ \sum_{k=1}^{N}\rho cp_k D\left(\frac{\partial Q_k}{\partial x_i} + \frac{\partial Q_k}{\partial \eta}\frac{\partial \xi}{\partial x_i} + \frac{\partial Q_k}{\partial \zeta}\frac{\partial c}{\partial x_i} + \frac{\partial y_k''}{\partial x_i}\right) \\
&\times\left(\frac{\partial Q_T}{\partial x_i} + \frac{\partial Q_T}{\partial \eta}\frac{\partial \xi}{\partial x_i} + \frac{\partial Q_T}{\partial \zeta}\frac{\partial c}{\partial x_i} + \frac{\partial T''}{\partial x_i}\right) \\
&+ \rho D\frac{\partial cp}{\partial x_i}\left[\frac{\partial Q_T}{\partial x_i} + \frac{\partial Q_T}{\partial \zeta}\frac{\partial c}{\partial x_i} + \frac{\partial \xi}{\partial x_i}\frac{\partial Q_T}{\partial \eta} + \frac{\partial T''}{\partial x_i}\right] \\
&+ \frac{\partial p}{\partial t} - \sum_{k=1}^{N} h_k\dot{\omega}_k - \rho cp\frac{\partial T''}{\partial t} - \rho cpu_i\frac{\partial T''}{\partial x_i} + cp\frac{\partial}{\partial x_i}\left(\rho D\frac{\partial T''}{\partial x_i}\right)
\end{aligned}
\tag{B.3}
$$

The terms inside the parenthesis in the sixth and seventh line can be developed further, and read :

$$
\begin{aligned}
&\frac{\partial Q_k}{\partial x_i}\left(\frac{\partial Q_T}{\partial x_i} + \frac{\partial Q_T}{\partial \eta}\frac{\partial \xi}{\partial x_i} + \frac{\partial Q_T}{\partial \zeta}\frac{\partial c}{\partial x_i} + \frac{\partial T''}{\partial x_i}\right) \\
&+ \frac{\partial Q_k}{\partial \eta}\frac{\partial \xi}{\partial x_i}\frac{\partial Q_T}{\partial x_i} + \frac{N_\xi}{D}\frac{\partial Q_k}{\partial \eta}\frac{\partial Q_T}{\partial \eta} + \frac{N_{\xi,c}}{D}\frac{\partial Q_k}{\partial \eta}\frac{\partial Q_T}{\partial \zeta} \\
&+ \frac{\partial Q_k}{\partial \zeta}\frac{\partial c}{\partial x_i}\frac{\partial Q_T}{\partial x_i} + \frac{N_{\xi,c}}{D}\frac{\partial Q_k}{\partial \zeta}\frac{\partial Q_T}{\partial \eta} + \frac{N_c}{D}\frac{\partial Q_k}{\partial \zeta}\frac{\partial Q_T}{\partial \zeta} + \frac{\partial Q_k}{\partial \zeta}\frac{\partial c}{\partial x_i}\frac{\partial T''}{\partial x_i} \\
&+ \frac{\partial y_k''}{\partial x_i}\left(\frac{\partial Q_T}{\partial x_i} + \frac{\partial Q_T}{\partial \eta}\frac{\partial \xi}{\partial x_i} + \frac{\partial Q_T}{\partial \zeta}\frac{\partial c}{\partial x_i} + \frac{\partial T''}{\partial x_i}\right)
\end{aligned}
\tag{B.4}
$$

Using the decomposition method on cp allows to developed further the expression in the height line of the eq. B.3:

$$
cp = cp_n(x_i, t, \xi, t) + cp'' \tag{B.5}
$$

with $cp_n = \langle cp|\eta,\zeta\rangle$

$$
\begin{aligned}
&\left(\frac{\partial cp_n}{\partial x_i} + \frac{\partial cp_n}{\partial \eta}\frac{\partial \xi}{\partial x_i} + \frac{\partial cp_n}{\partial \zeta}\frac{\partial c}{\partial x_i} + \frac{cp''}{\partial x_i}\right) \\
&\times \left(\frac{\partial Q_T}{\partial x_i} + \frac{\partial Q_T}{\partial \zeta}\frac{\partial c}{\partial x_i} + \frac{\partial \xi}{\partial x_i}\frac{\partial Q_T}{\partial \eta} + \frac{\partial T''}{\partial x_i}\right) \\
&= \frac{\partial cp_n}{\partial x_i}\left(\frac{\partial Q_T}{\partial x_i} + \frac{\partial Q_T}{\partial \zeta}\frac{\partial c}{\partial x_i} + \frac{\partial \xi}{\partial x_i}\frac{\partial Q_T}{\partial \eta} + \frac{\partial T''}{\partial x_i}\right) + \frac{\partial cp_n}{\partial \eta}\frac{\partial \xi}{\partial x_i}\frac{\partial Q_T}{\partial x_i} \\
&+ N_{\xi,c}\frac{\partial cp_n}{\partial \eta}\frac{\partial Q_T}{\partial \zeta} + N_\xi\frac{\partial cp_n}{\partial \eta}\frac{\partial Q_T}{\partial \eta} + \frac{\partial cp_n}{\partial \eta}\frac{\partial \xi}{\partial x_i}\frac{\partial T''}{\partial x_i} \\
&+ \frac{\partial cp_n}{\partial \zeta}\frac{\partial c}{\partial x_i}\frac{\partial Q_T}{\partial x_i} + N_c\frac{\partial cp_n}{\partial \zeta}\frac{\partial Q_T}{\partial \zeta} + \frac{\partial cp_n}{\partial \zeta}\frac{\partial c}{\partial x_i}\frac{\partial T''}{\partial x_i} + N_{\xi,c}\frac{\partial cp_n}{\partial \zeta}\frac{\partial Q_T}{\partial \eta} \\
&+ \frac{\partial cp''}{\partial x_i}\left(\frac{\partial Q_T}{\partial x_i} + \frac{\partial Q_T}{\partial \zeta}\frac{\partial c}{\partial x_i} + \frac{\partial \xi}{\partial x_i}\frac{\partial Q_T}{\partial \eta} + \frac{\partial T''}{\partial x_i}\right)
\end{aligned}
\tag{B.6}
$$

Replacing relation B.4 and B.6 into equation B.1 yields :

$$
\begin{aligned}
&\rho cp\frac{\partial Q_T}{\partial t} + \rho cpu_i\frac{\partial Q_T}{\partial x_i} - cp\frac{\partial}{\partial x_i}\left(\rho D\frac{\partial Q_T}{\partial x_i}\right)\\
&+ cp\frac{\partial Q_T}{\partial \eta}\left[\rho\frac{\partial \xi}{\partial t} + \rho u_i\frac{\partial \xi}{\partial x_i} - \frac{\partial}{\partial x_i}\left(\rho D\frac{\partial \xi}{\partial x_i}\right)\right]\\
&+ cp\frac{\partial Q_T}{\partial \zeta}\left[\rho\frac{\partial c}{\partial t} + \rho u_i\frac{\partial c}{\partial x_i} - \frac{\partial}{\partial x_i}\left(\rho D\frac{\partial c}{\partial x_i}\right)\right]\\
&= \rho N_\xi\left[cp\frac{\partial^2 Q_T}{\partial \eta^2} + \sum_{k=1}^{N}\frac{\partial Q_k}{\partial \eta}\frac{\partial Q_T}{\partial \eta} + \frac{\partial cp_n}{\partial \eta}\frac{\partial Q_T}{\partial \eta}\right]\\
&+ \rho N_c\left[cp\frac{\partial^2 Q_T}{\partial \zeta^2} + \sum_{k=1}^{N} cp_k\frac{\partial Q_k}{\partial \zeta}\frac{\partial Q_T}{\partial \zeta}\right]\\
&+ \rho 2N_{\xi,c}\left[cp\frac{\partial^2 Q_T}{\partial \eta\partial \zeta} + \sum_{k=1}^{N}\frac{cp_k}{2}\left(\frac{\partial Q_k}{\partial \eta}\frac{\partial Q_T}{\partial \zeta} + \frac{\partial Q_k}{\partial \zeta}\frac{\partial Q_T}{\partial \eta}\right) + \frac{1}{2}\left(\frac{\partial cp_n}{\partial \eta}\frac{\partial Q_T}{\partial \zeta} + \frac{\partial cp_n}{\partial \zeta}\frac{\partial Q_T}{\partial \eta}\right)\right]\\
&+ \rho cpD\frac{\partial \xi}{\partial x_i}\frac{\partial^2 Q_T}{\partial x_i\partial \eta} + \rho cpD\frac{\partial c}{\partial x_i}\frac{\partial^2 Q_T}{\partial x_i\partial \zeta}\\
&- \rho cp\frac{\partial T''}{\partial x_i} - \rho cpu_i\frac{\partial T''}{\partial x_i} + cp\frac{\partial}{\partial x_i}\left(\rho D\frac{\partial T''}{\partial x_i}\right)\\
&+ \left[\rho D\sum_{k=1}^{N} cp_k\left(\frac{\partial Q_k}{\partial x_i} + \frac{\partial y_k''}{\partial x_i}\right)\left(\frac{\partial Q_T}{\partial x_i} + \frac{\partial Q_T}{\partial \zeta}\frac{\partial c}{\partial x_i} + \frac{\partial \xi}{\partial x_i}\frac{\partial Q_T}{\partial \eta} + \frac{\partial T''}{\partial x_i}\right)\right]\\
&+ \left[\rho D\sum_{k=1}^{N} cp_k\left(\frac{\partial Q_T}{\partial x_i} + \frac{\partial T''}{\partial x_i}\right)\left(\frac{\partial \xi}{\partial x_i}\frac{\partial Q_k}{\partial \eta} + \frac{\partial c}{\partial x_i}\frac{\partial Q_k}{\partial \zeta}\right)\right]\\
&+ \rho D\left[\left(\frac{\partial cp_n}{\partial x_i} + \frac{\partial cp''}{\partial x_i}\right)\left(\frac{\partial Q_T}{\partial x_i} + \frac{\partial Q_T}{\partial \zeta}\frac{\partial c}{\partial x_i} + \frac{\partial \xi}{\partial x_i}\frac{\partial Q_T}{\partial \eta} + \frac{\partial T''}{\partial x_i}\right)\right]\\
&+ \rho D\left[\left(\frac{\partial Q_T}{\partial x_i} + \frac{\partial T''}{\partial x_i}\right)\left(\frac{\partial cp_n}{\partial \eta}\frac{\partial \xi}{\partial x_i} + \frac{\partial cp_n}{\partial \zeta}\frac{\partial c}{\partial x_i}\right)\right]\\
&+ \frac{\partial p}{\partial t} - \sum_{k=1}^{N} h_k\dot{\omega}_k
\end{aligned}
\tag{B.7}
$$

Finally taking the doubly-conditional average of B.7 with respect to ξ and c yields :

$$
\begin{aligned}
&\frac{\partial Q_T}{\partial t} + \langle u_i|\eta,\zeta\rangle \frac{\partial Q_T}{\partial x_i} = \\
&\langle N_\xi|\eta,\zeta\rangle \left[\frac{\partial^2 Q_T}{\partial \eta^2} + \frac{1}{cp_n}\left(\sum_{k=1}^{N} cp_k \frac{\partial Q_k}{\partial \eta} + \frac{\partial cp_n}{\partial \eta}\right)\frac{\partial Q_T}{\partial \eta} - \frac{1}{Y_{c,\Delta}}\left(\zeta\frac{\partial^2 Y_{c,\Delta}}{\partial \eta^2} + \frac{\partial^2 Y_{c,min}}{\partial \eta^2}\right)\frac{\partial Q_T}{\partial \zeta}\right] \\
&+ \langle N_c|\eta,\zeta\rangle \left[\frac{\partial^2 Q_T}{\partial \zeta^2} + \frac{1}{cp_n}\left(\sum_{k=1}^{N} cp_k \frac{\partial Q_k}{\partial \zeta} + \frac{\partial cp_n}{\partial \zeta}\right)\frac{\partial Q_T}{\partial \zeta}\right] \\
&+ 2\langle N_{\xi,c}|\eta,\zeta\rangle \left[\frac{\partial^2 Q_T}{\partial \eta \partial \zeta} + \frac{1}{cp_n}\sum_{k=1}^{N}\frac{cp_k}{2}\left(\frac{\partial Q_k}{\partial \eta}\frac{\partial Q_T}{\partial \zeta} + \frac{\partial Q_k}{\partial \zeta}\frac{\partial Q_T}{\partial \eta}\right)\right. \\
&\left. + \frac{1}{2cp_n}\left(\frac{\partial cp_n}{\partial \eta}\frac{\partial Q_T}{\partial \zeta} + \frac{\partial cp_n}{\partial \zeta}\frac{\partial Q_T}{\partial \eta}\right) - \frac{1}{Y_{c,\Delta}}\left(\frac{\partial Y_{c,\Delta}}{\partial \eta}\right)\frac{\partial Q_T}{\partial \zeta}\right] \\
&+ \frac{1}{Y_{c,\Delta}}\left(\zeta\frac{\partial Y_{c,\Delta}}{\partial t} + \frac{\partial Y_{c,min}}{\partial t}\right)\frac{\partial Q_T}{\partial \zeta} \\
&+ \frac{\langle \partial p/\partial t|\eta,\zeta\rangle}{\langle \rho|\eta,\zeta\rangle\, cp_n} - \sum_{k=1}^{N}\frac{\langle h_k|\eta,\zeta\rangle\,\langle \dot{\omega}_k|\eta,\zeta\rangle}{\langle \rho|\eta,\zeta\rangle\, cp_n} - \frac{\langle \dot{\omega}_c|\eta,\zeta\rangle}{Y_{c,\Delta}\,\langle \rho|\eta,\zeta\rangle}\frac{\partial Q_T}{\partial \zeta} \\
&+ \frac{e_{QT} + e_{T''} + e_{cp}}{\langle \rho|\eta,\zeta\rangle\, cp_n}
\end{aligned}
\tag{B.8}
$$

with e_{QT}, $e_{T''}$, e_{cp} expressed as follow:

$$
\begin{aligned}
e_{QT} &= \frac{\partial}{\partial x_i}\left(\rho cp D \frac{\partial Q_T}{\partial x_i}\right) + \left\langle cp\left(\rho D \frac{\partial \xi}{\partial x_i}\frac{\partial}{\partial x_i}\left(\frac{\partial Q_T}{\partial \eta}\right) + \rho D \frac{\partial c}{\partial x_i}\frac{\partial x}{\partial x_i}\left(\frac{\partial Q_T}{\partial \zeta}\right)\right)\right|\eta,\zeta\right\rangle \\
e_{T''} &= \left\langle \rho cp\left(\frac{\partial T''}{\partial x_i} + u_i\frac{\partial T''}{\partial x_i} + \frac{1}{\rho}\frac{\partial}{\partial x_i}\left(\rho D \frac{\partial T''}{\partial x_i}\right)\right)\right|\eta,\zeta\right\rangle \\
e_{cp} &= \left\langle \left[\rho D \sum_{k=1}^{N} cp_k\left(\frac{\partial Q_k}{\partial x_i} + \frac{\partial y_k''}{\partial x_i}\right)\left(\frac{\partial Q_T}{\partial x_i} + \frac{\partial Q_T}{\partial \zeta}\frac{\partial c}{\partial x_i} + \frac{\partial \xi}{\partial x_i}\frac{\partial Q_T}{\partial \eta} + \frac{\partial T''}{\partial x_i}\right)\right]\right|\eta,\zeta\right\rangle \\
&+ \left\langle \left[\rho D \sum_{k=1}^{N} cp_k\left(\frac{\partial Q_T}{\partial x_i} + \frac{\partial T''}{\partial x_i}\right)\left(\frac{\partial \xi}{\partial x_i}\frac{\partial Q_k}{\partial \eta} + \frac{\partial c}{\partial x_i}\frac{\partial Q_k}{\partial \zeta}\right)\right]\right|\eta,\zeta\right\rangle \\
&+ \left\langle \rho D\left[\left(\frac{\partial cp_n}{\partial x_i} + \frac{\partial cp''}{\partial x_i}\right)\left(\frac{\partial Q_T}{\partial x_i} + \frac{\partial Q_T}{\partial \zeta}\frac{\partial c}{\partial x_i} + \frac{\partial \xi}{\partial x_i}\frac{\partial Q_T}{\partial \eta} + \frac{\partial T''}{\partial x_i}\right)\right]\right|\eta,\zeta\right\rangle \\
&+ \left\langle \rho D\left[\left(\frac{\partial Q_T}{\partial x_i} + \frac{\partial T''}{\partial x_i}\right)\left(\frac{\partial cp_n}{\partial \eta}\frac{\partial \xi}{\partial x_i} + \frac{\partial cp_n}{\partial \zeta}\frac{\partial c}{\partial x_i}\right)\right]\right|\eta,\zeta\right\rangle
\end{aligned}
\tag{B.9}
$$

Bibliography

[1] Baba, Yuya and Kurose, Ryoichi. "Analysis and flamelet modelling for spray combustion". In: *Journal of Fluid Mechanics* 612 (2008), pp. 45–79.

[2] Barro, C., Tschanz, F., Obrecht, P., and Boulouchos, K. "Influence of post-injection parameters on soot formation and oxidation in a common-rail-diesel engine using multi-color pyrometry". In: *Proceedings of the ASME* (2012).

[3] Barro, Christophe, Pandurangi, Sushant, Meyer, Philipp, Boulouchos, Konstantinos, Elbert, Philipp, and Wright, Yuri M. *THE Post Injection: Coalescence of 3D CFD-CMC Simulation, 2D Visualizations in a Constant Volume Chamber and Application in a Modern Passenger Car Diesel Engine*. Tech. rep. SAE Technical Paper, 2015.

[4] Blomberg, Christopher Kim, Zeugin, Lucas, Pandurangi, Sushant S, Bolla, Michele, Boulouchos, Konstantinos, and Wright, Yuri M. "Modeling Split Injections of ECN (Spray A) Using a Conditional Moment Closure Combustion Model with RANS and LES". In: *SAE International Journal of Engines* 9.2016-01-2237 (2016).

[5] Bolla, Michele, Wright, Yuri M, Boulouchos, Konstantinos, Borghesi, Giulio, and Mastorakos, Epaminondas. "Soot formation modeling of n-heptane sprays under diesel engine conditions using the conditional moment closure approach". In: *Combustion Science and Technology* 185.5 (2013), pp. 766–793.

[6] Bondi, S and Jones, WP. "A combustion model for premixed flames with varying stoichiometry". In: *Proceedings of the Combustion Institute* 29.2 (2002), pp. 2123–2129.

[7] Borghesi, Giulio, Mastorakos, Epaminondas, Devaud, Cécile B, and Bilger, Robert W. "Modeling evaporation effects in conditional moment closure for spray autoignition". In: *Combustion Theory and Modelling* 15.5 (2011), pp. 725–752.

[8] Bray, Domingo, Pascale, and Vervisch, Luc. “Role of the progress variable in models for partially premixed turbulent combustion”. In: *Combustion and flame* 141.4 (2005), pp. 431–437.

[9] Brown, Byrne, and Hindmarsh. “VODE: A variable-coefficient ODE solver”. In: *SIAM journal on scientific and statistical computing* 10.5 (1989), pp. 1038–1051.

[10] Brown, Byrne, and Hindmarsh. “VODPK: A Variable-Coefficient Ordinary Differential Equation Solver with the Preconditioned Krylov method GMRES for the Solution of Linear Systems”. In: *available from Netlib* (1994).

[11] Bruel, P, Rogg, B, and Bray. “On auto-ignition in laminar and turbulent non-premixed systems”. In: *Symposium (International) on Combustion*. Vol. 23. 1. Elsevier. 1991, pp. 759–766.

[12] Cha, Chong M., Kosály, George, and Pitsch, Heinz. “Modeling extinction and reignition in turbulent nonpremixed combustion using a doubly-conditional moment closure approach”. In: *Physics of Fluids (1994-present)* 13.12 (2001), pp. 3824–3834.

[13] Cha and Pitsch. “Higher-order conditional moment closure modelling of local extinction and reignition in turbulent combustion”. In: *Combustion Theory and Modelling* 6.3 (2002), pp. 425–437.

[14] Chang, C.S., Zhang, Y., Bray, K. N. C., and ROGG, B. “Modelling and Simulation of Autoignition Under Simulated Diesel-Engine Conditions”. In: *Combustion Science and Technology* 113.1 (1996), pp. 205–219.

[15] Chen, JH, Choudhary, A, De Supinski, B, DeVries, M, Hawkes, ER, Klasky, S, Liao, WK, Ma, KL, Mellor-Crummey, J, Podhorszki, N, & al. “Terascale direct numerical simulations of turbulent combustion using S3D”. In: *Computational Science & Discovery* 2.1 (2009), p. 015001.

[16] Chen, Hawkes, E. R., Sankaran, R., Mason, S. D., and IM, H. G. “Direct numerical simulation of ignition front propagation in a constant volume with temperature inhomogeneities : I Fundamental analysis and diagnostics”. In: *Combustion and Flame* (2006).

[17] Cung, Khanh, Moiz, Abdul, Johnson, Jaclyn, Lee, Seong-Young, Kweon, Chol-Bum, and Montanaro, Alessandro. “Spray–combustion interaction mechanism of multiple-injection under diesel engine conditions”. In: *Proceedings of the Combustion Institute* 35.3 (2015), pp. 3061–3068.

[18] Darbyshire, OR and Swaminathan, N. "A presumed joint PDF model for turbulent combustion with varying equivalence ratio". In: *Combustion Science and Technology* 184.12 (2012), pp. 2036–2067.

[19] Darbyshire, OR, Swaminathan, N., and Hochgreb, S. "The effects of small-scale mixing models on the prediction of turbulent premixed and stratified combustion". In: *Combustion Science and Technology* 182.9 (2010), pp. 1141–1170.

[20] Desportes, A, Zellat, M, Desoutter, G, Abouri, D, Liang, Y, and Ravet, F. "A Combined Eulerian Lagrangian Spray Amortization (ELSA) in DI Diesel Combustion: Fully Coupled Eulerian/Lagrangian Spray With ECFM-CLEH Combustion Model". In: *21st International Multidimensional Engine User's Meeting at the SAE Congress, Detroit, MI, Apr.* Vol. 11. 2011.

[21] Domingo, P. and Vervisch, L. "Triple flames and partially premixed combustion in autoignition of non-premixed turbulent mixtures". In: *Symposium (International) on Combustion.* Vol. 26. 1. 1996, pp. 233–240.

[22] Domingo, Pascale, Vervisch, Luc, and Veynante, Denis. "Large-eddy simulation of a lifted methane jet flame in a vitiated coflow". In: *Combustion and Flame* 152.3 (2008), pp. 415–432.

[23] Doran. "A multi-dimensional flamelet model for ignition in multi-feed combustion systems". In: (2011).

[24] Doran, Eric M., Pitsch, and Cook, David J. "A priori testing of a two-dimensional unsteady flamelet model for three-feed combustion systems". In: *Proceedings of the Combustion Institute* 34.1 (2013), pp. 1317–1324.

[25] Echekki, Tarek and Mastorakos, Epaminondas. "Turbulent Combustion: Concepts, Governing Equations and Modeling Strategies". In: *Turbulent Combustion Modeling.* Springer, 2011, pp. 19–39.

[26] Ehleskog, Rickard. *The influence of Multiple injections on combustion : an experimental investigation.* Tech. rep. Chalmers University of Technology, 2007.

[27] El Wakil, MM and Uyehara, OA. "A THEORETICAL INVESTIGATION OF THE HEATING-UP PERIOD". In: (1954).

[28] Environment Audit Committee. *Environment Audit Committee fifth report - air quality.* 2010. URL: http://www.publications.parliament.uk/pa/cm200910/cmselect/cmenvaud/229/22902.htm..

[29] Eswaran, V and Pope, SB. "Direct numerical simulations of the turbulent mixing of a passive scalar". In: *Physics of Fluids (1958-1988)* 31.3 (1988), pp. 506–520.

[30] Felsch, C, Gauding, M, Hasse, C, Vogel, S, and Peters, N. "An extended flamelet model for multiple injections in DI Diesel engines". In: *Proceedings of the Combustion Institute* 32.2 (2009), pp. 2775–2783.

[31] Gao, Feng and O'Brien, Edward E. "A mapping closure for multispecies Fickian diffusion". In: *Physics of Fluids A: Fluid Dynamics (1989-1993)* 3.5 (1991), pp. 956–959.

[32] Girimaji, SS. "Assumed β-pdf model for turbulent mixing: Validation and extension to multiple scalar mixing". In: *Combustion Science and Technology* 78.4-6 (1991), pp. 177–196.

[33] Gopalakrishnan, Venkatesh and Abraham, John. "An investigation of ignition behavior in diesel sprays". In: *Proceedings of the Combustion Institute* 29.1 (2002), pp. 641–646.

[34] Hasse, C. and Peters, N. "A two mixture fraction flamelet model applied to split injections in a DI Diesel engine". In: *Proceedings of the Combustion Institute* 30.2 (2005), pp. 2755–2762.

[35] Hilbert, Renan and Thévenin, Dominique. "Autoignition of turbulent non-premixed flames investigated using direct numerical simulations". In: *Combustion and flame* 128.1 (2002), pp. 22–37.

[36] Hirt, Cyril W and Nichols, Billy D. "Volume of fluid (VOF) method for the dynamics of free boundaries". In: *Journal of computational physics* 39.1 (1981), pp. 201–225.

[37] Idicheria, Cherian A and Pickett, Lyle M. *Soot formation in diesel combustion under high-EGR conditions.* Tech. rep. Sandia National Laboratories, 2005.

[38] Idicheria, Cherian A and Pickett, Lyle M. "Effect of EGR on diesel premixed-burn equivalence ratio". In: *Proceedings of the Combustion Institute* 31.2 (2007), pp. 2931–2938.

[39] Ihme, Matthias and Pitsch, Heinz. "Prediction of extinction and reignition in nonpremixed turbulent flames using a flamelet/progress variable model: 1. A priori study and presumed PDF closure". In: *Combustion and flame* 155.1 (2008a), pp. 70–89.

[40] Ihme, Matthias and Pitsch, Heinz. "Prediction of extinction and reignition in nonpremixed turbulent flames using a flamelet/progress variable model: 2. Application in LES of Sandia flames D and E". In: *Combustion and flame* 155.1 (2008b), pp. 90–107.

[41] Im, HG, Chen, and Law, CK. "Ignition of hydrogen-air mixing layer in turbulent flows". In: 27.1 (1998), pp. 1047–1056.

[42] Kee, Robert J, Grcar, Joseph F, Smooke, MD, Miller, JA, and Meeks, E. *PREMIX: a Fortran program for modeling steady laminar one-dimensional premixed flames*. 1985.

[43] Kennedy, Christopher A and Carpenter, Mark H. "Several new numerical methods for compressible shear-layer simulations". In: *Applied Numerical Mathematics* 14.4 (1994), pp. 397–433.

[44] Kennedy, Christopher A, Carpenter, Mark H, and Lewis, R Michael. "Low-storage, explicit Runge–Kutta schemes for the compressible Navier–Stokes equations". In: *Applied numerical mathematics* 35.3 (2000), pp. 177–219.

[45] Klimenko, A. Yu and Bilger. "Conditional moment closure for turbulent combustion". In: *Progress in energy and combustion science* 25.6 (1999), pp. 595–687.

[46] Kolmogorov, Andrey Nikolaevich. "The local structure of turbulence in incompressible viscous fluid for very large Reynolds numbers". In: *Proceedings: Mathematical and Physical Sciences* 434.1890 (1991), pp. 9–13.

[47] Kreutz, TG, Nishioka, M, and Law, CK. "The role of kinetic versus thermal feedback in nonpremixed ignition of hydrogen versus heated air". In: *Combustion and flame* 99.3-4 (1994), pp. 758–766.

[48] Kronenburg, A. "Double conditioning of reactive scalar transport equations in turbulent nonpremixed flames". In: *Physics of Fluids (1994-present)* 16.7 (2004), pp. 2640–2648.

[49] Landenfeld, T, Sadiki, A, and Janicka, J. "A turbulence-chemistry interaction model based on a multivariate presumed beta-pdf method for turbulent flames". In: *Flow, turbulence and combustion* 68.2 (2002), pp. 111–135.

[50] Launder, Brian Edward and Spalding, Dudley Brian. "The numerical computation of turbulent flows". In: *Computer methods in applied mechanics and engineering* 3.2 (1974), pp. 269–289.

[51] Lebas, R., Blokkeel, G., Beau, P. -A., and Demoulin, F. -X. "Coupling Vaporization Model With the Eulerian-Lagrangian Spray Atomization (ELSA) Model in Diesel Engine Conditions". In: *SAE Technical Paper*. SAE International, Apr. 2005. DOI: 10.4271/2005-01-0213. URL: http://dx.doi.org/10.4271/2005-01-0213.

[52] Lehtiniemi, harry, Mauss, fabian, Balthasar, michael, and Magnusson, ingemar. "MODELING DIESEL SPRAY IGNITION USING DETAILED CHEMISTRY WITH A PROGRESS VARIABLE APPROACH". In: *Combustion Science and Technology* 178.10-11 (2006), pp. 1977–1997.

[53] Li, Juan, Zhao, Zhenwei, Kazakov, Andrei, and Dryer, Frederick L. "An updated comprehensive kinetic model of hydrogen combustion". In: *International Journal of Chemical Kinetics* 36.10 (2004), pp. 566–575.

[54] Liu, Shiling, Hewson, John C, Chen, Jacqueline H, and Pitsch, Heinz. "Effects of strain rate on high-pressure nonpremixed n-heptane autoignition in counterflow". In: *Combustion and flame* 137.3 ((2004)), pp. 320–339.

[55] Mastorakos. "Ignition of turbulent non-premixed flames". In: *Progress in Energy and Combustion Science* 35.1 (2009), pp. 57–97.

[56] Mastorakos, Baritaud, and Poinsot. "Numerical simulations of autoignition in turbulent mixing flows". In: *Combustion and Flame* 109.1 (1997), pp. 198–223.

[57] Mastorakos and Bilger. "Second-order conditional moment closure for the autoignition of turbulent flows". In: *Physics of Fluids (1994-present)* 10.6 (1998), pp. 1246–1248.

[58] Matheson, Tomas. "Presumed pdf modelling for turbulent spray combustion". In: (2016, PhD thesis).

[59] Mortensen, Mikael and Bilger. "Derivation of the conditional moment closure equations for spray combustion". In: *Combustion and Flame* 156.1 (2009), pp. 62–72.

[60] Nesbit, JE, Naber, JD, Lee, SY, Kurtz, E, Ge, HW, and Robarge, N. *23rd Annual Conference on Liquid Atomization and Spray Systems*. 2011.

[61] Nguyen, Phuc-Danh, Vervisch, Luc, Subramanian, Vallinayagam, and Domingo, Pascale. "Multidimensional flamelet-generated manifolds for partially premixed combustion". In: *Combustion and Flame* 157.1 (2010), pp. 43–61.

[62] O'Connor, J. and Musculus, M. "Post Injections for Soot Reduction in Diesel Engines: A Review of Current Understanding". In: *SAE Int. J. Engines* 6.1 (2013), pp. 400–421.

[63] Osher, Stanley and Sethian, James A. "Fronts propagating with curvature-dependent speed: algorithms based on Hamilton-Jacobi formulations". In: *Journal of computational physics* 79.1 (1988), pp. 12–49.

[64] Paola, Girogio De. “Conditional Moment Closure for Autoignition in Turbulent Flows”. In: (2007, PhD thesis).

[65] Passot, T and Pouquet, A. “Numerical simulation of compressible homogeneous flows in the turbulent regime”. In: *Journal of Fluid Mechanics* 181 (1987), pp. 441–466.

[66] Pei, Yuanjiang, Hawkes, Evatt R, and Kook, Sanghoon. “A comprehensive study of effects of mixing and chemical kinetic models on predictions of n-heptane jet ignitions with the PDF method”. In: *Flow, turbulence and combustion* 91.2 (2013), pp. 249–280.

[67] Peters, N. “Laminar flamelet concepts in turbulent combustion”. In: *Symposium (International) on Combustion*. Vol. 21. 1. 1988, pp. 1231–1250.

[68] Peters, N. *Turbulent combustion*. Cambridge university press, 2000.

[69] Petroleum. *The future of Petroleum*. 2015. URL: http://www.petroleum.co.uk/the-future-of-petroleum.

[70] Pickett. *Engine Combustion Network*. 2016. URL: http://www.sandia.gov/ecn/dieselSprayCombustion.php.

[71] Pitsch, Heinz. “Large-eddy simulation of turbulent combustion”. In: *Annu. Rev. Fluid Mech.* 38 (2006), pp. 453–482.

[72] Poinsot, Veynante, & al. “Theoretical and numerical combustion”. In: (2005).

[73] Pope, Stephen. *Turbulent flows*. 2000.

[74] Ranz, WE. “Evaporation from drops 1”. In: *Chem. Eng. Prog.* 48 (1952), p. 141.

[75] Ranz, WE. “Evaporation from drops: Part II”. In: *Chem. Engng. Prog.* 48 (1952), pp. 173–180.

[76] Reitz, Rolf D and Diwakar, R. *Effect of drop breakup on fuel sprays*. Tech. rep. SAE Technical Paper, 1986.

[77] Reveillon, Julien and Vervisch, Luc. “Analysis of weakly turbulent dilute-spray flames and spray combustion regimes”. In: *Journal of Fluid Mechanics* 537 (2005), pp. 317–347.

[78] Richardson, E.S, Chakraborty, N., and Mastorakos, E. “Analysis of direct numerical simulations of ignition fronts in turbulent non-premixed flames in the context of conditional moment closure”. In: *Proceedings of the combustion institute* 31.1 (2007), pp. 1683–1690.

[79] Ruan, S, Swaminathan, N, Bray, KNC, Mizobuchi, Y, and Takeno, T. "Scalar and its dissipation in the near field of turbulent lifted jet flame". In: *Combustion and Flame* 159.2 (2012), pp. 591–608.

[80] Salehi, Fatemeh, Talei, Mohsen, Hawkes, Evatt R., Yoo, Chun Sang, Lucchini, Tommaso, DfffdfffdfffdErrico, Gianluca, and Kook, Sanghoon. "Conditional moment closure modelling for {HCCI} with temperature inhomogeneities". In: *Proceedings of the Combustion Institute* (2014).

[81] Sarangi, Asish K., Garner, Colin P., McTaggart-Cowan, Gordon P., Davy, Martin H., Wahab, Emad, and Peckham, Mark. "The effects of split injections on high exhaust gas recirculation low-temperature diesel engine combustion". In: *International Journal of Engine Research* 14.1 (2013), pp. 68–79.

[82] Schneider, E, Maltsev, A, Sadiki, A, and Janicka, J. "Study on the potential of BML-approach and G-equation concept-based models for predicting swirling partially premixed combustion systems: URANS computations". In: *Combustion and Flame* 152.4 (2008), pp. 548–572.

[83] Skeen, Scott, Manin, Julien, and Pickett, Lyle M. "Visualization of ignition processes in high-pressure sprays with multiple injections of n-dodecane". In: *SAE International Journal of Engines* 8.2015-01-0799 (2015), pp. 696–715.

[84] Smith, Bilger, and Chen. "Modelling of nonpremixed hydrogen jet flames using a conditional moment closure method". In: *Symposium (International) on Combustion*. Vol. 24. 1. Elsevier. 1992, pp. 263–269.

[85] Smooke, Mitchell D. "Reduced kinetic mechanisms and asymptotic approximations for methane-air flames: a topical volume". In: *Reduced Kinetic Mechanisms and Asymptotic Approximations for Methane-Air Flames*. Vol. 384. 1991.

[86] Spalding, D Brian. "Development of the eddy-break-up model of turbulent combustion". In: *Symposium (International) on Combustion*. Vol. 16. 1. Elsevier. 1977, pp. 1657–1663.

[87] STAR-CD. "STAR-CD V4.20 Methodology". In: http://www.adapco.com (2004).

[88] Subramaniam, S. and Pope, S.B. "A mixing model for turbulent reactive flows based on Euclidean minimum spanning trees". In: *Combustion and Flame* 115 (1998), pp. 487–514.

[89] Swaminathan, N. and Bilger. "Analyses of conditional moment closure for turbulent premixed flames". In: *Combustion Theory and Modelling* 5.2 (2001), pp. 241–260.

[90] Valiño, Luis. “A field Monte Carlo formulation for calculating the probability density function of a single scalar in a turbulent flow”. In: *Flow, turbulence and combustion* 60.2 (1998), pp. 157–172.

[91] Veynante, D., Trouvé, A., Bray, KNC, and Mantel, T. “Gradient and counter-gradient scalar transport in turbulent premixed flames”. In: *Journal of Fluid Mechanics* 332 (1997), pp. 263–293.

[92] Veynante, Denis and Vervisch, Luc. “Turbulent combustion modeling”. In: *Progress in energy and combustion science* 28.3 (2002), pp. 193–266.

[93] Wright, YM, De Paola, G, Boulouchos, K, and Mastorakos, E. “Simulations of spray autoignition and flame establishment with two-dimensional CMC”. In: *Combustion and flame* 143.4 (2005), pp. 402–419.

[94] Wright, Yuri M, Margari, Ourania-Nektaria, Boulouchos, Konstantinos, De Paola, Giorgio, and Mastorakos, Epaminondas. “Experiments and simulations of n-heptane spray auto-ignition in a closed combustion chamber at diesel engine conditions”. In: *Flow, turbulence and combustion* 84.1 (2010), pp. 49–78.

[95] Yun, Hanho, Wermuth, Nicole, and Najt, Paul. *Development of robust gasoline HCCI idle operation using multiple injection and multiple ignition (MIMI) strategy*. Tech. rep. SAE Technical Paper, 2009.